Metabolic function in the ocular ecosystem relies on interactions between the retina and retinal pigment epithelium and remains robust in aging

Kristine Anastasia Tsantilas

A dissertation

submitted in partial fulfillment of the

requirements for the degree of

Doctor of Philosophy

University of Washington

2021

Reading Committee:

James B. Hurley, Chair

Peter S. Rabinovitch

Andrea E. Wills

Program Authorized to Offer Degree:

Biochemistry

University of Washington

Abstract

Metabolic function in the ocular ecosystem relies on interactions between the retina and retinal pigment epithelium and remains robust in aging

Kristine Anastasia Tsantilas

Chair of the Supervisory Committee:

James B. Hurley

Biochemistry

The vertebrate eye is a unique ecosystem comprised of a myriad of different cells that all function in concert to facilitate vision. The electrical signal in the eye that is transmitted to the brain begins with the retina, an ordered structure made up of glia and neurons. Highly specialized photoreceptor neurons begin that signaling cascade when struck by light. Photoreceptors interact constantly with the neighboring retinal pigment epithelium (RPE) which replenishes signaling molecules needed for photoreceptor signal transduction. However, these cells are also metabolically intertwined. When photoreceptors start to die, the RPE frequently goes with them, and the inverse has also been found. To better understand the metabolic adaptations and complex interplay between these two specialized cell-types, we examined the eye in health and under stress.

In a normal vertebrate eye, we found that the retina and retinal pigment epithelium have cooperative metabolic strategies that differ significantly from expected paradigms seen in the brain. The retina is known to be glycolytic, while the RPE appears to rely more on its mitochondria. We found that it is specifically photoreceptor neurons that are consuming glucose. Significant quantities of lactate are exported by the retina. The RPE appears to prefer lactate over glucose as a fuel. This indicates that the RPE passes along glucose to the retina, which generates lactate and exports it for the RPE to consume. While the retina predominantly relies on glycolysis, the size, quantity, distribution, and complexity of the mitochondria in photoreceptors were found to be incredibly dynamic depending upon circadian rhythm. Nightfall brought large, mitochondrially-connected networks and increased metabolic flux through succinate dehydrogenase.

We used a targeted GC-MS assay to probe the metabolic capacity of retina and RPE-choroid-sclera complexes (eyecup) when provided ^{13}C-labeled glucose or glutamine. The metabolism of the retina and eyecups appear to be remarkably resilient to stress. Mutations in NNT and Rd8, which effect metabolism and cellular structure, respectfully, do not impact reductive flux from glutamine. Advanced age also did not severely impact the metabolic capacity of either tissue. We identified a defect in glutamine metabolism of eyecups and a trend towards lower glutamine-driven OCR. Otherwise, glucose uptake, glucose flux, anaplerotic flux, and amino acid pools were unaffected in retinas and eyecups with age. Given the known functional decline of vision which we were able

to confirm using electroretinograms in aged mice, the near complete lack of change with age was intriguing. Future studies of the aged eye should consider the application of additional *in vivo* approaches to metabolic characterization. This will confirm if the intrinsic stability of these tissues' metabolism holds in the less hospitable environment of the aging eye and may still represent a viable treatment option for age-related vision loss and blindness.

Table of Contents

List of Figures and Tables

Figures

Supplementary Figures

Tables

Supplementary Tables

Glossary

AKG: α-ketoglutarate

ANLS: astrocyte-neuron lactate shuttle

BBB: blood-brain barrier

2-NBDG: (2-(*N*-(7-Nitrobenz-2-oxa-1,3-diazol-4-yl)Amino)-2-Deoxyglucose)

Ca^{2+}: calcium ion

CB: cell body

CNG: cyclic-nucleotide gated

cyto-GCaMP: cone cytosolic Ca^{2+} sensor GCaMP3

cyto-GFP: cone cytosolic GFP

DD: 24-h dark

ELAM (or SS-31): Elamipretide

ELAM+NMN: Elamipretide and nicotinamide mononucleotide

ER: endoplasmic reticulum

ER-GFP: cone endoplasmic reticulum targeted GFP

Eyecup: RPE-choroid-sclera complex

GAP: glyceraldehyde-3-phosphate

GAPDH: glyceraldehyde-3-phosphate dehydrogenase

GC-MS: gas chromatography-mass spectrometry

GCL: ganglion cell layer

GFAP: glial fibrillary acidic protein

GFP: green fluorescent protein

Glc: glucose

GLUT: glucose transport protein

gnat2: cone transducin alpha promoter (also TαCP)

GS: glutamine synthetase

hfRPE: human fetal RPE

IB: immunoblot

IHC: immunohistochemistry

INL: inner nuclear layer

IPL: inner plexiform layer

IPM: interphotoreceptor matrix

IS: inner segment

KRB: Krebs-Ringer Buffer

Lac: lactate

LC3: microtubule-associated protein 1 light chain 3

LD: 14-h/10-h light-dark

LDH: lactate dehydrogenase

MCI: mitochondrial complexity index

mEC: mouse eyecup

Mg^{2+}: magnesium ion

MGC: Müller glia cell

mito-cpYFP: cone mitochondrially targeted circularly-permuted YFP

MO: months-old

mRetina: mouse retina

MT-COX1: mitochondrial cytochrome C oxidase

mtDNA: mitochondrial DNA

NAD+: nicotinamide adenine dinucleotide

NMNAT: nicotinamide mononucleotide adenylyltransferase

NMN: nicotinamide mononucleotide

Nrl: neural retina-specific leucine zipper promoter

OCR: oxygen consumption rate

ONL: outer nuclear layer

OPL: outer plexiform layer

OS: outer segment

PDE6: generic symbol for photoreceptor cyclic GMP phosphodiesterases

PDE6c: cone phosphodiesterase subunit

PK: pyruvate kinase

PKM2: pyruvate kinase isoform M2

PR: photoreceptor

Pyr: pyruvate

Rd8: retinal degeneration 8

Rlbp: retinaldehyde binding protein promoter

RPE: retinal pigment epithelium

Rxn: reaction

SBFSEM: serial block-face scanning electron microscopy

SD: standard deviation

SE: standard error of the mean

SEM: scanning electron microscopy

SS: Szeto-Schiller

SS-31 (or ELAM): Szeto-Schiller peptide 31

TαCP (or gnat2): cone transducin alpha promoter

TCA: tricarboxylic acid

tdTomato: tandem dimeric tomato fluorescent protein

Tg: transgenic

Trβ2: thyroid hormone receptor beta 2 promoter

WT: wild-type

YFP: yellow fluorescent protein

ZT(#): Zeitgeber Time

Acknowledgments

I must begin by admitting for the record that I had no idea what pursuing a PhD would be like before I began... although as a first-generation graduate student, I had many hopes and hypotheses. Through this process, I learned a great deal about myself. This thesis represents only one conclusion of this time (albeit a wordy one, even for me). But I would be remiss if I didn't emphasize how many people **made** this experience – and made it an adventure.

The ecosystem of the Hurley and Brockerhoff laboratories was a place of creative exploration. Jim's boundless ingenuity was an inspiration. Sue exemplified scientific rigor. I learned so much from the graduate students, research scientists, postdoctoral fellows, and undergraduate researchers in this ecosystem. I wish to offer my gratitude to Michelle Giarmarco, Celia Bisbach, Whitney Cleghorn, Daniel Hass, Rachel Hutto, Mark Kanow, Jonathan Linton, Connor Jankowski, Benjamin Bauer, Kaitlyn Rutter, Brian Robbings, Daniel Brock, Ashlee Chisholm, William Ge, Jianhai Du, and Christopher Farnsworth. Ed Parker in the Vision Core and the laboratory of Jennifer Chao – especially Abbi Engel and Kelie Gonzalez helped make this place fun.

The work in this dissertation could not have happened without the team of professionals who cared for the mice and zebrafish. In the SLU mouse facility, I want to acknowledge Clara Suelen, Anthony Scott, and Csaba Nagy. In the UW SLU aquatics facility, I am grateful for the time and dedication of Stanley Kim, Tatiana Chua, and Jeanot Muster.

My scientific education and personal development benefited from neighboring ecosystems. The 2015 Biochemistry and BPSD cohorts made the first years of graduate school an adventure. I likely would not be writing these acknowledgements without the support I got from Erin Kirschner the last 6 years. Jennifer Trebby always reminded me to take a step back and be kind to myself. As part of my thesis committee, Andrea Wills, David Raible, and Jennifer Chao provided scientific and career advice. Martin Sadilek

was one of the most patient teachers I have ever had the pleasure to work with, and I hope that someday I can be a mentor to a young scientist the way he was for me.

The geroscience community at the University of Washington welcomed this graduate student. Admittedly, I have to imagine it was a strange sight to see me wandering around with a light microscope in a box asking about when I could come back to collect more eyeballs. Peter Rabinovitch always went the extra mile to help me advance my project and my career. I truly can't thank him enough. David Marcinek and the P01 helped me better understand research. Ellen Cravens and Shelby Knowles always kept me on track – in person and over Zoom. It was a pleasure working with the people in these groups who embody all the best parts of science, but I am especially grateful to Mariya Sweetwyne, Monica Sanchez-Contreras, Jeremy Whitson, Ana Valencia, Matt Campbell, and Huiliang Zhang. They give me hope that the future of science will be better than the past.

Many people helped get me to graduate school. Thanks to my friends from Phoenix that cheered me on from afar – Katrine (Katey!) Nickel, Heidi Neumann, Victoria Dirgo, and Kaylyn Adams. I had phenomenal mentors as a young(er) scientist. Patrick Pirrotte, Emma Farrell, Edward Skibo, and Neal Woodbury all have my gratitude.

Allison Maker and Arianne Caudal were the best support system I could have asked for. I'm excited to see the wonderful places we will go!

To my family, who were always with me through the good times and the bad – Tammy Tsantilas, Jim Tsantilas, Nick Tsantilas, Betty Hart (Nana), Tiffany and Travis Currier, Stella and Dean Tsantilas (Yiayia and Papou). I love you all, and hopefully we'll see each other more in 2021!

Although he's listed last, Ryan King is certainly not the least. He might even be… the King. Through his consistent support and reminding me to cherish the little things, here we are on the other side! Ryan, you truly light up my life. I love you.

Dedication

Dedicated to all of the women in my life who raised me up so that I could fly.

Especially my mom, Tammy
and my Nana, Betty.

Chapter 1 - Introduction

The vertebrate eye

It has been said that “the eyes are windows into the soul”. The astounding feats of nature that are the eye and the process of vision are profoundly unique in biology. An illustration of a cross-section of the human eye is shown in Figure 1.1A.

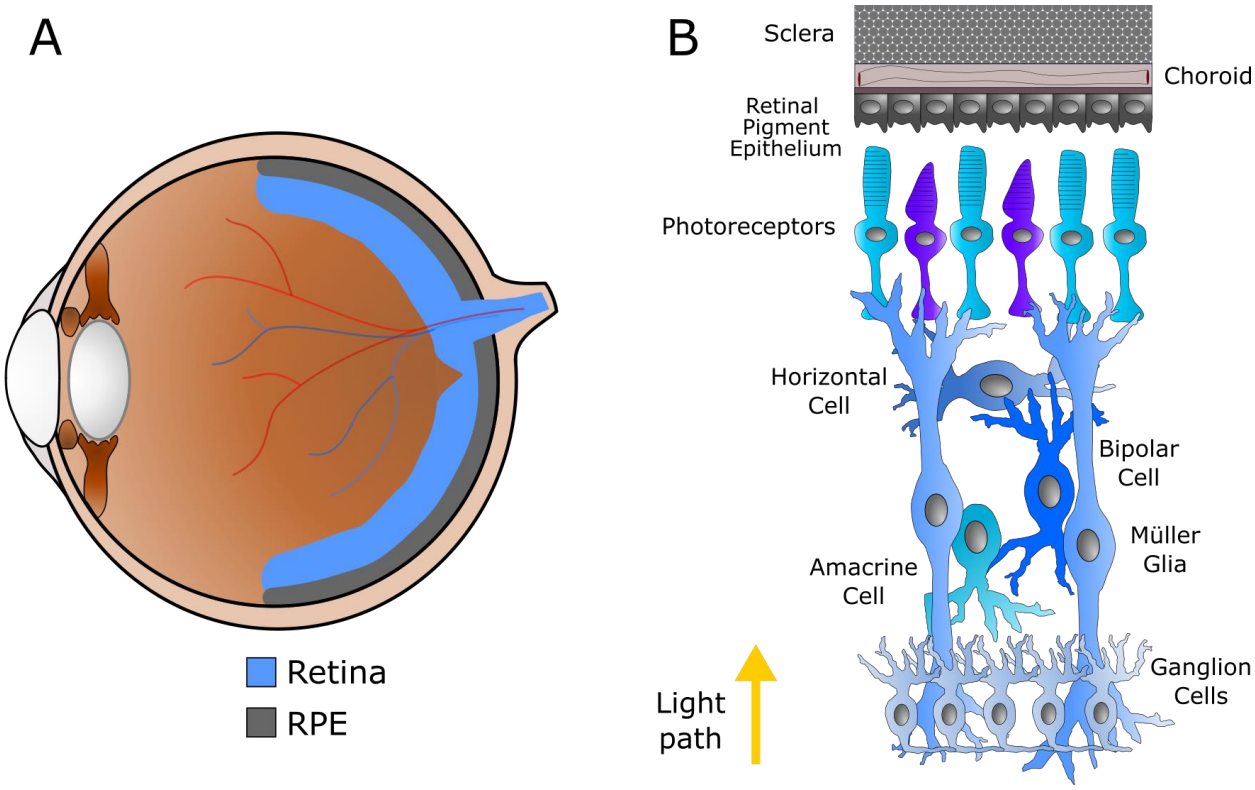

Figure 1.1: Many specialized tissues work in concert to facilitate vision in the vertebrate eye

An illustration of the vertebrate eye highlights the retina in blue and the retinal pigment epithelium (RPE) in gray, although the image is not to scale as the RPE is a monolayer of cells while the retina is a highly laminated tissue containing numerous cell types (A). If a cross-section of the back of the eye is taken, many of these cell types and their location relative to each other can be visualized (B).

In order to see, light from the environment must first pass through several layers of tissue - the cornea, lens, and vitreous. The light that breaks through must then strike the very back of the eye which is home to the retina, a highly laminated tissue comprised of different neurons and glia. The retina may begin the transmission of signals in concert with the retinal pigment epithelium – another tissue critical to visual function – on to the brain. The retina and RPE are two critical tissues that will be emphasized in this dissertation that are highlighted in relation to the rest of the eye in Figure 1.1A. The

critical cellular components of the retina and neighboring tissues are shown in more detail in Figure 1.1B.

The retina and photoreceptors

Of the tissues needed to form a functioning eye, the retina has captivated the imagination of neuroscientists, cell biologists, and medical professionals alike. A century has passed since Santiago Ramón y Cajal began probing the cellular architecture of the retina using the Golgi method and how this might impact its function (Piccolino, 1988). Of the diverse cell types that comprise the retina (Figure 1.1B), the photoreceptors represent that first point of contact between visual stimuli and the brain. There are two classes of photoreceptors: rods that facilitate vision in dim light and various sub-types of cones which are critical for color discernment, vision in bright light, and temporal resolution. These differing sensitivities are facilitated by different molecular components and mechanisms (Arshavsky et al., 2002; Kefalov, 2012). Although much of this work discusses photoreceptors, other neurons and are crucial for a functional retina. The radially-oriented Müller glia that span the whole retina provide structural, metabolic and homeostatic support for the entire retina (Vecino et al., 2016). Ganglion cells represent the terminal neurons in the eye leading to the optic nerve, which carries electrical signals to the brain (Dowling, 1987).

The retinal pigment epithelium (RPE) and choroid

Nutrients in the eye are predominantly sourced from a layer of blood vessels in the posterior segment of the eye called the choroid. In humans, mice, zebrafish and other vertebrate organisms, these blood vessels are situated between the sclera and RPE (Dowling, 1987). The RPE is a pigmented monolayer of cells that serves in many different capacities in the eye which were thoroughly reviewed by Olaf Strauss in 2005. Briefly, the RPE secretes signaling factors, absorbs light, and plays crucial roles in phototransduction, photoreceptor support, and transport of nutrients. At light onset, the RPE phagocytoses photoreceptor outer segments. The 11-cis-retinal that photoreceptors need to successfully complete the visual cycle is regenerated in RPE. Of particular importance to this work, the tight junctions formed between RPE cells

effectively forms a blood-retina barrier, mediating nutrient transport between the retina and the nearby choroidal blood supply (Strauss, 2005).

Models of vision: Highlighting human, mouse, and zebrafish eyes

Historically, models of the visual system have been quite diverse. Although mice and rats represent the most frequently used vertebrate models in recent years, rabbits (Barlow and Levick, 1965), tiger salamanders (Rozenblit and Gollisch, 2020), ground squirrels (Li, 2020), bullfrogs (Peterson and Miller, 1995), zebrafish (Brockerhoff et al., 1998; Chhetri et al., 2014; Gestri et al., 2012), raptors (Potier et al., 2020), goldfish (Dmitriev and Mangel, 2000), and non-human primates (Mustari, 2017; Neitz and Neitz, 2014) represent only a sample of the animal models in which humans have studied vision.

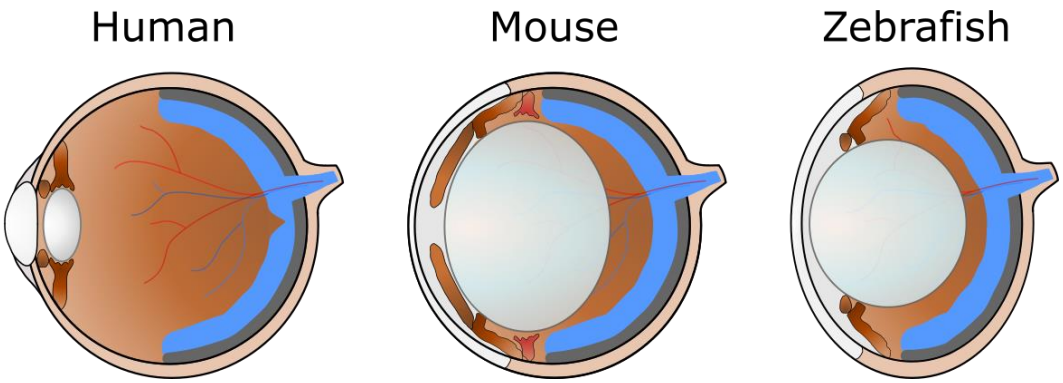

Figure 1.2: Illustrating broad structural differences in human, mouse, and zebrafish eyes.
Humans have smaller lenses and increased volume of vitreous relative to mice and zebrafish. Critically, mice and zebrafish lack a macula and fovea. This difference in retinal architecture limits some applications of these models in the study of vision. Note that the eyes are not scaled to the size of the organism in this image.

Considering multiple organisms can broadly increase our understanding of vision and offer avenues of potential treatment of disease. Selecting the model to support the planned experiments is crucial. Retinal composition differs significantly between these three species in terms of the fraction of rods and cones, as well as the sub-types of cones. The mouse retina is only 3% cone photoreceptors (Carter-Dawson and LaVail, 1979), while zebrafish retina contains more than 60% cones (Raymond et al., 2014). Cone photoreceptor sub-types can differ wildly between species and reflect their

environment. Humans have three types of cones (Hofer et al., 2005; Sabesan et al., 2015). Zebrafish are tetrachromats with a regular mosaic that includes UV-sensitive cones (Brockerhoff et al., 1998). Mice have two cone types (Szél et al., 1992), while the mantis shrimp has at least 12 distinct sub-types (Thoen et al., 2014). The study of light-mediated vision in the mouse is challenged by the scarcity of cone photoreceptors in the eye, whereas zebrafish represent a more tractable option for studying cones. Beyond composition, zebrafish are uniquely suited to study regeneration. Zebrafish possess the ability to regenerate their retina (Hitchcock and Raymond, 2004), and recent work in the optic nerve suggests this ability is maintained even in advanced age (Van houcke et al., 2017). Müller glia can behave as stem cells and repopulate cells (Thomas et al., 2016). A gene first identified in zebrafish as necessary for regeneration has been over-expressed in mouse Muller glia to generate new neurons (Jorstad et al., 2017).

Aging impact on vision

Life expectancy has been increasing (Figure 1.3A) in the United States and around the world (Roser et al., n.d.). The trajectory of aging in the United States (US Census Bureau, 2017) is trending towards a higher percentage of the population being aged 65 plus (Figure 1.3B), which is increasing rapidly with the “baby boomer” generation. Historically, the distribution of the population’s age has taken on a pyramid-like shape where there are more young people and fewer elderly (Figure 1.3C). However, by 2020 (Figure 1.3D), this distribution had shifted to where the number of people in different age brackets was similar in all but the highest age brackets (75+). Projections suggest that by 2060, the population age distribution in the US will look more like a column where age groups are more equal in number across all ages (Figure 1.3E). Increased resources in this field will be critical given what is currently known about the prevalence of age-related vision loss and how the population around the world is aging.

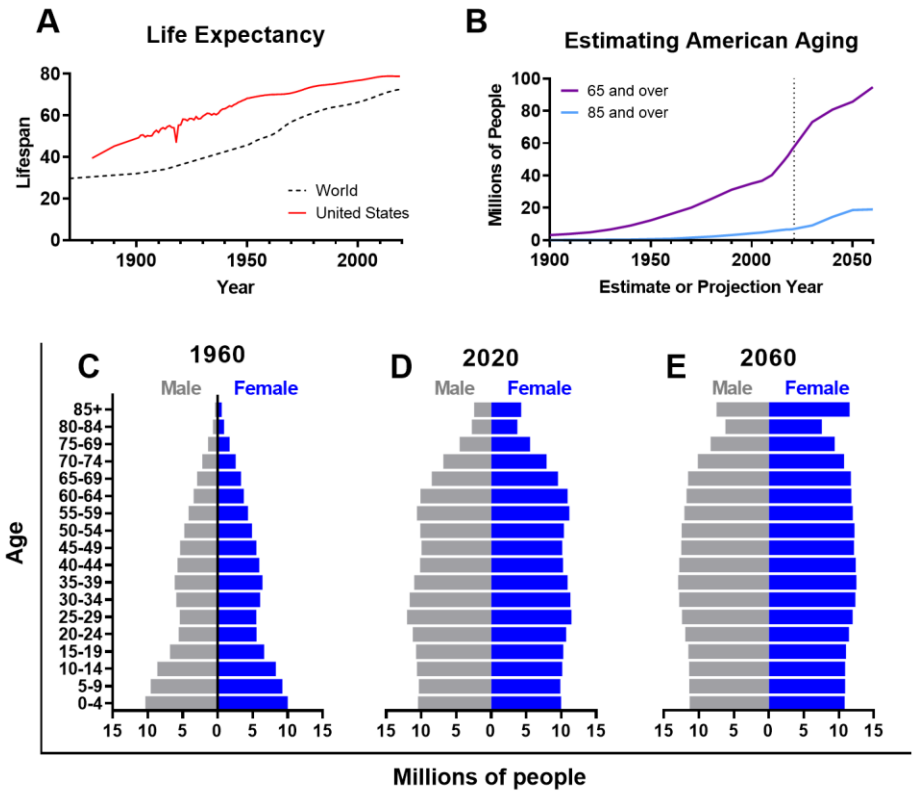

Figure 1.3: The human population is living longer and the US is having fewer offspring
Life expectancy data from OurWorldInData.org and population data from the US Census Bureau.

While the eye has captivated researchers for many years, the study of how aging impacts vision and the cellular processes needed to facilitate vision is relatively new. The first comprehensive studies of how the visual system changes due to aging are only about 50 years old (Owsley, 2011). Four major blinding disorders are intrinsically linked to aging processes: glaucoma, cataracts, diabetic retinopathy and age-related macular degeneration (Alavi, 2016; Crews et al., 2017; Klein and Klein, 2013). In the developed world, age-related macular degeneration (AMD) represents a leading cause of blindness in the elderly. Though estimates vary, approximately 25% of individuals by age 80 are affected by AMD. This works out to about 10 million people currently blind or at risk of becoming blind in the U.S. (Ambati and Fowler, 2012). In addition to increased risk of pathology, the general age-related loss of vision is a threat to healthspan (Richardson et al., 2016). Despite the prospect of increased longevity, many elderly people face reduced quality of life with increased risk of disability from falls, immobility,

and depression linked to visual impairment (Abou-Hanna et al., 2021; Crews et al., 2017; Heesterbeek et al., 2017; Saftari and Kwon, 2018). Improving age-related vision loss would enhance human healthspan around the world.

Age-related changes in ocular tissues

Nine primary, antagonistic and integrative hallmarks of aging have been defined (López-Otín et al., 2013) to describe the processes altered with aging. These hallmarks include declining proteostasis (Labbadia and Morimoto, 2015), epigenetic changes (Booth and Brunet, 2016; Pal and Tyler, 2016), metabolic alterations (Fontana et al., 2010; Soultoukis and Partridge, 2016) and mitochondrial dysfunction (Gonzalez-Freire et al., 2015). The visual system represents a critical and under-studied system in aging research in which these hallmarks are all known to be altered.

A series of physical changes in the eye occur in aging. Pupillary miosis (Guillon et al., 2016), and increased optical density and stiffness of the lens (Duncan et al., 1997; Michael and Bron, 2011) decrease luminance. In the retina there is an increase in inflammatory markers (Xu et al., 2008) and a loss of synaptic connections (Cavallotti et al., 2004; Samuel et al., 2011). In aging primate retina, glycolysis increases while ATP levels and cytochrome c oxidase levels decline (Kam et al., 2019b). RPE cells are lost, and those remaining tend to hypertrophy, become multinucleate (Chen et al., 2016) and accumulate age-associated deposits of lipofuscin and drusen (Bonilha, 2008; Gu et al., 2012). Various tissues in the aging murine eye exhibit changes in steady state metabolite levels (Wang et al., 2018).

Metabolism in the retina and RPE

Metabolic function is directly linked to the capability of neurons in both the retina and brain to process visual information (Niven and Laughlin, 2008). Among neuronal tissues, the retina has exceptionally high energetic requirements (Ames et al., 1992) and the visual response has been directly linked to retinal glycolytic and mitochondrial function (Winkler, 1981).

The metabolism of cells in the eye are highly specialized. It has been extensively documented that the retina is overwhelmingly glycolytic (Ames et al., 1992; Krebs, 1927; Warburg, 1925) and that a majority of the glucose taken up by the retinas is converted to lactate from the pyruvate generated from glycolysis and exported from the cells (Winkler et al., 2008). However, there are many types of cells in the retina including neurons and glia (Figure 1.1B). Discerning what type of cells were the source of the strong glycolytic flux in the retina required significant work in the field. An early model was the astrocyte-neuron lactate shuttle (ANLS) identified in the brain in which glia consume glucose, produce lactate, and neurons consume the lactate to use as fuel (Bélanger et al., 2011). However, there was evidence to suggest this was not the case in retina. In the traditional paradigm, glia express pyruvate kinase, the enzyme required for conversion of PEP to pyruvate. In the retina, pyruvate kinase was expressed in the photoreceptors, but not in surrounding Müller glia (Lindsay et al., 2014). Additionally, when photoreceptors are not present as in a degenerated AIPL1 mutant line, the amount of exported lactate was found to decrease significantly (Lindsay et al., 2014). Recent reports have shown that the up-regulation of glycolysis in degenerating photoreceptors can improve outcomes (Venkatesh et al., 2015; Zhang et al., 2016).

Given the propensity of the retina to use glucose, the separation of the retina from the choroidal blood supply begged the question – why does the RPE pass along glucose? RPE cells are known to express the glucose transporter GLUT1 (Lehmann et al., 2014) and altering glucose usage in RPE can be detrimental to the retina. Retinal degeneration was induced by increasing glycolysis (Kurihara et al., 2016; Zhao et al., 2011) or deleting glucose transporter, GLUT1, in RPE (Swarup et al., 2019). Recent work has found that the RPE relies less on glycolysis and more on mitochondria (Bisbach et al., 2020). In this dissertation, particular attention is paid to the retina, RPE, and the symbiotic metabolic relationship these tissues have.

Chapter 2 - Biochemical adaptations of the retina and retinal pigment epithelium support a metabolic ecosystem in the vertebrate eye

Citation

The work described in this chapter was published in *eLife*:

> **Biochemical adaptations of the retina and retinal pigment epithelium support a metabolic ecosystem in the vertebrate eye**
> Mark A Kanow, Michelle M Giarmarco, Connor SR Jankowski, Kristine Tsantilas, Abbi L Engel, Jianhai Du, Jonathan D Linton, Christopher C Farnsworth, Stephanie R Sloat, Austin Rountree, Ian R Sweet, Ken J Lindsay, Edward D Parker, Susan E Brockerhoff, Martin Sadilek, Jennifer R Chao, James B Hurley
> *eLife.* Sep 2017, 6:e28899; DOI: 10.7554/eLife.28899

Introduction

Mutations in any of more than 140 genes can cause photoreceptors in a vertebrate retina to degenerate (Bramall et al., 2010). Much has been gained by studying those genes and specific therapeutic strategies based on their functions are being developed (Sengillo et al., 2017). However, the biochemical diversity of those genes also suggests that the consequences of their loss or gain of function may converge onto a few essential metabolic processes (Punzo et al., 2009; Zhang et al., 2016). A more general understanding of what photoreceptors need to survive could lead to broadly applicable therapeutic strategies. With that in mind, we have been investigating the fundamental nature of energy metabolism in the retina and in the retinal pigment epithelium (RPE) (Du et al., 2016a, 2016b, 2015, 2013a, 2013b; Lindsay et al., 2014; Linton et al., 2010).

The sugar glucose fuels the outer retina and comes from the choroidal blood, but it first must traverse the RPE. The RPE is a monolayer of polarized cells between the choroid and retina that functions as a blood-retina barrier. RPE cells, bound together by tight junctions, express specific transporter proteins on their opposing basolateral and apical surfaces (Lehmann et al., 2014). Glucose from the choroid enters RPE cells through transporters on the basolateral surface. If metabolic enzymes within the RPE cell do not consume it, the glucose moves down a concentration gradient toward the apical surface and exits through transporters to the retina.

Most glucose that reaches the retina is consumed in glycolysis and converted to lactate. In the 1920's Warburg and Krebs identified both retinas and tumors as relying mostly on 'aerobic glycolysis' (Krebs, 1927; Warburg, 1925), a type of metabolism that converts glucose to lactate even when O_2 is available (Figure 1.3B). Photoreceptors in the outer retina are the likeliest site of aerobic glycolysis (Chinchore et al., 2017; Du et al., 2016a; Lindsay et al., 2014; Medrano and Fox, 1995; Wang et al., 1997; Winkler, 1981). The importance of aerobic glycolysis for photoreceptor survival and function is not yet clear, but it is thought to support anabolic activity (Chinchore et al., 2017; Rajala et al., 2016; Rueda et al., 2016; Venkatesh et al., 2015; Zhang et al., 2016).

Energy metabolism in RPE cells is strikingly different from photoreceptors. RPE cells are specialized for a type of mitochondrial energy metabolism called reductive carboxylation (Du et al., 2016b) that can support redox homeostasis. The reliance of RPE on mitochondrial metabolism is in contrast to aerobic glycolysis in photoreceptors, and this motivated us to directly compare the metabolic features of retina and RPE.

Recent reports used genetic manipulations to qualitatively alter energy metabolism either in photoreceptors or in RPE cells in vivo. In one study, glycolysis in rods was enhanced by blocking expression of SIRT6 (Zhang et al., 2016). Another study enhanced glycolysis in cones by activating mTORC1 (Venkatesh et al., 2015). Both found that more glycolytic photoreceptors are more robust; degeneration of photoreceptors was delayed in retinas afflicted by a mutation associated with retinitis pigmentosa (Venkatesh et al., 2015; Zhang et al., 2016). In contrast, when glycolysis in RPE cells was enhanced by knocking out VHL (Kurihara et al., 2016) or by knocking out an essential mitochondrial transcription factor (Zhao et al., 2011), the neighboring photoreceptors died.

These in vivo findings are seemingly contradictory when considered only from a cell autonomous perspective. Why does enhancing glycolysis benefit some cells and endanger others? Here we propose a context for those findings: the retina and RPE function as a metabolic ecosystem. We show that photoreceptors are the primary cells in the retina that take up glucose. Photoreceptors convert glucose to lactate, which then fuels neighboring cells in the retina. We report that lactate can suppress glycolysis in RPE cells, protecting glucose so that more of it can reach the retina. Based on this evidence, we propose a model in which each cell of the retina and RPE performs an essential metabolic function that promotes survival of the retina-RPE ecosystem.

Results

Photoreceptors express a glucose transporter.

Cells need a membrane protein to take up glucose, so we evaluated expression of glucose transporters in mouse tissues using immunoblot (Figure 2.1A). Consistent with previous findings (Badr et al., 2000; Gospe et al., 2010) we found that retina and RPE express GLUT1, and confirmed that the protein immunoreactive with the GLUT1 antibody is membrane associated (Figure 2.1B). GLUT3 was detected only in brain. GLUT4 was detected in heart and muscle as expected, but not in the retina.

Immunohistochemistry (IHC) of mouse retinas shows that GLUT1 immunoreactivity overlaps with cytochrome oxidase subunit 1 (MT-COX1) (Figure 2.1C), which identifies rod inner segments by the unique elongated shape of their mitochondria (Figure 2.1E). We examined the ultrastructure of this region using serial block face scanning electron microscopy (SEM), which revealed that rod mitochondria extend beyond the ends of the Müller glial cell (MGC) apical processes (Figure 2.1E). These fine structures are devoid of mitochondria, and small spherical mitochondria line up within the MGCs along the outer limiting membrane, just beneath the apical processes (Figure 2.1F and arrowheads in Figure 2.1C).

To visualize MGCs specifically, we labeled them with an antibody to glutamine synthetase (GS) in Figure 2.1D. These long cells extend from the outer limiting membrane to the ganglion cells (see Figure 2.1), and dual labeling showed that most GLUT1 immunoreactivity in MGCs is in the inner retina (Figure 2.1D). GLUT1 immunoreactivity also overlaps with a marker specific for rod photoreceptors, rod arrestin (Figure 2.1G), and with GFP expressed from the rod-specific Nrl promoter (Figure 2.1H). The distribution of GLUT1 immunoreactivity supports the idea that photoreceptors can take up glucose released from the apical side of the RPE.

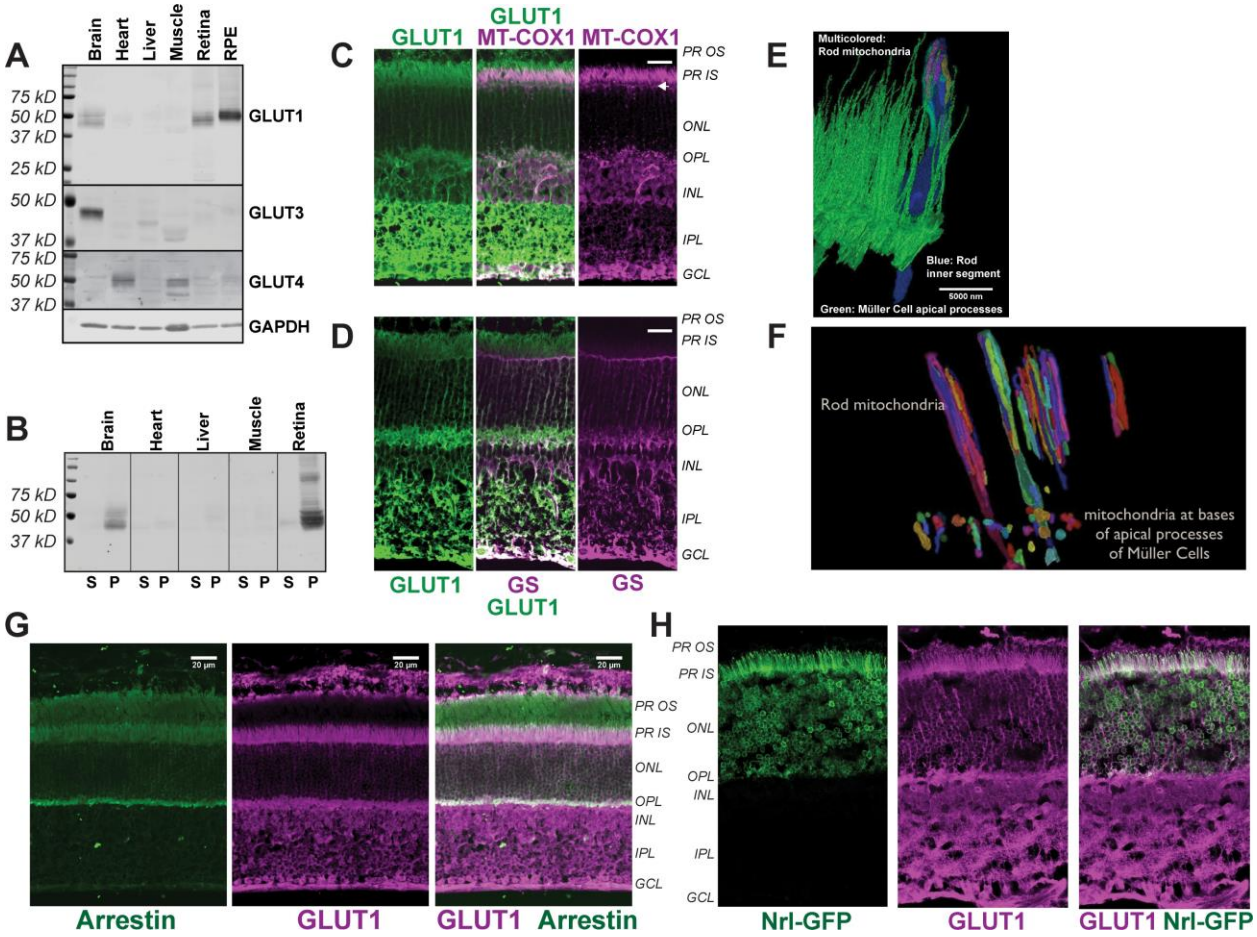

Figure 2.1: Distribution of GLUT1 in retina.
(A) Immunoblot analysis of mouse tissue homogenates confirms GLUT1 is a major glucose transporter in retina and RPE. 1 mg protein was loaded per lane. No antibodies that we could validate were available for GLUT2; the Human Protein Atlas reports no GLUT2 mRNA transcripts in retina (Uhlén et al., 2015). The blot shown is representative of 3 experiments. (B) Evidence that the protein immunoreactive with the GLUT1 antibody is membrane associated. Equivalent percentages of total supernatant (S) and total pellet (P) were probed with the GLUT1 antibody. (C) GLUT1 immunoreactivity in mouse retina. Rod inner segments are identified by their mitochondria labeled with mitochondrial cytochrome oxidase antibody (MT-COX1). White arrowhead indicates the layer of MGC mitochondria. (D) MGCs identified by glutamine synthetase (GS) immunoreactivity. (E) Serial block face SEM of mouse retina. The inner segment of one rod cell is shown in blue with its mitochondria multi-colored; green structures are MGC apical processes. (F) Differences in rod and MGC mitochondrial in mouse retina, with small MGC mitochondria located just below the outer limiting membrane. For clarity not all of the mitochondria are shown. (G) Distributions of rod arrestin and GLUT1 in a partially light-adapted mouse retina. (H) Distributions of GLUT1 and GFP expressed from the rod-specific Nrl promoter. PR OS, photoreceptor outer segment; PR IS photoreceptor inner segment; ONL, outer nuclear layer; OPL, outer plexiform layer; INL inner nuclear layer; IPL inner plexiform layer; GCL, ganglion cell layer. Scale bars in C, D and G represent 20 µm.

Dietary glucose enters the retina primarily through photoreceptors.

To determine which retinal cells take up glucose in an eye of a living animal, we used oral gavage to introduce a fluorescent derivative of 2-deoxy glucose (2-NBDG)

(Yoshioka et al., 1996) into stomachs of mice. We harvested the retinas either 20 or 60 min after gavage, mounted them on filter paper, and cut 300–400 µm slices for imaging by confocal microscopy (Giarmarco et al., 2018, 2017). 2-NBDG fluorescence is strongest in the photoreceptor layer (Figure 2.2A), and surprisingly stronger in the outer retina than in the inner retina even though mouse inner retinas are vascularized. 2-NBDG fluorescence does not overlap with MGCs, visualized by transgenic expression of tdTomato (Wohl and Reh, 2016), though in rare instances there was overlap at MGC end feet. The results summarized and quantified in Figure 2.2C show that glucose reaching the outer retina is taken up primarily by photoreceptors.

The images in Figure 2.2A are of live unfixed mouse retinas where most of the photoreceptors are rods. To resolve whether cones also import 2-NBDG, we similarly introduced 2-NBDG by oral gavage into adult zebrafish, whose retinas are more enriched with cones (Raymond et al., 2014). 30 min after gavage, cones in a retinal slice are intensely fluorescent (Figure 2.2B). As in mouse retinas, there was little 2-NBDG uptake into MGCs, which in these retinas were marked with tdTomato expressed from a GFAP promoter (Shin et al., 2014). Data quantified in Figure 2.2D indicate that cones can also take up glucose from the blood.

Carbons from glucose are metabolized in RPE cells differently than in retina. Most of the glucose taken up into a retina is used to make lactic acid (Du et al., 2016a; Krebs, 1927; Medrano and Fox, 1995; Wang et al., 1997; Winkler, 1981). In the eye of a living animal, glucose from the choroidal blood first must first pass through the RPE cell monolayer before it can reach the retina. We hypothesized that the energy metabolism of RPE cells might minimize their consumption of glucose, maximizing the amount of glucose passing through to the retina.

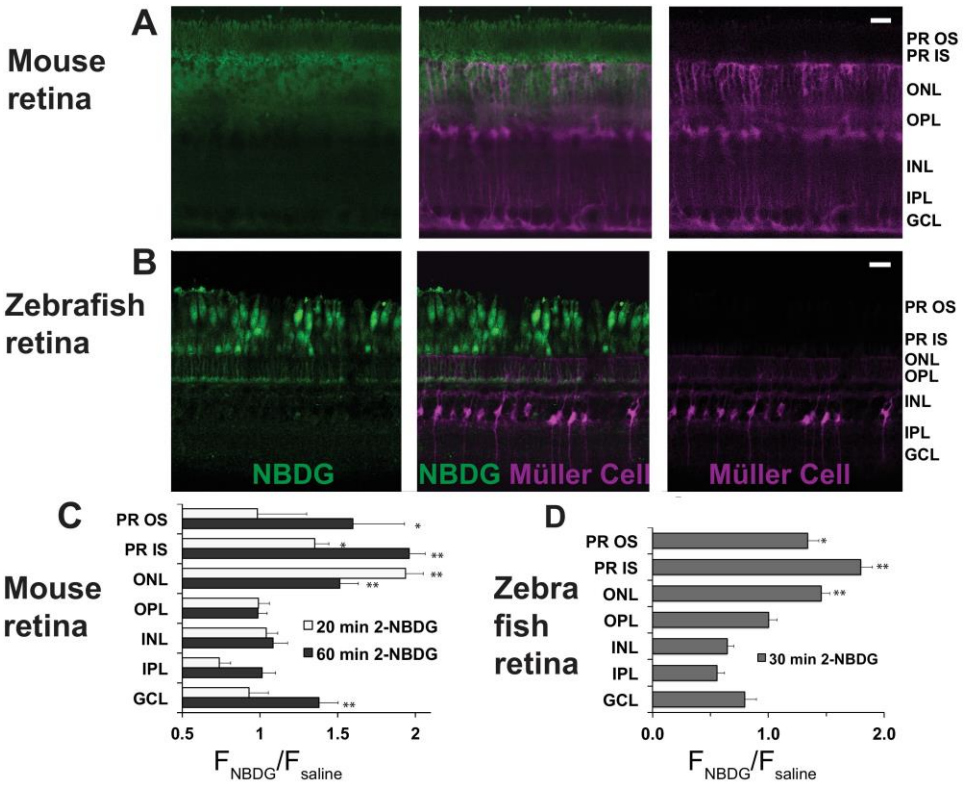

Figure 2.2: Fluorescent glucose (2-NBDG) accumulates in photoreceptors after oral gavage. (A) 2-NBDG (green) accumulation in a mouse retina 20 min after oral gavage. MGCs are identified by tdTomato expression in cells in which the Rlbp1 promoter is active. (B) 2-NBDG accumulation in a zebrafish retina 30 min after oral gavage. MGCs are identified by tdTomato expressed from the GFAP promoter. Labels on the right of panels A and B represent approximate positions of the retinal layers. (C) Quantification of 2-NBDG fluorescence from mouse retinas (n = 5 animals, 17 slices for 20 min 2-NBDG; 3 animals, 8 slices for 1 hr 2-NBDG; 3 animals, 8 slices for saline). $F_{NBDG/Fsaline}$ compares fluorescence from retinas of mice gavaged with 2-NBDG vs. with saline. Error bars report SE. (D) Quantification of 2-NBDG fluorescence from zebrafish retinas (3 animals, 8 slices for 30 min 2- NBDG; 2 animals, 3 slices for saline). PR OS, photoreceptor outer segments; PR IS, photoreceptor inner segments; ONL, outer nuclear layer; OPL, outer plexiform layer; INL, inner nuclear layer; IPL, inner plexiform layer; GCL, ganglion cell layer. Scale bars represent 20 µm. * indicates $p<0.05$ and ** indicates $p<0.01$ for the comparison of F_{NBDG} to F_{saline}.

To compare glucose metabolism in RPE and retina we initially used two preparations, mouse retina (mRetina) and cultured human fetal RPE cells (hfRPE). The retinas were freshly dissected from mouse eyes. hfRPE cells were grown 4–6 weeks in culture to form a monolayer with tight junctions and a transepithelial resistance similar to native human RPE (>200 $\Omega*cm^2$). Due to its similarity to native RPE cells, this hfRPE preparation has been widely used to study RPE metabolism and to model RPE-related diseases such as age-related macular degeneration (Ablonczy et al., 2011; Adijanto and Philp, 2014; Blenkinsop et al., 2015; Johnson et al., 2011; Sonoda et al., 2009).

We added ^{13}C labeled glucose to both preparations and then used gas chromatography-mass spectrometry (GC-MS) (Du et al., 2015) to compare incorporation of ^{13}C into glycolytic and other intermediates. The pattern of ^{13}C labeling from the [1,2] ^{13}C glucose isotopologue can be used to distinguish metabolites generated by glycolysis versus the pentose phosphate pathway (Metallo et al., 2009). Metabolites with one ^{13}C ('m1') are generated from glucose oxidation in the pentose phosphate pathway, whereas metabolites with two 13C ('m2') are produced when glucose enters glycolysis. In a previous report (Du et al., 2016b) we used [1,2] ^{13}C glucose to show that <2% of metabolic flux from glucose goes through the pentose phosphate pathway in both mRetina and hfRPE.

Consistent with retinal reliance on aerobic glycolysis, total lactate and succinate are more abundant in mRetina than in hfRPE, whereas citrate and a-ketoglutarate are more abundant in hfRPE (Figure 2.3A). In a time course, the initial rate at which ^{13}C from glucose incorporates into the intracellular pool of lactate is at least eight times faster in mRetina than in hfRPE (Figure 2.3B). Citrate and a-ketoglutarate pools are larger and fill more gradually in hfRPE cells than in retina, indicating a large oxidative metabolic capacity of RPE mitochondria. It is important to note that interpretation of retinal metabolic flux in Figure 2.3 is complicated by the presence of multiple cell types and multiple compartments within each cell type.

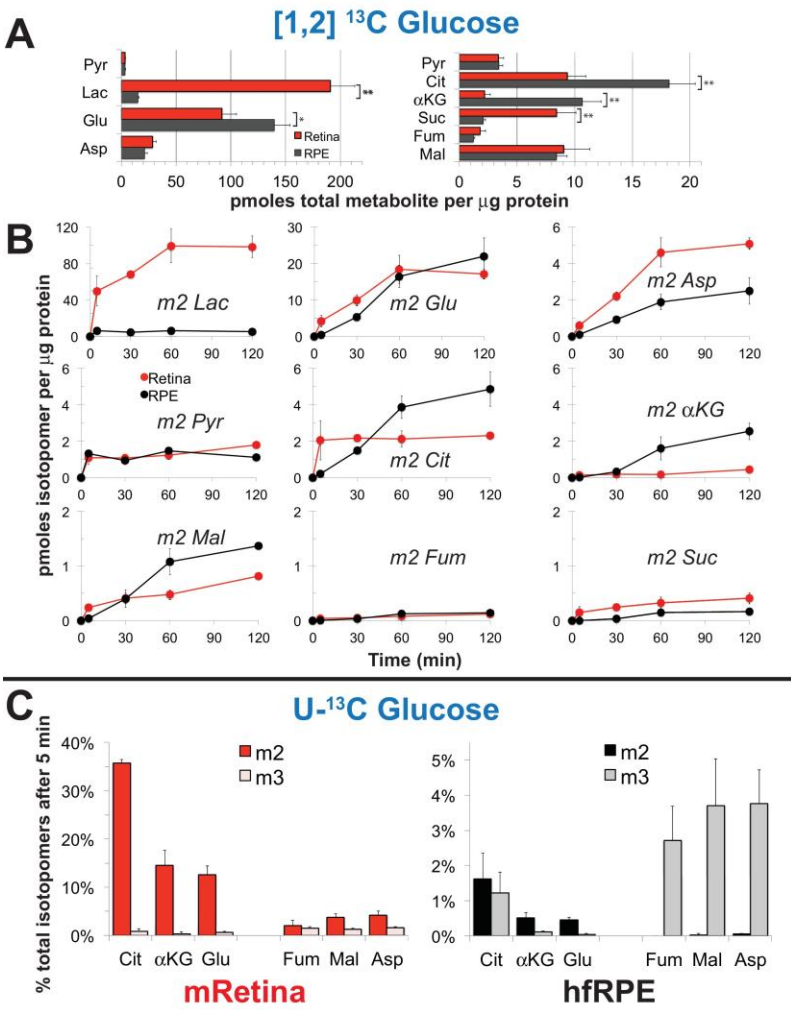

Figure 2.3: Differences in metabolic flux in retina and RPE. (A) Total metabolite levels (pmoles per mg protein) in mRetina (red) and hfRPE (black). Note the different scales for the left and right panels. n = 11; *p<0.05 and **p<0.01. (B) Incorporation of 13C from [1,2] ^{13}C glucose into metabolites in mRetina and hfRPE cells (pmoles per mg protein). Each of the isotopologues shown is derived from glucose metabolized by glycolysis. Note the different scales for the top, middle and bottom panels. (n = 3 for each time point; error bars represent SD) (C) Incorporation in mRetina and hfRPE cells of ^{13}C from 5 mM U-^{13}C glucose into metabolites after 5 min. The % of total isotopologues that are m2 and m3 are shown.

Pyruvate resulting from glycolysis must be decarboxylated to fuel oxidative metabolism in mitochondria. To compare relative rates of pyruvate carboxylation and decarboxylation, we incubated mRetina and hfRPE with U-^{13}C glucose. Mitochondrial intermediates with two ^{13}C ('m2') are produced by decarboxylation of pyruvate, whereas those with three ^{13}C ('m3') are made from carboxylation of pyruvate. (See Figure 2.5B for an overview of these pathways.) Decarboxylation of pyruvate predominates in mRetina, whereas carboxylation is more prominent in hfRPE (Figure 2.3C), suggesting that retina and RPE cells metabolize glucose differently. RPE cells also use reductive carboxylation an alternative pathway to make NADPH (Du et al., 2016b). We propose that these adaptations minimize consumption of glucose in RPE cells so they can maximize transport of glucose from the choroid to the retina.

Confirmation of metabolic specializations of the retina and RPE in a mouse eye

The cultured hfRPE cell is a well characterized model that has been used to evaluate RPE metabolism (Adijanto and Philp, 2014), as well as to study diseases like age-related macular degeneration (Johnson et al., 2011). *In vitro* studies have focused on cultured hfRPE cells because RPE cells isolated from adult eyes can de-differentiate in culture. However, cultured adult human RPE is not better than hfRPE as a representation of native RPE (Blenkinsop et al., 2015) in terms of transepithelial resistance and gene expression. hfRPE cultures used in this study are of a similar age in culture as those in other published studies.

Nevertheless, it is important to confirm that the metabolic differences between mRetina and hfRPE reported in Figure 2.3 reflect bona fide differences between retina and RPE in an eye. We performed metabolic analyses using isolated mRetina and a mouse eyecup (mEC) preparation in which the RPE remained intact after the retina was removed. Although the choroid and sclera are included in the mEC, the RPE layer is more metabolically active than the sclera and it is accessible to added metabolites. We incubated freshly separated retinas and mECs in medium containing glucose, then analyzed metabolites by GC-MS. The total lactate/citrate ratio in mRetina is nearly 30 times higher than in mEC (Figure 2.4A), similar to the comparison of mRetina and hfRPE.

The data shown in Figure 2.3 and Figure 2.4A report the amounts of intracellular metabolites, but metabolites made from glucose, most notably lactate, could be exported to the medium. To quantify exported metabolites, we incubated mRetinas, mECs and hfRPE cells with U-^{13}C glucose and used GC-MS to quantify ^{13}C labeled lactate and pyruvate as they accumulated in the medium (Figure 2.4B and C). mRetinas, hfRPE cells and mECs exported ^{13}C lactate and ^{13}C pyruvate, but mRetina releases ^{13}C lactate into the medium ~20 times faster than either hfRPE or mEC.

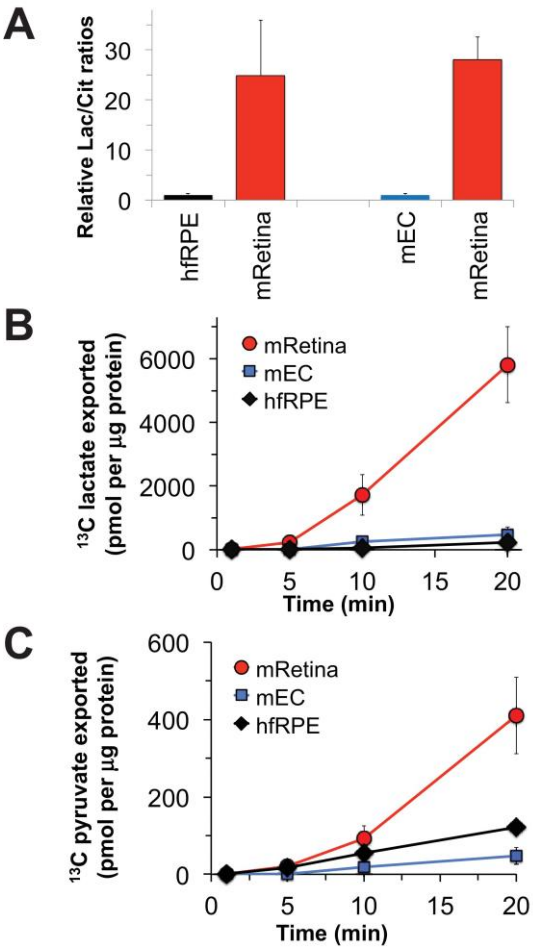

Figure 2.4: Comparisons of metabolic flux in mouse retina (mRetina), mouse eyecup (mEC), and human fetal RPE (hfRPE).
(A) Ratios of total intracellular lactate/citrate in both hfRPE and mEC are about 1/25 of the lactate/citrate ratio in mRetina. (B) Accumulation of m3 ^{13}C lactate in the medium in which either mRetina (n = 4), mEC (n = 4) or hfRPE (n = 3) were incubated with 5 mM U-13C glucose. (C) Accumulation of m3 ^{13}C pyruvate in the media in which either mRetina (n = 4), mEC (n = 4) or hfRPE (n = 3) were incubated with 5 mM U-^{13}C glucose. Error bars report SE.

RPE cells can use lactate as a fuel

We previously confirmed that mouse retinas convert glucose into lactate (Du et al., 2016a) and retinas release more lactate than other neuronal tissues (Du et al., 2013b). Figure 2.3 and Figure 2.4 in this report show that mouse retinas produce and release more lactate than RPE cells. To determine if RPE cells are capable of using lactate exported from a retina as an alternative fuel, we incubated hfRPE cell monolayers with either 5 mM U-^{13}C glucose or 10 mM U-^{13}C lactate/1 mM unlabeled glucose. After 5 or 10 min, incorporation of ^{13}C into metabolites was quantified with GC-MS. hfRPE cells incorporate ^{13}C rapidly into pyruvate from both ^{13}C glucose and ^{13}C lactate (Figure 2.5A). However, ^{13}C from lactate accumulates at least 20 times faster into citrate pools than ^{13}C from glucose. Substantial amounts of 'm3' labeled malate (Figure 2.5B) confirm that pyruvate carboxylation is a major metabolic pathway in hfRPE.

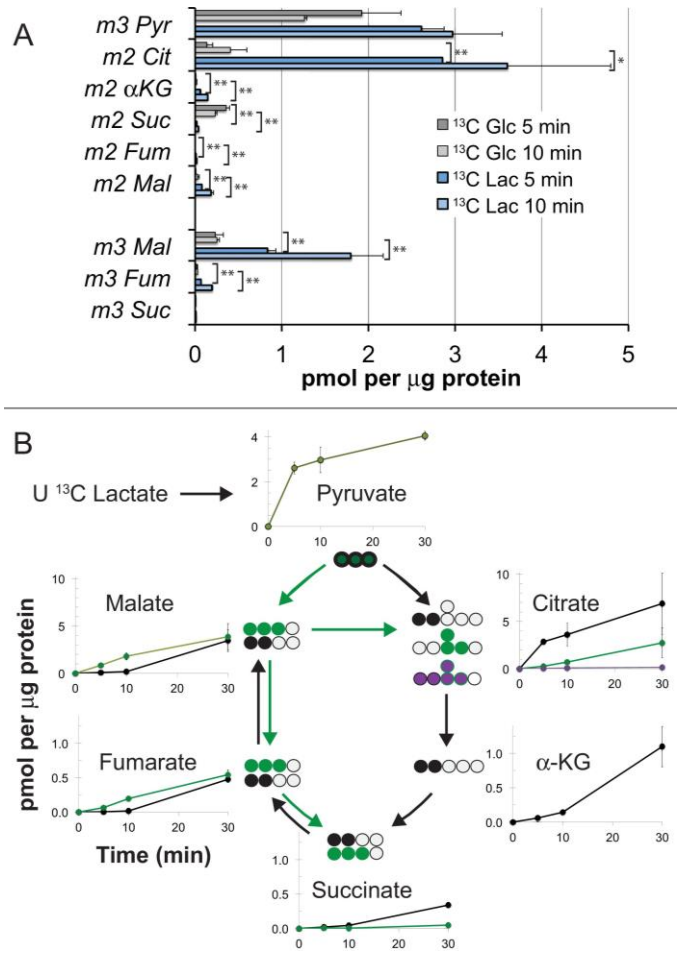

Figure 2.5: Incorporation of ^{13}C from lactate into metabolic intermediates in hfRPE cells. (A) Comparison of initial rates of labeling (at 5 and 10 min after introduction of labeled fuel) from 5 mM U-^{13}C glucose vs. from 10 mM U-^{13}C lactate (with 1 mM unlabeled glucose also present). Citrate and malate take up label faster from lactate than from glucose. (B) Time courses of incorporation of ^{13}C from 10 mM U-^{13}C lactate (with 1 mM unlabeled glucose also present) into hfRPE metabolites accompanied by schematic illustrations of the labeled species in the context of the TCA cycle. (n = 2–3 for each time point; error bars represent range or SD).

To confirm that mEC can also utilize lactate, we compared incorporation of ^{13}C from U-^{13}C lactate into metabolic intermediates in hfRPE, mRetina and mEC. Compared to mRetina, hfRPE and mEC incorporated more 'm3' malate, aspartate and fumarate (Figure 2.6). Lactate metabolism in hfRPE is more similar to mEC than mRetina, and is indicative of pyruvate carboxylation.

Lactate can suppress glucose catabolism in RPE cells

Figure 2.5 and Figure 2.6 show that RPE cells can consume lactate as fuel, and we next asked if lactate could suppress consumption of glucose. We hypothesized (Figure 2.7A) that lactate dehydrogenase (LDH) in RPE cells uses lactate to reduce cytosolic NAD^+ to NADH as it does in other cells (Hung et al., 2011). Since NAD^+ is required for glycolysis, depletion of NAD^+ by lactate and LDH could reduce glucose consumption.

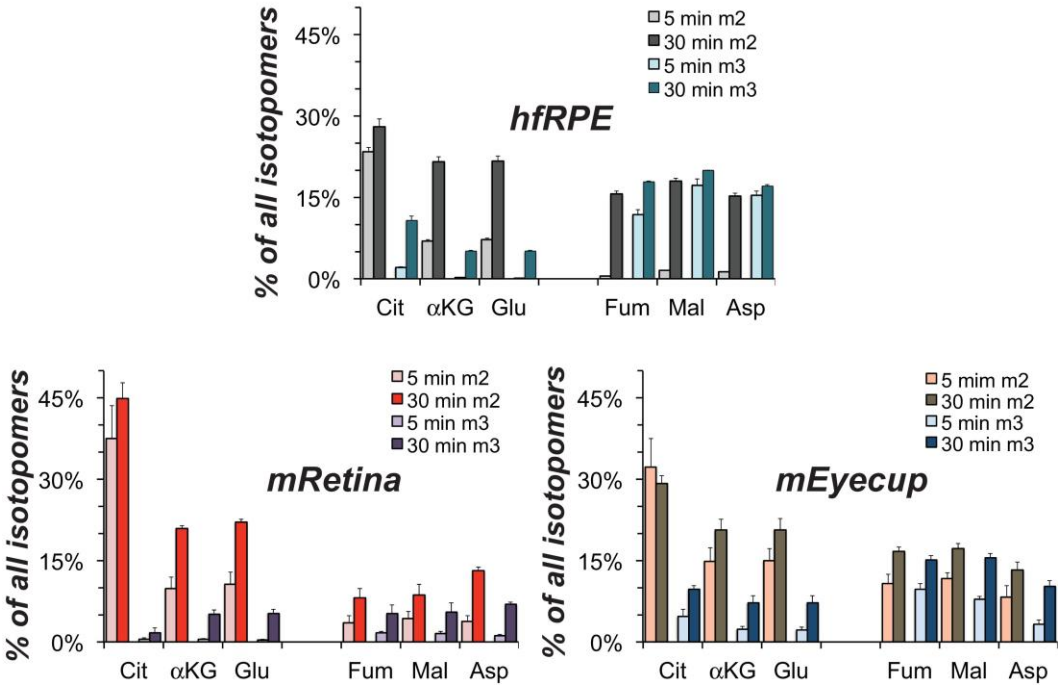

Figure 2.6: Comparison of lactate metabolism in hfRPE with lactate metabolism in mouse retinas and mouse eyecups with retinas removed.
The high relative abundance of m3 metabolites derived from carboxylation reactions and the high abundance of fumarate, malate and aspartate in hfRPE cells resemble the metabolite distributions in the RPE enriched eyecup more than the distributions in retina. Each preparation was incubated with 10 mM U-^{13}C lactate for the 5 or 30 min and metabolites were extracted, derivatized and quantified by GC-MS. (n = 2 for hfRPE, n = 3 for mEyecup and n = 4 for mRetina; error bars represent range or SD).

We tested the effect of bathing hfRPE cells in lactate on their conversion of NAD^+ into NADH using a perifusion apparatus with an inverted microscope to measure total NADH fluorescence (Santos et al., 2017) from hfRPE monolayers. After equilibrating cells with 5.5 mM glucose, the perifusion medium was changed to supply 5.5 mM glucose with varying concentrations of lactate and pyruvate (Figure 2.7B, top). Lactate in the medium substantially increases NADH fluorescence, whereas pyruvate drives it to its oxidized state (Figure 2.7B, bottom). These results confirm that in RPE cells, exogenous lactate can deplete NAD^+ by reducing it to NADH.

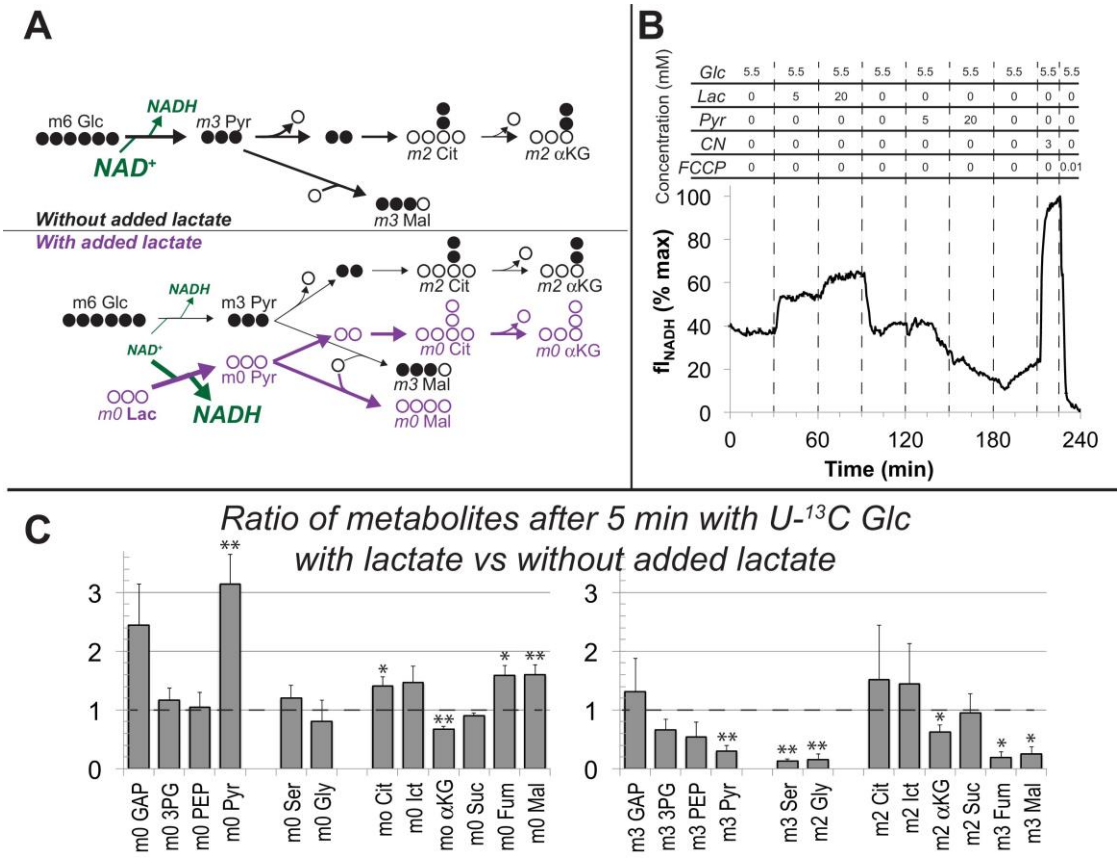

Figure 2.7: Lactate suppresses oxidation of glucose by hfRPE cells.
(A) Schematic prediction of how U-^{13}C Glc ('m6 Glc') would be metabolized without lactate (top) vs. with lactate (bottom). We hypothesized that lactate would suppress glycolysis of m6 Glc by depleting NAD+ and that unlabeled (m0) pyruvate and TCA cycle intermediates would become more abundant. (B) Effect of lactate and pyruvate on total cellular NADH measured by fluorescence in a monolayer of hfRPE cells. The trace shows the average from 3 individual cells and is representative of 3 experiments. (C) Ratios of metabolites after 5 min incubation with U-^{13}C Glc in the presence or absence of unlabeled lactate (20 mM). Left, lactate substantially increases the total amounts of unlabeled (m0) GAP, pyruvate, citrate, isocitrate, fumarate and malate in hfRPE cells. Right, lactate suppresses the incorporation of ^{13}C from 5 mM ^{13}C Glc into glycolytic and TCA intermediates. (n = 3; error bars represent SE, * indicates $p<0.05$ and ** indicates $p<0.01$ for the comparison of with vs. without added unlabeled lactate)

To determine if lactate-induced NAD$^+$ depletion suppresses glycolysis in hfRPE cells, we incubated hfRPE cell monolayers with 5 mM U-^{13}C glucose in the absence or presence of unlabeled lactate, then used GC-MS to quantify incorporation of ^{13}C from glucose into glycolytic and TCA cycle intermediates. 20 mM lactate was selected based on previous measurements of retina and RPE (Kolko et al., 2016; Matschinsky et al., 1968), and because native RPE in an eye is exposed to high levels of lactate released from the retina. Unlabeled lactate increases pools of unlabeled pyruvate, citrate, isocitrate, fumarate and malate (Figure 2.7C, left). Consistent with the results in Figure

2.5, carbons from lactate are incorporated rapidly into the TCA cycle through both pyruvate carboxylation and decarboxylation.

Addition of unlabeled lactate also causes accumulation of glyceraldehyde-3-phosphate (GAP), the triose phosphate immediately upstream of the glyceraldehyde-3-phosphate dehydrogenase (GAPDH) reaction that requires NAD^+. Lactate diminishes incorporation of ^{13}C from U-^{13}C glucose into intermediates downstream of the GAPDH reaction (Figure 2.7C, right), consistent with suppressed GAPDH activity. Lactate does not diminish incorporation of ^{13}C from glucose into 'm2' citrate or isocitrate, perhaps reflective of enhanced TCA cycle activity from anaplerotic supplementation of unlabeled intermediates (Figure 2.7C, left). We conclude that exogenous lactate can suppress glycolysis in hfRPE cells.

20 mM lactate seems non-physiological because it is higher than the <2–2.5 mM concentration normally in human serum (Wacharasint et al., 2012), and the 7–16 mM range in mouse serum (Burgess and Sylvén, 1962). We found similar suppression of glycolysis using 10 mM lactate; formation of 'm3', but not 'm0' glycolytic intermediates was diminished (Figure 2.8A,B). We also measured the effect of pyruvate, which drives formation of oxidized NAD^+ (Figure 2.7B). Pyruvate and its amino derivative, alanine, cause redistributions in the relative amounts of specific glycolytic and mitochondrial intermediates (Figure 2.8C–F).

Lactate can enhance transport of glucose across a monolayer of hfRPE cells

By suppressing glycolysis (Figure 2.7, Figure 2.8), we hypothesized that lactate can enhance the net flow of glucose across the RPE. The simplest version of this hypothesis is that lactate minimizes consumption of glucose, so that more glucose can translocate from the basolateral to the apical side of the RPE.

To test this hypothesis, we measured the influence of lactate on transport of glucose across a monolayer of hfRPE cells. We grew hfRPE cells on transwell filters to confluence in a sealed monolayer, then added U-^{13}C glucose to the basolateral

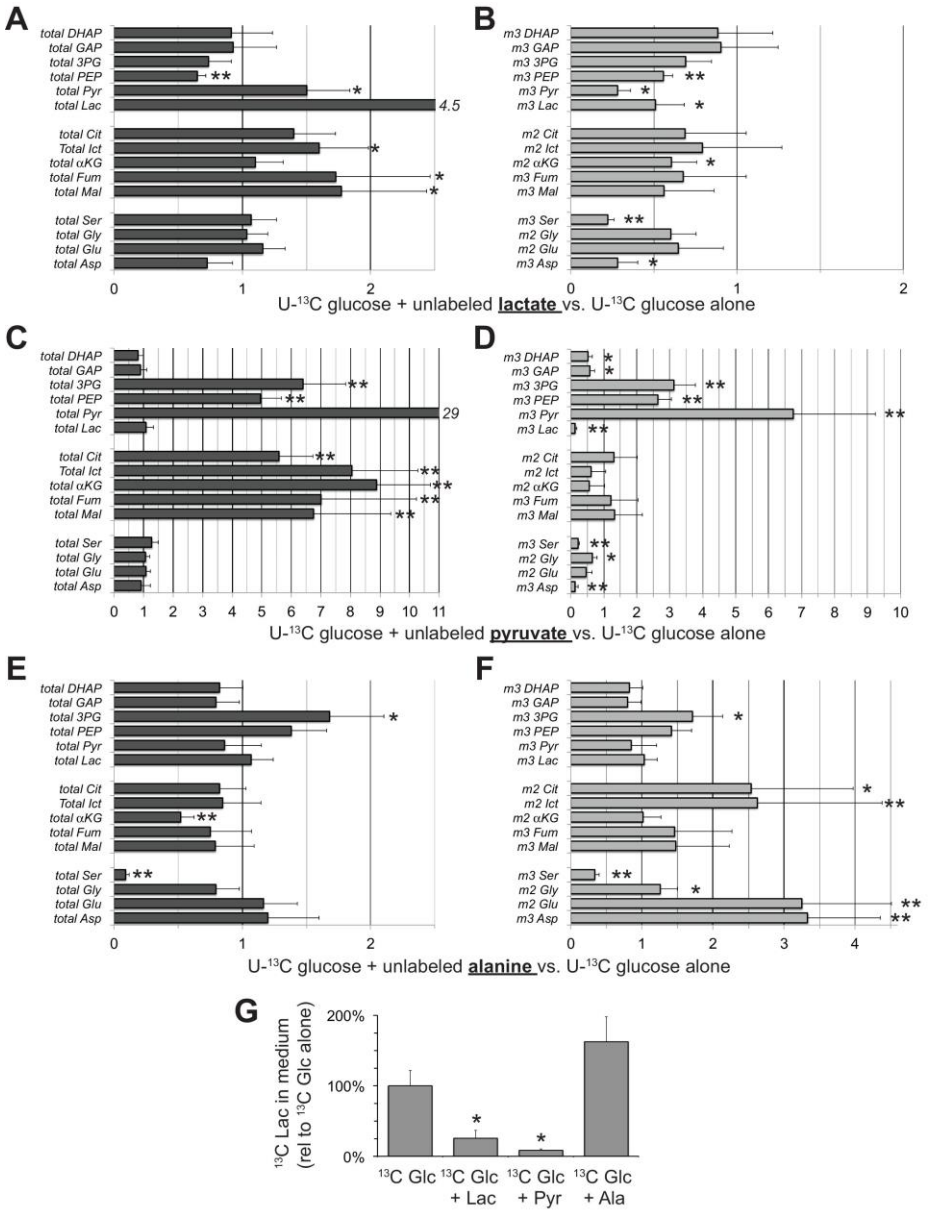

Figure 2.8: Effects of lactate, pyruvate and alanine on metabolic flux from U-^{13}C glucose in hfRPE cells.
Each bar graph compares the ratio of metabolites with vs. without the addition of 10 mM of either unlabeled lactate (A,B) pyruvate (C,D) or alanine (E,F). A, C and E report the ratios for the total of all isotopologues of each metabolite, and B, D and F report the ratios for specific labeled metabolites (m2 or m3). Panel G shows the effects of adding unlabeled lactate, pyruvate or alanine on the release of ^{13}C lactate generated by glycolysis of U-^{13}C glucose. Metabolites were extracted, derivatized and quantified after 5 min incubation with 5 mM U-^{13}C glucose (n = 3) or 5 mM U-^{13}C glucose plus 10 mM unlabeled lactate (n = 3), pyruvate (n = 3) or alanine (n = 3). Error bars report SD. *p<0.05; **p<0.01.

chamber where RPE cells would face the choroidal blood supply in an eye. GC-MS was used to quantify accumulation of ^{13}C glucose in the apical chamber, where RPE cells normally would face a lactate-rich retina. We performed this experiment in the presence or absence of 10 mM unlabeled lactate on the apical side (Figure 2.9A). Unlabeled lactate in the apical medium substantially increases the accumulation of ^{13}C glucose on the apical side (Figure 2.9B, C), an effect more pronounced with 2 mM (Figure 2.9F) instead of 5 mM ^{13}C glucose (Figure 2.9E). Unlabeled lactate in the apical compartment also suppresses accumulation of ^{13}C pyruvate and ^{13}C lactate on the

apical side (Figure 2.9B, C). These results are consistent with exogenous lactate suppressing of glycolysis in the RPE.

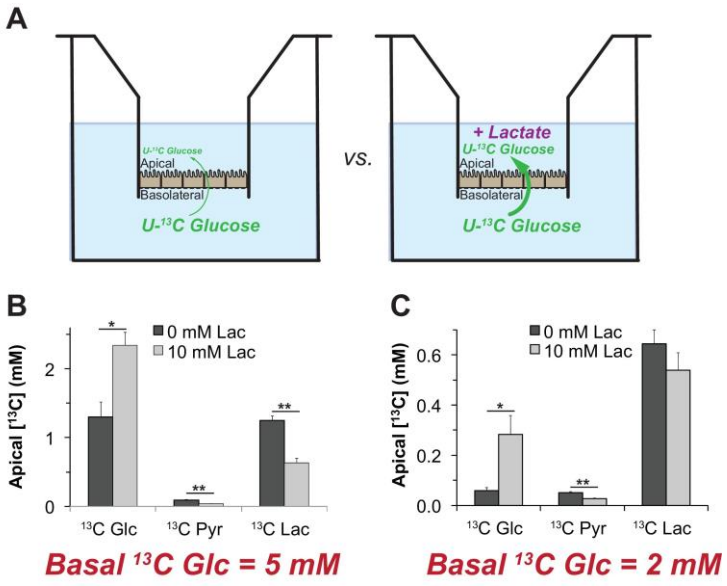

Figure 2.9: Lactate can enhance transport of glucose across a monolayer of RPE cells.
(A) Strategy to evaluate the effect of lactate on transport of glucose across a monolayer of RPE cells. We hypothesized that without lactate (left) glycolysis consumes glucose before it can cross the RPE cell monolayer. With lactate on the apical side (right) glycolysis would be partially suppressed so more glucose can cross the monolayer without being consumed by glycolysis. (B,C) Glucose on the apical side after 8 hr. These panels compare the concentrations of ^{13}C Glc, ^{13}C Pyr and ^{13}C Lac in the apical chamber 8 hr after 5 mM (B) or 2 mM (C) ^{13}C Glc was added to the basolateral chamber (n = 3).

We focused on effects of lactate because it is more physiologically relevant than pyruvate or alanine. In separate experiments with mouse retinas we found that pyruvate is released from mouse retinas release pyruvate at only 6.7 ± 2.3% the rate of lactate release, and alanine is released at only 0.4 ± 0.1% of that rate (SD, n = 13). Together these findings suggest that high concentrations of lactate released from the retina can hinder glycolysis in the RPE so that more glucose reaches the retina.

Discussion

Model for a network of metabolic interdependence between the retina and RPE

Figure 2.10 summarizes the retina-RPE metabolic ecosystem model. We propose that lactate from photoreceptors suppresses glycolysis in the RPE so more glucose can reach the retina.

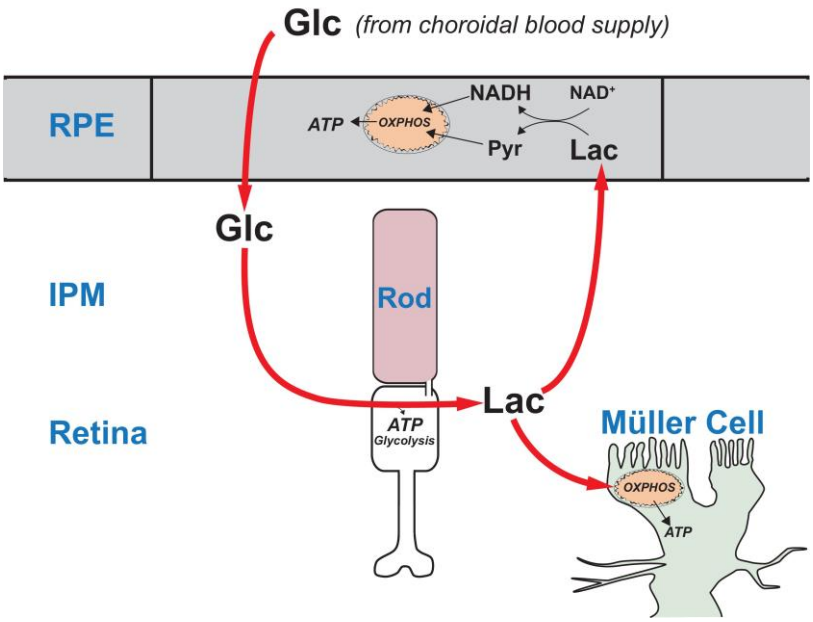

Figure 2.10: A working model that describes the flow of metabolic energy in the retina-RPE ecosystem.
Photoreceptors convert glucose into lactate and release the lactate into the interphotoreceptor matrix (IPM). Lactate suppresses glycolysis in RPE cells by depleting NAD^+. Lactate also fuels metabolic activity in Müller cells, which lack key enzymes that would be required for glycolysis.

Previous evidence that cells in the retina have specific metabolic roles

Photoreceptors but not MGCs appear to have the enzymes and transporters needed for glycolysis. Pyruvate kinase catalyzes the last step of glycolysis and is highly enriched in photoreceptors (Casson et al., 2016; Chinchore et al., 2017; Lindsay et al., 2014; Rajala et al., 2016; Rueda et al., 2016) but not MGCs in mouse retina (Lindsay et al., 2014). MGCs also do not express hexokinase (Rueda et al., 2016), the enzyme required for the first step of glycolysis. Furthermore, lactate, rather than glucose, is the most effective source (Lindsay et al., 2014) of carbon for glutamine synthesis by MGCs (Riepe and Norenburg, 1977) in mouse retinas.

Based on these observations, we proposed that MGCs in a retina are fueled by lactate from photoreceptors (Hurley et al., 2015). The findings in this report further suggest the central metabolic role of photoreceptors in retinal energy metabolism is to convert glucose to lactate, which both RPE and MGCs can use as fuel (Figure 2.10).

Significance of aerobic glycolysis in the retina

Aerobic glycolysis in photoreceptors is thought to enhance their anabolic capacity (Chinchore et al., 2017; Lindsay et al., 2014; Rajala et al., 2016) but our model suggests an additional purpose. In the laminated structure of an eye, the RPE separates the

retina from its nutrient source. To maintain their glucose supply, we propose that photoreceptors must produce and release lactate to fuel MGCs and suppress glycolysis in the RPE.

The relationship between the 'retinal ecosystem' model and recent *in vivo* findings from genetically altered photoreceptors and RPE

In RPE cells *in vitro*, glucose is metabolized differently in the presence of additional fuels like lactate, pyruvate and alanine (Figure 2.7 and Figure 2.8), and lactate can protect glucose from consumption (Figure 2.9B, C). However, more direct evidence is needed to validate the model in Figure 2.10 in a living animal, including genetic manipulations of photoreceptor and RPE cells and *in vivo* analyses of their phenotypes. Consistent with the model, recent genetic studies reported that photoreceptors engineered to be more glycolytic are more robust, while photoreceptors degenerate when glycolysis is enhanced in RPE cells (Kurihara et al., 2016; Venkatesh et al., 2015; Zhang et al., 2016; Zhao et al., 2011). When photoreceptors are more glycolytic they produce more lactate, which suppresses glycolysis in the RPE; more glucose reaches the retina.

The concept of a metabolic ecosystem and its relationship to retinal disease

The model in Figure 2.10 could explain the linkage between age-related macular degeneration and accumulation of mitochondrial DNA damage in RPE cells (Terluk et al., 2015). When RPE mitochondria fail the cells become more dependent on glycolysis, and photoreceptors may starve if insufficient glucose reaches the retina.

The concept of a metabolic ecosystem also has implications for other types of retinal disease. Mutations in rod-specific genes cause both rods and then cones to degenerate, even though the cones are not affected directly by the mutation (Punzo et al., 2012). One reason is that loss of a cone viability factor normally produced by rods may contribute to cone degeneration (Aït-Ali et al., 2015). Another factor may also contribute to the secondary loss of cones: a retina without rods makes less lactate (Du et al., 2016a).

We have shown in this report that, without lactate to suppress glycolysis, RPE cells oxidize more glucose. This may explain why healthy rods and cones are shorter and dysmorphic in an environment where most of the surrounding photoreceptors have degenerated (Duong et al., 2017; Lewis et al., 2010). The loss of lactate production in rod-deficient retinas may limit the rate at which glucose can reach cones. This is consistent with starvation of cones (Punzo et al., 2009) and accumulation of 2-NBDG in RPE cells (Wang et al., 2016) when rods degenerate. Further, an alternative supply of glucose can rescue those cones from degeneration (Wang et al., 2016).

The importance of other fuels in the metabolic ecosystem

This study highlights one way that RPE, photoreceptors and MGCs can work together as an ecosystem of metabolically specialized and interdependent cells. Our investigation focused on lactate because so much of it is exported from the retina, but glycogen (Senanayake et al., 2006), fatty acids (Joyal et al., 2016; Reyes-Reveles et al., 2017), ketone bodies (Adijanto and Philp, 2014), glutamine (Du et al., 2016b), proline (Chao et al., 2017), and metabolites from other metabolic pathways (Chao et al., 2017; Rueda et al., 2016) also must contribute significantly to this metabolic ecosystem. Future investigations should optimize conditions to reliably quantify the kinetics of glucose transport across RPE cells.

It also will be important to evaluate glucose transport across RPE cells in the context of intracellular glycogen. Based on previous findings (Senanayake et al., 2006) it is likely that glycogen in RPE cells functions as a glucose buffer that acts either directly in the glucose transport pathway or as a side pathway. Experiments that exploit the availability of ^{12}C and ^{13}C isotopologues of glucose may divulge the role that glycogen plays in glucose transport across RPE cells.

Recent studies showed that oxidation of fatty acids by the RPE can supply the retina with ketone bodies (Adijanto and Philp, 2014), and that RPE can oxidize fatty acids from photoreceptor phagocytosis(Reyes-Reveles et al., 2017). Like lactate, fatty acids may also suppress glucose consumption by the RPE. Altogether, these studies suggest that

energy homeostasis in retina and RPE relies on a complex and specialized interplay between metabolically distinct cells. A better understanding of this metabolic ecosystem could be used to develop general therapeutic strategies that are effective for multiple types of retinal degenerative diseases.

Materials & Methods

Animals

All research was authorized by the University of Washington Institutional Animal Care and Use Committee. Mice in the C57BL/6J background were maintained in the University of Washington South Lake Union vivarium at 27.5 °C on a 14 hr/10 hr light-dark cycle. C57BL/6J does not carry the rd8 mutation in the Crb1 gene (Mattapallil et al., 2012). Transgenic mice expressing eGFP under the Nrl promoter (Akimoto et al., 2006) (RRID:IMSR_JAX:021232), or tdTomato under the Rlbp-CRE promoter (Wohl and Reh, 2016) were described previously.

Transgenic heterozygote zebrafish in the AB background were maintained in the University of Washington South Lake Union aquatics facility at 27.5 °C on a 14 hr/10 hr light-dark cycle. Fish used for experiments were male and female siblings between 12–24 months old. A transgenic line stably expressing tdTomato in Müller cells (GFAP:tdTomato) was described previously (Shin et al., 2014). Prior to gavage experiments, fish were fasted >18 hr and dark-adapted >12 hr.

Antibodies

Arrestin1, D9F2 (from Larry Donoso and Cheryl Craft)	IHC:	1:200
GLUT1, (AbCam, ab115730; RRID:AB_10903230)	IB:	1:200,000, 0.86 ng/mL
	IHC	1:1000, 0.17 mg/mL
GLUT3, (AbCam, ab41525; RRID:AB_732609)	IB:	1:5000, 0.136 mg/mL
GLUT4, (AbCam, ab654; RRID:AB_305554)	IB:	1:5000
Glutamine synthetase, (Millipore, MAB302; RRID:AB_2110656)	IHC:	1:1000
MTCO1 (Abcam, ab14705; RRID:AB_2084810)	IHC:	1:2000

Tissue preparations for immunoblotting

Frozen tissue samples were homogenized in RIPA buffer (150 mM NaCl, 1% Triton X-100, 0.05% sodium deoxycholate, 0.1% SDS, 50 mM Tris, pH 8.0) with a mixed phosphatase and protease inhibitor cocktail (ThermoFisher 88668), briefly sonicated, then rocked at 4 °C for 30 min. Samples were then spun at 13,300 RPM at 4 °C for 15 min, and the supernatant was normalized for loading by BCA assay to 20 mg/tissue. RPE protein lysate was prepared according to a described protocol (Wei et al., 2016). To prepare membrane fractions, frozen tissue samples were homogenized in PBS (0.14 M, pH 7.4) with a mixed phosphatase/protease inhibitor cocktail, then rocked at 4 °C for 30 min. Samples were then spun at 45,000 rpm at 4 °C, the supernatant (cytosolic fraction) drawn off and saved, and the pellet (membrane fraction) resuspended in an equal volume of PBS. After mixing with 5X Laemmli loading buffer, 1 mL benzonase (Millipore 70746) was added. Each tissue was then loaded with equal volumes of cytosolic and membrane fraction.

Immunoblotting

Samples were run on 12%, self-cast acrylamide gels and transferred onto PVDF membranes (Millipore IPFL00010). Following protein transfer, membranes were blocked with LI-COR Odyssey Blocking Buffer (LI-COR, 927–40000) for 1 hr at room temperature. Primary antibodies were diluted in blocking buffer and incubated overnight at 4 °C. Membranes were washed, incubated with secondary antibody (LI-COR IRDye 800CW, 926–32210, (RRID:AB_621842), and 926–32211, (RRID:AB_ 621843),1:5000 1 hr at room temperature, and washed again. Imaging was performed using the LI-COR Odyssey CLx Imaging System (RRID:SCR_014579).

Immunohistochemistry

Retinal eyecups were micro-dissected from C57BL/6J mice and were fixed in 4% paraformaldehyde in PBS, rinsed with PBS, incubated in a sucrose gradient (5%, 10%, and 20%), embedded into OCT and cryosectioned at 20 µm. Mouse sections were washed in PBS, then blocked in IHC buffer (5% normal donkey serum diluted in PBS with 2 mg/mL BSA and 0.3% Triton X-100) for 1 hr. Primary antibodies were diluted in

IHC blocking buffer as specified, and applied to blocked cryosections overnight at 4℃. Secondary antibodies were diluted at 1:3000 in IHC blocking buffer, and applied to mouse retina sections for 1 hr in darkness. Sections were washed in PBS three times, and mounted with SouthernBiotech Fluoromount-G (Fisher Scientific) under glass coverslips and visualized using a Leica SP8 confocal microscope with a 63X oil objective. Images were acquired at a 4096x4096 pixel resolution with a 12-bit depth using Leica LAS-X software (RRID:SCR_013673).

RPE cell culture

Human fetal eyes with a gestational age of 16–20 weeks were harvested and shipped overnight on ice in RPMI media containing antibiotics from Advanced Bioscience Resources Inc. (Alameda, CA). Dissections of fetal tissue were performed within 24 hr of procurement and followed a modified version of the dissection protocol in order to isolate the retinal pigment epithelium (RPE) (Sonoda et al., 2009). The fetal RPE sheets were incubated at 37 °C with 5% CO_2 and cultured in RPE media. The RPE media consisted of Minimum Essential Medium alpha (Life Technologies) supplemented with 5% (vol/vol) fetal bovine serum (Atlanta Biologicals), N1-Supplement (Sigma-Aldrich), Nonessential Amino Acids (Gibco), and a Penicillin-Streptomycin solution (Gibco). Isolated fetal RPE reached confluency about 3–4 weeks after dissection and was then passaged using a 0.25% Trypsin-EDTA solution (Gibco) and passed through a 40 µm nylon cell strainer (BD Falcon) in order to collect a suspension of single cells. After counting, the RPE cells were plated onto 0.3 cm^2 cell culture inserts (Falcon) coated with Matrigel (Corning) at a seeding density of 100,000 cells per insert. Cells grown on these inserts were cultured in RPE media containing 1% (vol/vol) FBS. Transepithelial resistance was measured weekly after 2 weeks in culture using a Millicell ERS-2 Epithelial Volt-Ohm Meter (Millipore).

Oral gavage

Mice were fasted overnight in the dark, and gavaged the next morning in ambient light. A micro- syringe fitted with a 22 gauge 1.5” straight 1.25 mm ball-tip needle was used to orally administer 100 µL of either saline or 50 mM 2-NBDG (Invitrogen, Carlsbad, CA)

dissolved in water. Successfully gavaged mice were returned to darkness during the 2-NBDG incubation period.

Zebrafish were gavaged using methods described previously (Collymore et al., 2013) under red light. Briefly, overnight fasted adult zebrafish were anaesthetized >1 min with 150 mg/mL MS-222 in fish water. Fish were placed in a slit cut in a cellulose sponge soaked with MS-222 solution, and the sponge was rotated to orient the fish mouth up. A micro-syringe fitted with thin, flexible 1 mm OD plastic tubing was used to orally administer 5 µL of either fish water or 30 mM 2-NBDG. Gavaged fish were immediately placed into a recovery tank of fresh fish water and monitored briefly using a UV flashlight for regurgitation of 2-NBDG. Successfully gavaged fish were returned to darkness during the 2-NBDG incubation period.

Tissue slicing and imaging

Gavaged mice were euthanized by asphyxiation with CO_2. Zebrafish were euthanized in an ice bath followed by cervical dislocation. Euthanized animals were enucleated, and the retinas dissected away under red light into cold Ringer's solution (133 mM NaCl, 2.5 mM KCl, 1.5 mM NaH_2PO_4, 2 mM $CaCl_2$, 1.5 mM $MgCl_2$, 10 mM HEPES, 10 mM D-glucose, 1 mM sodium lactate, 0.5 mM L-glutamine, 0.5 mM reduced glutathione, 0.5 mM sodium pyruvate, 0.3 mM sodium ascorbate, pH 7.4). Isolated retinas were mounted on filter paper (0.45 µm pore, mixed cellulose, Millipore) and flattened with gentle suction. After peeling away remaining RPE, flat-mounted retinas were sliced into 300–400 µm slices using a tissue slicer (Stoelting). Slices were rotated 90° and the filter paper edges buried in strips of wax on a coverslip for imaging at room temperature. Fresh retinal slices were imaged at room temperature using a Leica SP8 confocal microscope with a 40X water objective; excitation/emission wavelengths were 488/525–575 nm for 2-NBDG, and 559/580–630 nm for tdTomato. Leica LAS-X (RRID:SCR_013673) software was used to acquire images at 2048 x 2048 pixel resolution with 12 bit depth, and Z-stacks imaged every 0.5 µm over a tissue depth of 10–30 µm.

Image analysis

ImageJ software (RRID:SCR_002285) was used for quantification of 2-NBDG fluorescence in fresh retinal slices. 10 slices of each Z-stack were maximum intensity projected, and retinal layers were identified by morphology and expression of transgenic markers. For every slice, 3 small uniformly sized rectangular regions of interest (ROIs) were placed randomly in each retinal layer, and mean fluorescence intensity of each ROI was measured. Average 2-NBDG fluorescence in each layer was divided by the autofluorescence of corresponding retinal layers from animals gavaged with saline or water.

Metabolic flux analysis

Isolated mouse retina or confluent human fetal RPE cells were changed into pre-warmed Krebs-Ringer bicarbonate buffer (KRB) containing, depending on the experiment, [1,2] ^{13}C glucose, U-^{13}C glucose, or U-^{13}C lactate (Sigma) as described elsewhere (Du et al., 2013b; 2015; 2016b). Both retinas and RPE cells were incubated for the specified time points. Metabolites from each time point were extracted and analyzed by gas chromatography mass spectrometry (GC-MS, Agilent 7890/5975C) as described in detail (Du et al., 2013a, 2013b).

Measurement of U-^{13}C glucose transport across hfRPE cells on transwell filters

After maturation for 4–6 weeks in culture, hfRPE cells grown on transwell filters (Millicell HA 0.45 µm pore size 0.6 cm^2) were changed into 500 µL of DMEM containing 1% FBS on each side. 5 mM U-^{13}C glucose (Cambridge Isotope Laboratories) was included in the medium in the basolateral side while various concentrations of sodium lactate were added to the apical side, while maintaining a constant pH. Apical side medium was collected at 8 hr to analyze the transported U-^{13}C glucose by liquid chromatography coupled with triple quadrupole mass spectrometry (Waters Xevo TQ Tandem mass spectrometer with a Waters ACQUITY system with UPLC) as reported in detail (Du et al., 2015).

Live-cell imaging NAD(P)H autofluorescence

Cultured hfRPE cells were attached to cover slips that were previously coated with a thin layer of Matrigel (Corning, Corning NY) diluted 1:30 1–2 days prior to the imaging experiment. NAD(P)H was imaged and quantified similarly to a previous study (Jung et al., 2009). Cells were perifused with KRB (supplemented with 0.1% bovine serum albumin and 1% penicillin streptomycin fungizone (Invitrogen)) at a flow rate of ~0.1 mL/min at 37 °C on the stage of a Nikon Eclipse TE-200 inverted microscope. Fluorescence imaging of NAD(P)H was measured with emission detected at 460 nm by a CoolSnap HQ2 CCD camera (Photometrics, Tucson, AZ) through a 40X Super Fluor Nikon objective (DIC H/N2) during excitation at 360 nm via a Xenon lamp (Lambda LS-1620, Sutter Instrument Company, Novato, CA). NAD(P)H fluorescence integration time was 50 msec. The software package Elements (Nikon) was used to drive the data acquisition. At the completion of each protocol, the steady-state levels of relative fluorescence (RFU) during exposure of KCN and subsequently FCCP were measured and this data was used to normalize the RFU data. The normalization of the NAD(P)H signal was as a percent of RFU_{FCCP} and RFU_{KCN}, defined as 0% and 100% respectively for each cell.

Serial block face SEM

Mouse eyes were enucleated, the anterior half was dissected away, and the eyecup was cut in half. Tissue was fixed in 4% glutaraldehyde in 0.1 M sodium cacodylate buffer, pH 7.2, at room temperature (RT), then stored overnight at 4 °C. Samples were washed 4 times in sodium cacodylate buffer, postfixed in osmium ferrocyanide (2% osmium tetroxide/3% potassium ferrocyanide in buffer) for 1 hr on ice, washed, incubated in 1% thiocarbohydrazide for 20 min, and washed again. After incubation in 2% osmium tetroxide for 30 min at RT, samples were washed and en bloc stained with 1% aqueous uranyl acetate overnight at 4 °C. Samples were finally washed and en bloc stained with Walton's lead aspartate for 30 min at 60 °C, dehydrated in a graded ethanol series, and embedded in Durcupan resin. Serial sections were cut at 60 nm thickness and imaged with 6 nm pixel size using a Zeiss Sigma VP scanning electron microscope fitted with a Gatan 3View2XP ultramicrotome apparatus. Imaged stacks

were concatenated and aligned using TrakEM2 (RRID:SCR_008954). Unless stated otherwise, five washes with water were used for all wash steps.

Statistical analyses

R (RRID:SCR_001905) with R Commander was used to perform one-way ANOVA for NBDG gavage experiments.

Reproducibility

Each set of data has been reproduced the number of times (n) described in each figure legend. ‘n’ refers to the number of retinas, eyecups or hfRPE wells that were analyzed. We did not make comparisons between mutant animals so n refers to the number of technical replicates, not the number of biological replicates.

Acknowledgments

The work described in this chapter was published in *eLife*. The other authors that contributed to this study were Mark A. Kanow (first author), Michelle M. Giarmarco, Connor S.R. Jankowski, Abbi L. Engel, Jianhai Du, Jonathan D. Linton, Christopher C. Farnsworth, Stephanie R. Sloat, Austin Rountree, Ian R. Sweet, Ken J. Lindsay, Edward D. Parker, Susan E. Brockerhoff, Martin Sadilek, Jennifer R. Chao, and James B Hurley. This study was supported by funding from NIH EY06641 and NIH EY017863 to JBH, NIH EY026020 to SEB, NEI core grant EY001730 and P30 DK-17047 (Cell Function Analysis Core), NSF GRFP 2013158531 and NIH NEI 5T32EY007031 to MMG, and NIH EY026030 to JRC.

Chapter 3 - Daily mitochondrial dynamics in cone photoreceptors

Citation

The work described in this chapter was published in the *Proceedings of the National Academy of Science* (PNAS):

Daily mitochondrial dynamics in cone photoreceptors

Michelle M. Giarmarco, Daniel C. Brock, Brian M. Robbings, Whitney M. Cleghorn, Kristine A. Tsantilas, Kellie C. Kuch, William Ge, Kaitlyn M. Rutter, Edward D. Parker, James B. Hurley, Susan E. Brockerhoff

Proceedings of the National Academy of Sciences. Nov 2020, 117 (46) 28816-28827; DOI: 10.1073/pnas.2007827117

The PNAS publication and supplementary information are available online: https://www.pnas.org/content/117/46/28816

Introduction

Photoreceptor cells in the retina are highly metabolically active. Their energy demands change throughout the day to support phototransduction (Okawa et al., 2008) and regeneration of outer segment (OS) disks (LaVail, 1976). Photoreceptors consume more energy as ATP in darkness than in light (Okawa et al., 2008) and some additional ATP comes from mitochondrial metabolism (Du et al., 2016a).

Energy production can be influenced by mitochondrial fission, fusion, and new growth (mitogenesis). Smaller, fragmented mitochondria typically consume less oxygen (Chen et al., 2005). Mitogenesis is influenced by many factors, including circadian rhythms (De Goede et al., 2018). In neurons mitogenesis can occur far away from the cell body (Van Laar et al., 2018). Mitochondria can form networks (Bleck et al., 2018) and folds of cristae within mitochondria can be remodeled (Cogliati et al., 2016). These dynamic processes contribute to cell health; mitochondrial dysfunction is associated with neurodegenerative diseases (Chen and Chan, 2009; Cieri et al., 2017; Wong et al., 2019), including retinal degeneration (Lefevere et al., 2017; Litts et al., 2015).

Over 90% of glucose taken up by photoreceptors is used for aerobic glycolysis(Ames et al., 1992; Winkler, 1981). Nevertheless, they have a large cluster of mitochondria in the apical portion of the inner segment, the ellipsoid, just below the OS. The density and organization of mitochondrial clusters vary among species, but they are present in photoreceptors of all vertebrates examined, including fish (Tarboush et al., 2014), ground squirrels (Sajdak et al., 2019), mice (Kanow et al., 2017), and humans (Nag and Wadhwa, 2016). In photoreceptors of some species, all mitochondria reside within the cluster, while in mammals with vascularized inner retinas mitochondria are also present at synaptic terminals (Bentmann et al., 2005; Stone et al., 2008). In cultured chicken retinas, mitochondrial dynamics are circadian (Chang et al., 2018), but diurnal changes in mitochondrial structure and function in photoreceptors

in intact eyes have not been explored. Daily exposure to sometimes intense light and high rates of energy production suggest that mitochondrial turnover may be important for photoreceptor health. Structural and functional changes to mitochondria could enable photoreceptors to meet increased ATP requirements in darkness.

In this report we describe daily changes that occur in zebrafish cone photoreceptor mitochondria. Zebrafish provide a useful model to dissect mitochondrial dynamics in specific photoreceptor subclasses. Zebrafish undergo typical vertebrate behavioral and biological circadian rhythms(Cahill, 2002; Vatine et al., 2011), and their retinas have four cone subtypes (red, green, blue, and ultraviolet [UV]) organized in a tiered, mosaic pattern. Each cone type can be identified by its unique morphology and position in the outer retina (Raymond et al., 1995), and each maintains a large cluster of mitochondria just below the OS (Tarboush et al., 2014). Our results indicate that mitochondrial clusters in cones undergo diurnal remodeling consistent with enhanced energy production in darkness.

Results

To examine mitochondrial cluster function and dynamics throughout the day, we collected retinas at six timepoints from adult zebrafish under 14-h/10-h light-dark (LD) or 24-h dark (DD) conditions. Retinas were used for imaging and biochemical experiments. Figure 3.1A illustrates individual cone cell structures with immunohistochemistry (IHC) and electron microscopy (EM). Cone subtypes were differentiated by double cone position, nuclear morphology, and presence of a distinct large mitochondrion at the base of UV cone clusters (Figure 3.1A, white arrows). At night zebrafish cone ellipsoids and OSs extend distally into the retinal pigment epithelium (RPE); in the morning they retract back toward the nuclear layer (SI Appendix, Fig. S1A). This daily process of retinomotor movements is regulated by light exposure and the circadian clock(Hodel et al., 2006; Menger et al., 2005).

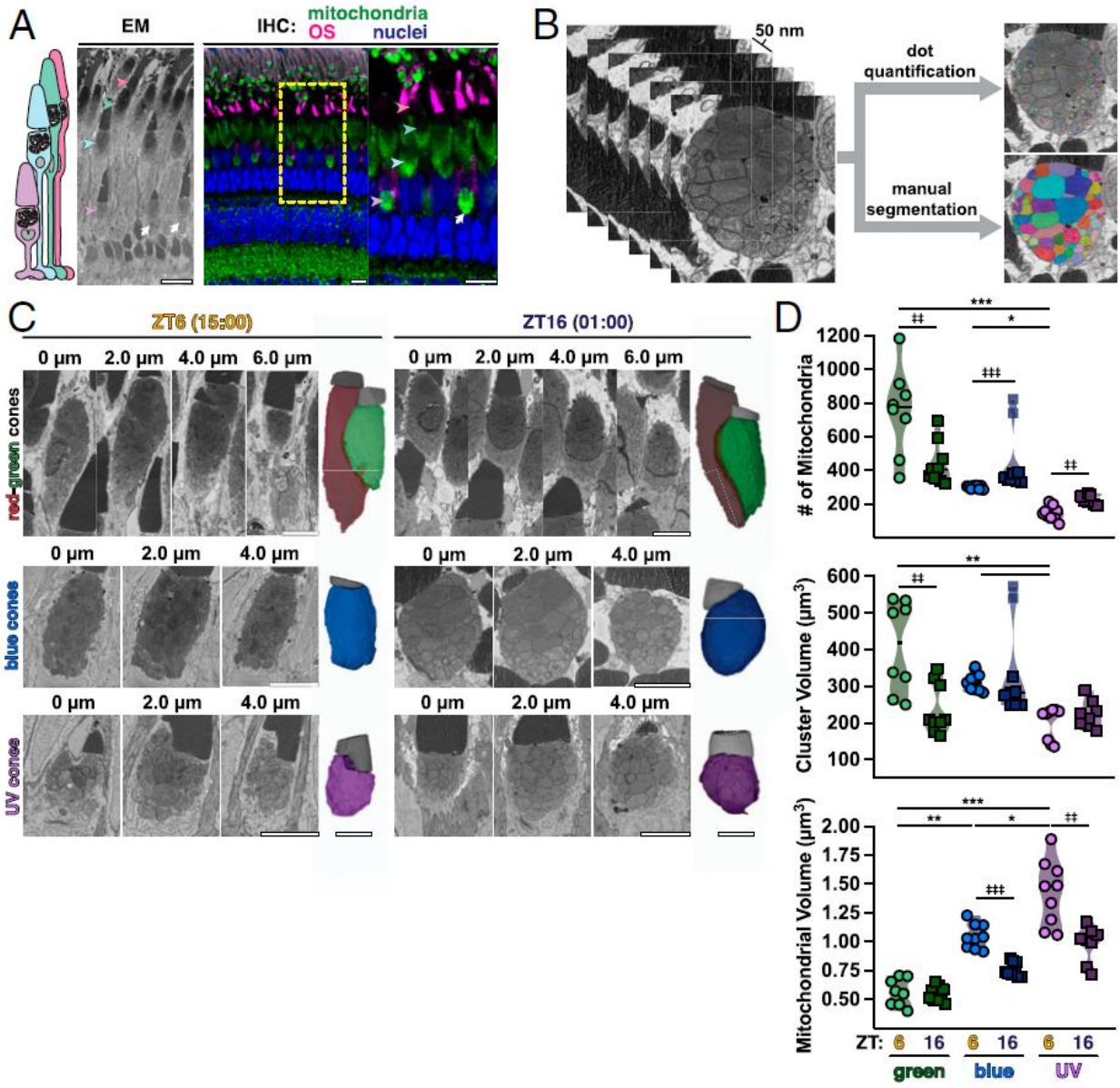

Figure 3.1: At night single cones have more small mitochondria.

(A) Schematic of zebrafish cone subtypes (Left), with EM (Middle) and IHC (Right) images of zebrafish outer retina. IHC images are stained for all mitochondria (green), red-green cone OSs (magenta), and nuclei (blue). Arrowheads indicate corresponding UV, blue, green, and red cone mitochondrial clusters; white arrows, megamitochondria at UV cluster bases. Yellow box, zoomed-in area. (Scale bars, 10 µm.) (B) Example 50-nm Z-stack from SBFSEM used for 3D analysis via manual segmentation or rapid dot quantification. (C) Z-stacks from SBFSEM with 3Drendered mitochondrial clusters (colored) and OSs (gray) from green, blue, and UV cone subtypes in daytime at ZT6 (15:00) and night at ZT16 (01:00). (Scale bars, 5 µm.) (D) Violin plots of mitochondrial number, cluster volume, and mitochondrial volume from dot quantification and manual segmentation; lines represent median. Cone subtypes are represented by respective colors at ZT6 (circles) and ZT16 (squares). *,‡P < 0.05. **, ‡‡P < 0.01. ***,‡‡‡P < 0.001. SI Appendix, Table S2 lists statistical information and Ns from each group.

Zebrafish Single Cones Have More Small Mitochondria at Night

We performed detailed three-dimensional (3D) analyses of cone mitochondrial clusters using 50 nm Z-sections collected by serial block-face scanning electron microscopy (SBFSEM) (Figure 3.1B and Movie S1). Image stacks were analyzed using either a rapid dot quantification method or manual segmentation to compare mitochondrial number, size, shape, and location between day (15:00, Zeitgeber Time 6 [ZT6]) and night (01:00, ZT16). Individual red-green, blue, and UV cone image stacks with corresponding 3D renderings of mitochondrial clusters and OSs at ZT6 and ZT16 are presented in Figure 3.1C. SI Appendix, Fig. S2 presents 3D renderings with mitochondrial numbers and cluster volumes for all cells in this study.

We found that at night, blue and UV cone mitochondria increase in number by 17 ± 10% and 57 ± 6%, respectively (Figure 3.1D, Top). These changes did not coincide with an increase in cluster volume (Figure 3.1D, Middle); on average, volumes of individual blue and UV cone mitochondria decreased at night by 29 ± 3% and 31 ± 6%, respectively (Figure 3.1D, Bottom). One animal in the study (SI Appendix, Fig. S2, fish 7) had overall larger cones than all others, and its blue cones were identified as outliers using a robust regression followed by outlier identification test (transparent markers at ZT16 in Figure 3.1D). For transparency we included these two cones in the analysis, but this did not affect the conclusions. Green cones, which in zebrafish exist in red-green double cones, appeared in two populations at both timepoints. Four animals in our study have very large green cones (>700 mitochondria), while the green cones of four other animals are smaller (300 to 450 mitochondria) (Figure 3.1D and SI Appendix, Fig. S2). Despite this bimodal population, mitochondrial volume for green cones is maintained between 0.4 and 0.7 μm3 at ZT6 and ZT16. This suggests that single and double cone subtypes undergo different cycles of mitochondrial dynamics.

Mitochondrial cluster shape was also examined for each cone subtype using transgenic zebrafish expressing YFP targeted to cone mitochondria (gnat2:mito-cpYFP) (Giarmarco et al., 2017), counterstained with antibodies targeting components of the

mitochondrial respiratory chain (SI Appendix, Fig. S1A and Table S1 lists antibodies used).

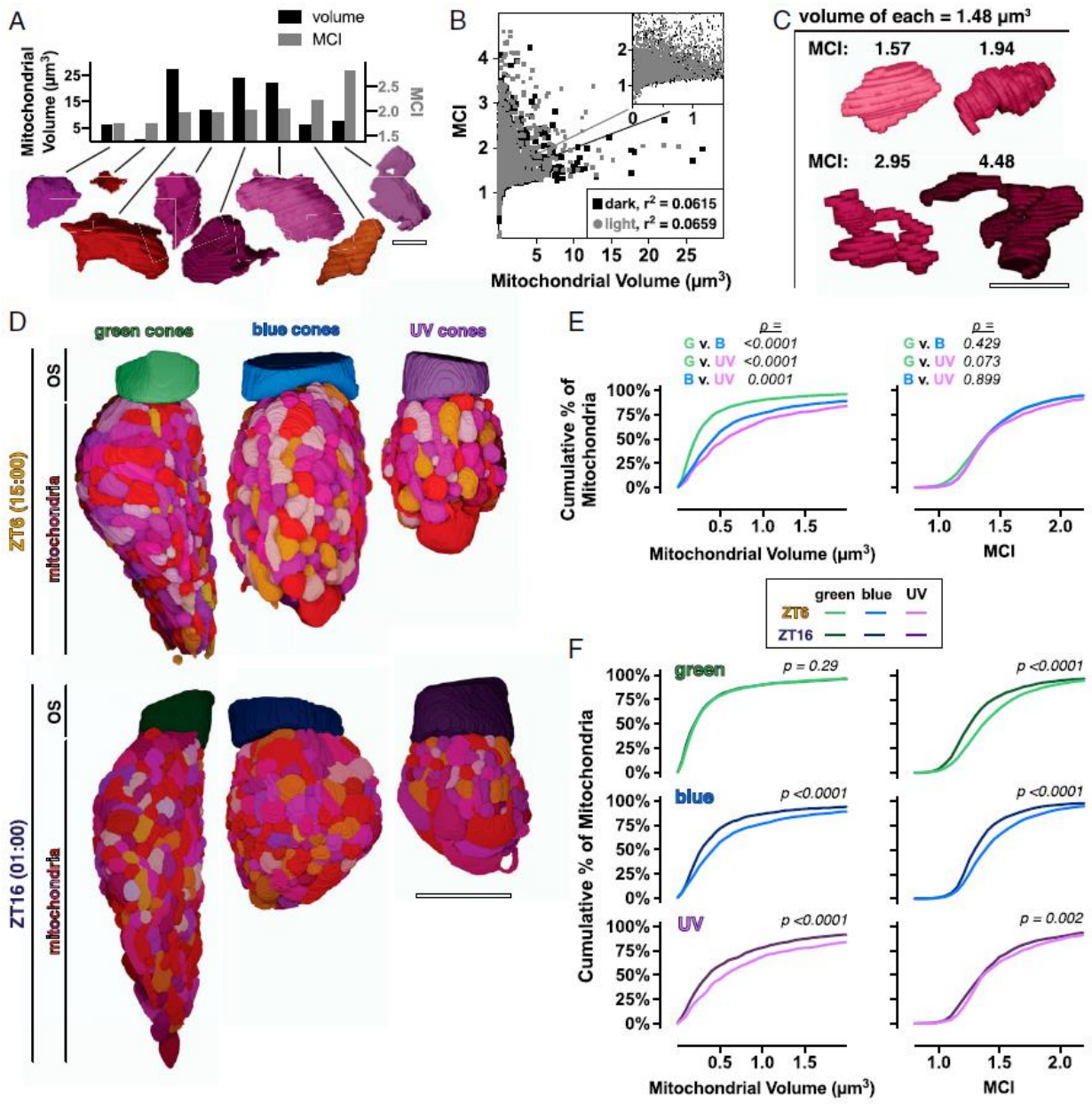

Figure 3.2: At night cones have more simple mitochondria

(A) Three-dimensional renderings of eight manually segmented cone mitochondria with corresponding quantifications of volume (Left axis, black bars) and MCI (Right axis, gray bars). (Scale bar, 2 μm.) (B) Cross-correlation plot of mitochondrial volume and MCI for individual mitochondria at ZT16 (black squares) and ZT6 (gray circles). (C) Three-dimensional renderings of single mitochondria with equal volumes (1.48 μm3) over a range of MCIs. (Scale bar, 2 μm.) (D) Three-dimensional renderings from manual segmentation of mitochondria and OSs in green, blue, and UV cones at ZT6 and ZT16. (Scale bar, 5 μm.) (E) Cumulative frequency distributions for mitochondrial volume and MCI comparing mitochondria between cone subtypes at ZT6. (F) Cumulative frequency distributions for cone subtypes, comparing mitochondrial volume and MCI at ZT6 (light lines) and ZT16 (dark lines). ZT6 curves are also presented in E; SI Appendix, Table S2 lists Ns from all groups.

Individual cone mitochondrial cluster lengths and circularity ratios were calculated. For all cone types, cluster length increases at night by ~50% (SI Appendix, Fig. S1 B, Top), but cluster width, reflected by the circularity ratio, decreases at this time (SI Appendix, Fig. S1 B, Bottom). Both LD and DD groups exhibited cyclical changes in cluster morphology.

Cone Mitochondria within Clusters Vary in Size and Complexity

Surface area and volume of each manually segmented mitochondrion was used to calculate mitochondrial complexity index (MCI), a size-insensitive measure of morphological complexity (Vincent et al., 2019). Mitochondria within clusters were heterogeneous in volume and MCI (Figure 3.2A), and MCI was poorly correlated with volume (Figure 3.2B). Four individual mitochondria with the same volume but different. MCIs are presented in Figure 3.2C. Compared to mouse cones, zebrafish cone mitochondria are simpler on average but occupy a larger volume (SI Appendix, Fig. S3).

Mitochondria in Cone Subtypes Are Morphologically Distinct, and More Simple Mitochondria Appear at Night

Our analyses also revealed morphological distinctions between cone subtypes. Clusters in green cones are longer (SI Appendix, Figs. S1C and S2) and have smaller mitochondria (Figure 3.1D). Figure 3.2D and Movie S2 depict 3D renderings of manually segmented green, blue, and UV cone clusters. At ZT6, green, blue, and UV mitochondria have significantly different distributions of mitochondrial volume, with mitochondrial volumes largest in UV cones and smallest in green cones, but cone subtypes do not have significantly different MCI distributions (Figure 3.2E). To compare mitochondrial volume and MCI between day and night, we analyzed manually segmented green, blue, and UV cones at ZT6 and ZT16. At ZT16, mitochondria are significantly smaller in blue and UV cones, but not green cones (Figure 3.2F). The MCI of all cone subtypes shifts significantly toward having more simple mitochondria at night. These results suggest that green cones can alter their mitochondrial complexity without changing volume.

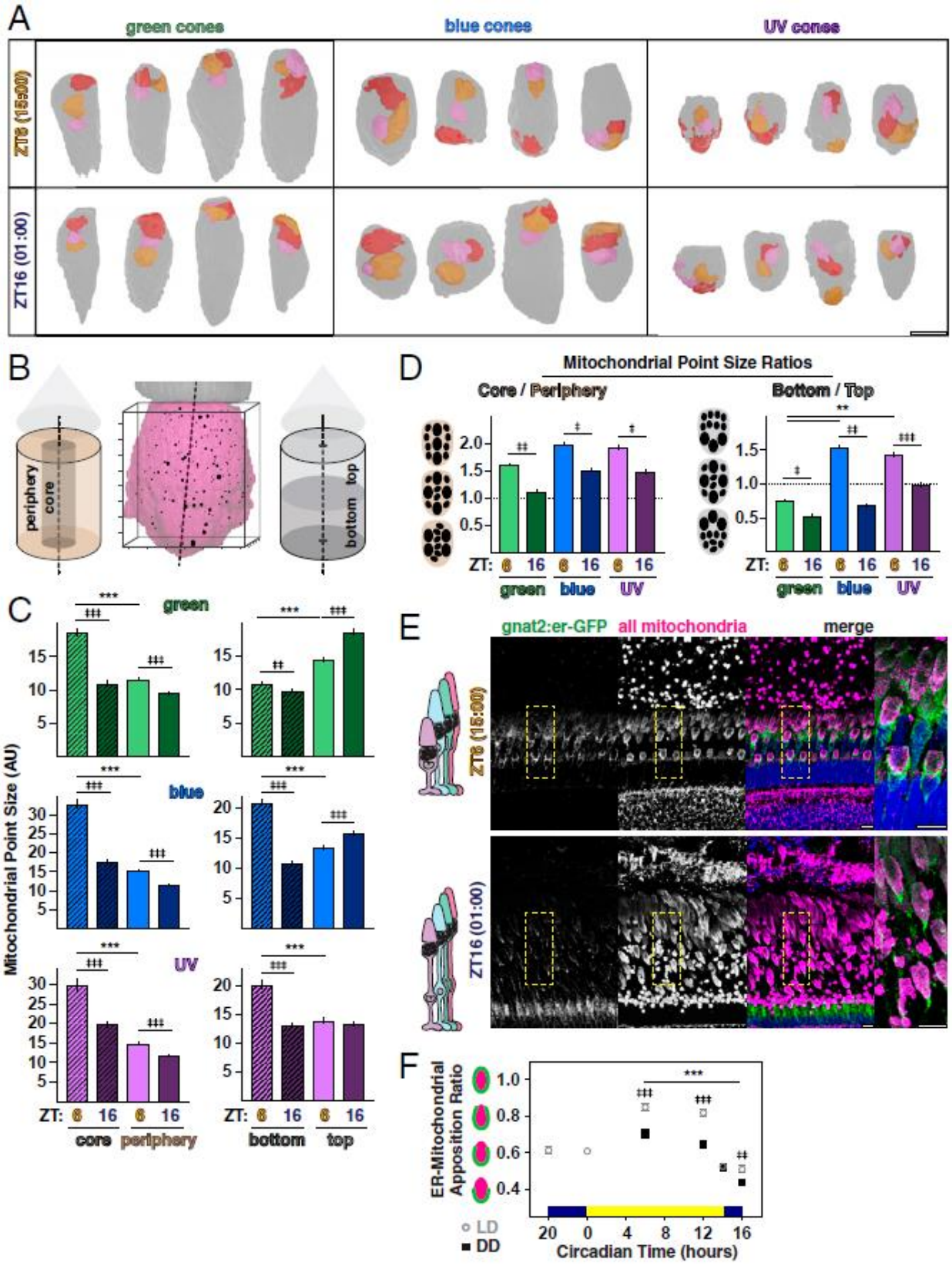
A
green cones
blue cones
UV cones
ZT6 (15:00)
ZT16 (01:00)
B
periphery
core
bottom
top
C
green
blue
UV
Mitochondrial Point Size (AU)
ZT: 6 16 6 16
core periphery
bottom top
D
Mitochondrial Point Size Ratios
Core / Periphery
Bottom / Top
ZT: 6 16 6 16 6 16
green blue UV
E
gnat2:er-GFP
all mitochondria
merge
ZT6 (15:00)
ZT16 (01:00)
F
ER-Mitochondrial Apposition Ratio
LD
DD
Circadian Time (hours)

Figure 3.3: Distribution of mitochondrial size across the cluster changes throughout the day

(A) Three-dimensional renderings of the three largest mitochondria in manually segmented cones at ZT6 and ZT16. OSs are oriented toward the top; ellipsoids, gray. Largest mitochondrion, red; middle, orange and smallest, pink. (Scale bar, 5 μm.) (B) Three-dimensional rendering of cone ellipsoid (magenta) and OS (gray) overlaid with the corresponding point cloud. Individual mitochondria are represented at their X-Y-Z locations; point size corresponds to relative mitochondrial size. Points were separated into core and peripheral or top and bottom populations. Axis ticks, 1 μm. (C) Quantification of mean mitochondrial point size in regions of the cluster for cone subtypes at ZT6 and ZT16. (D) Mitochondrial point size ratios quantifying regional core–periphery and bottom–top distributions of mitochondrial size reported in C for cone subtypes at ZT6 and ZT16. In C and D, ‡P < 0.05; **P < 0.01; ‡‡P < 0.001; ***,‡‡‡P < 0.0001. (E) IHC images of transgenic zebrafish outer retina expressing cone-targeted er-GFP (green) overlaid with mitochondrial and nuclear stains (magenta and blue, respectively) at ZT6 and ZT16. Yellow boxes, zoomed-in areas. (Scale bars, 10 μm.) (F) Quantification of mean ER–mitochondrial apposition in blue and UV cones from IHC for LD or DD groups. ‡‡P < 0.01. ***,‡‡‡P < 0.0001. SI Appendix, Table S2 lists statistical information and Ns from all groups.

Megamitochondria Associate in the Cluster Core

Cones of several species (Knabe et al., 1997; Tyrrell et al., 2019; Utsumi et al., 2020), including zebrafish (Kim et al., 2005), contain large megamitochondria. To examine the distribution of megamitochondria in zebrafish cone clusters, we 3D rendered the three largest mitochondria in manually segmented cones in their respective clusters. In all cone subtypes, megamitochondria localize within the cluster core, often in direct contact (Figure 3.3A). We did not detect striking differences in megamitochondria between day and night, but note that the volume, location, and complexity of megamitochondria vary between cone subtypes (SI Appendix, Fig. S4). Megamitochondria in green cones localize to the top of the cluster and are relatively uniform in size and of average complexity. Single cones contain distinct megamitochondria whose volume comprises 12 to 22% of the cluster. We observed several megamitochondria with projections extending toward the cluster periphery, and UV cone megamitochondria are unusually complex.

Mitochondria in the Cluster Core Are Smaller at Night

To examine the distribution of mitochondrial sizes across the cluster, each mitochondrion from SBFSEM analyses was plotted as a single point in 3D using its center X-Y-Z coordinates (Figure 3.3B). For manual segmentation, point size was proportional to mitochondrial volume. For dot quantification, point size was proportional to the number of dots needed to track each mitochondrion; larger points represent

larger or more branched mitochondria. Points were separated into peripheral and core populations according to distance from the cluster 3D central axis. Similarly, top and bottom populations were defined by proximity to the OS or cluster base. Mitochondrial point sizes were quantified in relation to cluster position (Figure 3.3C), and ratios of core/periphery and top/bottom were used to assay relative size distribution (Figure 3.3D).

At ZT6, cones have significantly more large mitochondria at the cluster core, compared to the periphery (Figure 3.3C and D, Left). At ZT16 average mitochondrial point size decreases 30 to 45% in the core and ~30% in the periphery; size also decreases ~35 to 50% at the bottom of the cluster (Figure 3.3C). Conceptually, this represents a shift toward more small mitochondria at the base of the cluster at night (Figure 3.3D). Compared to single cones, green cones underwent similar changes to mitochondrial size distribution, but maintain a significantly larger population of small mitochondria at the cluster base (Figure 3.3D, Right). These data suggest that in daytime all cones maintain a population of small mitochondria at the cluster periphery; at night mitochondrial size becomes more uniform across the cluster.

Endoplasmic Reticulum–Mitochondrial Appositions Peak in Daytime

In other cells the organelle endoplasmic reticulum (ER) initiates mitochondrial fission (Friedman et al., 2011; Korobova et al., 2013), a process that occurs at the end of mitogenesis (Amiri and Hollenbeck, 2008). Zebrafish cone ER primarily contacts mitochondria at the cluster base and periphery (Giarmarco et al., 2017), where mitochondrial size is most dynamic. We examined the cone ER network surrounding mitochondria at all timepoints. Using sections from LD or DD transgenic zebrafish expressing GFP targeted to cone ER (gnat2:er-GFP) (George et al., 2014), we performed IHC with antibodies against the mitochondrial respiratory chain (Figure 3.3E). To quantify potential ER contacts for individual blue and UV cone clusters, ER–mitochondrial apposition ratios were calculated by dividing the longest length of ER adjacent to the cluster by the cluster length.

In the daytime, ER tightly associates with the entire cluster surface and is densely packed around its base (Figure 3.3E, Top). At night, apposition ratios decrease as the ER becomes more diffuse and extends less toward the OS (Figure 3.3E, Bottom and Figure 3.3F). This shows that the ER network changes to accommodate the mitochondrial cluster and is consistent with the shift toward larger mitochondria at the top and periphery of single cone clusters at night (Figure 3.3D). At most timepoints ER–mitochondrial apposition ratios are lower for the DD group (Figure 3.3F), suggesting that light exposure drives tighter ER–mitochondrial associations.

Mitogenesis Genes Peak before Night Onset

Increased mitogenesis could result in more cone mitochondria at night. Mitogenesis is controlled at the transcriptional level (Ploumi et al., 2017; Scarpulla et al., 2007): upstream signals lead to mitochondrial DNA (mtDNA) replication, protein synthesis, and fission creating new mitochondria (Figure 3.4A). We measured mRNA transcript levels of mitogenesis genes using qPCR with whole retinas (Artuso et al., 2012) (SI Appendix, Table S3 lists primers; SI Appendix, Table S4 lists fitting parameters for cosinor curves). The early nuclear transcription factors *pgc1α* and *pgc1β* rise in the morning, while the mitochondrial transcription factor *tfam*, DNA polymerase *polg1*, and deacetylase *sirt3* all peak before night onset (Figure 3.4B). Together this suggests that canonical mitogenesis increases at night in whole retinas.

Transcripts encoding the mitochondrial fusion protein mfn2 rise in the morning (Figure 3.4C, Top), suggesting fusion could mediate the corresponding decrease in mitochondrial number in cones; a recent study found that cones contribute roughly half of the mitochondrial proteins in adult zebrafish retina (Hutto et al., 2020). No significant changes were detected in the zebrafish cone mitochondrial enlarging factor *es1* (Masuda et al., 2016) (Figure 3.4C, Middle). As a control we examined *aanat2* (Wang et al., 2015), which displays robust circadian changes in expression (Figure 3.4C, Bottom). Transcript levels between LD and DD groups were similar, and *tfam*, *polg1*, and *sirt3* met statistical cutoffs for rhythmicity, indicating that retinal expression of mitogenesis genes is regulated primarily by the circadian clock.

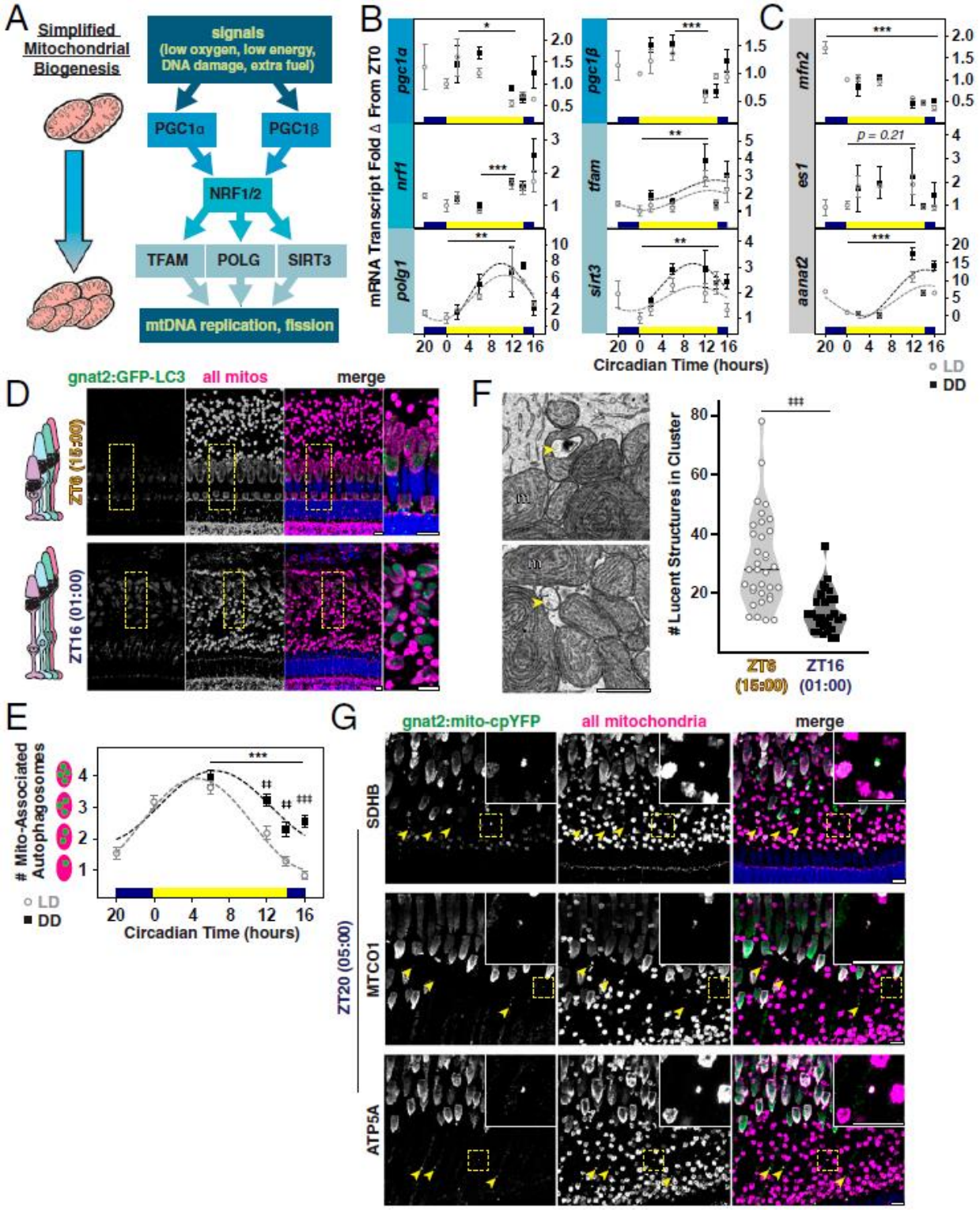

Figure 3.4: Mitogenesis genes peak in the evening, when fewer autophagosomes associate with mitochondrial clusters

(A) Simplified pathway for mitogenesis. (B and C) Quantification of mRNA transcripts from whole retinas measured using qPCR: in B, six mitogenesis genes, and in C, the mitochondrial fusion factor mfn2, the mitochondrial enlargement factor es1, and a control gene aanat2. LD, open circles; DD, black squares. *P

< 0.05. **P < 0.01. ***P < 0.0001. (D) IHC images of transgenic zebrafish outer retina expressing cone-targeted GFP-LC3 (green) overlaid with mitochondrial and nuclear stains (magenta and blue, respectively) at ZT6 and ZT16. Yellow boxes, zoomed-in areas. (Scale bars, 10 μm.) (E) Quantification of mitochondrial LC3-positive puncta in blue and UV cones from IHC for LD or DD groups. ‡‡P < 0.001. ***,‡‡‡P < 0.0001. (F, Left) SEM images of lucent autophagosomal structures (yellow arrowheads) inside and between cone mitochondria (m). (Scale bar, 1 μm.) (F, Right) Violin plots quantifying lucent structures in clusters at ZT6 (empty circles) and ZT16 (black squares); lines represent median. ‡‡‡P < 0.0001. (G) IHC images of transgenic cone-targeted mito-cpYFP (green) counterstained for SDHB, MTCO1, or ATP5A (magenta) and nuclei (blue) at 05:00 (ZT20). Yellow arrowheads and Insets indicate mislocalized mitochondria. (Scale bars, 10 μm.) SI Appendix, Table S2 lists statistical information and Ns from all groups

Mitochondrial-Associated Autophagosomes Peak in Daytime

A selective form of autophagy called mitophagy clears damaged or unnecessary mitochondria (Youle and Narendra, 2011). While several pathways can trigger mitophagy (Kawajiri et al., 2010; Strappazzon et al., 2015), all coalesce on recruitment of LC3 to maturing mito-autophagosomes. We performed IHC at all timepoints using LD or DD transgenic zebrafish expressing GFP fused to LC3 in cones (gnat2:GFP-LC3) (George et al., 2014) and antibodies against the mitochondrial respiratory chain (Figure 3.4D). LC3-positive autophagosomes overlapping with blue and UV cone mitochondrial clusters were quantified. The number of mitochondrial-associated autophagosomes increases twofold at light onset (Figure 3.4E). While changes to autophagosome numbers met statistical cutoffs for circadian rhythmicity, more mitochondrial-associated autophagosomes were present in the DD group in the evening, possibly indicative of enhanced mitochondrial turnover in prolonged darkness.

When viewed using EM, autophagosomes appear as lucent, multivesicular structures (Figure 3.4F, Left, yellow arrowheads), while mitochondria are electron dense and contain cristae folds. We validated our IHC findings by quantifying the number of electronlucent structures in all cone mitochondrial clusters imaged using SBFSEM. More lucent structures are present in clusters at ZT6 (Figure 3.4F, Right), when more mitochondrial-associated autophagosomes were detected using IHC. Several clusters contain >30 lucent structures in the daytime, suggestive of a mitophagic event at this timepoint.

Cone Mitochondria Mislocalize toward the Cell Body Hours before Light Onset

Degraded mitochondrial material canonically enters the endolysosomal pathway (Strappazzon et al., 2015), but in neurons it can translocate and leave the cell (Davis et al., 2014; Melentijevic et al., 2017). Mitochondria mislocalize toward the nucleus in degenerating human cones (Litts et al., 2015) and in a zebrafish cone model of mitochondrial calcium overload (Hutto et al., 2020). Four hours before light onset (05:00, ZT20), we observed mislocalized cone mitochondria using IHC with gnat2:mito-cpYFP transgenic zebrafish and three different mitochondrial respiratory chain markers (Figure 3.4G, yellow arrowheads). The structures are feasibly the size of a single mitochondrion (0.5- to 1-μm length), contain both cone mito-cpYFP and respiratory proteins, and lie between the cluster and the nucleus. They were present only at overnight timepoints ZT16 and ZT20, and in multiple animals over two generations. While we could not unequivocally identify these structures in SBFSEM, mitochondrial trafficking may occur between the cluster and cell body prior to light onset.

Mitochondria Share Material and Extrude It from the Cell in Darkness

In nearly all cones, we found dark deposits inside and between mitochondria throughout the day in SBFSEM images (Figure 3.5A, Top). Similar deposits are present in published EM images of cone mitochondrial clusters in other zebrafish (figure 2 of (Tarboush et al., 2014)), walleye (figures 5 and 7 of (Januschka et al., 1987)), frogs (figure 2 of (Mercurio and Holtzman, 1982)), pigeons (figure 16 of (Ishikawa and Yamada, 1969)), shrews (figures 2, 7, and 10 of (Lluch et al., 2003)), and ground squirrels (figure 5 of (Sajdak et al., 2019)), as well as mice and albino zebrafish (SI Appendix, Figs. S3 and S5, yellow arrowheads). When manually segmented and 3D rendered, we found these electron-dense lamellar whorls can span several micrometers, contacting the matrices of multiple mitochondria and/or the OS (Figure 3.5A, Bottom). Most deposits lie inside of single mitochondria, but they appear in the cytosol and occasionally cross the plasma membrane (Figure 3.5B, Top). This apparent extrusion most often occurs as single events, but some cells displayed multiple concurrent exit sites (Figure 3.5B, Bottom).

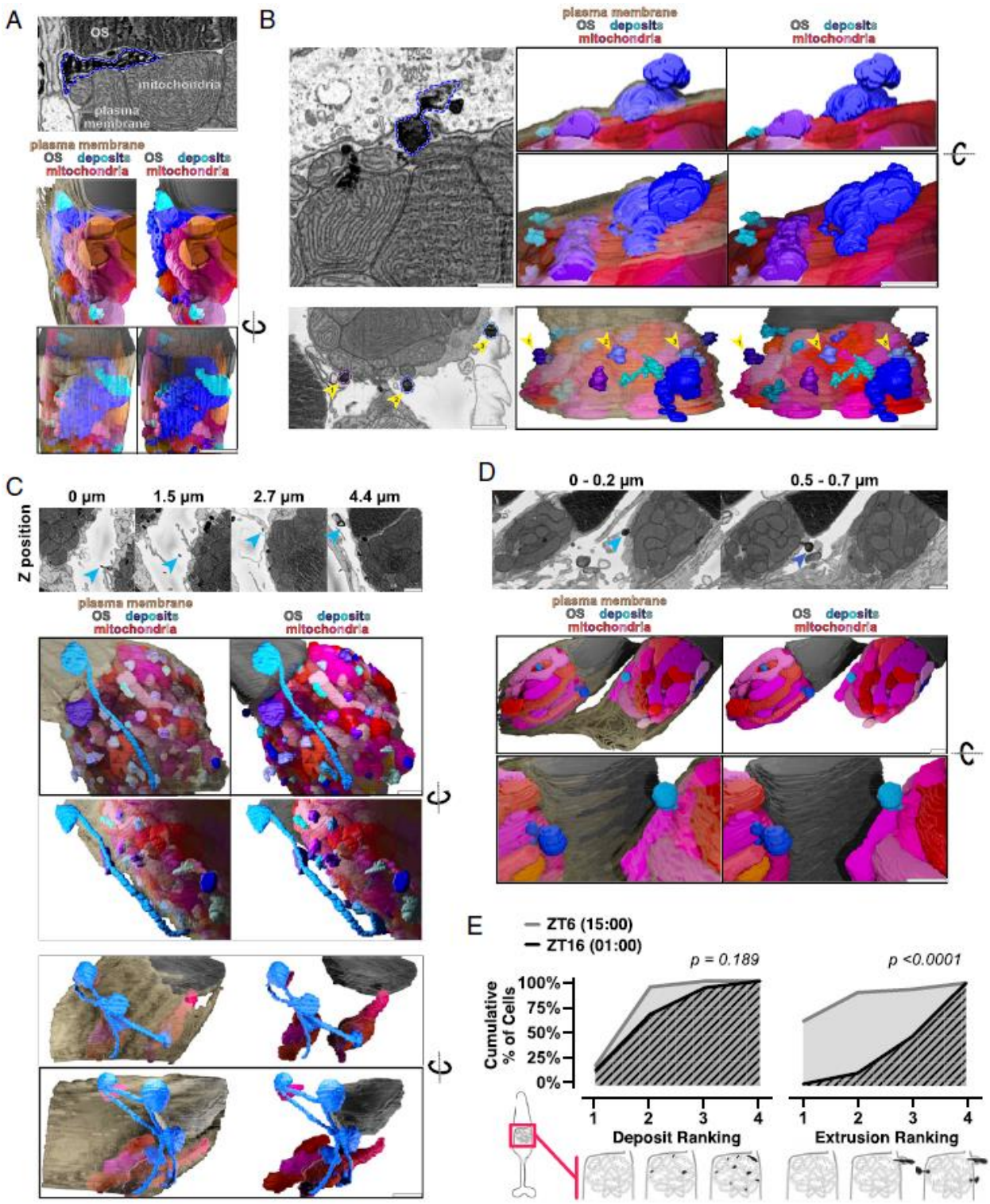

Figure 3.5: Mitochondria share material and extrude it from the cell in darkness

(A) SBFSEM image (Top) of deposits associated with cone mitochondria and corresponding 3D renderings (Bottom). One large deposit (blue outline) below the OS is associated with multiple mitochondria. (B) SBFSEM images showing extrusion of mitochondrial-associated deposits from cones, with 3D renderings. (B, Top) Extrusion of one deposit (blue outline). (B, Bottom) Multiple extrusion events

in one cell (blue-violet outlines, yellow arrows). (C) SBFSEM images showing stalks and networks in the extracellular space, and corresponding 3D renderings. (C, Middle) One extruded deposit tethered to mitochondria by a stalk (blue arrows). (C, Bottom) Branched network of extruded material contacting three distinct populations of cone mitochondria from one cell. (D) Extrusion of mitochondrial-associated deposits from two neighboring rods. (D, Top) SBFSEM minimum intensity projections over 0.2-μm depth highlighting extrusion events (blue arrows). (D, Bottom) Three-dimensional rendering. (All scale bars, 1 μm.) Beige, plasma membrane; gray, OSs; reds, mitochondria; blues, deposits. (E) Quantification of deposits and extrusion events at ZT6 (gray) and ZT16 (black). For deposits: 1 (no mitochondrial deposits) to 4 (every mitochondrion having a deposit). For the number of extrusion events: 1 (no events) to 4 (more than three events). SI Appendix, Table S2 lists Ns from all groups.

Other neurons can eject mitochondrial material via nanotunnellike extensions (Melentijevic et al., 2017). Three-dimensional analysis revealed that in cones, extruded material either remains near the cell surface or forms stalks that can reach 5 μm, terminating in diffuse lamellar extracellular sacs (Figure 3.5C, Top and Movie S3). The stalks appear as 40- to 90-nm electron-dense rings surrounding a hollow core. In the extracellular space stalks and sacs can connect, creating networks that link discrete populations of mitochondria within a cluster (Figure 3.5C, Bottom and Movie S4). These deposits and their extrusion in darkness were observed in nearly all cones but seldom in rods; in one instance extrusion was observed in two neighboring rods (Figure 3.5D).

To quantify cone mitochondrial deposits and extrusion events in day and night, we used a ranking system to blindly score clusters imaged with SBFSEM. The presence of mitochondrial deposits is similar between day and night (Figure 3.5E, Left). However, extrusion events occur almost exclusively at night, and most cells had multiple events (Figure 3.5E, Right). While the composition of the deposits is not known, they provide a physical link between cone mitochondria and the interphotoreceptor matrix (IPM).

Mitochondrial Succinate Metabolism Is More Active in Darkness Due to Altered Succinate Dehydrogenase Activity

Mitochondrial metabolism in whole mouse retinas is more active in darkness (Du et al., 2016a). However, ~96% of photoreceptors in mouse retinas are rods (Tsukamoto et al., 2001), while zebrafish retinas have ~50% cones (Larison and Bremiller, 1990; Raymond et al., 2014). To measure mitochondrial activity in cones, we performed enzyme histochemistry with fresh-frozen retina sections from LD or DD albino zebrafish

collected throughout the day. Some albino mouse (LaVail et al., 1987) and zebrafish (Vihtelic et al., 1999) strains undergo light-induced retinal degeneration, but under normal facility lighting our albino zebrafish display healthy central retinal morphology and mitochondrial clusters (SI Appendix, Fig. S5). Activities of succinate dehydrogenase (SDH, complex II) and cytochrome c oxidase (COX, complex IV) were assayed separately (Andrews et al., 1999); their roles in mitochondrial metabolism are highlighted in Figure 3.6A. Histochemistry was performed for all timepoints in parallel, and stain intensities of single cones were measured from light microscopy images (Figure 3.6B).

While COX activity remains robust and stable throughout the day, SDH activity in cones increases 25 to 30% in darkness (Figure 3.6C). SDH activity in the DD group is elevated at all times of day, suggesting possible repression of SDH activity by light in cones. Additionally SDH activity appears primarily in red-green double cones, compared to strong COX activity observed in all cone subtypes, rods, and the inner retina (Figure 3.6B, arrowheads).

As validation, we used metabolite labeling coupled with gas chromatography mass spectrometry (GC-MS) to assay activity of SDH in light- or dark-adapted zebrafish retinas around ZT6. Whole retinas were incubated with U-^{13}C labeled succinate (dark green boxes, Figure 3.6A), which SDH converts to U-^{13}C fumarate; fumarate is readily interconverted to malate via the enzyme fumarase (Andersen, 1980). Labeled fumarate and malate accumulate faster in dark-adapted retinas (Figure 3.6D). A 2.75-fold higher initial rate of formation for both fumarate and malate (Figure 3.6E) is consistent with higher SDH activity in darkness observed using histochemistry. To determine if succinate uptake was altered in darkness, we assayed labeled metabolites in media after 60 min, but did not find significantly lower amounts of labeled succinate (Figure 3.6F). Figure 3.6G depicts steady-state metabolite labeling in retinas and media after 60 min in light or darkness; succinate levels are similar in light and dark, but metabolites downstream of SDH accumulate in the media.

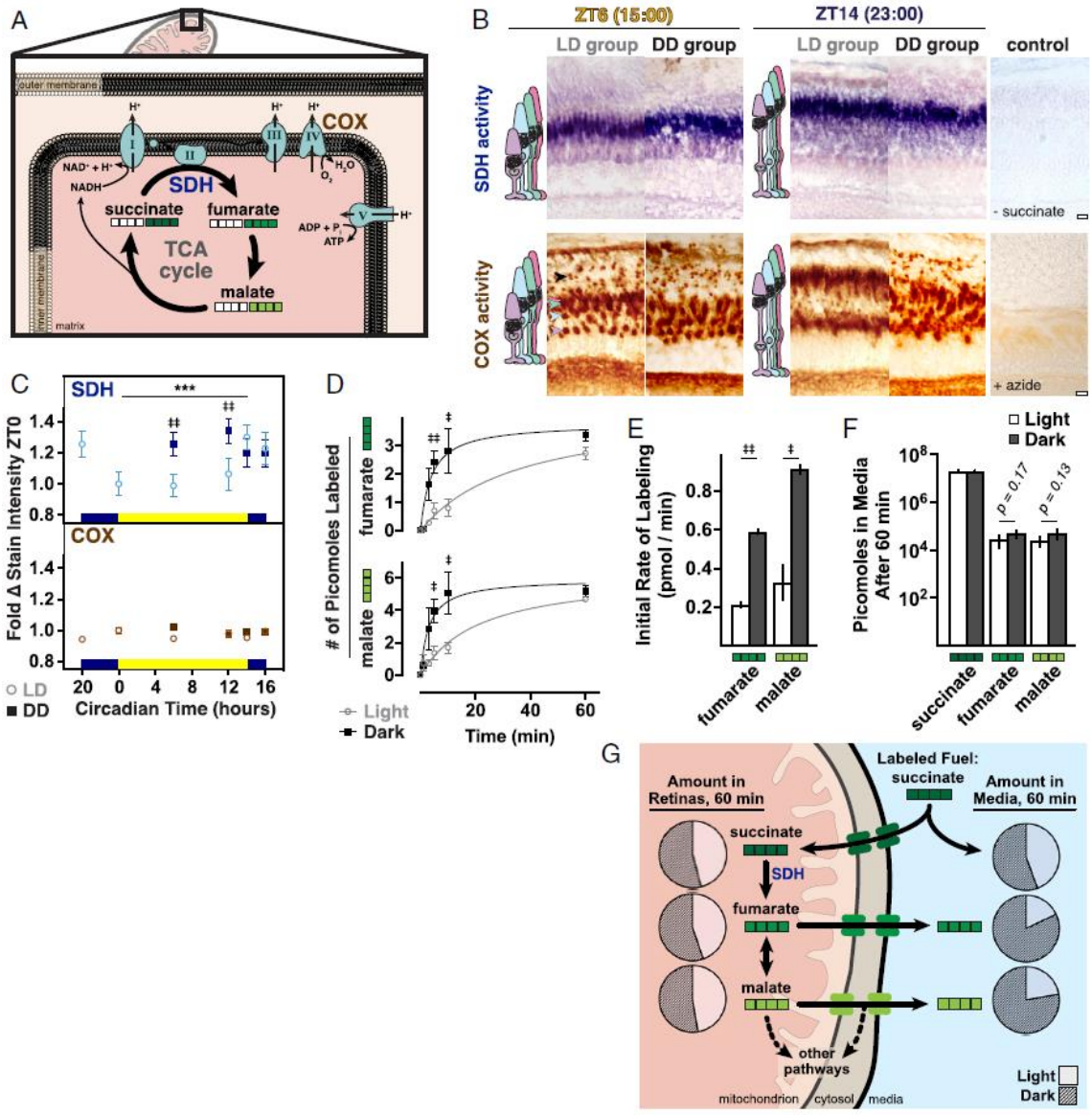

Figure 3.6: Mitochondrial metabolism is more active in darkness due to altered SDH activity

(A) Schematic of SDH in the tricarboxylic acid (TCA) cycle and electron transport chain, including COX also assayed in B. White squares represent ^{12}C carbons; green squares,^{13}C carbons for labeling experiments (D–F). (B) Light microscopy images of histochemical staining for SDH (blue) and COX (brown) activities. Shown are frozen sections from albino zebrafish at ZT6 and ZT14 (23:00) from LD and DD groups. Negative controls lacked substrate or contained an inhibitor. Arrowheads indicate corresponding cone subtype and rod (black) mitochondrial clusters. (Scale bars, 10 μm.) (C) Quantification of mean SDH and COX stain intensities in single clusters from LD (open circles) or DD (dark squares) groups; data normalized to ZT0. ‡‡P < 0.001. ***P < 0.0001. (D) Mean incorporation of ^{13}C label from U-^{13}C succinate into fumarate and malate. Whole retinas from light- or dark-adapted zebrafish were incubated in U-^{13}C succinate in light or dark; ^{13}C incorporation was determined with GC-MS. (E) Initial rates of formation of fumarate and malate from U-13C succinate in light and dark from the first 5 min of incubation. In D and E, ‡P < 0.05; ‡‡P < 0.001. (F) Amounts of U-^{13}C-labeled succinate, fumarate, and malate in media after 60-min light or dark incubation with retinas in U-^{13}C succinate. SI Appendix, Table S2 lists P values and Ns from all groups. (G) Schematic of steady-state metabolites inside and outside of retinas after 60-min incubation with labeled succinate. Pie charts denote relative amounts of metabolites in light (unfilled areas) and dark (filled areas).

Discussion

Comparisons of Cone Mitochondria between Species and Cone Subtypes

In zebrafish cones, hundreds of heterogeneous mitochondria pack between the nucleus and OS (Tarboush et al., 2014). In this report we quantified mitochondrial number, size, complexity, and 3D distribution in zebrafish cone subtypes. Compared with mouse cones (Sloat et al., 2016) (SI Appendix, Fig. S3), zebrafish cone mitochondria are more numerous, smaller, and densely packed, with elaborate cristae patterning (Perkins et al., 2003). The dense packing and disparate mitochondrial volumes between cone subtypes may reflect nutrient and oxygen access in the avascular zebrafish retina (Stone et al., 2008); double cones closer to the RPE and blood supply could fuel more mitochondria. These spatial constraints, the high SDH activity we observed in double cones, and previous studies showing unique metabolic activity in short wavelength cones (Kam et al., 2019a; Nork et al., 1990) suggest that diverse metabolic strategies support cone subtypes.

Half the animals in our SBFSEM study had larger green cone mitochondrial clusters than the others; the same retinal area was imaged for all animals and single cones did not display this feature. Retinomotor movements occur in cone subtypes at slightly different times (Menger et al., 2005), so our timepoints may have captured intermediate states for green cones. Alternately, zebrafish green cones may exist as multiple subtypes. Blue and UV cones in zebrafish each express one form of the light-sensitive protein opsin; green cones express four opsins across the adult retina (Chinen et al., 2003; Takechi and Kawamura, 2005), but single-cell analysis is needed to determine if green cone subtypes exist.

Mitochondrial Size in Photoreceptors

Mitochondrial size is linked to energetic output; in other cells smaller mitochondria respire less (Chen et al., 2005; Maryanovich et al., 2015). However, in zebrafish cones small, morphologically simple mitochondria may contribute more toward energy production. Zebrafish single cone mitochondria are smaller and simpler at night, when

energy demands and mitochondrial respiration are likely highest. Small mitochondria in cones populate the cluster periphery, closest to oxygen and fuels. Cristae in these small mitochondria generally display the organized, linear structure linked to higher energetic output (Perkins et al., 2003).

Like other species (Knabe and Kuhn, 1996; Vihtelic et al., 1999) zebrafish cones form megamitochondria, maintained by the enlargement factor ES1 (Masuda et al., 2016; Utsumi et al., 2020). We did not detect changes to *es1* mRNA transcripts in whole retinas, but observed juxtaposed megamitochondria in all cones throughout the day. The biological role of megamitochondria is unknown, but their densely packed cristae suggest roles beyond canonical respiration (SLAUTTERBACK, 1965). Membrane lipids concentrated in megamitochondrial cristae can form a conduit for oxygen (Desaulniers et al., 1996; Urschel and O'Brien, 2008). Many cone megamitochondria exhibit a central body with projections extending toward the cluster periphery; these projections toward the ER could be a site for mitogenesis (Knabe and Kuhn, 1996). Further, cone megamitochondria (Knabe et al., 1997; Lluch et al., 2003) and mitochondrial-derived ellipsosomes (MacNichol et al., 1978; Nag and Bhattacharjee, 1995) in other species guide light toward the OS. Zebrafish visual sensitivity is regulated by light and the circadian clock (Li and Dowling, 1998), so daily mitochondrial rearrangements may contribute to vision.

Mitochondrial Turnover in Photoreceptors

Maintenance of healthy mitochondria and mtDNA is crucial, particularly in the retina. mtDNA mutations (Lefevere et al., 2017) and disrupted autophagy (Rodríguez-Muela et al., 2015) are associated with retinal degeneration, and aging human cones accumulate mtDNA mutations and mitochondrial abnormalities (Barron et al., 2001; Nag and Wadhwa, 2016). In some forms of age-related macular degeneration, cone mitochondrial clusters remodel and mitochondria translocate toward the nucleus (Litts et al., 2015). Genes required for mitogenesis (Scarpulla et al., 2007) undergo circadian changes in retinal expression in a manner that supports mitogenesis at night onset, although it is unknown which retinal cell(s) this occurs in. At ER–mitochondrial contact

sites the ER stimulates mitophagy (Hamasaki et al., 2013) by recruiting autophagic machinery (Huang et al., 2018) and initiating mitochondrial fission (Friedman et al., 2011). In single cones, ER concentrates around the cluster during the day, when clusters contain more autophagosomes and fewer mitochondria. Together this suggests that cones undergo daily mitochondrial turnover involving ER.

SDH Activity and Potential Regulation in the Retina

Fewer mitochondria during the day could result in the reduced cone SDH activity we detected using histochemistry. Zebrafish cones have higher SDH activity than other retinal cells, consistent with studies of human (Andrews et al., 1999; Barron et al., 2001) and salamander retinas (Moore and Guberg, 1974). Cone SDH activity increases at night, when regulation from the zebrafish circadian clock (Cahill, 2002; Li et al., 2008) could promote mitochondrial succinate uptake (Cai et al., 2019). However, we did not find evidence of increased succinate uptake in darkness, and frozen sections used for histochemistry don't require transporters for substrate uptake. Thus, our observations of cone SDH activity likely resulted from changes to expression or posttranslational modifications, rather than succinate availability.

Light (Gu et al., 2002; Popov et al., 2010) and time of day (Akimoto et al., 2005; Reddy et al., 2006) can affect SDH expression in other cells. Additionally, SDH can be regulated by competitive inhibition (Ackrell et al., 1974; Potter and Dubois, 1943), phosphorylation (Acín-Pérez et al., 2014; Nath et al., 2015), acetylation (Cimen et al., 2010), and succinylation (Park et al., 2013). mRNA transcripts for the mitochondrial deacetylase SIRT3 increase in retinas prior to night onset, but regulation of SDH by SIRT3 in retinas has not been explored. In photoreceptors, both SIRT3 and the mitochondrial desuccinylase SIRT5 are necessary for normal function (Lin et al., 2016). Further, cristae structure can influence respiration (Cogliati et al., 2016; Guo et al., 2018), in part by driving SDH supercomplexation (Blanchette-Mackie and Scow, 1983). SDH catalyzes a reversible reaction in mouse retinas (Bisbach et al., 2020); we used succinate to quantify forward capacity of SDH.

Mitochondrial Deposits in Photoreceptors

In photoreceptors, whorled deposits contact the matrices of multiple mitochondria. The deposits are distinct from melanosomes; they are present in albino zebrafish photoreceptors. We did not investigate their composition, but they resemble osmiophilic structures observed in and around mitochondria of other cells, proposed to have roles in lipid metabolism (figure 8 of (Blanchette-Mackie and Scow, 1983) and figure 4 of (Tarlow et al., 1977)), mitochondrial degradation (Soubannier et al., 2012; Sugiura et al., 2014), and peroxisome synthesis (Sugiura et al., 2017). Further, ER stacks can encircle mitochondria, forming a lamellar structure to initiate mitophagy (Huang et al., 2018). Collectively this suggests that photoreceptor mitochondrial deposits may mediate lipid homeostasis and/or mitochondrial clearance.

Nightly Extrusion of Mitochondrial Material

Mitochondrial deposits are extruded from cones at night. The events we report are morphologically distinct from photoreceptor endocytosis (Hollyfield et al., 1985; Hollyfield and Rayborn, 1987), exocytosis (Rea et al., 2004; Wen et al., 2017), and from published examples of mitochondrial extrusion in other cells (Gasko and Danon, 1972; Géminard et al., 2002; Lyamzaev et al., 2008; Simpson and Kling, 1968; Unuma et al., 2015). Unlike these events, extrusion of cone mitochondrial deposits shows no evidence of fusion with the plasma membrane, and the released material remains associated with the cell surface and underlying mitochondria. The extruded material can connect to the extracellular space via thin stalks that terminate in diffuse lamellar sacs. Neurons have been reported to release and tether mitochondrial material (Davis et al., 2014; Melentijevic et al., 2017) via thin stalks ∼200 nm wide and terminal multivesiculate sacs of ∼3-µm diameter.

The extracellular structures attached to photoreceptors are smaller (∼60-nm stalks and ∼1-µm sacs), and sacs do not contain vesicles. The stalks are smaller than tunneling nanotubes (Gerdes and Carvalho, 2008), which can transport mitochondria (Lu et al., 2017; Sartori-Rupp et al., 2019; Wang and Gerdes, 2015). Photoreceptors can exchange proteins via an unknown mechanism (Ortin-Martinez et al., 2017), but we did

not observe connections between cones. The extracellular structures could link cones to the IPM, a scaffold of carbohydrates and bound proteins (Hollyfield, 1999; Ishikawa et al., 2015) where cones occupy a distinct metabolic microenvironment (Adler and Southwick, 1992; Johnson et al., 1986). At night the zebrafish outer retina becomes disorganized by retinomotor movements, so the extracellular structures could physically anchor cones to the IPM.

In summary, we report a quantitative analysis of daily mitochondrial dynamics in cone photoreceptors. At night, when energy demands are likely highest, a mitogenesis event in retinas precedes increases in cone metabolic activity and the number of small mitochondria in single cones. During the day, mitochondrial number decreases, perhaps mediated by fusion and/or mitophagy. We also report a dense lamellar material that is shared between mitochondria and extrudes from the cell at night, sometimes forming extracellular networks. These daily changes to cone mitochondria can support energy production at night, regulated by light and the circadian clock. This study did not include phototransduction mutants or lengthy dark adaptation; differences we report between LD and DD groups could be attributed to effects of light masking and/or master circadian rhythms (Altimus et al., 2010; Mrosovsky et al., 1999). Elucidating the makeup of mitochondrial deposits, regulation of SDH, role of ER–mitochondrial contacts, and rates and locations of mitochondrial turnover in healthy cones will contribute to an understanding of how mitochondrial abnormalities in aging and disease affect vision.

Materials & Methods

Zebrafish Maintenance and Retina Collection

Research was authorized by the University of Washington Institutional Animal Care and Use Committee. Wild-type, transgenic, and albino adult zebrafish were maintained on a 14-h/10-h light/dark cycle. Twenty-four hours prior to experiments, fish were fasted in either continuous darkness (DD) or standard room light (LD). See SI Appendix for details about fish lines and sample collection.

Serial Block-Face Scanning Electron Microscopy

Wild-type or albino zebrafish eyes were fixed and prepared in resin blocks as described previously (Kanow et al., 2017). Serial sections were cut at 50-nm thickness and imaged in the outer retina, 100 to 200 μm from the optic nerve. Z-stack images were processed and measured using the TrakEM2 plugin for ImageJ (research resource identifier [RRID]:SCR_008954). See SI Appendix for details about sample preparation and image analysis.

Immunohistochemistry

Albino or transgenic zebrafish eyes were fixed, cryosectioned, stained, and confocal imaged as described previously (Hutto et al., 2020). Z-stacks from each timepoint were blindly analyzed using ImageJ (RRID:SCR_002285). SI Appendix, Table S1 lists antibodies and stains; see SI Appendix for details about sample preparation and image analysis.

Quantitative PCR

RNA was extracted from wild-type zebrafish eyes, reverse transcribed into cDNA, and analyzed using qPCR as described in SI Appendix. Primer sequences are reported in SI Appendix, Table S3. Cosinor curves fitted to each dataset were used to determine circadian rhythmicity according to cutoff values (more than twofold change and $P < 0.05$ from ANOVA analysis) (DeVera and Tosini, 2020); data meeting this cutoff display dashed lines. SI Appendix, Table S4 lists fitting parameters and statistics.

Enzyme Histochemistry

Histochemical enzyme activity was assayed similarly to previous studies in human (Andrews et al., 1999) and mouse retina (Chinchore et al., 2017). Briefly, albino zebrafish eyes were dissected, frozen in optimal cutting temperature compound and cryosectioned for parallel staining. SDH and COX activity stain solutions were applied for 10 min at 37 °C, then washed, mounted, and imaged with a light microscope. Stain intensity of single cones was blindly quantified using ImageJ. See SI Appendix for details about sample preparation and image analysis.

Isotopic ^{13}C Succinate Labeling and Mass Spectrometry

Light- or dark-adapted wild-type zebrafish eyes were dissected and incubated in 1 mM D-[U-^{13}C]-succinate with 1 mM unlabeled glucose for the specified timepoints, then washed in phosphate buffered saline and flash frozen in liquid nitrogen. Metabolites were extracted from retinas, derivatized, and analyzed using GC-MS. See SI Appendix for details about sample collection and metabolite analysis.

Data Analysis

Data were processed using Microsoft Excel (RRID:SCR_016137); statistical tests were performed using GraphPad Prism (RRID:SCR_002798). SI Appendix, Table S2 lists experimental numbers (Ns) and statistical analysis methods for each figure. The 3D renderings and animations from SBFSEM were created using Blender (RRID:SCR_008606) (Giarmarco, 2020).

Data Availability

Single cell data from IHC, SBFSEM, histochemistry, succinate labeling data have been deposited in Open Science Framework (https://osf.io/qaed8).

Acknowledgments

The work described in this chapter was published in the *Proceedings of the National Academy of Science*. The other authors that contributed to this study were Michelle M. Giarmarco (first author), Daniel C. Brock, Brian M. Robbings, Whitney M. Cleghorn, Kristine A. Tsantilas, Kellie C. Kuch, William Ge, Kaitlyn M. Rutter, Edward D. Parker, James B. Hurley, and Susan E. Brockerhoff. Funding for this work was provided by the University of Washington (UW) Art and Rita Levinson undergraduate research scholarship (D.C.B.), NIH NEI 5T32-EY007031 (M.M.G. and K.M.R.), NIH NEI R01-EY026020 (S.E.B.), NIH NEI R01-EY06641 (J.B.H.), NIH NIA T32-AG000057 (K.A.T.), and the UW Vision Core grant NIH NEI P30-EY001730 (to Maureen Neitz). We thank

Amandeep Dhami, Ashlee Evans, Carson Adams, Stephanie Sloat, and Alexey Merz for help with data analysis and thoughtful discussion; Stan Kim provided zebrafish care at the UW Institute for Stem Cell and Regenerative Medicine Aquatics Center.

Chapter 4 - The importance of mouse strain selection to characterize function and metabolism in the eye: A short study of the Rd8 mutation and the loss of NNT

Introduction

The laboratory mouse (*Mus musculus*) has been used as a model of vision for well over 100 years (Hopkins, 1927). The C57Bl/6 mouse is the most popular choice in biomedical research (Bryant, 2011). However, this nomenclature is deceiving as C57Bl/6 mice do not presently exist. Rather, modern experiments are being done with any of the numerous substrains of C57Bl/6 mice that were all derived from the inbred C57Bl parent strain.

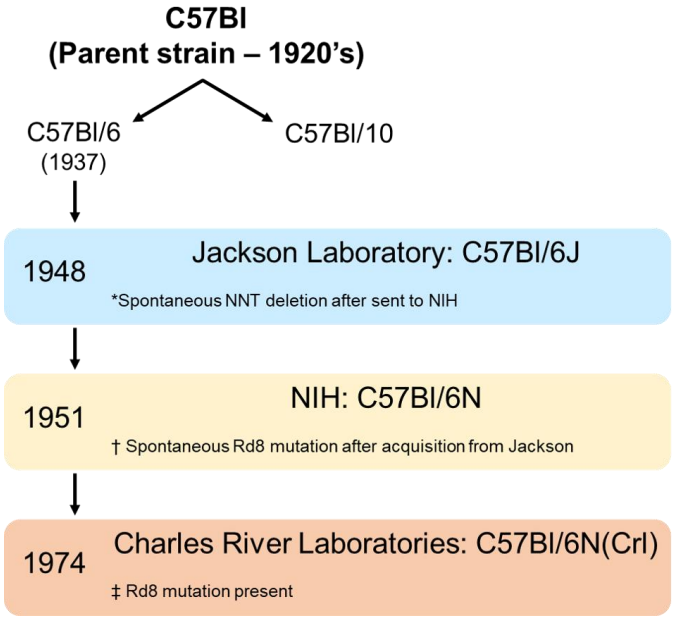

Figure 4.1: Derivation of the C57Bl/6J and C57Bl/6N substrains examined in this chapter, including notations regarding the NNT deletion in 6J and the Rd8 retinal degeneration mutation in 6N.

All mice that have C57Bl in their name were derived from the same stock of animals that were propagated in the 1920's. These animals were split into C57Bl/10 and C57Bl/6 in 1937. This work only examined the C57Bl/6 substrains. The C57Bl/6J mice as they are known today first sent to the Jackson Laboratory. Mice from this colony were sent to the National Institutes of Health in 1951 and would become the C57Bl/6N mice, which were in turn sent to Charles River Laboratories in 1974. The NNT and Crb1 mutations occurred after the mice that would generate the 6J and 6N substrains had already been separated,

A brief summary of the derivation of the substrains considered in this chapter is illustrated in Figure 4.1, and described here based on previous thorough reports (Mekada et al., 2009; Song and Hwang, 2017).

The C57Bl parent strain was initially established in the 1920s and branched into C57Bl/10 or to C7Bl/6 in 1937. These C57Bl/6 mice were maintained by the Jackson Laboratory and became what is now C57Bl/6J (6J). In 1951, C57Bl6 mice were sent to the National Institutes of Health and these mice became what is now C57Bl/6N (6N). In

1974, the NIH sent some of their C57Bl/6 stock to Charles River Laboratories, which are now the C57Bl/6NCrl mice.

Of the numerous C57Bl/6 substrains, 6J and 6N are commonly used as “wild-type” mice. However, both of these substrains have a series of behavioral (Banks et al., 2015; Bryant et al., 2008; Matsuo et al., 2010) and genetic (Mekada et al., 2009; Simon et al., 2013) differences - including some deleterious mutations - that may confound interpretation of experimental results.

The J and N substrains of C57Bl/6 carry a multitude of mutations (Table 4.1). For example, both 6J and 6N begin to experience hearing loss at a younger age than other strains of mice (Kane et al., 2012). The 6J substrain has severely decreased melatonin secretion, which could hinder the use of this animal to study normal circadian rhythm (Roseboom et al., 1998). In this study, we focused on the impact of nonfunctional nicotinamide nucleotide transhydrogenase (NNT) in the 6J substrain and the Rd8 retinal degeneration induced by a single base pair deletion in crumbs-like 1 (Crb1) in 6N mice.

Table 4.1: Overview of well-known mutations in C57Bl/6J and C57Bl/6N

Strain	Mutations		Phenotypes
C57Bl/6J	4-exon deletion in NNT	Toye Cox 2005 Diabetologia	Impaired glucose tolerance
	(-/-) Cdh23^{ahl}	Kane Johnson 2012 Hearing Res	Partial cause of accelerated hearing loss starting at 10 MO
	Truncated Aanat	Roseboom Klein 1998 Mol Brain Res	Severely decreased melatonin secretion
C57Bl/6NCrl	Crb1^{Rd8}	Chang Heckenlively 2002 Vis Res, Mattapallil Caspi 2012 IOVS	Retinal degeneration
	(-/-) Cdh23^{ahl}	Kane Johnson 2012 Hearing Res	Partial cause of accelerated hearing loss starting at 10 MO

NNT is a mitochondrial protein that generates NADPH by driving hydride transfer from NADH to NADP+ in order to generate NADPH (Zhang et al., 2017). Four exons of NNT – numbered 7 through 11 – were lost in 6J along with a missense mutation in exon 1 (Toye et al., 2005). As the mutation is not present in 6N, the NNT deletion occurred after the C57Bl/6 mice were sent to the NIH from the Jackson Laboratory (Figure 4.1). Mutations in NNT can lead to glucocorticoid deficiency syndrome, diabetes, and heart problems in humans (Bainbridge et al., 2015; Fujisawa et al., 2015; Jazayeri et al.,

2015; Rydström, 2006). Dysfunction in NNT effects mitochondrial signaling and redox state (Ho et al., 2017; Ronchi et al., 2013; Santos et al., 2017). In the retinal pigment epithelium (RPE), reductive carboxylation was found to be an important metabolic pathway (Du et al., 2016b). NNT knockdown was found to decrease reductive carboxylation and stimulate glucose catabolism (Gameiro et al., 2013). Given the disproportionately large flux of glutamine through reductive carboxylation in RPE cells relative to other tissues, we sought to examine this process in eyecups and determine if the loss of NNT in 6J mice impacted reductive carboxylation flux.

The second mutation we considered was the single base pair deletion in Crumbs-like 1 (Crb1) that arose spontaneously in the C57Bl/6N substrain. This single deletion at nt3481 leads to a frameshift and premature stop codon following amino acid 1207 (Mehalow et al., 2003). Consequently, these mice have Rd8 retinal degeneration (Chang et al., 2002; Mattapallil et al., 2012; Mehalow et al., 2003). Mutations in Crb1 are a known genetic cause of both retinitis pigmentosa and Leber Congenital Amaurosis (Den Hollander et al., 1999; Lotry et al., 2001) which both cause severe visual impairment. Crb1 is critical in photoreceptor morphogenesis and zonula adherens junction (Mehalow et al., 2003). For vision researchers, caution in the selection of the C57Bl/6 substrain for their work is critical as the 6N substrain is homozygous for Rd8 retinal degeneration, and any mice derived from this substrain could be a carrier. This is particularly important when crosses between strains are necessary to generate knock-outs or transgenics mice. However, the 6J substrain does not carry this mutation (Mattapallil et al., 2012). In our own work, we sought to determine how Rd8 mutation impacts metabolism in young animals.

In the study of retinal metabolism, metabolic genes and mutations that lead to ocular degeneration are of particular concern. Given the popularity of the C57Bl/6 substrains, but especially 6J and 6N, we sought to examine the effect the NNT deletion or Rd8 mutation in Crb1 in these strains had on function and metabolism. To do so, we used metabolic flux and scotopic ERGs in three common inbred mouse strains: C57Bl/6J, C57Bl/6N, and 129S1/SvImJ. Selection of 129S1/SvImJ as a control was primarily due

to the fact that it is not albino, no obvious visual degenerative phenotypes we found in a literature search, and it is frequently used to generate stem cell knock-out lines.

Results

Genotyping to identify NNT and Crb1 alleles in two "wild-type" mouse substrains

We were able to observe the wild-type and mutant alleles of these two genes using four different genotyping reactions. In NNT, a Del Rxn (NNT deletion in 6J) and a WT Rxn (WT NNT in 6N). In Crb1, an Rd8 Rxn (Crb1 base pair deletion in 6N) and a WT Rxn (WT Crb1 in NNT). These results are shown in Figure 4.2.

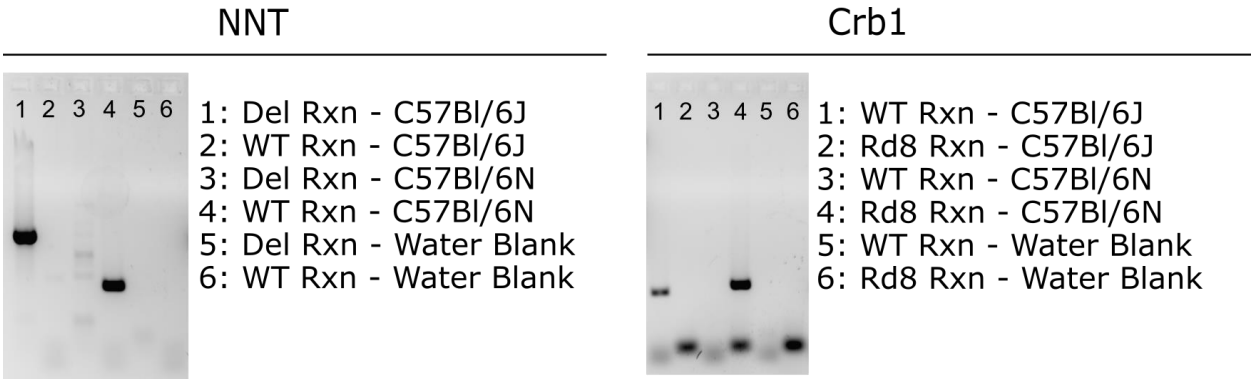

Figure 4.2: Genotyping of NNT and Crb1 for Rd8 in vendor-purchased C57Nl/6J and C57Bl/6N.

The wild-type NNT gene (WT Rxn) and the truncation of NNT present in C57Bl/6J (Del Rxn) are tested in each animal and can confirm homozygosity and heterozygosity. The same is true of the Crb1 reactions which test for WT Crb1 (WT Rxn) and the point mutation in Crb1 causing Rd8 (Rd8 Rxn). Based on the presence of primer dimers in the Crb1 reactions, the quantity of primers likely needs optimization. Water blanks are included for each PCR as a control.

As a control, consideration of a third, widely-available and commonly used inbred mouse strain without Rd8 and with functional NNT was necessary. Albino mice were not considered to avoid differential impact of light exposure to the eye. The 129S1/SvImJ (129S1) strain was selected after a literature search did not reveal any clear indications of known retinal degeneration. However, it was not clear if the various 129 mouse strains had been crossed with C57Bl/6J or C57Bl/6N in the derivatization of the lines. We sought to confirm the genetic status of 129S1/SvImJ at the NNT and Crb1 loci.

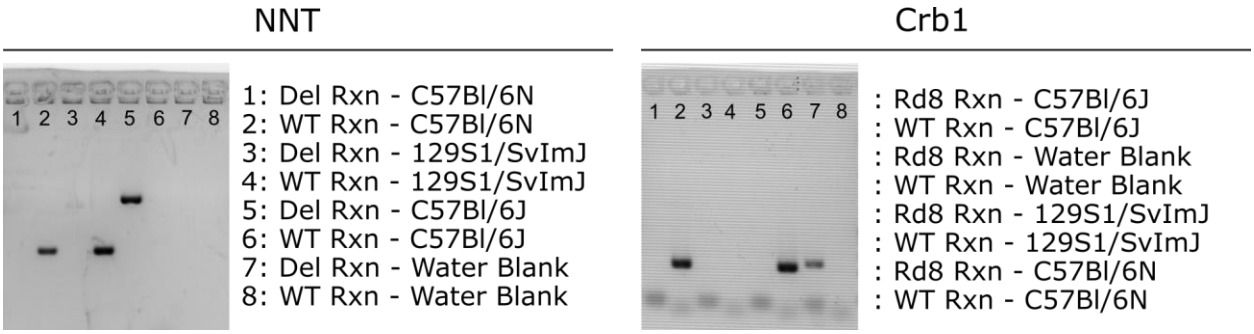

Figure 4.3: Genotyping of 129S1/SvImJ for wild-type and mutant forms of NNT and Crb1.

To determine is 129S1 could serve as a control for the loss of NNT in 6J and the Rd8 mutation in 6N, we used four different PCR reactions: Del Rxn (NNT deletion in 6J), WT Rxn (WT NNT in 6N), Rd8 Rxn (Crb1 base pair deletion in 6N), and WT Rxn (WT Crb1 in NNT), DNA from 6J and 6N mice were run through these reactions in parallel as controls, alongside a water blank.

Alongside control reactions testing wild-type and mutant NNT and Crb1 genes in C57Bl/6J and C57Bl/6N, 129S1 mice were genotyped using the same WT and mutant reactions (Figure 4.3). The 129S1 mice were found to have wild-type alleles in the NNT and Crb1 genes based on the genotyping assay employed here.

Scotopic ERG response is similar in 6J, 6N, and 129S1

To determine if the loss of NNT effects visual function, we compared the scotopic, rod-mediated a-wave responses of 8-10 week-old female 6J and 6N to the 129S1 that have function NNT and no Rd8 mutation. There was no observed change in the scotopic a-wave between the 6J and 129S1 mice (Figure 4.4). At approximately two months of age, there were no significant differences between 6N and 6J, nor 6N and 129S1.

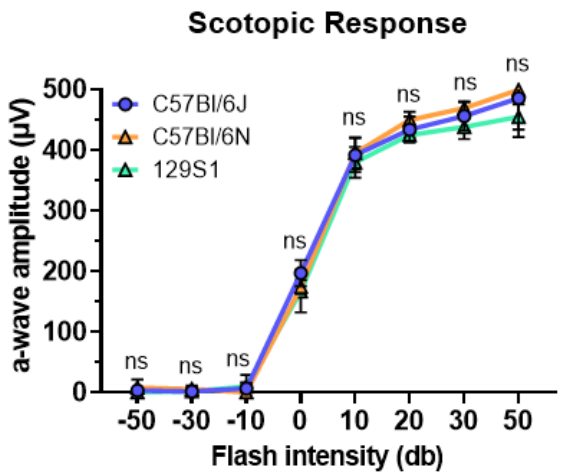

Figure 4.4: No difference between 6J, 6N, or 129S1 was seen in scotopic a-wave response.

Scotopic a-wave response 8 msec after the flash stimulus shows essentially no difference in 6J, 6N, or 129S1.Relative to 129S1 associated with the NNT mutation in 6J or the Rd8 mutation present in 6N. Normality of the data was tested using Shapiro-Wilk test. At each flash intensity, comparisons between the 3 strains were considered using either 1-way ANOVA with Holm-Šídák's multiple comparisons test or Kruskal-Wallis test with Dunn's multiple comparisons test.

Flux through the Krebs cycle differs subtly between 6J, 6N, and 129S1

We used gas chromatography-mass spectrometry to quantify the degree and directionality of glutamine flux after a 60 minute incubation in 2 mM U-^{13}C-glutamine with 5mM unlabeled glucose (Figure 4.5). In retinas and eyecups, the quantity of metabolite that had incorporated ^{13}C was used to examine oxidative and reductive reactions. Additionally, due to what ended up being a fortuitous error, a fourth group was added to the three strains of interest. A group of C57Bl/6N mice were incubated in U-^{13}C-glutamine alone without unlabeled glucose.

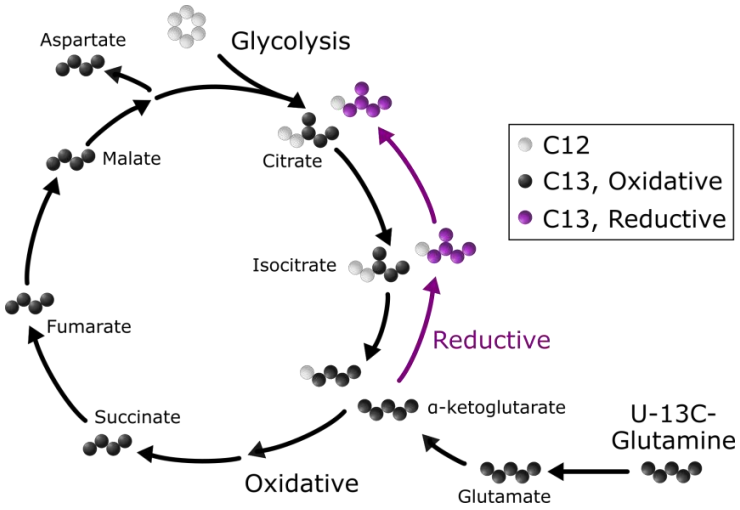

Figure 4.5: Schematic illustrating how U-^{13}C-glutamine flux was traced through the Krebs cycle.

Oxidative flux (forward) through the Krebs cycle is shown with black arrows. Reductive flux, or reductive carboxylation, is indicated with purple arrows.

In terms of the amount of glutamine entering the tissues and being incorporated as part of M5 glutamate or M5 alpha-ketoglutarate (AKG), there were only a few small changes

(Figure 4.6). Retinas were quite stable (A), and eyecups showed only a statistically significant change in M5 AKG between 6J and 129S1 (B). When glucose is withheld from 6N retinas and eyecups, the percent of labeled M5 glutamate increased relative to explants that were provided glucose in addition to glutamine.

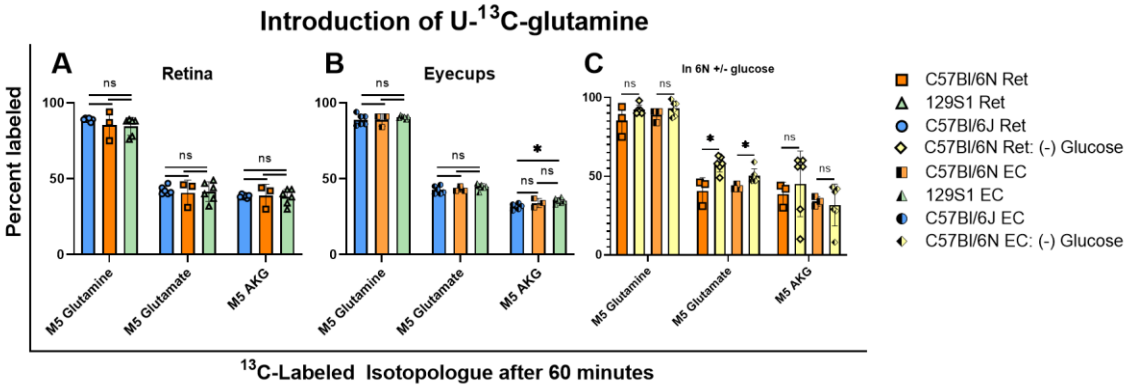

Figure 4.6: M5 Glutamine, glutamate, and AKG did not change drastically between strains.
After incubation of retina and eyecup explants in U-^{13}C-glutamine with glucose, there were no significant changes in retinas (A). In eyecups, the only significant change was in M5 AKG between 6J and 129S1 (B). When glucose is withheld from 6N retinas and eyecups (C), M5 glutamate was increased in both explants relative to samples that included glucose. Normality was tested using Shapiro-Wilk test. The difference between 3 strains was examined with 2-way ANOVA and Tukey's multiple comparisons test, while examining the 6N strain with and without glucose multiple Mann-Whitney tests followed by Two-stage step-up (Benjamini, Krieger, and Yekutieli) test were used.

We examined how withholding glucose effects oxidative and reductive flux through the Krebs Cycle by examining the percent of M4 and M5 Krebs cycle intermediates (Figure 4.6). Although none of the changes between retina and eyecup explants incubated with and without glucose reached statistical significance, there were interesting trends to consider for future studies. Retina oxidative flux was mostly unchanged, but M4 aspartate increased (A). Reductive flux in M5 isocitrate and M5 citrate trended higher when glucose was withheld in retinas (B). In eyecups, oxidative (D) and reductive (E) flux did not change significantly, although M5 isocitrate trended slightly higher. When the degree of citrate usage is considered as a percent of both possible directions (M4/M4+M5 and M5/M4+M5), retinas appeared to have increased their reductive flux (C). Although we observed a statistically significant difference in eyecups, the degree of change was reduced, and the directionality was reversed (F).

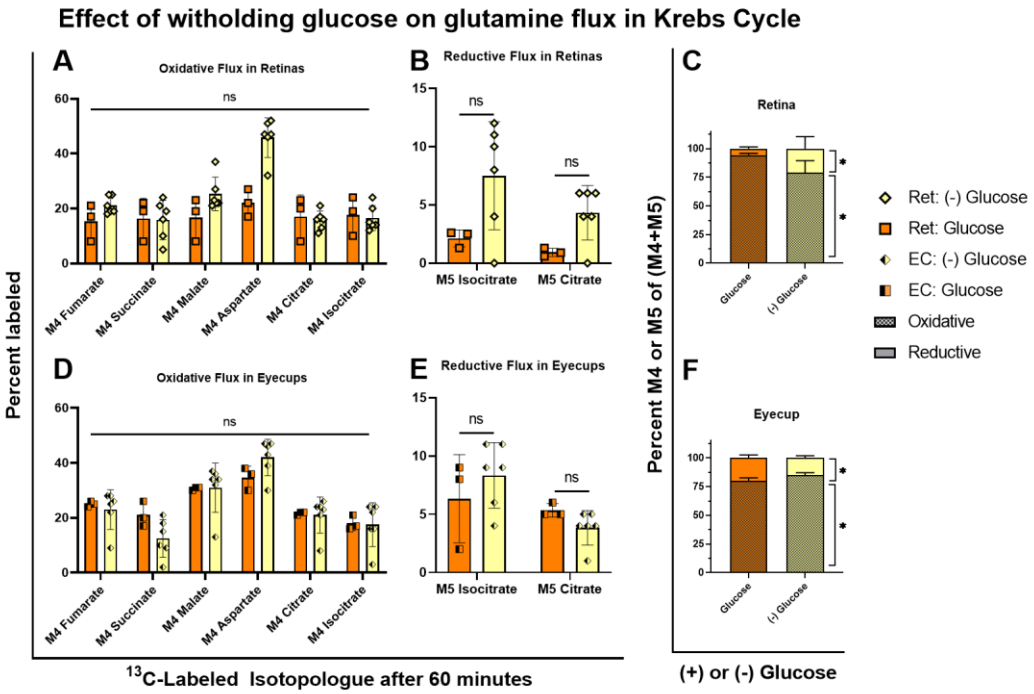

Figure 4.7: Withholding glucose may increase reductive carboxylation in 6N retinas and eyecups.

We examined oxidative (A) and reductive (B) flux in retinas and observed no statistically significant changes. In eyecups, we also observed no changes in oxidative (D) and reductive (E) flux. To broadly determine the directionality of glutamine flux, the percent of M4/M4+M5 and M5/M4+M5 citrate was examined in retinas and eyecups. Reductive carboxylation flux increased in retinas when glucose was withheld (C). Conversely, in eyecups glucose decreased marginally when glucose is withheld, but was found to be statistically significant (F). Normality was tested using Shapiro-Wilk test. The difference between the 6N strain with and without glucose was examined either multiple Mann-Whitney tests or multiple unpaired t-tests followed by Two-stage step-up (Benjamini, Krieger, and Yekutieli) test.

Glutamine flux through the Krebs cycle in 6J, 6N, and 129S1 differed in a few small ways. Oxidative flux in retinas (A) was unchanged aside from a significant decrease in M4 fumarate between 6J and 129S1. M5 isocitrate and M5 citrate was lower in 6N relative to 6J, and M5 isocitrate was also decreased in 6N relative to 129S1 (B). Eyecup oxidative flux was unchanged between the 3 species (D). M5 isocitrate was significantly increased in 129S1 relative to 6J and 6N (E). When flux is considered as a percent of (M4/M4+M5 and M5/M4+M5), 6N reductive flux is decreased relative to 6J and 129S1 (C). In eyecups, 129S1 reductive flux is increased relative to 6J and 6N (F).

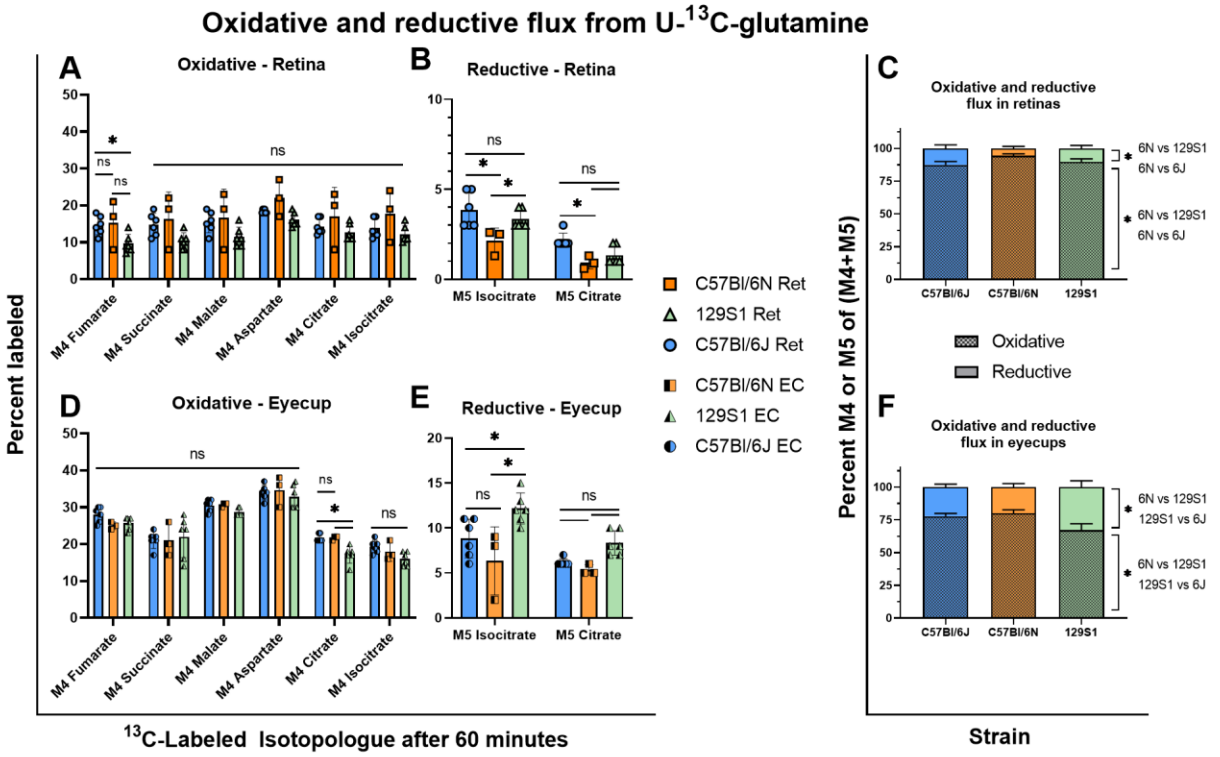

Figure 4.8: There are marginal changes in glutamine flux between 6J, 6N, and 129S1.

Oxidative flux in retina was unchanged beyond a decrease in M4 fumarate in 129S1 compared to 6J (A). Reductive flux to M5 isocitrate decreased in 6N relative to 6J and 129S1, and M5 citrate decreased in 6J relative to 6N (C). Eyecup flux in the oxidative (D) direction was not different by strain except for a drop in 129S1 relative to 6J. M5 isocitrate was lower in 6J and 6N relative to 129S1 (E). Normality was tested using Shapiro-Wilk test. The difference between 3 strains was examined with 2-way ANOVA and Tukey's multiple comparisons test followed by Two-stage step-up (Benjamini, Krieger, and Yekutieli) test were used.

Discussion

Loss of NNT nor the Rd8 mutation does not affect scotopic vision in young mice

We used single-flash scotopic ERGs with a range of flash intensities to determine if scotopic function was impacted by the NNT deletion in 6J or the Rd8 mutation in 6N. At the 2 month timepoint we considered, there was no observed difference in the a-wave derived from rod photoreceptors in these three strains. These results confirm a previous study that found the Rd8 mutation in 6N leads to a loss in the a-wave and more severe declines in the negative scotopic response threshold as early as 4 months of age (Saul

et al., 2017). It also suggests that the loss of NNT in 6J is not impacting vision relative to 129S1 mice which have functional NNT.

Rd8 may reduce reductive carboxylation in the eye

This study represented early evidence that reductive carboxylation can occur outside of an RPE cell culture model. True to previous findings, the percent of reductive flux was higher in eyecups than in their matched retinas. Some of these results also suggested the withholding glucose may be sufficient to increase reductive carboxylation. Although we only performed this experiment in 6N mice, future experiments in other mouse strains or species would be important for validation.

We identified significant changes in glutamine flux through the Krebs cycle between strains, although they were not consistent within the metabolic pathways examined. Overall, glutamine anaplerosis through the standard oxidative reactions (M4 isotopologues) was mostly unchanged in retinas and eyecups across the three strains considered. The most conserved changes we observed were suggestive of a modest decline in reductive carboxylation in 6N mice. Percent labeling in M5 isocitrate and M5 citrate reflective of reductive carboxylation of glutamine was decreased in 6N relative to 6J, and relative to 129S1 for isocitrate. The same trend of 6N having lower levels of reductive carboxylation than 6J or 129S1 was seen in eyecup M5 isocitrate, although the strain difference had mostly disappeared at M5 citrate with only 129S1 trending higher than 6N. When the proportion of citrate flux in the oxidative or reductive direction was considered, the decreased reductive flux was still clear. In eyecups, however, 129S1 appeared to have higher flux towards reductive carboxylation relative to 6J and 6N. This is likely reflecting the slightly higher value of 5 citrate label seen in 129S1 eyecups that did not meet the threshold of significance. Given that reductive carboxylation in the eye has historically been found to be more important in RPE, the finding that Rd8 may further decrease the already lessened reliance on the pathway may reflect the slow degeneration occurring in the retinal photoreceptors (Mehalow et al., 2003). That 129S1 mice may gave increased reductive carboxylation in eyecups merits further consideration.

Due to challenges in reagent acquisition, it is important to note that the metabolomics data was acquired in slightly older mice around 4 months of age. We observed only marginal differences in metabolism despite a known loss of scotopic function in 6N mice by 4 months (Saul et al., 2017).

Important caveats to 129S1 comparisons

Much like C57Bl/6 mice, the 129 inbred mice have undergone a series of genetic branching steps. The 129 family has been broken down further into three broad sub-families and into additional substrains within them: parental, *ter*, and steel (Simpson et al., 1997). The 129S1/SvImJ substrain stems from the steel family, and like all substrains derived from the 129 line, carry a mutation in Disrupted-in-schizophrenia 1 (Disc1) protein (Clapcote and Roder, 2006). This mutation has been implicated in human neurological disease including, as the protein name aptly suggests, schizophrenia, but also depression, and bipolar disorder (Thomson et al., 2013). However, a crucial aspect of this disease link was overlooked at the strain selection stage of this study. In a yeast model, Disc1 mutations lead to mitochondrial dysfunction (Park et al., 2010). Others have found that Disc1 is involved in mitochondrial trafficking (Norkett et al., 2016; Ogawa et al., 2014). The search term [129S1/SvImJ AND Disc1 AND mitochondria] in PubMed resulted in no publications, but there is some evidence that 129S1/SvImJ mice recapitulate behavioral changes associated with human psychiatric disorders (Gómez-Sintes et al., 2014; Moy et al., 2007). Thus, while it is likely not valid to state that the metabolic results in this study reflect a truly “wild-type” condition, future studies are needed to reveal if the loss of Disc1 in mice results in mitochondrial dysfunction. Likely, the only way to examine the impacts of Rd8 and NNT deletion with confidence is to use a genetically modified mouse on the C57Bl/6 background that has had either the Crb1 mutation or the NNT deletion corrected. However, this oversight only further serves to illustrate that careful selection of a mouse strain and intensive literature review of known mutations is critical for a successful experiment.

Materials & Methods

Mouse husbandry

Three inbred strains of laboratory mice were used in these experiments. C57Bl/6J (Strain ID: 000664) and 129S1/SvImJ (Strain ID: 002448) mice were purchased from Jackson Laboratories (Bar Harbor, ME). C57Bl/6N mice were purchased from Charles River Laboratories (Wilmington, MA). All mice were female and examined by ERG at 8-10 weeks and/or by metabolic flux at 19-20 weeks.

DNA extraction

A “HotSHOT” genomic DNA preparation (Truett et al., 2000) was used to acquire short DNA segments suitable for genotyping PCR reactions. Table 4.2 summarizes the necessary reagents and their composition.

Table 4.2: HotSHOT genomic DNA isolation reagent formulation.

Buffer	pH	Reagent	Concentration (mM)
Alkaline Lysis	12	NaOH	25
		EDTA	0.2
Neutralization	5	Tris-HCl	40

Approximately 2 mm tail clips were taken from each mouse and heated to 95°C for 30 minutes in 75 µL of alkaline lysis buffer. After samples were removed from heat, 75 µL of neutralization buffer was added. The DNA preparation was vortexed quickly, the supernatant collected, and stored at 4°C in the short-term, or frozen at -20°C for long-term storage. If the DNA was found to be too concentrated due to a failed PCR, the DNA was diluted with a 1:1 mixture of the alkaline lysis buffer and neutralization buffer.

Genotyping

In order to determine if 129S1/SvImJ was a viable model to examine the effects of NNT loss without the complication of Rd8Text, two complementary genotyping approaches were used. In parallel, DNA from each animal was subjected to PCR in four separate reactions: WT in Crb1, mutant (Rd8) in Crb1, WT in NNT, and deletion (Del) in NNT.

Table 4.3: Primer sequences for WT and mutant NNT and Crb1 reactions.

Gene and direction	Reaction(s) using primer	Sequence
Crb1 Forward 1	WT	GTGAAGACAGCTACAGTTCTGATC
Crb1 Forward 2	Mutant	GCCCCTGTTTGCATGGAGGAAACTTGGAAGACAGCTACAGTTCTTCTG
Crb1 Reverse	WT, Mutant	GCCCCATTTGCACACTGATGAC
NNT Forward 1	WT	GTGCATTGAACCCTCAAAGG
NNT Forward 2	Mutant	GTAGGGCCAACTGTTTCTGC
NNT Reverse 1	WT	CAGGTAAGAAAGCTCCTGTTTT
NNT Reverse 2	Mutant	TCCCCTCCCTTCCATTTAGT

To determine if the Rd8 mutation was present in Crb1, a modified version of the genotyping protocol detailed by Mehalow and colleagues was used (Mattapallil et al., 2012; Mehalow et al., 2003). The forward primers distinguish between the WT and Rd8 sequence with a common reverse primer. To examine the state of NNT, the WT primer amplifies exon 7 which would be missing in C57Bl/6J. The forward and reverse primers needed to identify mice carrying the deletion are located in exons 6 and 12 which, due to the 4 exon deletion, now exist in close proximity and can be amplified. The protocol for NNT genotyping was kindly provided by the laboratory of Joseph A. Baur at the University of Pennsylvania.

Table 4.4: PCR reaction conditions to identify WT/mutant NNT and WT/mutant Crb1.

Reaction Component	NNT		Crb1	
	WT (6N)	Mutant (6J)	WT	Mutant (Rd8)
DNA (µL)	2	2	1	1
2X PCR mix (µL)	10	10	12.5	12.5
H_2O (µL)	6	6	3.5	5.5
10 mM Crb1 Forward 1 (µL)	Not used	Not used	4	Not used
10 mM Crb1 Forward 2 (µL)	Not used	Not used	Not used	2
10 mM Crb1 Reverse 1 (µL)	Not used	Not used	4	4
10 mM NNT Forward 1 (µL)	1	Not used	Not used	Not used
10 mM NNT Forward 2 (µL)	Not used	1	Not used	Not used
10 mM NNT Reverse 1 (µL)	1	Not used	Not used	Not used
10 mM NNT Reverse 2 (µL)	Not used	1	Not used	Not used
Total reaction volume (µL)	20	20	25	25

The primers used for both assays are listed in Table 4.3. It is important to note that it is necessary to run both WT and mutant reactions for each gene in order to rule out if the mouse is homozygous or heterozygous or a given mutation described here. Different amounts of DNA, primers, and, and total reaction volume were needed for each gene. The PCR reaction conditions for individual samples are described in Table 4.4 for both NNT and Crb1. The denaturation, annealing and extension steps of PCR occur at different temperatures and with slight variations on timing between the reactions (Table 4.5), thus at least 3 separate runs of the thermal cycler were necessary to complete the 4 reactions needed to characterize NNT and Crb1 in each mouse. The resulting PCR products were run in a self-cast 2% agarose gel formulated with 1X TAE and ethidium bromide.

Table 4.5: PCR reaction conditions for WT/mutant NNT and WT/mutant Crb1.

Temperature and duration		NNT- WT (6N)	NNT – Mutant (6J)	Crb1 – WT and Mutant (Rd8)
Denaturation		94ºC (2 min)	94ºC (2 min)	95ºC (3 min)
PCR Cycles	1	94ºC (30 sec)	94ºC (30 sec)	95ºC 30 seconds
	2	52ºC (30 sec)	54ºC (30 sec)	65ºC 30 seconds
	3	72ºC (30 sec)	72ºC (60 sec)	72ºC 30 seconds
	Total	30 cycles	35 cycles	30 cycles
Cooling		72ºC (5 min)	72ºC (5 min)	72ºC (7 min)

Scotopic electroretinograms

Prior to any scotopic experiments, mice were dark-adapted overnight, and electrodes placed with night vision goggles under infrared light. Mice were anesthetized with isoflurane, and eyes dilated with 2.5 % phenylephrine (Akorn, Inc; NDC 174780201-15) and 1% tropicamide (Bauch + Lomb; NDC 24208-585-64). Gold electrodes were placed on each cornea. A reference and ground electrode were positioned on the back of the head. Mice were placed inside a UTAS Visual Diagnostic System with BigShot Ganzfeld with UBA-4200 amplifier (LKC Technologies; Gaithersburg, MD). Recordings were elicited using flashes of LED white light at increasing flash intensities with two-minute pauses between individual flashes under scotopic (-50 to 50 dB) conditions. Readings were calibrated such that 0 db = 2.5 cd*s/m2. The a-wave amplitude was measured 8

ms after flash stimulus. Readings were taken from both eyes whenever possible and examined as an average of both eyes. If the reading from one eye was not viable due to difficulty with electrode placement, the eye with the best response was analyzed.

Isolation of retinas and eyecups

Animals were euthanized by awake cervical dislocation. Eyes were enucleated with curved forceps and cleared of attached hair, muscle, connective and adipose tissue. The globe was punctured with a 20-24 gauge needle just above the ora serrata. The cornea, iris and lens were removed. The opened globe was placed back into fresh HBSS. The retina was carefully separated from the RPE-choroid-sclera complex (eyecup). The inside of the eyecup was verified to be free of visible pieces of retina. If still attached, the optic nerve was removed from the eyecup. The separated tissues were then placed in metabolic flux medium (Krebs Ringer Buffer plus added metabolites) for metabolic flux experiments or left in HBSS to process for OCR.

Metabolic flux incubations

Metabolite standards and buffer components were purchased from Sigma-Aldrich (MilliporeSigma; St. Louis, MO). Heavy-labeled metabolites were from Cambridge Isotope Laboratories, Inc (Tewksbury, MA). Incubation medium was formulated as follows:

- Krebs's Ringer Buffer (KRB): 98.5 mM NaCl, 4.9 mM KCl, 1.2 mM KH_2PO_4, 1.2 mM $MgSO_4$, 20 mM HEPES, 2.6 mM CaCl, 25.9 mM $NaHCO_3$
- Labeled glucose alone, labeled glutamine alone, or labeled glutamine with unlabeled glucose:
    - 5 mM U-^{13}C-D-glucose (99% isotopic purity)
    - 2 mM U-^{13}C-glutamine (99% isotopic purity)
    - 2 mM U-^{13}C-glutamine (99% isotopic purity) with 5 mM unlabeled (^{12}C) glucose

Individual dishes of 2 mL of incubation medium were equilibrated in a humidified incubator at 37°C and 5% CO_2 for 1 hour prior to running experiments. Tissues were incubated for 60 minutes in U-^{13}C-glutamine incubation medium or for 30 minutes in U-

^{13}C-D-glucose incubation medium. At time, tissues were removed from incubation medium, quickly washed in HBSS, and snap frozen. The incubation medium was mixed in the dish, aliquoted, and snap frozen. All samples were stored at -80°C until extraction.

Metabolite extraction of retina and eyecup explants

All extractions were performed in batches over numerous days. Tissue was extracted in 80% methanol, 100 µM methylsuccinate chilled over dry ice. Tissues were homogenized and sonicated (Duty cycle: 90, output control: 2, 10 pulses) over wet ice. Proteins were precipitated on dry ice for 45 minutes, the supernatant was collected after a 25-minute 17,000 x g spin at 4°C. Samples were lyophilized to dryness the same day and stored at -80°C until analysis by GC-MS.

Analysis of metabolites by GC-MS

Metabolite standards between 1.25-25 µM in a final derivatization volume of 20 µL were used to generate calibration curves. Samples were incubated at 37°C for 90 minutes in 10 µL of 20 mg/mL methoxyamine (MilliporeSigma) in pyridine (MilliporeSigma). 10 µL of neat N-tertbutyldimethylsilyl-N-methyltrifluoroacetamide (MilliporeSigma) was added and the samples incubated for one hour at 70°C. Derivatized samples were transferred from Eppendorf tubes to 2 mL vials (Agilent - 5182-0715) containing high recovery glass inlets (Agilent - 5183-2085). Samples were sealed with lids containing PTFE silicone septa (Agilent - 5182-0717).

Each sample was analyzed using a splitless injection of 1 µL within 24 hours of derivatization via a 49 minute gradient on an Agilent 7890/5975C GC-MS system (Agilent Technologies; Santa Clara, CA). Two Agilent columns with differing stationary phases were used: a 5% Diphenyl / 95% Dimethylpolysiloxan (DB-5MS:128-5522) with a flow rate of 0.8 mL/min, and a phenyl methyl silox film (HP-5MS: 19091S-433I) with a flow rate of 1 mL/min. For all derivatized metabolites, target ions were used for quantification and isotopologue distribution determination, and a qualifier ion for identity confirmation. Peak areas for SIM ions were obtained in MSD ChemStation (Agilent

Technologies; Santa Clara, CA) with manual verification of automated peak integrations. IsoCor v1 (Millard 2012) was used to correct for natural ^{13}C abundance and determine percent enrichment of ^{13}C. In individual metabolite isotopologues, the number of incorporated ^{13}C is represented shorthand by “Mx”, where x is the number of ^{13}C (M0, M1, M2, etc.). We considered the percent labeled for key isotopologues and used the corrected AUC post-IsoCor to calculate the percentage of (M4/M4+M5) and (M5/M4+M5).

Statistical analysis

Normality of the data was tested using the Shapiro-Wilk test ($\alpha = 0.05$). At each flash intensity used in ERGs, comparisons between the 3 strains were considered using either 1-way ANOVA with Holm-Šídák's multiple comparisons test or Kruskal-Wallis test with Dunn’s multiple comparisons test. Metabolomics data was examined using 2-way ANOVA and Tukey's multiple comparisons test when comparing all 3 strains, or when examining the 6N strain with and without glucose, either multiple Mann-Whitney tests or multiple unpaired t-tests followed by Two-stage step-up (Benjamini, Krieger, and Yekutieli) test.

Acknowledgments

The work in this chapter was conceptualized by Kristine A. Tsantilas. The genotyping and metabolomics was performed by Kristine A. Tsantilas and Brian Robbings. Whitney M. Cleghorn performed the ERGs and Jonathan D. Linton performed the retina and eyecup dissections.

This work was supported by NIH funding to Kristine Tsantilas (Genetic Approaches to Aging Training Grant T32 AG000057), James B. Hurley (Determinants of Rod and Cone Response Characteristics 5R01EY006641, and Control of Photoreceptor Metabolism 5R01EY017863), and Susan E. Brockerhoff (2R01EY026020).

Chapter 5 - Aging in the vertebrate retina

Introduction

Aging is associated with vision loss which contributes to disability and reduces quality of life (Klein and Klein, 2013; Owsley, 2011). Over the course of physiological aging, tissues in the eye exhibit functional decline. The retinal pigment epithelium (RPE) accumulates lipofuscin and drusen, Bruch's membrane thickens, and overall cellular organization decreases (Bonilha, 2008; Brunk and Terman, 2002; Chen et al., 2016; Crabb, 2014; Gu et al., 2012; Karunadharma et al., 2010). These alterations are also characteristic of age-related macular degeneration (AMD), a severe disease associated with aging that is a leading cause of vision loss (Alavi, 2016; Ambati and Fowler, 2012; Bhutto and Lutty, 2012; Inana et al., 2018; Klein and Klein, 2013). Within the neural retina, mitochondria are damaged (Eells, 2019; Nag and Wadhwa, 2016; Wang et al., 2010), synaptic connections between cells deteriorate (Cavallotti et al., 2004; Samuel et al., 2011), and the functional capacity of photoreceptors is compromised.

Although aging is the top risk factor in many diseases, preclinical models of age-related blinding diseases often do not include advanced age as a variable. Omitting age as a variable in preclinical models may have contributed to the lack of laboratory interventions successfully translated into human trials in diseases such as AMD. Understanding the contributions of aging alone to visual decline will be crucial to distinguish between age-related visual decline and age-related visual disease.

In mice and humans, scotopic and photopic electroretinograms (ERGs) decline with age (Freund et al., 2011; Kergoat et al., 2001; Kolesnikov et al., 2010; Wang et al., 2018). Manipulating metabolism *ex vivo* directly influences ERG response (Winkler, 1981). Increasing evidence suggests there is extensive metabolic interplay between the highly glycolytic retina and the retinal pigment epithelium (Haydinger et al., 2020; Kanow et al., 2017; Warburg, 1925) and that metabolic changes in RPE can affect the retina. Increasing or disrupting glucose conduction in the RPE can result in retinal degeneration (Kurihara et al., 2016; Swarup et al., 2019; Zhao et al., 2011). Similarly, aging represents a form of gradual, natural decay that impacts the eye. Metabolic changes are a hallmark of aging (López-Otín et al., 2013) in many tissues. Although

steady-state metabolite levels differ in tissues isolated from young and middle-aged mouse eyes (Wang et al., 2018), to our knowledge the cross-talk between aging and central energy metabolism in the mammalian retinal ecosystem has not been examined. When characterizing age-related metabolic changes, it is not always clear whether the observed alterations are intrinsic to the tissue, or due to differences in vascularization or nutrient availability. An *ex vivo* approach to metabolic characterization (Du et al., 2015) can facilitate the identification of intrinsic metabolic changes.

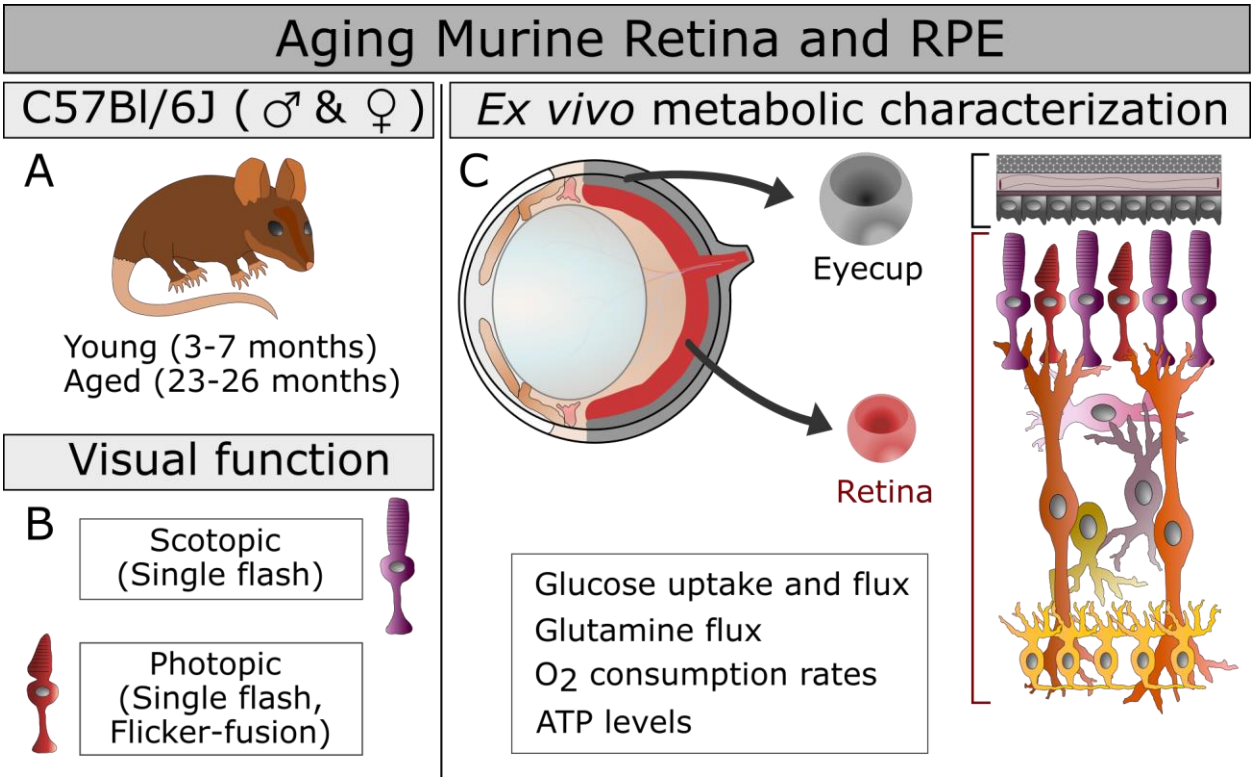

Figure 5.1: Study structure to characterize function and metabolism in aged mouse eyes.

The study design is presented including the mouse groups, ages, and sex (A), the measures of visual function employed (B), and the ex vivo approaches to characterizing metabolism (C) in the aging eye. The functional metabolic measurements are listed below the structure of the murine eye (C, top left) from which we isolated two explants in this study (C, center): the retina RPE-choroid complex that includes the RPE, choroid, and sclera that has been cleared of connective tissue (Eyecup). The cellular composition of these explants (C, right) is highlighted with retinal cells shown in shades or red, purple, orange and yellow, while the eyecup is shaded in variations of gray.

To investigate the relationship between functional decline and energy metabolism in aging retina and RPE (Study structure in Figure 5.1), we measured visual function *in vivo* by ERG and interrogated intrinsic alterations of metabolism by analyzing *ex vivo*

tissue explants using a continuously flowing perifusion device, stable isotope tracers, and targeted metabolomics.

Results

Scotopic and photopic vision declines in aging mice

We recorded ERGs under scotopic and photopic conditions in young (4-5 months) and aged (26 months) male mice. Single flash scotopic ERGs measured rod-mediated vision. The amplitude of the a-wave was extracted from raw traces (Figure 5.2A) 8 msec after the flash and averaged (Figure 5.2B). Responses declined significantly between young and aged mice at -30 db and between 0-50 db. This is consistent with previous findings that a-waves decline in mice as early as 16 months (Kolesnikov et al., 2010; Wang et al., 2018).

Cone-mediated vision was characterized by examining the b-wave amplitude in raw traces (Figure 5.2C) in single-flash photopic ERGs. The b-wave amplitude declined significantly in aged animals relative to young (Figure 5.2D) at the flash intensities tested. The a-wave and b-wave declined proportionally with age. Temporal resolution was considered by flicker-fusion ERG, which used a 5 db flashing light at frequencies between 20-50 Hz. An overall loss in temporal resolution was seen in the raw responses. Examples of averaged responses at 37 Hz are shown from young (Figure 5.2E) and aged (Figure 5.2F) mice. After Fast Fourier Transformation, the response magnitude was found to decline in aging (Figure 5.2G). Although the degree of change was variable, the magnitude declined significantly with age at all frequencies tested except 50 Hz. When the area under the curve was taken for each individual mouse and plotted as an average (Figure 5.2H), the overall decline in temporal resolution with age was clear.

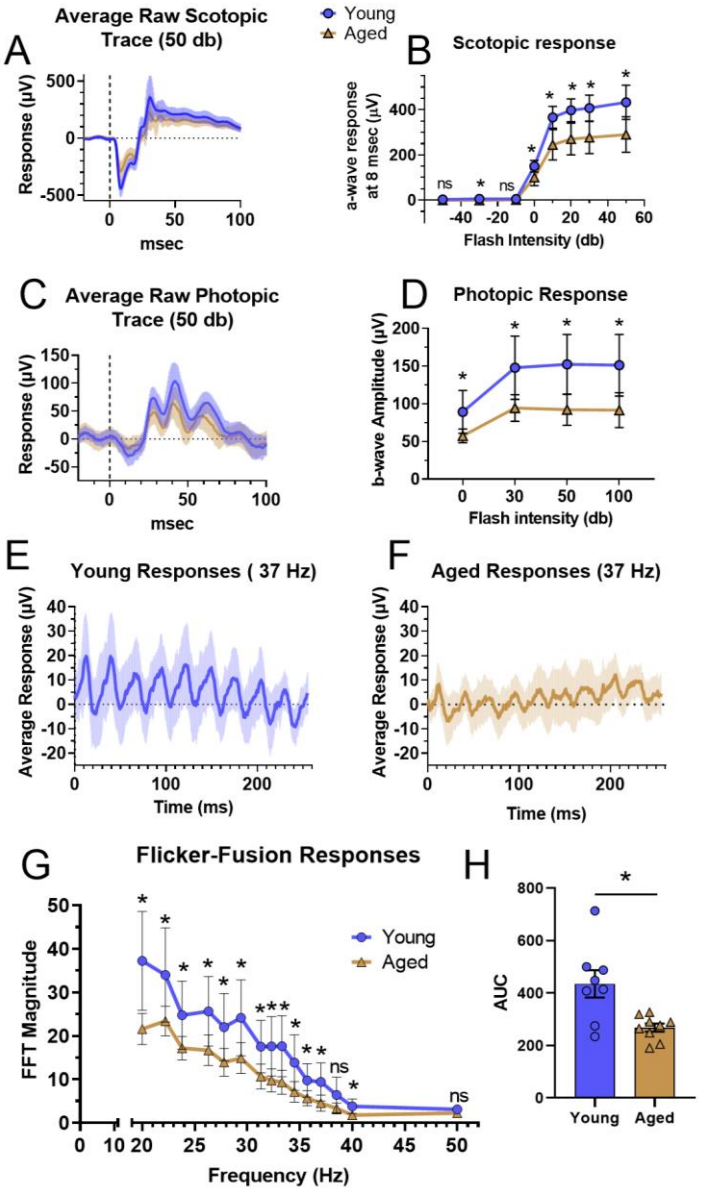

Figure 5.2: Visual function declines in aging mice.

Single-flash ERGs were used to assess scotopic and photopic function in the retina. The averaged scotopic response curve in response to a 50 db flash (A) and the resulting a-wave measurements from -50 to 50 db light at 8 ms after the flash (B) show a decline in the response of rod circuitry with aging. Sample sizes are 8 for young and 9 for aged. In photopic conditions (Background light of 30 cd/m^2), the average response curve to a 50 db flash (C) and the resulting b-wave magnitude from flashes of magnitude 0 to 100 db (D) show a decline in the response of rod circuitry with aging. Sample sizes are 12 for young and 9 for aged. Photopic function and temporal resolution were examined with a 5 db flash which flickered between frequencies of 20-50 Hz. The averaged response to 5 db light flickering at 37 Hz is shown for young (E) and aged animals (F). The young have a more uniform and stronger response to equivalent stimuli than aged animals. Aging decreased the magnitude of the response at equivalent frequencies (G) as calculated by Fast Fourier Transform. Average AUC of curves for individual mice are shown (H). Sample sizes are 8 for young and 9 for aged. Panels show the average ± standard deviation. Normality of data was determined using the Shapiro-Wilk test and p-values were calculated using Mann-Whitney tests (* = $p < 0.05$, marker of non-significance enclosed in parentheses). Error bars represent the standard deviation.

Metabolic flux from glucose is preserved in retinal explants cultured ex vivo

We sought to determine if glucose usage in the retina and RPE were altered at an age with known functional decline (Figure 5.2). We first considered whether the tissues ability to consume glucose from their media was compromised as a result of age-related decline. Retinas and eyecups were isolated from young or aged male mice and pooled – four explants for each replicate. We found clear differences between retinas (Figure 5.3A) and eyecups (Figure 5.3B) in the uptake of glucose from the medium. By 30

minutes, the more rapid usage of glucose by the retina is clear (Figure 5.3C). We identified no age-related decline in glucose usage in either tissue. Although the experiment is severely underpowered, it suggests that the ability of retinas and eyecups to consume glucose ex vivo is not altered with aging.

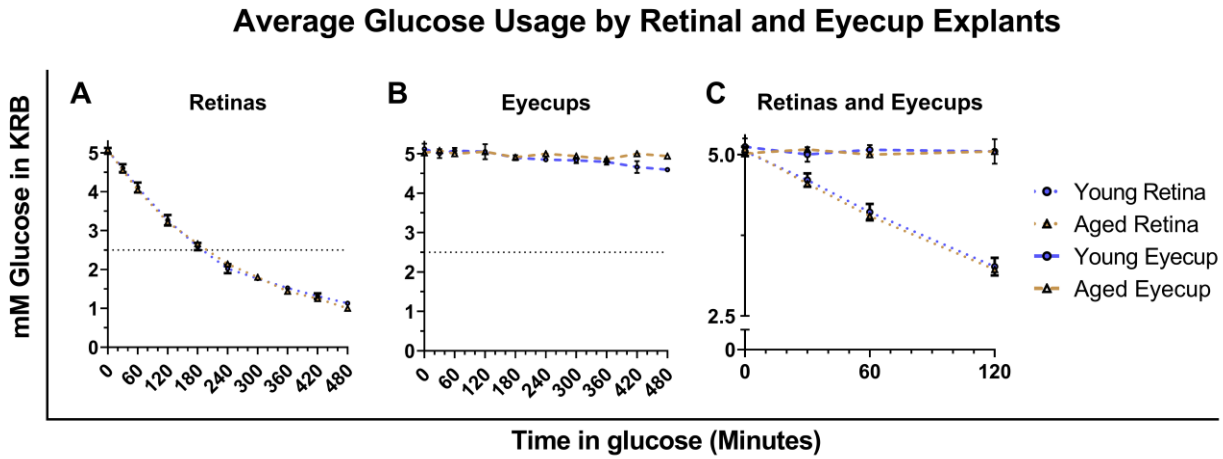

Figure 5.3: Glucose usage by young and aged retinas and eyecups.

Glucose uptake was monitored in retina and eyecup explants ex vivo by pooling four of each tissue, incubating in 5 mM glucose, and measuring the concentration with a glucometer across 8 hours. The retinal explants (A) consumed glucose more quickly than eyecups (B), and the difference is visible after 30 minutes (C). There was no significant effect of age in either tissue. There were 3 young replicates of each tissue, but only a single replicate of the aged tissues.

Retina and eyecups were isolated from young (3-5 months) and aged male (26 months) and female (23-25 months) mice. To probe metabolic flux directly, retina and eyecup explants were incubated in KRB with U-^{13}C-Glucose for 2, 10, 20, 30, or 45 minutes. Labeled metabolites generated from glucose in tissues and incubation media were measured by GC-MS (Figure 5.5A). Metabolites were quantified in terms of pmol or nmol metabolite per µg of protein. We examined metabolites in the tissue or exported by the tissue and considered the percent of the total pool labeled with ^{13}C, and product:reactant ratios for particular steps in glycolysis and the TCA cycle (Figure 5.4A).

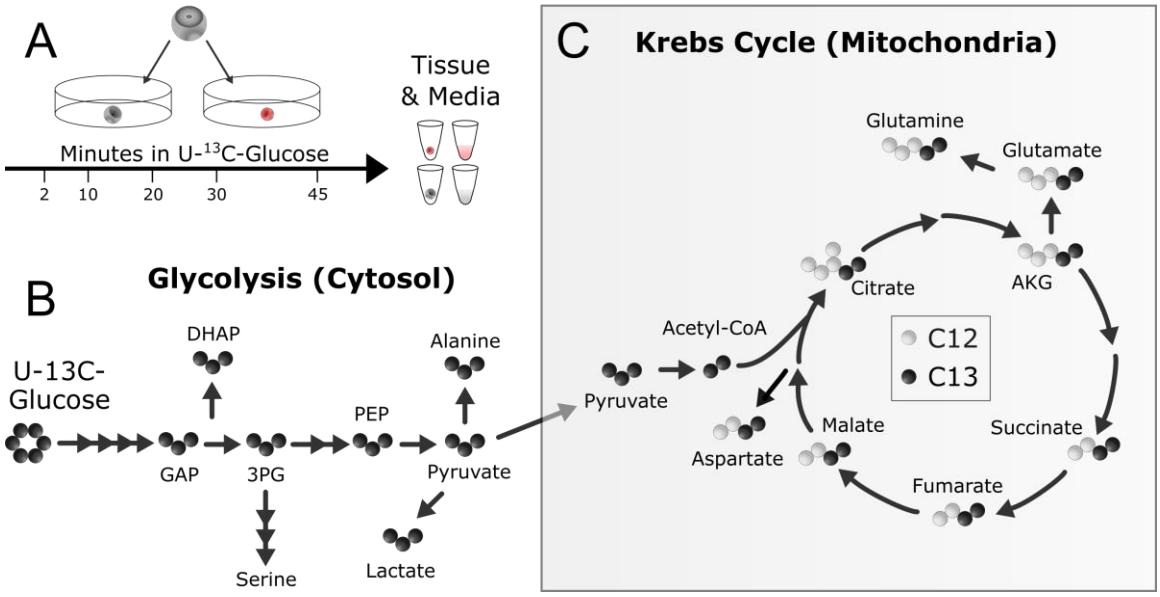

Figure 5.4: Tracing ^{13}C from glucose in downstream glycolysis and the Krebs cycle.

Metabolic activity was examined by incubating retinal and RPE-choroid (eyecup) explants in U-^{13}C-glucose between 2-45 minutes. The tissue was washed and frozen, and aliquots of the incubation media were collected for analysis (A). GC-MS was used to quantify M3 isotopologues in glycolysis (B) and M2 intermediates in the Krebs Cycle in young and aged tissues.

In tissues, we first examined glycolytic intermediates (Figure 5.4B) in retina and eyecup. We found no consistent change in pool size, percent ^{13}C-incorporation, and labeled isotopologues in either tissue (Supplementary Figure 5.2). There was no significant change in export of M3 lactate from retinas (Figure 5.5A) or eyecups (Figure 5.5B) into incubation medium. We examined product:reactant ratios at 30 minutes in both tissues when label incorporation had stabilized. There were no substantial age-associated changes in glycolytic reactions in the retina (Figure 5.5C and E) or eyecup (Figure 5.5D and E). Glycolytic function appears preserved in both tissues.

We next considered how age impacts Krebs cycle intermediates (Figure 5.4C). As with glycolysis, we saw no consistent changes in retinas (Supplementary Figure 5.3A-C) or eyecups (Supplementary Figure 5.3D-F) in pool size, percent ^{13}C incorporation, or labeled isotopologues. There were no significant age-related changes in product:reactant ratios in retinas (Figure 5.5F) or eyecups (Figure 5.5G) at the same 30-minute time point considered for glycolysis. Age did not significantly impact the Krebs cycle in retinas and eyecup explants.

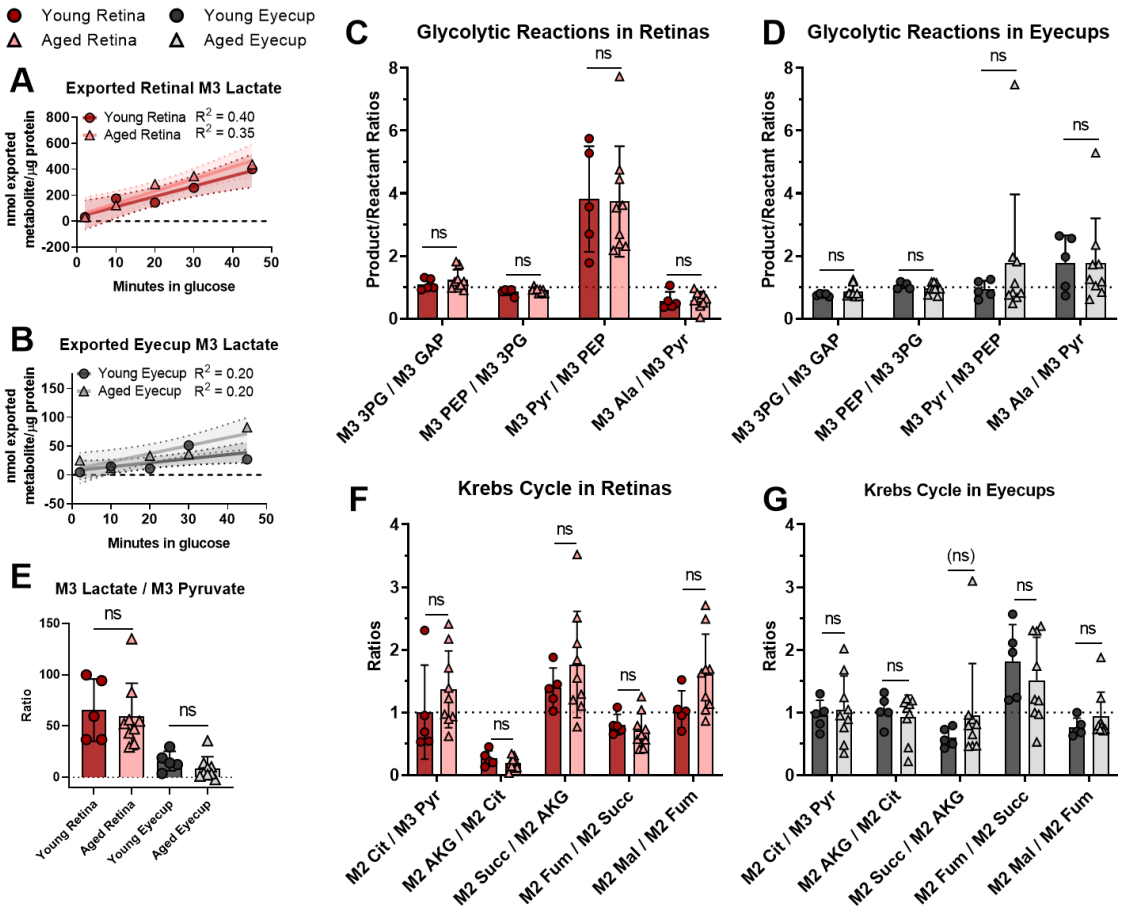

Figure 5.5: Glucose metabolism is remarkably stable in aged retinas and eyecups

Labeled intermediates downstream of glucose (Figure 5.4) were quantified in terms of percent ^{13}C incorporation, pmol of ^{13}C-labeled isotopologue per µg of protein in the retinal or eyecup explant, and product:reactant ratios. Percent incorporation, pool sizes, and amount of isotopologue are shown in Supplementary Figure 5.2 and Supplementary Figure 5.3. To examine glycolytic activity, the amount of exported M3 lactate was measured in the incubation media of retinas (A) and eyecups (B). One aged eyecup at 30 minutes was found to be an outlier by Grubb's test (alpha = 0.05, $p < 0.05$) and removed. The slope of the lines were all non-zero in retina ($p_{young} = 0.002$, $p_{aged} = 0.0003$) and eyecups ($p_{young} = 0.03$, $p_{aged} = 0.009$), but showed no significant age-related change (Regression slope: $p_{retina} = 0.7$, $p_{eyecup} = 0.3$). Within tissues, product:reactant ratios in glycolysis and common exit points to other pathways were plotted at 30 minutes because both tissues had reached a steady state. No significant age-related changes were seen in retina (C, E) or eyecup (D, E). Moving into the Krebs Cycle (B) at 30 minutes, no statistically significant age-related were observed in retina (F) or eyecup (G) explants. Normality of data was determined using the Shapiro-Wilk test and p-values were calculated for age-related comparisons using unpaired t-tests (* = $p < 0.05$) or Mann-Whitney tests (# = $p < 0.05$, marker of non-significance enclosed in parentheses). Error bars represent the standard deviation, except in Panels A and B which show the 95% confidence interval for the linear regression.

Abbreviations: Glyceraldehyde 3-phosphate (GAP), Dihydroxyacetone phosphate (DHAP), 3-phosphoglycerate (3PG), Phosphoenolpyruvate (PEP), Pyruvate (Pyr), Alanine (Ala), Citrate (Cit), α-ketoglutarate (AKG), Succinate (Succ), Fumarate (Fum), Malate (Mal)

Sexual dimorphism can influence outcomes in biological studies (Karp et al., 2017), and can differentially impact the visual system generally (Shaqiri et al., 2018) and in the context of aging (Du et al., 2017; Zetterberg, 2016). We considered glucose processing in young and aged female mice in parallel to males at 2 minutes. Total protein content in retinas was unchanged between males and females (Supplementary Figure 5.1A), however in eyecups (Supplementary Figure 5.1B) there was a change in aged males that was accounted for by normalizing all values to protein content in tissues. There were no significant contributions of age or sex in pool size or isotopologues (Figure 5.6A and B) in retina or eyecups (Figure 5.6C and D). No sex-dependent differences in aging retinal or eyecup metabolism were found.

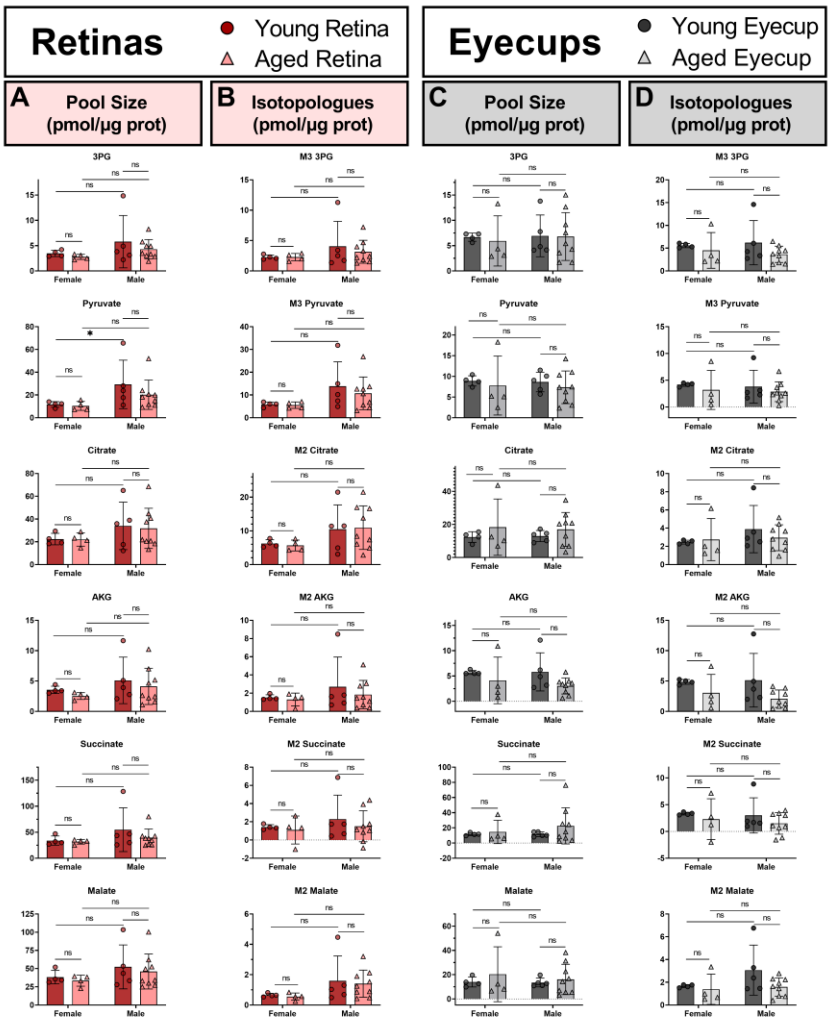

Figure 5.6: Sex did not impact glucose metabolism in aged females.

Sex differences between males (26 months) and females (23-25 months) were examined by individually plotting glycolytic and Krebs cycle intermediates measured in young and aged mice after a 2 minute incubation in 5 mM U-^{13}C-glucose. The male values are the same 2 minute samples shown in Figure 5.5, Supplementary Figure 5.2, and Supplementary Figure 5.3. The pool size (A) and isotopologues (B) in young and aged retina of both sexes are listed for select glycolytic and Krebs cycle intermediates. For the same metabolites in eyecups, the pool size (C) and isotopologues (D) are shown. Values shown are the mean ± standard deviation. Sample size = 4-9 depending on age and sex. Normality of data was determined using the Shapiro-Wilk test and changes associated with aging and sex were examined using Kruskal-Wallis and Dunn's multiple comparison tests.

Glutamine metabolism is altered ex vivo in aged eyecups

Mitochondrial dysfunction is a known hallmark of aging (López-Otín et al., 2013). To more directly investigate mitochondrial metabolism in aged ocular tissues we examined the usage of glutamine and succinate, which are oxidized by mitochondria in the RPE (Bisbach et al., 2020; Du et al., 2016b).

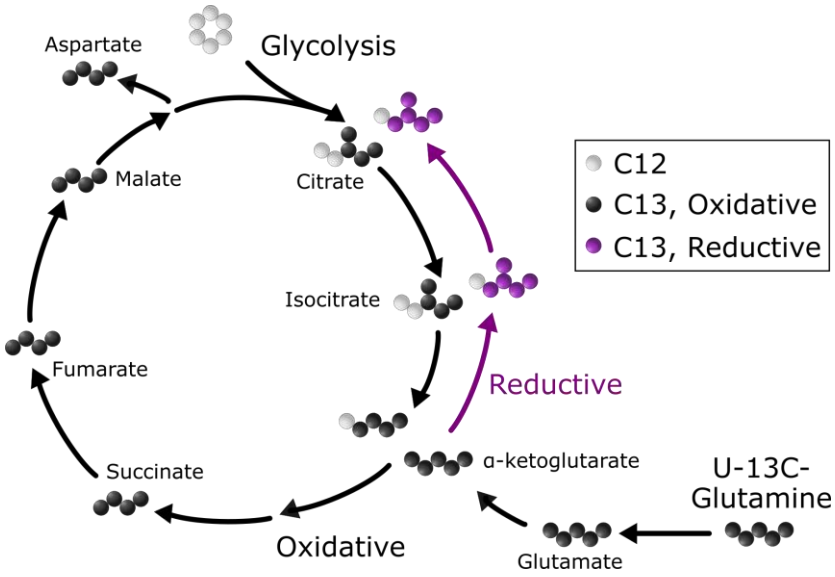

Figure 5.7: Schematic illustrating U-^{13}C-glutamine flux through the Krebs cycle.

Oxidative flux (forward) through the Krebs cycle is shown with black arrows. Reductive flux, or reductive carboxylation, is indicated with purple arrows.

Glutamine usage in ex vivo eyecup and retina explants was measured in 5 mM ^{12}C-glucose and 2 mM U-^{13}C-glutamine for 20 or 90 minutes (Figure 5.7). Metabolite pool size was diminished in aged eyecups at both timepoints (Supplementary Figure 5.5A) in glutamine, glutamate, and the downstream Krebs cycle metabolites α-ketoglutarate, fumarate, malate, and aspartate. Since we did not observe this defect in eyecups supplied with glucose alone (Figure 5.5), we hypothesized aged eyecups may have a defect in mitochondrial glutamine metabolism. After incubation in ^{13}C labeled glutamine, M5 glutamine, glutamate, and α-ketoglutarate (Figure 5.8A-C) were significantly lower in aged eyecups. Levels of M4 Fumarate, M4 malate, and M4 aspartate (Figure 5.8D-F) trended lower in aged eyecups compared to young. The percent labeled with ^{13}C (Figure 5.8G-L) varied by metabolite. Notably, M5 glutamine, M4 fumarate, M4 malate, and M4 aspartate were consistently lower in young eyecups at 20 minutes, but had essentially matched the aged by 90 minutes. The product:reactant ratio of M5

glutamate/M5 glutamine (Supplementary Figure 5.5B) decreased with age. These data suggest that glutamine anaplerosis is diminished in the aged eyecup.

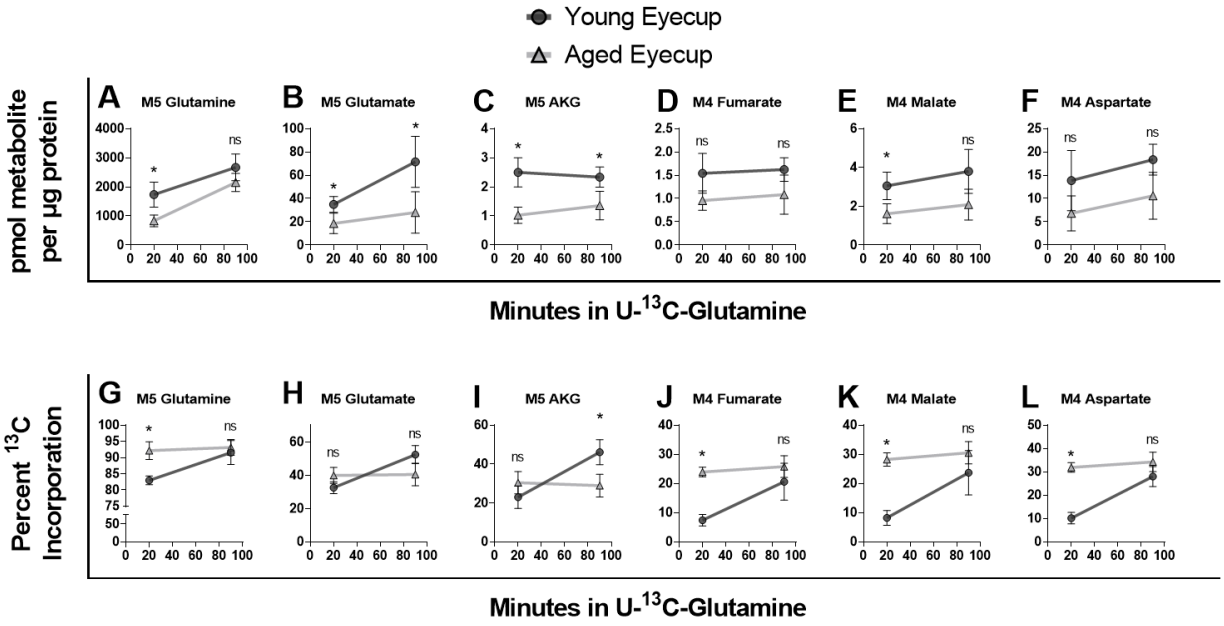

Figure 5.8: An age-related defect was identified in eyecup glutamine metabolism.

Metabolic activity with glutamine - and in the mitochondria more broadly - was examined by incubating eyecup explants in U-^{13}C-glutamine for 20 or 90 minutes. The main isotopologues generated by U-^{13}C-glutamine examined in this study in Figure 5.7. The M4 and M5 labeled isotopologues entering into and proceeding through the Krebs cycle were quantified in terms of pmol of ^{13}C-labeled isotopologue per µg of protein in eyecup explants (A-F) or percent ^{13}C incorporation (G-L). These changes can be related back to pool size and product:reactant ratios, which are included in Supplementary Figure 5.5. Normality of data was determined using the Shapiro-Wilk test and p-values were calculated for age-related comparisons using Mann-Whitney tests (* = $p < 0.05$, marker of non-significance = ns). Error bars represent the standard deviation.

The same analysis was performed in retinas. In contrast, no significant age-related changes in pool size or ^{13}C-labeled intermediates (Supplementary Figure 5.4A and C) were observed. The percent incorporation at 20 minutes was higher in later Krebs cycle intermediates of aged retinas, but younger retina label uptake nearly matched aged by 90 minutes (Supplementary Figure 5.4B), although it was still lower. No significant changes in product:reactant ratios (Supplementary Figure 5.4D) were observed.

We postulated the declines in eyecup glutamine metabolism indicated a decline in mitochondrial function. We approximated mitochondrial function by measuring oxygen consumption rate (OCR) and ATP levels in young and old retinas and eyecups.

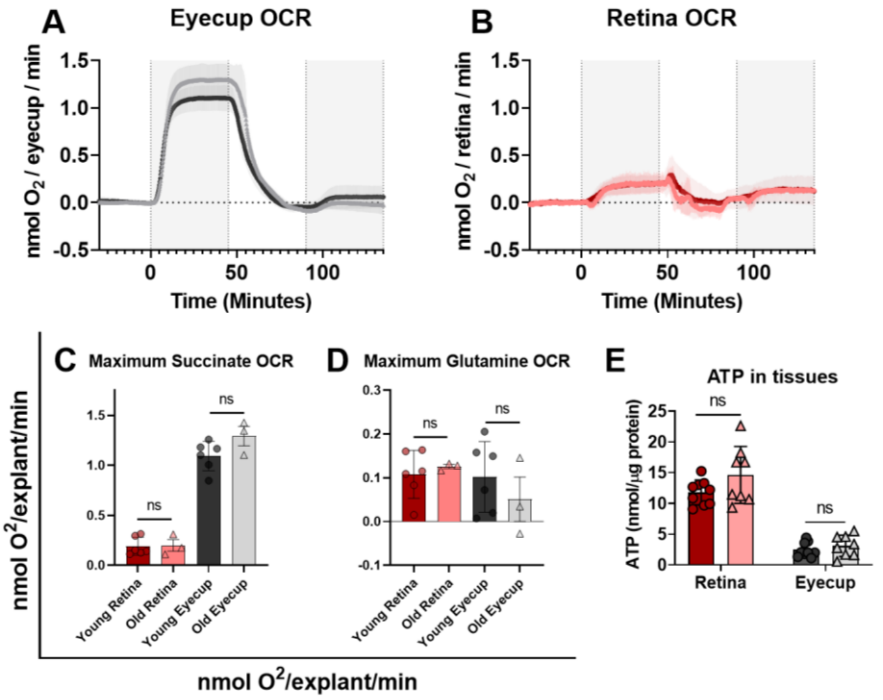

Figure 5.9: Retinal and eyecup mitochondrial function is stable *ex vivo* with age.

Oxygen consumption was measured in terms of nmol O_2 per retina or eyecup per minute using a continuous perifusion system. The values were normalized by subtracting the baseline consumption in 5 mM glucose for eyecups (A) and retina (B). The basal oxygen consumption values (not normalized) are listed in Supplementary Table 5.1. There was a modest increase in aged eyecup oxygen consumption in response to succinate (Shaded area between 0-45 minutes), although it does not reach statistical significance (C). There was no discernable change with age in retinas (C). In response to glutamine (D), retina OCR was unchanged with age while eyecups trended lower. We observed no substantial changes in steady-state ATP levels with age when measured using the Molecular Probes® ATP Determination Kit (E). Normality of data was determined using the Shapiro-Wilk test and p-values were calculated) for age-related comparisons using Mann-Whitney tests (* = $p < 0.05$, marker of non-significance enclosed in parentheses). Error bars represent the standard deviation.

Succinate is a mitochondrial respiratory substrate that is preferentially oxidized by the RPE (Bisbach et al., 2020). Succinate-driven OCR was calculated for each animal by taking the maximum steady-state OCR of tissue respiring on 5 mM glucose + 5 mM succinate and subtracting the 5 mM glucose baseline OCR in eyecups (Figure 5.9A, first shaded area) and retinas (Figure 5.9B, first shaded area). As reported previously, succinate stimulates OCR in eyecups to a significantly greater degree compared to retina (Bisbach et al., 2020). Neither retinas nor eyecups exhibited significant age-related changes in succinate-stimulated O_2 consumption (Figure 5.9C). Glutamine can be fed into the Krebs cycle. Glutamine-driven OCR was calculated for each animal as

was done with succinate in 5 mM glucose + 5 mM glutamine in eyecups (Figure 5.9A, second shaded area) and retinas (Figure 5.9B, second shaded area). The maximum glutamine-stimulated OCR was not significantly impacted in retina or eyecups, although in aged eyecups OCR trended lower (Figure 5.9D). Further replication of this work is needed. Steady-state OCR values are listed in Supplementary Table 5.1. Steady-state levels of ATP (Figure 5.9E) also showed negligible changes.

Amino acid pools are generally stable with age

The pool size of a subset of amino acids were also measured using GC-MS in the same mice considered in Figure 5.5, Supplementary Figure 5.2, and Supplementary Figure 5.3 The amino acids were grouped based on their abundance in terms of the pmols of metabolite per µg of protein in the explant – low, moderate, and high. In retinas (Figure 5.10A-C) and eyecups (Figure 5.10D-F), we saw no significant changes with age.

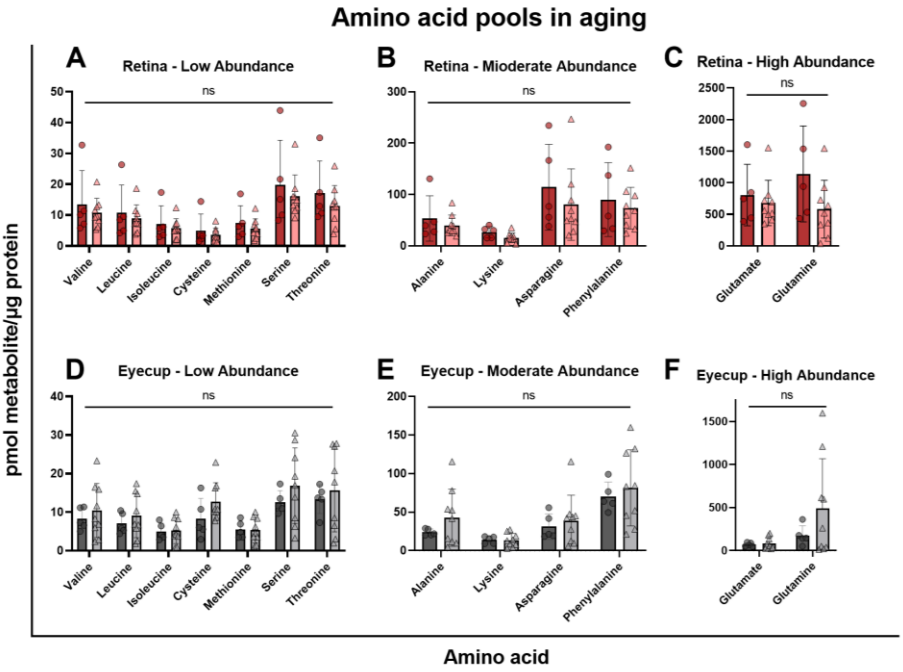

Figure 5.10: Amino acid pool size is unaffected with age.

In retinas and eyecups, there were no significant changes in lower (A,D), moderate (B,E), and high (C,F) abundance amino acid pool size with age. Normality was determined using the Shapiro-Wilk test and p-values were calculated using Mann-Whitney tests. Error bars represent the standard deviation.

Anaplerotic processes unchanged with age when measured *ex vivo*

Beyond glycolysis and oxidative metabolism in the Krebs cycle, glucose and glutamine anaplerosis can be used to regenerate Krebs cycle intermediates. Oxaloacetate can be

generated from pyruvate via pyruvate carboxylase and has been known to be expressed in glia (Lao-On et al., 2018; Schousboe et al., 2019).

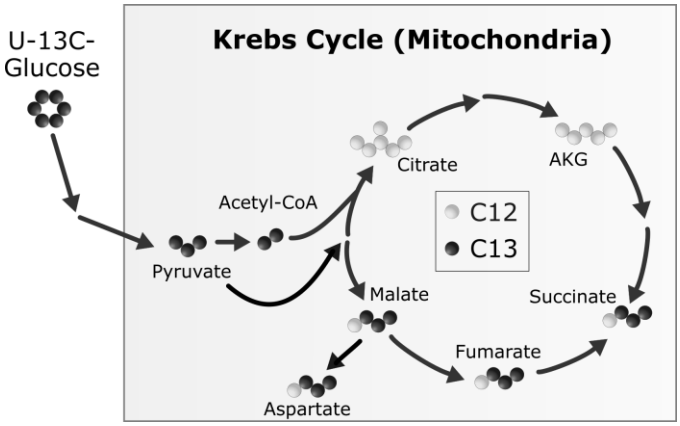

Figure 5.11: Tracing products of pyruvate carboxylase, an anaplerotic reaction from glucose-derived metabolism.

We considered whether the amount of M3 Krebs cycle intermediates generated from anaplerosis of glucose was altered in aging. M3 Krebs cycle intermediates that had been generated from M3 pyruvate could be differentially identified within the same samples in which M2 isotopologues were measured in Figure 5.5 and Supplementary Figure 5.3.

We have been unable to reliably detect oxaloacetate in our GC-MS method. Thus, intermediates downstream of M3 oxaloacetate were considered, including M3 Aspartate, M3 Malate, M3 fumarate, and M3 succinate. We found no significant changes associated with aging in the retina (A) or the eyecup (Figure 5.12). The anaplerotic flux through pyruvate carboxylase appears to be stable in aged explants.

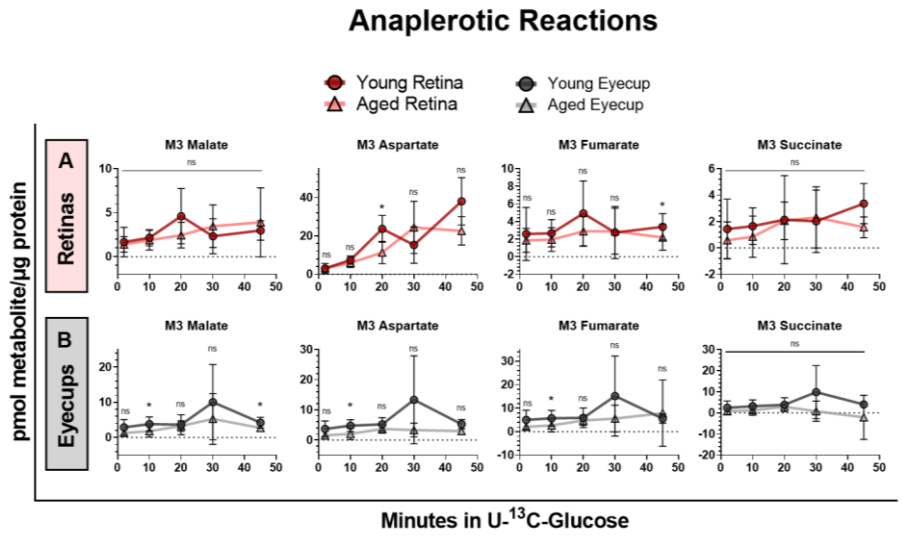

Figure 5.12: Anaplerosis via pyruvate carboxylase from M3 pyruvate is unchanged with age.

In the same animals, M3 isotopologues of malate, aspartate, succinate, and fumarate were measured in retinas (A) and eyecups (B). Normality was determined by Shapiro-Wilk test and p-values were calculated using Mann-Whitney tests. Error bars represent the standard deviation.

Finally, reductive carboxylation is an anaplerotic pathway known to occur in the mitochondria of retina and RPE in culture, although to a lower degree in retina (Du

Hurley Chao 2016 PNAS). We examined this process in the same mice where oxidative flux was examined in Figure 5.8, Supplementary Figure 5.4, and Supplementary Figure 5.5. We considered the conversion of M5 glutamine to different isotopologues of citrate. M4 citrate is made via oxidative flux, and M5 citrate is generated through reductive flux. We were able to show that RPE cells from a mouse explant can and do perform reductive carboxylation and to a higher degree than their matched retinas. However, we identified no significant difference due to aging in retina or eyecup (Figure 5.13).

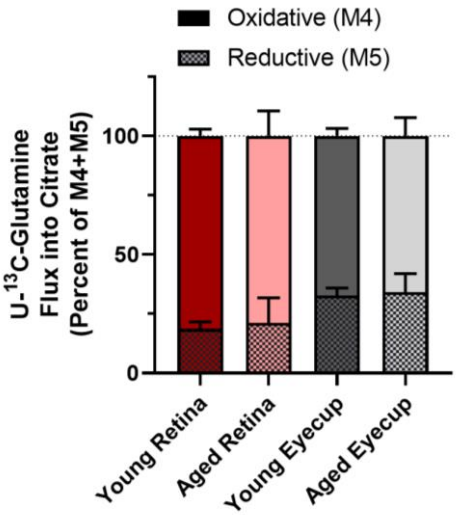

Figure 5.13: Reductive carboxylation is unaltered in retinas and eyecups with age.

The flux of glutamine through the oxidative and reductive pathways in the Krebs cycle

Discussion

Retinal function is impaired with aging

Aging drastically alters visual function in humans (Freund et al., 2011; Kergoat et al., 2001). We observed the same trend in 26 month-old C57Bl/6J mice where rod function, cone function, and photopic temporal resolution declined relative to young mice (Figure 5.2). By 26 months, C57Bl/6J mice are roughly equivalent to 79 year-old humans (Jackson Laboratory, n.d.) and the functional changes observed are representative of advanced age, as roughly 25% of the population would have died (Yuan et al., 2011, 2009). We hypothesized that this decrease in function would correlate with reduced glucose metabolism and mitochondrial function in aged retina and eyecup explants.

Retinal glucose metabolism is remarkably stable with age

Rapid aerobic glycolysis in the retina is required for visual function (Haydinger et al., 2020; Winkler, 1981). . Despite the observed decline in response to light, the metabolism of the aged retina in terms of glucose and glutamine metabolism is stable *ex vivo*. We identified no change in glucose uptake in a pilot study (Figure 5.3). Glycolysis had reached a steady-state, but both glycolytic and Krebs cycle intermediates (Figure 5.5, Supplementary Figure 5.2, Supplementary Figure 5.3) were essentially unchanged between young and aged retinas. There was no observed effect of sex (Figure 5.6), and mitochondrial OCR and ATP levels were also unchanged (Figure 5.9). Amino acid pool size and anaplerotic reactions through pyruvate carboxylase and reductive carboxylation of glutamine were not impacted in the aging retina. Glutamine metabolism is linked to synaptic transmission through the neurotransmitter glutamate (Hamberger et al., 1979). However, it is unlikely the minor defect we observed in the percent incorporation of ^{13}C from U-^{13}C-glutamine in late Krebs cycle intermediates (Supplementary Figure 5.4) will impact neurotransmission. We postulate that aging retina is robust and retains metabolic function on par with young retinas despite significant physiological decline in vivo.

Eyecup glutamine metabolism is impaired in aging mice

Glucose uptake (Figure 5.3), glucose metabolism, and amino acid pools appears to also be preserved in aging eyecups (Figure 5.5, Supplementary Figure 5.2 and Supplementary Figure 5.3). Anaplerotic reactions converting pyruvate to oxaloacetate via pyruvate carboxylase and the reductive carboxylation of glutamine were not effected by aging. However, oxidative glutamine metabolism in aged eyecups is significantly different from young. Although the sample size used (n = 4-5) leaves subtle differences challenging to identify, we found that the pool size (Supplementary Figure 5.5) and isotopologues were decreased with age. However, the percent ^{13}C incorporation into glutamine intermediates (Figure 5.8) remained stable in aging eyecups compared to the increasing percent in young. We hypothesize that this indicates aged eyecups are deficient in glutamine metabolism and reach their maximum metabolic capacity faster

than their younger counterparts. While the decreased M5 Glutamate:M5 Glutamine ratio could be indicative of decreased glutaminase activity in aging RPE, enzyme activity assays from glutaminase to fumarase would allow more targeted identification of the source of the defect in glutamine metabolism we observed. While the reduction in glutamine-driven OCR did not reach significance, it is interesting to note that this supports the metabolic flux data indicating a reduction in metabolic capacity.

The decline in glutamine flux seen in aged eyecups may be linked to glutathione redox state, which has been shown to be altered significantly in the aging eye. From whole eye homogenates, the ratio of reduced/oxidized glutathione was found to decline alongside a marked increase in protein-glutathione mixed disulfides (Rebrin et al., 2003). Given that some of the key functions of the RPE are light absorption and phagocytosis and degradation of photoreceptor outer segments (Strauss, 2005), it is not difficult to imagine these cells are under heightened oxidative stress in aging. A decrease in reduced glutathione availability could negatively impact these cells.

Putting the metabolic flux results into context with other aging tissues

Both metabolic changes and mitochondrial dysfunction are hallmarks of aging (López-Otín et al., 2013). Glycolytic capacity declines with age in tissues like the brain and effector T Cells (Angelin et al., 2017; Camandola and Mattson, 2017; Goyal et al., 2017; Weyand and Goronzy, 2016). Young hearts subsist on fatty acid oxidation, but switch to glycolysis and ketone body usage in aging and heart failure (Chiao and Rabinovitch, 2015; Ritterhoff and Tian, 2017). Liver and skeletal muscle experience metabolic shifts with age (Demontis et al., 2013; Garvey et al., 2014; Nishikawa et al., 2014; Ohlendieck, 2011; Rui, 2014; Vitorica et al., 1981).

Our results show that metabolism in retina and RPE are surprisingly robust in aging relative to these other systems despite functional visual decline in aged mice *in vivo*. This may indicate that the main driver of metabolic change in the aging eye is not intrinsic, but is due to nutrient or oxygen availability from blood. Blood vessel function around the retina has been shown to decline in aging people (Lin et al., 2019; Orlov et

al., 2019; Wei et al., 2017). Oxygen extraction is lower in aged human retina (Bata et al., 2019). Retina and eyecup explants are exposed to ambient oxygen and levels of glucose (5 mM) that are physiological to young mice, with few barriers to transport. Within the aged animal, these tissues may have restricted access to nutrients and oxygen due to the aforementioned declines in circulation and oxygen extraction. While retina and eyecup maintain their metabolic function in aging *ex vivo*, they may still experience a non-cell autonomous functional decline.

Considerations for future studies

A complementary in vivo approach is necessary to determine whether metabolic changes in the aging eye are due solely to intrinsic properties of the tissues or may be related to alterations in the vasculature and tissue structure. We will utilize direct infusion of ^{13}C-labeled fuels(TeSlaa et al., 2021) to test this hypothesis. Our study focused on fuels of known importance in retina and RPE (glucose, glutamine, and succinate), but other metabolic pathways known to be important in these tissues merit consideration in the aging eye (Adijanto et al., 2014; Bisbach et al., 2020; Du et al., 2016b; Izuta et al., 2017; Yam et al., 2019).

Finally, it is important to consider that mitochondria have diverse functions outside of cellular respiration (Abate et al., 2020; Hoppins, 2014; Tait and Green, 2012). Abundance of Krebs cycle intermediates provides a direct link to epigenetic change (Bénit et al., 2014; Salminen et al., 2014). Mitochondrial dysfunction is also involved in aging and cellular signaling that can have broad implications in an organ system (Abate et al., 2020; Bratic and Larsson, 2013; Bratic and Trifunovic, 2010; López-Otín et al., 2013; Sun et al., 2016; Wiley et al., 2016). While the tissues in the eye we examined - especially the retina - appear to be resilient to age-related defects in metabolism, future research will be critical to improve understanding of how the mitochondria in the retina and RPE can influence the broader ocular ecosystem.

Materials & Methods

Mouse ages, origin, and housing

C57Bl/6J mice of both sexes were obtained from the National Institute of Aging aged rodent colony (Bethesda, MD) and Jackson Laboratories (Bar Harbor, ME; Stock No: 000664). Young (3-7 months) and aged (23-26 months) mice were housed in groups of 5 or less in vivariums with ad libitum access to food (Rodent Diet 5053) and water. Some aged male mice were treated with saline via osmotic minipumps or provided water by bottle for 8 weeks prior to euthanasia as controls for separate studies unrelated to the eye. No differences were observed in ocular metabolism between untreated and control mice. Mice were confirmed free of the Crb1 mutation found in Rd8 models of retinal degeneration using a previously published PCR genotyping protocol (Mattapallil et al., 2012; Mehalow et al., 2003). The light/dark cycle was 14 hours of light and 10 hours of dark. Experiments complied with the policies of the Animal Care and Use Committee at the University of Washington and the ARVO Statement for the Use of Animals in Ophthalmic and Vision Research.

Electroretinogram (ERG) set-up

Mice were dark adapted overnight (~17 hours), anesthetized with isoflurane, and eyes dilated with 2.5 % phenylephrine (Akorn, Inc; NDC 174780201-15) and 1% tropicamide (Bauch + Lomb; NDC 24208-585-64). Gold electrodes were placed on each cornea. A reference and ground electrode were positioned on the back of the head. Mice were placed inside a UTAS Visual Diagnostic System with BigShot Ganzfeld with UBA-4200 amplifier (LKC Technologies; Gaithersburg, MD). Readings were taken from both eyes, and the eye with the best response was considered. Scotopic assays were performed first, followed by photopic flicker or photopic single-flash experiments under a continuous 30 cd/m2 background light.

Single-flash ERGs

Recordings were elicited using flashes of LED white light at increasing flash intensities with two minute pauses between individual flashes under scotopic (-50 to 50 dB) and

photopic (0 to 100 dB flashes, 30 cd/m^2 background light) conditions. Readings were calibrated such that 0 db = 2.5 cd*s/m^2. The a-wave amplitude was measured 8 ms after flash stimulus. The b-wave amplitude was measured as the magnitude from the a-wave minimum to the b-wave maximum.

Flicker-fusion ERGs

Temporal resolution was measured using a 5 db flash of varied frequencies (20-50 Hz) under photopic conditions. Ten second pauses were taken between frequencies and repeated 9 times each. Measurements were taken at 0.5 s intervals for a total of 512 points in 0.255 s (sampling frequency = 2003.91 samples/s). At each frequency, replicates were averaged. Figure 5.2E and F show examples of these raw values at 37 Hz. A waveform was generated and the magnitude calculated using Fast Fourier Transform (Microsoft Excel Data Analysis ToolPak). The sampling frequency was 2003.9 samples/s and the step value was 3.91.

Isolation of retinas and eyecups

Animals were euthanized by awake cervical dislocation. Eyes were enucleated, cleared of excess tissue, and the retina separated from the RPE-choroid-sclera complex (eyecup) in Hanks' Balanced Salt Solution (Gibco; Grand Island, New York) within approximately 5 minutes. Tissues for ATP determination were snap frozen and stored in liquid nitrogen. Those for flux or OCR were used immediately.

Metabolic flux and metabolite extraction

Metabolite standards and buffer components were purchased from Sigma-Aldrich (MilliporeSigma; St. Louis, MO). Product numbers are included in Supplementary Table 5.2. Incubation medium was formulated as follows:

- Krebs's Ringer Buffer (KRB): 98.5 mM NaCl, 4.9 mM KCl, 1.2 mM KH_2PO_4, 1.2 mM $MgSO_4$, 20 mM HEPES, 2.6 mM CaCl, 25.9 mM $NaHCO_3$
- Either 5 mM U-^{13}C glucose alone or 5 mM unlabeled glucose and 2 mM U-^{13}C glutamine

U-^{13}C metabolic tracers (99% isotopic purity) included ^{13}C labeled D-Glucose and L-Glutamine (Cambridge Isotope Laboratories, Inc; Tewksbury, MA). Incubations, tissue extractions, and media extractions were performed as described previously(Du et al., 2015) with minimal changes. Some samples were split in half by volume before drying. All samples were spiked with methylsuccinate, L-norvaline, or L-norleucine as process and instrument controls. Metabolites were stored at -80°C until analysis.

GC-MS analysis

Metabolite standards between 1.25-35 µM were used to generate calibration curves. The derivatization and selected ion monitoring (SIM) methods have been described in detail30 with few changes. The incubation length with N-tertbutyldimethylsilyl-N-methyltrifluoroacetamide (MilliporeSigma; St. Louis, MO) was increased to 60 minutes. Samples were analyzed using a 49 minute gradient on an Agilent 7890/5975C GC-MS system (Agilent Technologies; Santa Clara, CA). Two Agilent columns were used: a DB-5MS (128-5522) and an HP-5MS (19091S-433I) with flow rates of 0.8 mL/min or 1 mL/min, respectively. For all derivatized metabolites, we used target ions for quantification and isotopologue distribution determination, and a qualifier ion for identity confirmation. Supplementary Table 5.2 describes SIM method details for individual metabolites. Peak areas for SIM ions were obtained in MSD ChemStation (Agilent Technologies; Santa Clara, CA) with manual verification of automated peak integrations. IsoCor v2 was used (Millard et al., 2019, 2012) to correct for natural ^{13}C abundance and determine percent enrichment of ^{13}C. In individual metabolite isotopologues, the number of incorporated ^{13}C is represented shorthand by “Mx”, where x is the number of ^{13}C (M0, M1, M2, etc.).

Oxygen consumption rate

For each replicate, two retinas or four eyecups were quartered and loaded into a perifusion system that assesses oxygen consumption as described (Sweet et al., 2002a, 2002b) with minimal changes. Tissue was perifused with Krebs-Ringer buffer maintained at equilibrium with 21% O_2, 5% CO_2, and 74% N_2 by an artificial lung and supplemented with 0.1 g/100mL BSA, 1X antibiotic-antimycotic (Gibco; Grand Island,

NY), and 5 mM glucose. Succinate (5 mM) was added when testing mitochondrial function. Flow rate over live tissue averaged 61.9 ± 5 µL/minute. OCR was calculated as the product of flow rate times the difference in outflow and inflow oxygen levels. Data was reported as a change in OCR after subtracting off the baseline OCR measured in 5 mM glucose alone.

Glucose uptake

For each replicate, four retinas or four eyecups were pooled. Incubation buffer was formulated with 5 mM glucose and KRB at an initial volume of 1 mL. Incubations were performed in a humidified incubator at 37°C and 5% CO_2 for a total of 8 hours. At each timepoint, the dish was moved out of the incubator, a 12 µL aliquot pulled, and the dish immediately placed back into the incubator. From that aliquot, at least 2 µL was used to measure glucose in duplicate measurements of 1 µL with a commercial glucometer (Accu Chek Performa, Roche Diagnostics). The precision of the glucometer was confirmed with a calibration curve of glucose standards prior to running the experiment. Values were converted to mM after measurement by the glucometer in mg/dL.

ATP measurements

The pool of ATP in retinas and eyecups extracted in boiling water (Yang et al., 2002) was measured via luminescence with the Molecular Probes® ATP Determination Kit per the manufacturer's instructions. Values were normalized to protein content in the pellet and supernatant.

Protein concentration for normalization

Protein pellets were solubilized in RIPA buffer (150 mM NaCl, 1% Triton X-100, 0.5% sodium deoxycholate, 0.1% SDS, 50 mM Tris pH 8.0, 1X HALT protease/phosphatase inhibitor) and quantified using the Pierce™ BCA Protein Assay Kit per manufacturer’s instructions.

Grouping and statistics

Sample collection from young and aged groups occurred at different times. Sample sizes represent biological replicates. Extractions, derivatization, and sample runs were processed in batches including both ages, genders, matched retinas, eyecups, and/or their media, and random timepoints. To account for circadian contributions, the time of death for animals used in glucose flux, glutamine flux, and OCR are plotted in Supplementary Figure 5.1. Normality of data was determined using the Shapiro-Wilk test. Differences between young and old animals were examined using Mann-Whitney tests (* = $p < 0.05$) and those associated with age and sex were considered using Kruskal-Wallis and Dunn's multiple comparison tests. Values that did not reach statistical significance are marked "ns".

Extended Data

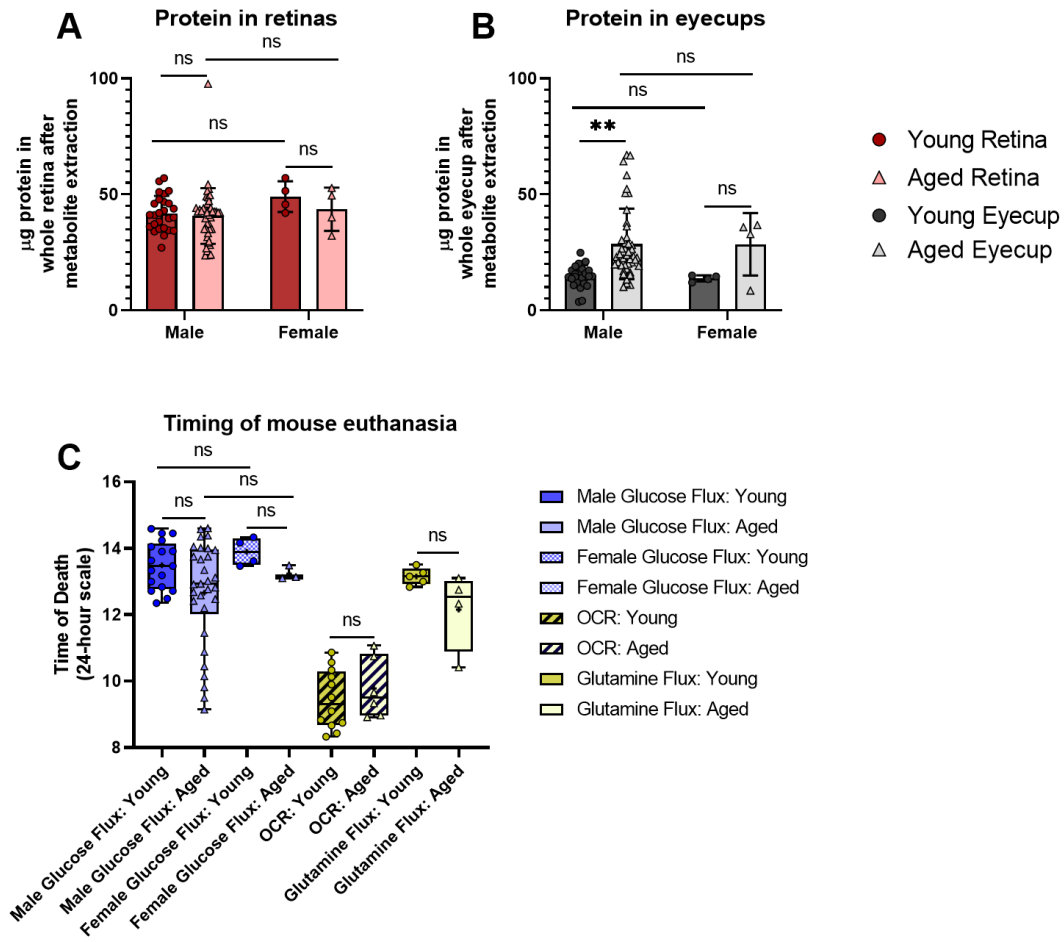

Supplementary Figure 5.1: Normalization to protein content and consideration of circadian rhythm in sample collection.

Sample collection time and quantity of tissue were considered during this study. We observed no significant difference in the protein content between young and aged retinas (A) of either sex in our glucose timecourse. A group of eyecup samples trended significantly higher (B) and increased the average, but this was found to correlate with the individual who collected the samples. Differences in tissue quantity were controlled for in the study by normalizing all values to total protein in the tissue. Values are plotted as the mean ± standard deviation. The normality of data was determined using the Shapiro-Wilk test. Age and sex-related differences were tested (* = $p < 0.05$, ** = $p < 0.0001$) using the Kruskal-Wallis and Dunn's multiple comparison tests. The time of death for all animals used in the flux and OCR experiments (C) except for a single aged female mouse, whose time of death was not noted but was known to occur between the hours plotted. We did not observe any clear differences related to the time of day the sample was collected. Boxes represent the median, minimum, and maximum. Means are marked with a cross (+). The normality of data was determined using the Shapiro-Wilk test. The age and sex-related differences in glucose flux were tested using the Kruskal-Wallis and Dunn's multiple comparison tests. Age-related differences in glutamine flux and OCR were tested using Mann-Whitney tests.

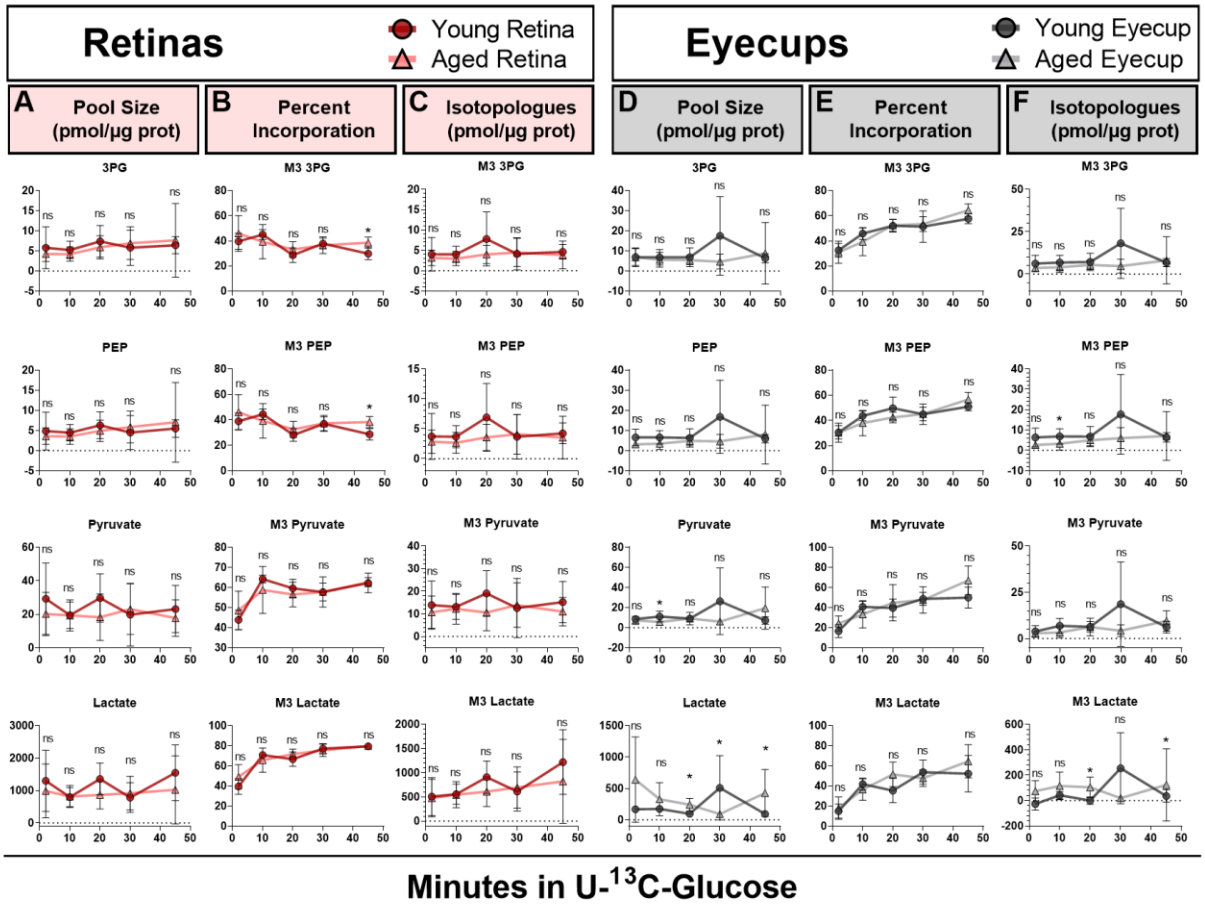

Supplementary Figure 5.2: Individually plotted glycolytic intermediates reveal no consistent and significant age-related changes in retina or eyecup glucose metabolism.

Individually plotted glycolytic intermediates from the glucose time course in retinas and eyecups. The pool size (A), percent ^{13}C incorporation (B), and isotopologues (C) in the retina are listed for select glycolytic intermediates. In eyecups for the same glycolytic intermediates, the pool size (D), percent ^{13}C incorporation (E), and isotopologues (F) are shown. Values shown are the mean ± standard deviation. Sample size = 4-9 depending on the age, tissue, and timepoint. Note that these graphs and sample sizes consider two outliers that were removed by Grubb's test (alpha = 0.05, $p < 0.05$): one young retina at 20 minutes and one aged eyecup at 30 minutes. Both were more than 10-fold higher than other tissues at the same timepoints. Normality of data was determined using the Shapiro-Wilk test and p-values were calculated for age-related comparisons using Mann-Whitney tests (* = $p < 0.05$). Error bars represent the standard deviation.

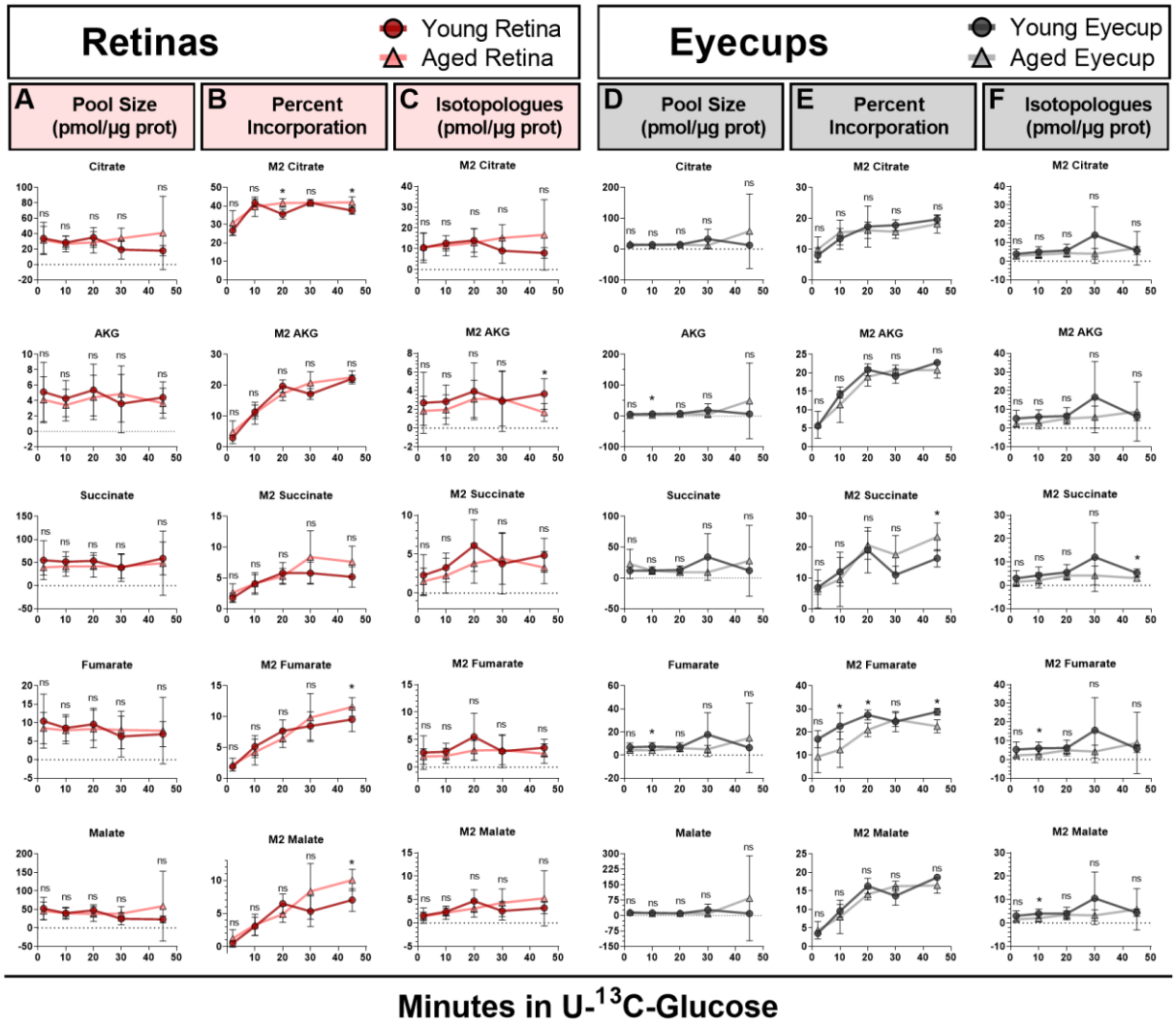

Supplementary Figure 5.3: Individually plotted Krebs Cycle intermediates reveal no consistent and significant age-related changes in retina or eyecup glucose metabolism.

Individually plotted Krebs cycle intermediates from the glucose time course in retinas and eyecups. The pool size (A), percent ^{13}C incorporation (B), and isotopologues (C) in the retina are listed for select Krebs cycle intermediates. In eyecups for the same intermediates, the pool size (D), percent ^{13}C incorporation (E), and isotopologues (F) are shown. Values shown are the mean ± standard deviation. Sample size = 4-9 depending on the age, tissue, and timepoint. Note that these graphs and sample sizes consider two outliers that were removed by Grubb's test (alpha = 0.05, $p < 0.05$): one young retina at 20 minutes and one aged eyecup at 30 minutes. Both were more than 10-fold higher than other tissues at the same timepoints. Normality of data was determined using the Shapiro-Wilk test and p-values were calculated for age-related comparisons using Mann-Whitney tests (* = $p < 0.05$). Error bars represent the standard deviation.

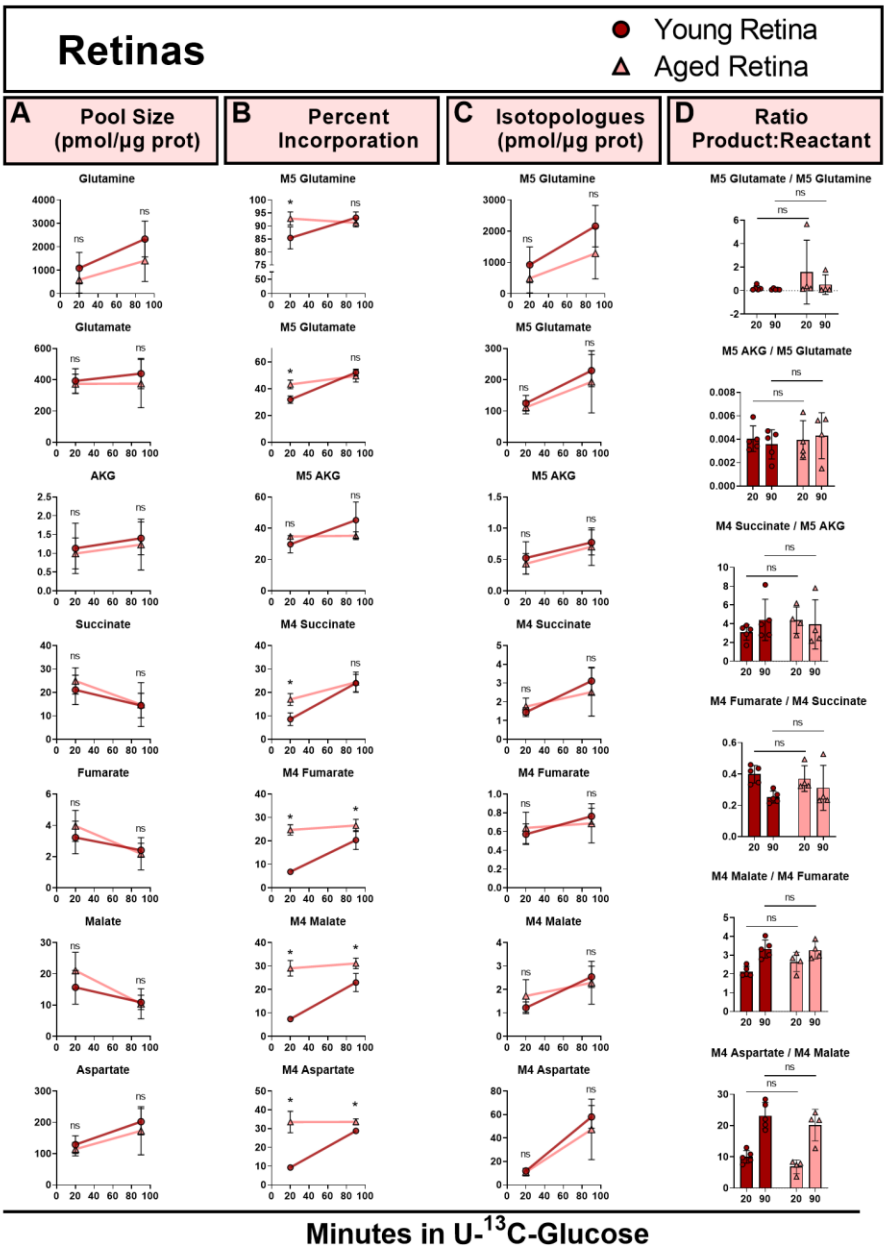

Supplementary Figure 5.4: Retinal explant glutamine metabolism has few age-related changes

Examining intermediates entering and within the Krebs cycle from a glutamine time course (20 and 90 minutes) in retinas. The pool size (A) is unchanged. The percent ^{13}C incorporation (B) remains unchanged in aged retinas at both times, while it is consistently lower in young retinas at 20 minutes for all intermediates (except for AKG) but has matched the aged by 90 minutes. The quantity of labeled isotopologues (C), and the product:reactant ratios (D) in the retina show no significant changes. Values shown are the mean ± standard deviation. Sample size is 5 for young and 4 for aged at both timepoints. Normality of data was determined using the Shapiro-Wilk test and p-values were calculated using Mann-Whitney tests (* = $p < 0.05$).

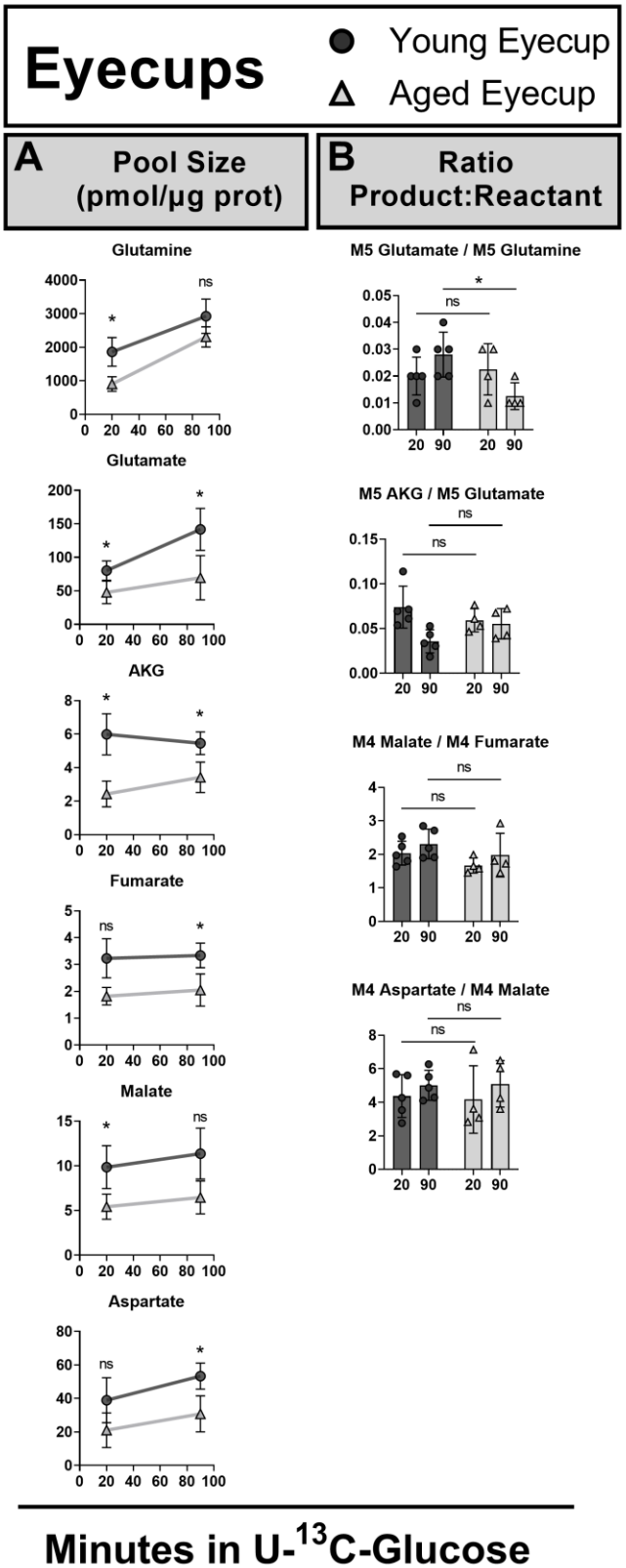

Supplementary Figure 5.5: Pool sizes and product:reactant ratios in young and aged eyecups indicate an age-related decline in glutamine flux.

Intermediates entering and within the Krebs cycle from a glutamine time course (20 and 90 minutes) in eyecups. Pool sizes (A) are generally lower in aged eyecups, while product:reactant ratios (B) were found to have minimal significant changes. Only the ratio of M5 glutamate/M5 glutamine decreased slightly in aged eyecups. Although succinate isotopologues were searched for in these experiments, they were not reliably above the limit of detection in eyecups, thus we could not determine any age-related changes involving succinate in eyecups. Values shown are the mean ± standard deviation. Sample size is 5 for young and 4 for aged at both timepoints. Normality of data was determined using the Shapiro-Wilk test and p-values were calculated using unpaired t-tests (* = $p < 0.05$) or Mann-Whitney tests (# = $p < 0.05$, marker of non-significance enclosed in parentheses).

Supplementary Table 5.1: Average basal *ex vivo* O_2 consumption in explants

Tissue	Age	n	Basal O_2 consumption*	Max O_2 consumption with succinate†	Basal O_2 after succinate #	Max O_2 consumption with glutamine‡
Retina	Young	6	1.90 ± 0.4	2.04 ± 0.4	1.9 ± 0.5	1.99 ± 0.5
	Aged	3	2.14 ± 0.4	2.34 ± 0.4	2.15 ± 0.5	2.27 ± 0.5
Eyecup	Young	6	0.52 ± 0.3	1.62 ± 0.3	0.47 ± 0.3	0.57 ± 0.4
	Aged	3	0.56 ± 0.2	1.85 ± 0.2	0.50 ± 0.2	0.55 ± 0.2

* Basal nmol O_2/min ± SD in glucose alone measured between -30 and 0 minutes

† Maximum basal nmol O_2/min ± SD with succinate was measured between 20 and 45 minutes

Basal nmol O_2/min ± SD in glucose alone between 80 and 90 minutes after succinate, but before addition of glutamine where OCR was stable

‡ Maximum basal nmol O_2/min ± SD with glutamine was measured between 120 and 135 minutes

Supplementary Table 5.2: Metabolite standards for method development and normalization.

Metabolite	Product number	Retention Time 1* (mins)	Retention Time 2† (mins)	Derivatized Mass	Number of TBDMS	Number of MeOx	Target Fragment	Target Ions	Qualifier Fragment	Qualifier Ion
3-PG	P7127	37.2	36.27	642	4	0	M-57	585-588	M-159	483
α-ketoglutarate	75890	26.99	25.97	403	2	1	M-57	346-351	M-15	388
Alanine	A7627	16.86	15.93	317	2	0	M-57	260-263	M-85	232
Asparagine	A4284	32.3	31.13	474	3	0	M-57	417-421	M-159	315
Aspartate	A6558	29.66	28.56	475	3	0	M-57	418-422	M-85	316
Carbonate	N/A	17.15	16.3	319	2	1	M-57	262	M-15	304
Citrate	S4641	37.1	36.12	648	4	0	M-57	591-597	M-189	459
Cysteine	C7352	30.5	29.45	463	3	0	M-57	406-409	M-159	378
DHAP	D7137	32.84	32.15	541	3	1	M-57	484-487	M-85	526
Fumarate	F1506	22.8	21.53	344	2	0	M-57	287-291	M-15	329
GABA	A2129	22.01	20.86	331	2	0	M-57	274-278	M-15	316
GAP	G5251	32.45	31.75	541	3	1	M-57	484-487	M-85	456
Glutamate	G8415	31.71	30.6	489	3	0	M-57	432-437	M-159	330
Glutamine	G3126	34.23	33.06	488	3	0	M-57	431-436	M-159	329
Isocitrate	I1252	37.25	36.31	648	4	0	M-57	591-597	M-189	459
Isoleucine	I2752	21.21	20.26	359	2	0	M-57	302-308	M-85	274
Lactate	L7022	15.51	12.8	318	2	0	M-57	261-264	M-85	233
Leucine	L8912	20.5	19.6	359	2	0	M-57	302-308	M-85	274
Lysine	L5501	33.55	32.38	488	3	0	M-57	431-437	M-159	329
Malate	M1000	28.82	27.83	476	3	0	M-57	419-423	M-15	461
Methionine	M5308	26.14	25.09	377	2	0	M-57	320-325	M-85	292
Methylsuccinate‡	M81209	22.17	21.09	360	2	0	M-57	303	M-15	345
Norleucine‡	N6877	21.51	20.66	359	2	0	M-57	302-308	M-85	274
Norvaline‡	N7627	19.88	18.95	345	2	0	M-57	288-293	M-85	260
PEP	P7127	30.85	29.9	510	3	0	M-57	453-456	M-15	495
Phenylalanine	P5482	28.45	27.36	393	2	0	M-57	336-345	M-85	308
Pyruvate	P4562	9.58	8.87	231	1	1	M-57	174-177	M-131	100
Serine	S4500	26.49	25.56	447	3	0	M-57	390-393	M-159	288
Succinate	14160	22.04	20.89	346	2	0	M-57	289-293	M-15	331
Threonine	T8625	26.98	26.14	461	3	0	M-57	404-408	M-85	376
Valine	V0500	19.53	18.65	345	2	0	M-57	288-293	M-85	260

* In method 1, a DB-5MS column with a flow rate of 0.8 mL/min was used. Column length was 25 m with an inner diameter of 200 µm, and a 0.33 µm nonpolar phenyl arylene polymer film.

† In method 2, a HP-5MS with a flow rate of 1 mL/min was used. Column length was 30 m with an inner diameter of 250 µm, and a 0.25 µm 5% phenyl methyl silox film.

‡ Symbol denotes an internal standard.

Acknowledgments

Much of the work described in this chapter was deposited as a preprint on bioRxiv on April 6th, 2021 (DOI: 10.1101/2021.04.06.438698). The experiments in this chapter represent the combined efforts of several laboratories and dedicated individuals who contributed experimentation, time, and thoughtful discussions. Those who were authors on the paper include Whitney M. Cleghorn, Celia M. Bisbach, Jeremy A. Whitson, Daniel T. Hass, Brian M. Robbings, Martin Sadilek, Jonathan D. Linton, Austin M. Rountree, Ana P. Valencia, Mariya T. Sweetwyne, Matthew D. Campbell, Huiliang Zhang, Connor S.R. Jankowski, Ian R. Sweet, David J. Marcinek, Peter S. Rabinovitch, and James B. Hurley.

In the laboratories of James B. Hurley and of Susan E. Brockerhoff, we also wish to thank Michelle M. Giarmarco, Mark A. Kanow, Kelie Gonzalez, Benjamin H. Baur, and Chris C. Farnsworth. Expertise in the biology of aging, and thoughtful discussion were provided by the laboratories of Peter S. Rabinovitch and David J. Marcinek. In addition to other authors, Jeanne Fredrickson and Rudolph Stuppard. Clara Suelen, Anthony Scott, and Csaba Nagy provided care for the mice in this study. Finally, the authors thank Susan E. Brockerhoff, Jennifer R. Chao, David W. Raible, and Andrea E. Wills for thoughtful discussion. Funding for this work was provided by the NIA, NEI, and NIDDK:

NIH/NIA

- Peter S. Rabinovitch and David J. Marcinek - Mitochondrial Protective Interventions, Aging and Healthspan: 5P01AG001751
- Kristine A. Tsantilas T32 - Genetic Approaches to Aging Training Grant T32 AG000057
- Kristine A. Tsantilas T32 - Biological Mechanisms for Healthy Aging Training Grant T32 AG066574
- Mariya T. Sweetwyne K01 - Mitochondrial Protection to Derive Expanded Aged Renal Glomerular Progenitor Cells: K01 AG062757-02

NIH/NEI

- James B. Hurley R01 - Determinants of Rod and Cone Response Characteristics: 5R01EY006641

- James B. Hurley R01 - Control of Photoreceptor Metabolism: 5R01EY017863
- Celia M. Bisbach F31 - Understanding the role of cytosolic NADH production in maintaining aerobic glycolysis in the retina: F31EY031165
- Daniel T. Hass T32 - Vision Training Grant: T32EY007031

- **NIH/NIDDK**
- Ian R, Sweet - Cell Function Analysis Core of the Diabetes Research Center: P30 DK017047

Chapter 6 - Interventions to ameliorate ocular aging

Introduction

There are many physiological changes associated with aging in the eye that cause a loss of visual function in aging. This decline contributes to disability and reduces healthspan. Severe age-related pathologies including diabetic retinopathy (DR), age-related macular degeneration (AMD), and glaucoma (Crews et al., 2017; Klein and Klein, 2013). Although these blinding diseases are common, unfortunately many lack effective treatments and the field suffers from a lack of certainty as to their causes. Thus, despite the prospect of increased longevity, many elderly people face reduced quality of life with increased risk of disability from falls, immobility, and depression linked to visual impairment (Abou-Hanna et al., 2021; Crews et al., 2017; Heesterbeek et al., 2017; Saftari and Kwon, 2018). Improving age-related vision loss would enhance human healthspan around the world.

Neurons are energetically demanding (Niven and Laughlin, 2008). Among neuronal tissues, the retina has exceptionally high energetic requirements (Ames et al., 1992). Visual function is directly linked to glycolytic and mitochondrial function in the retina (Winkler, 1981). Nutrients including the glucose necessary for a healthy retina must first pass through the retinal pigment epithelium (RPE). Metabolic changes in the RPE can be detrimental to the retina. Increasing glycolysis (Kurihara et al., 2016; Zhao et al., 2011) or removing the glucose transporter, GLUT1, in RPE (Swarup et al., 2019) caused the retina to degenerate. Various tissues in the aging murine eye exhibit changes in steady state metabolite levels (Wang et al., 2018). In aging primate retina, glycolysis increases while ATP levels and cytochrome c oxidase levels decline (Kam et al., 2019b).

In addition to being a hallmark of aging (López-Otín et al., 2013), mitochondrial dysfunction is linked to neurological diseases (Cabral-Costa and Kowaltowski, 2020). In the eye, some hereditary forms of retinal degeneration (Blasiak et al., 2013) and common age-related blinding diseases such as glaucoma, DR, and AMD are linked to mitochondrial dysfunction (Blasiak et al., 2013; Ferrington et al., 2016; Jarrett et al., 2010; Karunadharma et al., 2010). Targeting mitochondrial function represents an

opportunity to improve healthspan that is impacted by age-related vision loss. In this report we considered two mitochondrial therapeutics - nicotinamide mononucleotide (NMN) and elamipretide (ELAM) impact.

Nicotinamide mononucleotide adenylyltransferase (NMNAT) converts NMN into nicotinamide adenine dinucleotide (NAD). The redox state of NAD - oxidized (NAD+) or reduced (NADH) – is tightly regulated and compartmentalized in cells (Koch-Nolte et al., 2011). NAD interacts with many different families of proteins including sirtuins, (ADP-ribosyl)transferases, and poly(ADP-ribosyl)polymerases and the signaling duration is limited by NADases like CD38 and CD157 (Di Stefano and Conforti, 2013; Koch-Nolte et al., 2011). When a crucial part of the NAD+ salvage pathway - nicotinamide phosphoribosyltransferase (NAMPT) - is knocked-out in rod photoreceptors, the retina degenerates, but can be rescued by exogenous NMN (Lin et al., 2016). Critically, NAD+ concentrations decline with age in many tissues (Prolla and Denu, 2014; Verdin, 2015). Restoration of NAD+ levels can restore some of the function lost in aging by blocking CD38 or by administration of NMN (McReynolds et al., 2020; Mills et al., 2016; Son et al., 2016; Whitson et al., 2020). One of these studies also provided strong evidence that aging vision in C57Bl/6N mice is restored by NMN (Mills et al., 2016). However, this strain is known to carry the *rd8* mutation, which is caused by a single nucleotide deletion in Crb1 that causes retinal degeneration (Aredo et al., 2015; Mattapallil et al., 2012). Although this complicates the interpretation of these results, it is a promising indicator along with previously published works that NMN could ameliorate age-related visual decline.

A class of amphipathic tetrapeptides called Szeto-Schiller (SS) peptides have been tapped as potential therapeutics for their cell-permeable, antioxidant, and mitochondrial targeting properties (Birk et al., 2014, 2013; Szeto, 2006; Zhao et al., 2005, 2004). Of these SS peptides, a fluorescent analog, SS-19, has been shown to accumulate in mitochondria (Berezowska et al., 2003). Significant effort has gone into characterizing another mitochondria-targeting SS peptide, SS-31 or elamipretide (ELAM). ELAM has been shown to have a high affinity for cardiolipin (Birk et al., 2013) or cardiolipin-

enriched membranes (Mitchell et al., 2020). Other work has linked ELAM treatment effects to the function of the electron transport chain (Chavez et al., 2020) and alterations of the biophysical properties of cardiolipin-enriched membranes (Mitchell et al., 2020). The combined antioxidant and apparent mitochondrial rejuvenating properties of ELAM reduce age-related decline in skeletal muscle (Campbell et al., 2019; Siegel et al., 2013), cardiac muscle (Chiao et al., 2020; TeSlaa et al., 2021; Whitson et al., 2020; Zhang et al., 2020), kidneys (Sweetwyne et al., 2017), and brain (Tarantini et al., 2018). ELAM treatment is also effective at treating visual decline in models of glaucoma and diabetic retinopathy (Alam et al., 2015; Wu et al., 2019), which has linked mitochondrial dysfunction to ocular disease.

Finally, the field of geroscience has begun considering the administration of multiple interventions simultaneously – or a “polypharmacological” approach (Castillo-Quan et al., 2019; Whitson et al., 2020). In this report we examine how nicotinamide mononucleotide (NMN), elamipretide (ELAM), and a combination of the two drugs administered simultaneously (ELAM+NMN) impact aging vision and metabolism in *ex vivo* retinal and RPE-choroid (eyecup) explants.

Results

Study organization

To determine whether age-related vision loss could be ameliorated by targeting mitochondrial dysfunction, we examined visual function by electroretinogram and quantified metabolism by metabolic flux and measuring oxygen consumption in mice treated with ELAM, NMN, or a combination of both (ELAM+NMN). Mice were treated for 8 weeks with either ELAM by osmotic pump, NMN in drinking water, or both simultaneously (Figure 6.1). Functional measurements were acquired after about 6 weeks of treatment.

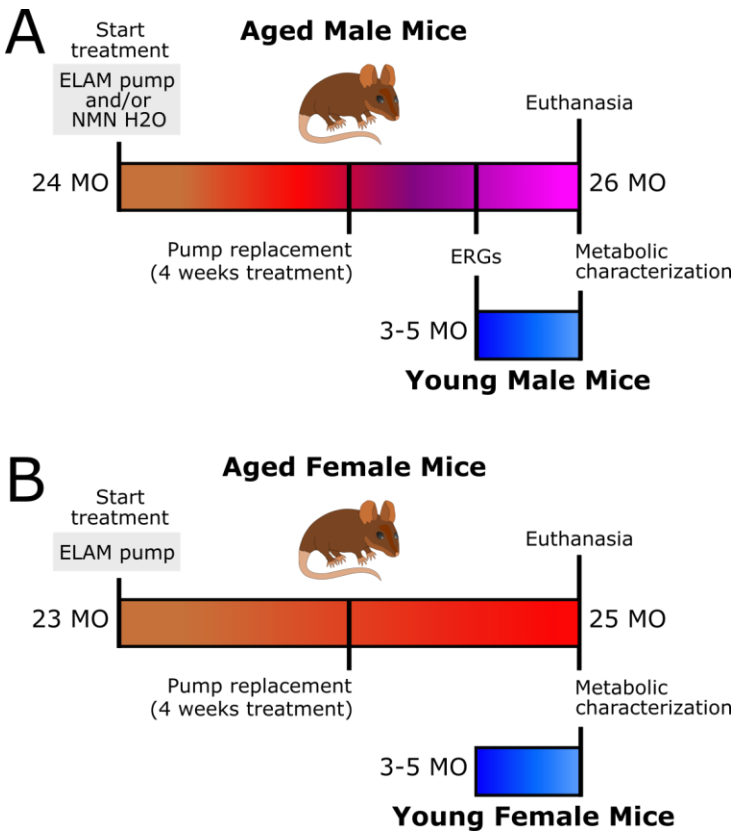

Figure 6.1: ELAM, NMN, and ELAM+NMN) study design.

Young and aged mice were examined in this study. Aged male mice were treated with ELAM, NMN, or a combination of ELAM+NMN for 8 weeks beginning at 24 MO. The ELAM and ELAM+NMN cohorts were subjected to ERGs, and the impact of ELAM and NMN on metabolic aging was measured (A). Aged female mice were treated with ELAM for 8 weeks beginning at 23 MO and the impact of ELAM on metabolic aging was measured (B).

The control group represents three different approaches where no significant differences were found: untreated mice, mice fitted with osmotic minipumps containing saline to control for ELAM, and mice who were provided ad libitum access to bottled water to control for NMN. We examined the metabolic function of retinas and eyecups isolated from untreated aged mice and minipump-treated mice by measuring the percent of ^{13}C incorporation into metabolites extracted from explants that had been provided U-^{13}C-glucose. We found no differences in either tissue between untreated mice and minipump-treated mice at 30 or 45 minutes (Figure 6.2).

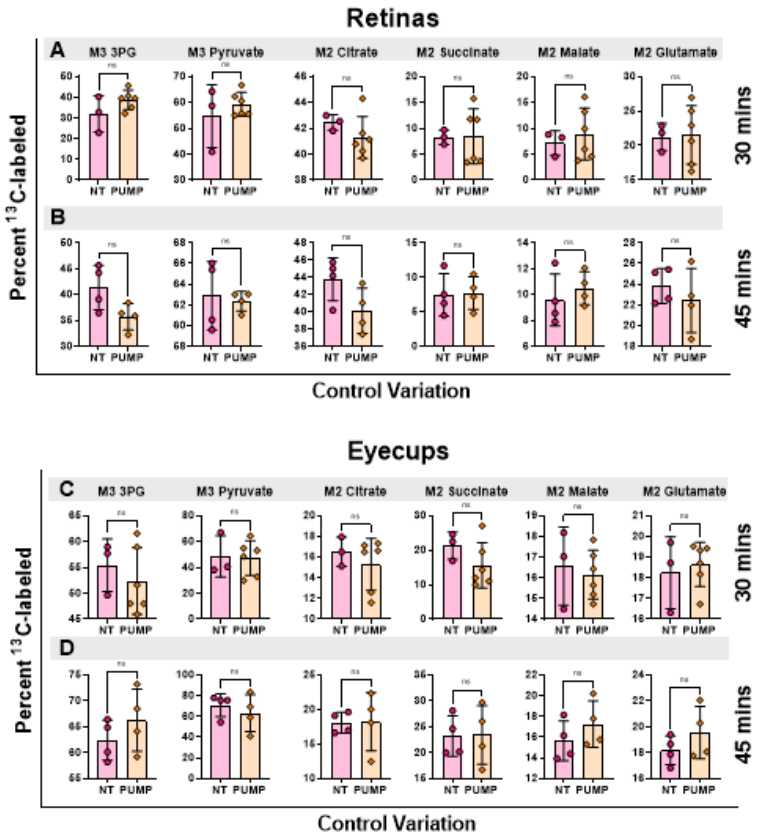

Figure 6.2: Pooling of multiple control types.

The feasibility of pooling controls that were untreated or had been implanted with a saline minipump for 8 weeks was examined by comparing the percent of ^{13}C incorporation from U-^{13}C-glucose in retinal and eyecup explants at 30 and 45 minutes. No significant difference was observed in retina (Rows A and B) or eyecup (Rows C and D). All values are plotted as the mean ± SD. The sample size is 3 for NT at 30 minutes, 6 for pumps at 30 minutes 4 for NT at 45 minutes, and 4 for pumps at 45 minutes. Statistical significance was examined between young and 24 months at individual flash intensities using unpaired t-tests (* = p <0.05).

Rod- mediated vision improved in a subset of animals with ELAM and ELAM+NMN

Scotopic vision, or rod-mediated vision associated with low-light conditions, was measured in aged male mice after 6 weeks of controls, ELAM, NMN and ELAM+NMN treatment. Unfortunately, all but a single mouse from the NMN cohort died prior to the follow-up measurement of unknown causes, thus no results were available to report in this study.

To measure scotopic function, we used ERGs under dark adaptation and examined the response to single flashes of light ranging from -50 to 50 db. The amplitude of the a-wave response – the electrical signal originating from photoreceptors - was extracted at 8 ms after the flash stimulus to avoid contribution of the b-wave that predominantly originates from the inner retinal neurons. In Figure 6.3, the average response at 0 db (Figure 6.3A-B) and 50 db (Figure 6.3C-D) was considered in young and 24 MO male

mice. By averaging the a-wave amplitude for all mice at each flash intensity (E), it was clear that scotopic response had declined significantly with aging by 24 MO.

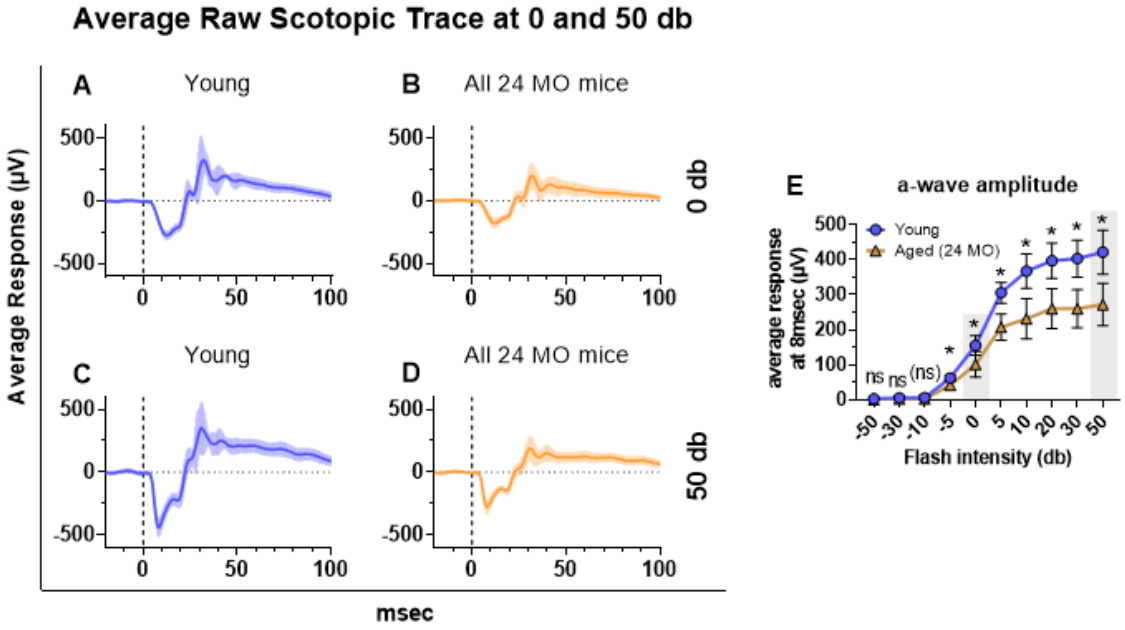

Figure 6.3: Raw scotopic traces of young and 24 MO mice in response to 0 (A and B) and 50 db flashes (C and D).

The amplitude extracted from the a-wave at 8 msec after the flash stimulus indicated a decline with age at flash intensities -5 db or higher (E). Scotopic vision is diminished in 24 MO mice relative to younger mice. The 24 MO group plotted in (B) and (D) includes all controls of treated mice in Figure 6.4Figure 6.4 and Figure 6.5Figure 6.5. Samples size is 8 for young and 23 for the 24 MO group. All values are plotted as the mean ± SD. Normality of the data in Panel E was tested using the Shapiro-Wilk test (α = 0.05). Statistical significance was examined between young and 24 months at individual flash intensities using unpaired t-tests (* = p <0.05) or Mann-Whitney tests (# = p < 0.05, marker of non-significance enclosed in parentheses).

The same approach was used in tandem with aged mice that, beginning at 24 MO, had been treated with ELAM or ELAM+NMN for 6 weeks. At 0 db (Figure 6.4A-F) and 50 db (Figure 6.4Figure 6.4G-L), differences in response were difficult to assess visually between groups at baseline or after 6 weeks of treatment.

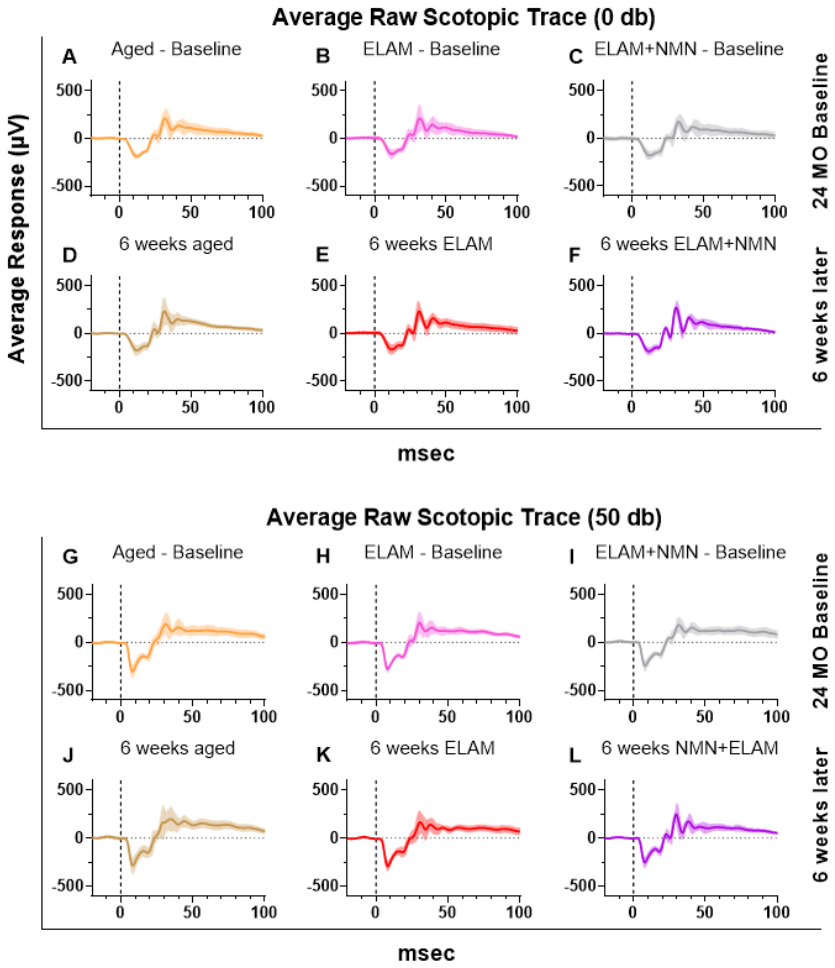

Figure 6.4: Scotopic response to 0 db flash at baseline and after 6 weeks of ELAM, ELAM+NMN, or matched controls.

Mice were treated with ELAM or ELAM+NMN, with their respective controls, starting at 24 MO. Scotopic function was measured 6 weeks later. The raw traces in response to a 0 db flash show minimal change in aged mice between baseline (A) and after 6 weeks (D). The same is true for ELAM-treated mice before (B) and after (E) treatment, and ELAM+NMN mice before (C) and after (F) treatment. The raw scotopic traces in response to a brighter 50 db flash stimulus show minimal change in baseline/after 6 weeks for aged mice (G and J), ELAM-treated mice before (H and K), ELAM+NMN mice (I and L). All values are plotted as the mean ± SD. The sample size is 9 for the aged, 8 for the ELAM, and 6 for the ELAM+NMN groups, respectively.

After extracting the a-wave response at the flash stimuli between -50 and 50 db, there did not appear to be significant benefit to average scotopic responses due to ELAM (Figure 6.5B) or ELAM+NMN (Figure 6.5C) relative to controls (Figure 6.5A). When the response of individual animals is considered pre- and post-treatment for both regiments at 0 db (Figure 6.5D) and at 50 db (Figure 6.5Figure 6.5E), the a-wave response frequently increased after 6 weeks in a subset animals.

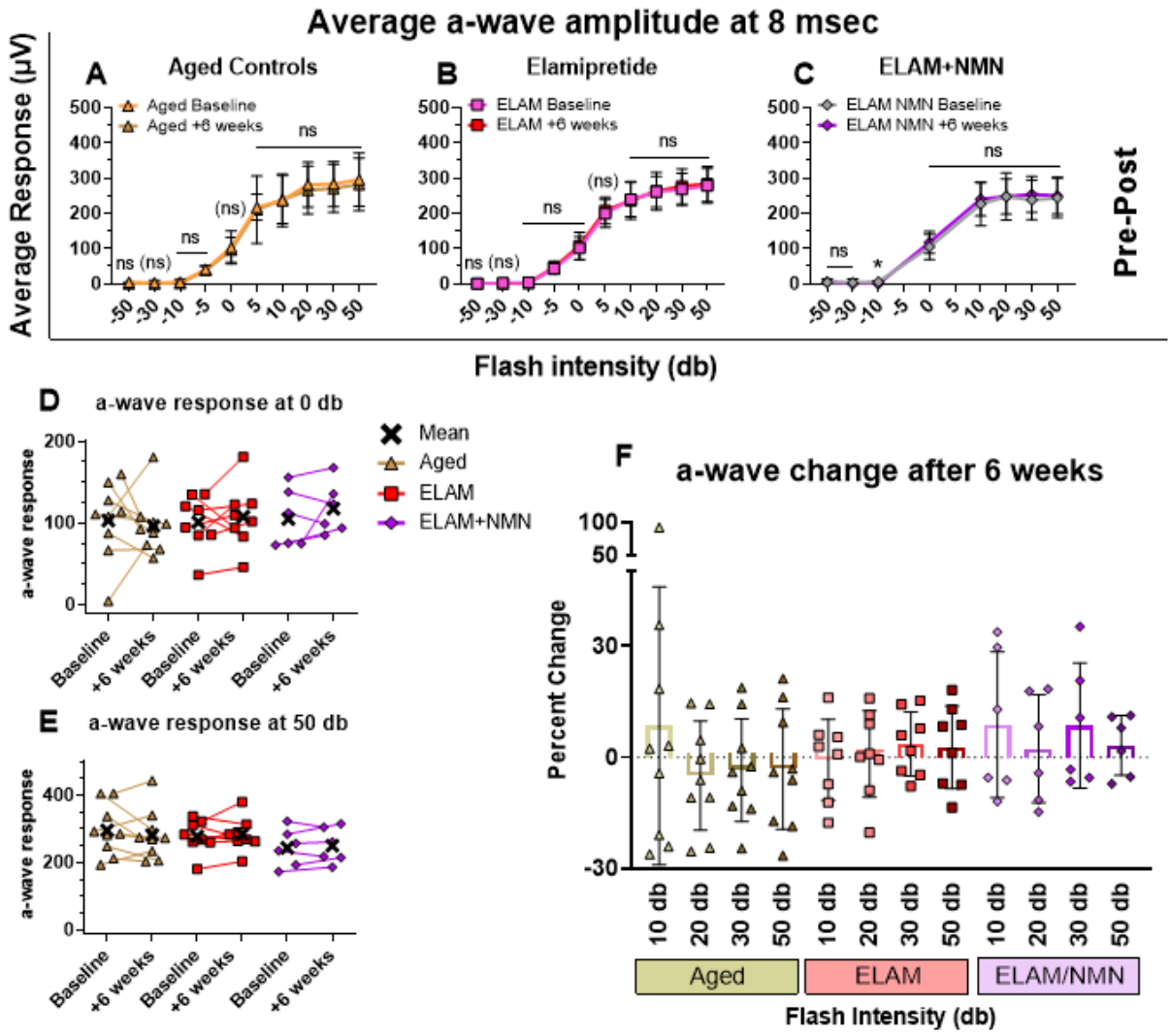

Figure 6.5: The a-wave amplitude was examined in young, aged, and in aged mice with ELAM or ELAM+NMN treatment.

The amplitude of the a-wave was examined preceding and following 6 weeks of ELAM or ELAM+NMN treatment alongside their respective controls. The a-wave amplitude 8 msec after the flash stimulus indicated a decline with age at flash intensities of -5 db or higher. With the exception of a statistically significant difference with a 10 db flash in ELAM+NMN-treated mice (C), we identified no significant differences between 24 MO mice measured at baseline and the response of the same mouse measured in the same eye 6 weeks later in aged (A), ELAM (B), and ELAM+NMN (C) groups. When considered individually, the results were varied. Scotopic function in many mice either improved or remained stable in the ELAM and ELAM+NMN groups at 0 db (D) and 50 db (E), while the controls often declined relative to baseline. However, when the percent change between baseline and 6 weeks after treatment is examined (F) in higher intensity flashes, a trend emerged. Controls tended to decrease, while the mice treated with ELAM or ELAM+NMN tended to improve. The impact of ELAM and ELAM+NMN on scotopic vision is modest. All values are plotted as the mean ± SD. The sample size is 9 for aged, 8 for ELAM, and 6 for the ELAM+NMN group, respectively. Normality of the data was tested using the Shapiro-Wilk test ($\alpha = 0.05$). Statistical significance between paired measurements in Panels C and D was examined using paired t-tests (* = $p < 0.05$) or Wilcoxon matched-pairs signed rank tests (# = $p < 0.05$, marker of non-significance enclosed in parentheses).

The same is true if the a-wave response is examined in terms of the percent change after treatment relative to baseline in the same animal (Figure 6.5F). Interestingly, on average the a-wave declined in the control group while it was maintained or increased with either ELAM or ELAM+NMN.

Cone-mediated vision improved in a subset of animals with ELAM

As a complement, cone-mediated vision associated with well-lit conditions, or photopic vision, was measured in aged male mice after 6 weeks of ELAM treatment. To measure photopic function, we used ERGs under a low background light and examined the response to single flashes of light ranging from 0 to 100 db. A more intense background light was also used with a high intensity (100 db) flash. The amplitude of the b-wave response which primarily occurs as a result of electrical signals originating from inner retinal neurons was taken from the very base of the a-wave to the peak of the b-wave.

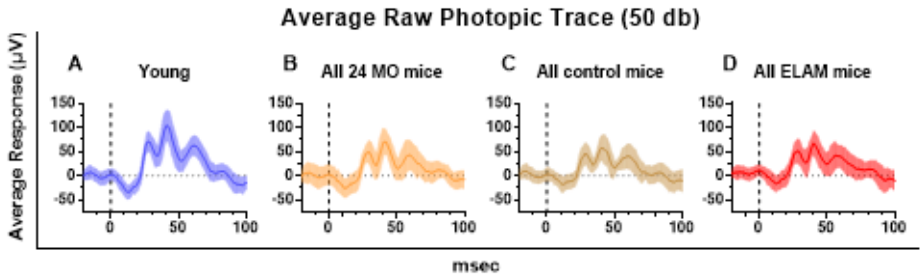

Figure 6.6: Retinal response to 50 db flash in photopic conditions.

The raw photopic traces of young, 24 MO and 26 MO mice in response to a 50 db in lit conditions indicates that the b-wave amplitude declines with aging. After the flash stimulus, the amplitude was measured from the minimum of the a-wave to the maximum point of the b-wave. Although the photopic response is diminished in 24 and 26 MO mice relative to younger mice, when considered as an average the controls and ELAM-treated mice do not appear largely different from 24 MO controls. All values are plotted as the mean ± SD. The 24 MO group plotted in (B) includes all controls of treated mice in Figure 6.7 and Figure 6.8, while panels C and D include additional mice after 6 weeks of treatment that did not have matched baseline and post-treatment measurements. The sample size is 12 for young, 9 for the 24 and 26 MO aged, and 8 for the ELAM group, respectively.

In Figure 6.6, the average response at 50 db was considered in young, 24 MO, and then 6 weeks later either in ELAM-treated mice or age-matched controls. The

magnitude of the young animals photopic b-wave (Figure 6.6A) response was stronger relative to all of the aged mice examined – with and without ELAM.

Due to issues in method development, a smaller group of animals received pre- and post-treatment ERG measurements. The number of animals shown in Figure 6.6 includes all baseline measurements taken at 24 MO and all measurements available at 26 MO regardless of whether a baseline measurement was taken. Thus, the number of biological replicates in Figure 6.7 and Figure 6.8 is lower and only representative of mice with measurements taken at baseline and 6 weeks

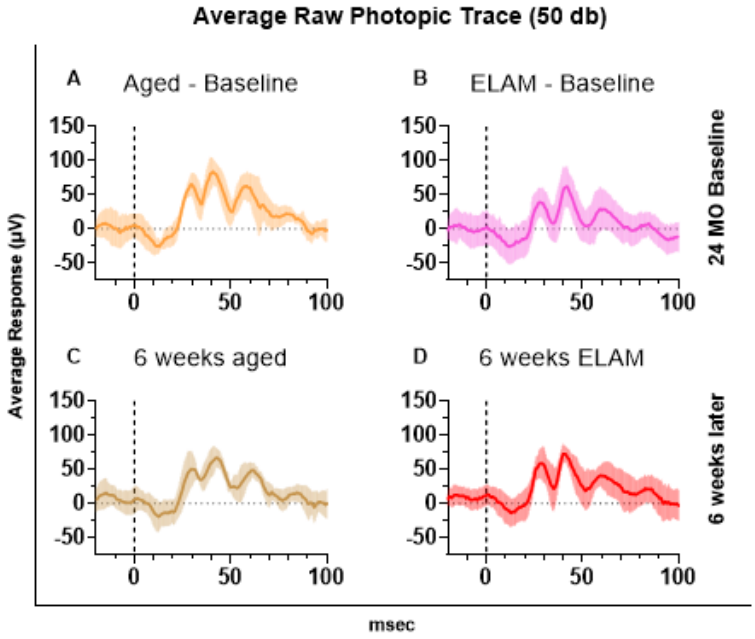

Figure 6.7: Photopic response at baseline and after 6 weeks of ELAM or matched controls.

Photopic vision was measured in the same animals at 24 MO and after 6 weeks of treatment with either ELAM or a control. Taken as an average, the raw response to a 50 db flash did not differ significantly from the control groups baseline (A) to the same mice after 6 weeks (C). Additionally, no obvious change in the response was observed in ELAM-treated mice at baseline (B) compared to 6 weeks of treatment (D). All values are plotted as the mean ± SD. The sample size is 4 for the aged and 5 for the ELAM group.

The same approach was used in mice that had received paired measurements at baseline and after 6 weeks of ELAM or in controls. The average photopic trace to a 50 db flash showed negligible differences in ELAM-treated (Figure 6.7A and B) or matched controls (Figure 6.7C and D). When the b-wave amplitude at each flash intensity considered was averaged for each treatment (Figure 6.7A), the response under photopic conditions had declined significantly by 24 MO under moderate background lights. There was no significant change on average in controls six weeks later.

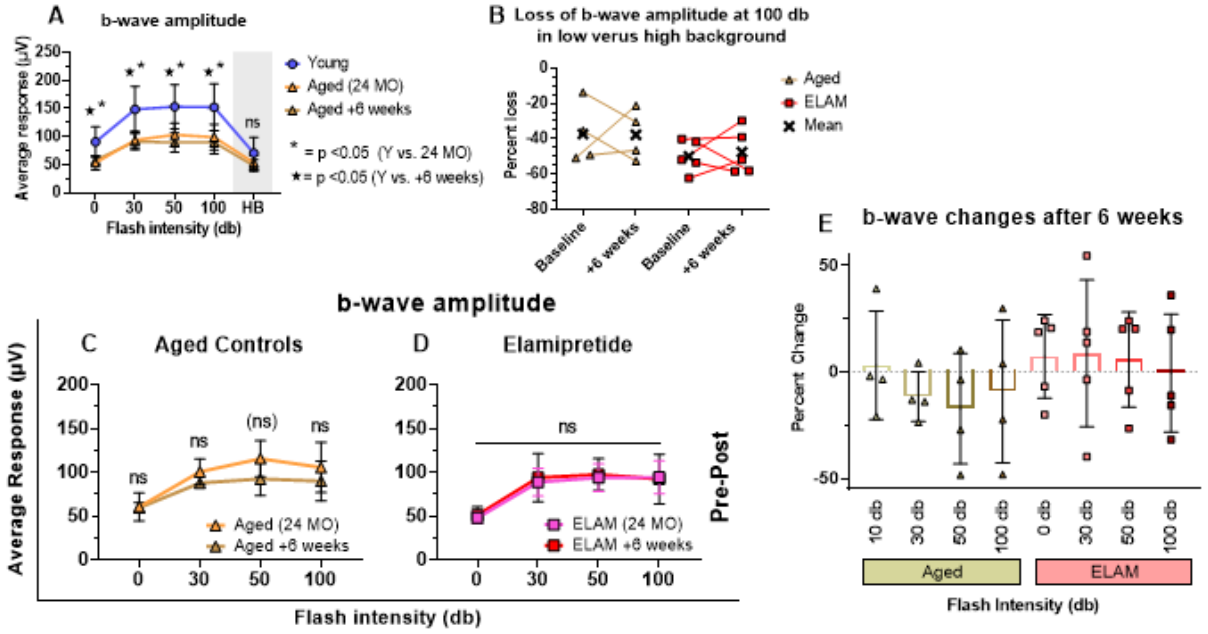

Figure 6.8: The b-wave amplitude is impacted by age and ELAM treatment.

We sought to determine how cone-mediated vision was impacted by aging and ELAM-treatment by examining the amplitude of the b-wave in photopic conditions. The b-wave amplitude declined with age from 0-100 db where the amplitude in both 24 and 26 MO mice (A) was significantly lower than young mice. Upon exposure to the 100 db (High) flash in high background conditions (1000 cd/m^2), both young and aged mice experienced a drop in response (in gray). Panel A includes unmatched animals, thus the sample size is 12 for the young, 9 for the 24 MO and 9 for the 26 MO. When treated with ELAM, no obvious difference in response to this intense light exposure is observed (B). From 0-100 db under moderate photopic conditions (30 cd/m^2) no statistically difference was observed between the aged group at baseline compared to 6 weeks later (C), nor in the same approach for ELAM treatment (D). When the percent change between baseline and 6 weeks after treatment is examined (E), a trend emerged. Controls tended to decrease, while the mice treated with ELAM tended to improve, although the impact of ELAM on photopic vision is modest. All values are plotted as the mean ± SD. The sample size for matched measurements is 4 for the aged and 5 for ELAM. Normality of the data was tested using the Shapiro-Wilk test (α = 0.05). Differences in panel A were tested with 2-way ANOVA followed by Tukey's multiple comparisons test (p <0.05). Statistical significance between paired measurements in Panels C and D was examined using paired t-tests (* = p <0.05) or Wilcoxon matched-pairs signed rank tests (# = p < 0.05, marker of non-significance enclosed in parentheses).

Under a more intense background and with a strong 100 db flash (gray background, Figure 6.8A), we observed no average difference in response associated with aging. Both young and aged animals (At 24 and 26 MO) experienced a percent loss in the b-wave amplitude in response to 100 db flashes under these more intense challenges. After ELAM-treatment, there were indications of improved photopic function relative to controls. Under the more intense background light, the percent loss in b-wave amplitude improved in some animals after 6 weeks of ELAM (Figure 6.8B).

From 0-100 db under moderate background light, we observed a trend towards decreased responses in the control group after 6 weeks (Figure 6.8C). The same trend lower was not seen after ELAM treatment (Figure 6.8D) where the response on average was unmoved after 6 weeks of treatment. These findings are supported by the percent change in the b-wave response at individual flash intensities (Figure 6.8F). After 6 weeks from the baseline measurements, control mice tended to have worse responses and a subset of ELAM-treated mice improved. It is important to consider that the data in Figure 6.8 represents sample sizes of 4 for the aged and 5 for the ELAM group. Although our study is underpowered, this result shows a promising trend that ELAM-treatment could impact photopic circuitry in the eye.

Aging temporal resolution loss is stabilized with ELAM treatment

In addition to the eye's ability to process information in different levels of light, we considered how aging impacts temporal resolution, which can be indicative of the organism's ability to identify and track moving objects (Fleishman et al., 2019; McComb et al., 2010).

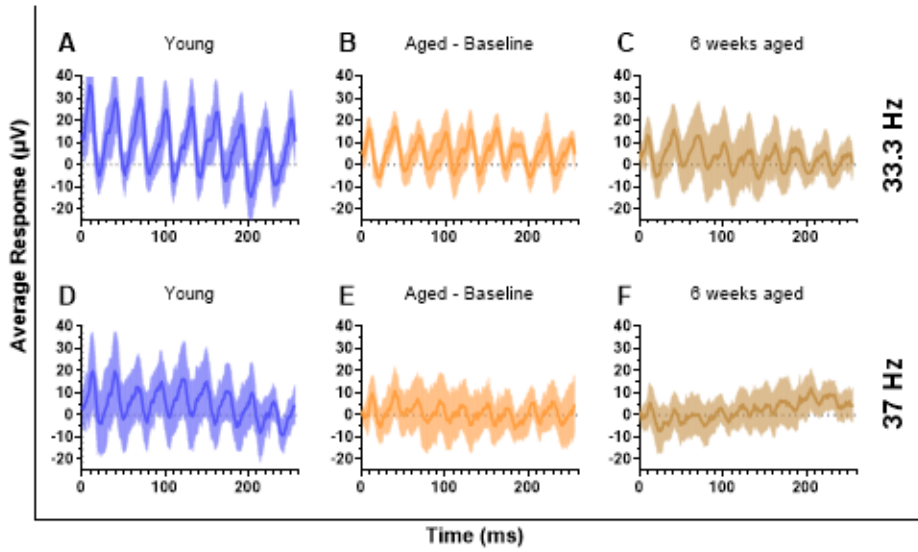

Figure 6.9: Temporal resolution was examined using flicker-fusion ERGs.

The light intensity was maintained at 5 db, while the frequency of the flash was varied between 20-50 Hz. Traces from young, 24 MO, and 26 MO mice at two frequencies are shown at 33.3 Hz in A,B, and C and 37 Hz in D, E, and F. At 33.3 Hz, the periodicity of the response was clearer than with a more rapid flicker

at 37 Hz. Lower amplitudes and less regular responses to the flickering light were seen with increased age, although the difference between 24 and 26 months was subtle at both frequencies. The aged data in B, C, E, and F of this panel is plotted again in Figure 6.10 (33.3 Hz flash) and in Figure 6.11 for (37 Hz flash) for context alongside ELAM treated mice. All values are plotted as the mean ± SD. The sample size is 8 for young, 9 for aged controls, and 9 for the ELAM group.

To test this, we used flicker-fusion ERGs, in which the mouse is anesthetized and the response of the retina is measured. The mouse is shown flickering light that was kept at a constant intensity (5 db) while the frequency of the flash was varied from 20-50 Hz. The animal being unconscious ensured that our measurement was due solely to the visual system rather than changes in behavior that may impact optomotor movement assays used to assess spatial acuity and temporal resolution.

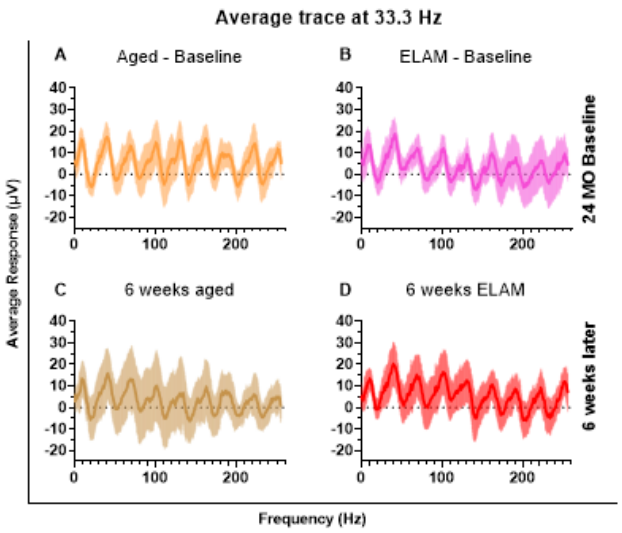

Figure 6.10: Impact of ELAM on flicker-fusion ERG response at 33.3 Hz.

The impact of ELAM on the age-related decline in temporal resolution was examined using 5 db light at 33.33 Hz alongside controls using flicker-fusion ERGs. The periodicity of the response was similar in pre- and post-treatment measurements in both aged controls (A and C) and ELAM-treated mice (B and D). All values are plotted as the mean ± SD. The sample size is 9 for controls and 9 for ELAM groups, respectively.

The raw traces show the response of the young and aged retina to flickering light at 33.3 Hz and at 37 Hz (Figure 6.9). A few trends emerged – the responses at 33.3 Hz displayed more periodicity than those at 37 Hz, which represents a faster rate of flickering and would be more difficult to discern. There appears to be a decline in the strength and periodicity of the response in 24 MO (Figure 6.9B and E) and 26 MO (Figure 6.9C and F) mice relative to the young (Figure 6.9A and D). The same analysis was done in controls and ELAM-treated mice after 6 weeks at 33.3 Hz and 37 Hz. At 33.3 Hz, there was no visually obvious treatment-related differences (Figure 6.10). However, at 37 Hz (Figure 6.11), the change in response varied subtly between the

controls and ELAM-treated mice. In aged controls at 24 MO (A), the response to 37 Hz flashing appeared to be slightly better compared to the 24 MO mice pre-ELAM treatment (B). After 6 weeks, the controls response appeared less regular (C). Although variability was higher, on average, the ELAM treated group had improved relative to baseline after 6 weeks (D).

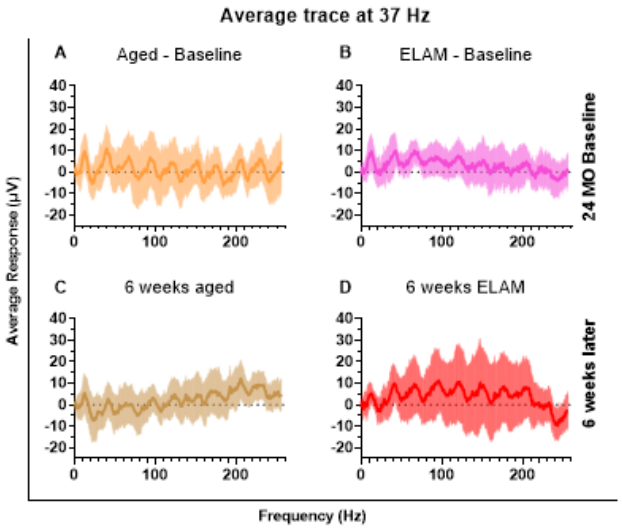

Figure 6.11: Impact of ELAM on flicker-fusion ERG response at 37 Hz.

The impact of ELAM on the age-related decline in temporal resolution was examined using 5 db light at 37 Hz alongside controls using flicker-fusion ERGs. At this higher frequency, the response tended to decline in controls (A) after 6 weeks (C) while in the ELAM group mice, the response from 24 MO (B) appeared to remain consistent or improve slightly after 6 weeks (D). All values are plotted as the mean ± SD. The sample size is 9 for controls and 9 for ELAM groups, respectively.

Drawing a quantitative comparison between the temporal response of young, aged, and ELAM-treated mice was done by applying a Fast Fourier Transform (FFT) to the individual raw responses that are plotted as averages in Figure 6.9, Figure 6.10, and Figure 6.11. The resulting magnitude was considered as an average in each group. A total of 15 frequencies were examined (Figure 6.12A-F) inclusive of 20-50 Hz. Relative to young animals, the FFT magnitude declined significantly by 24 MO.

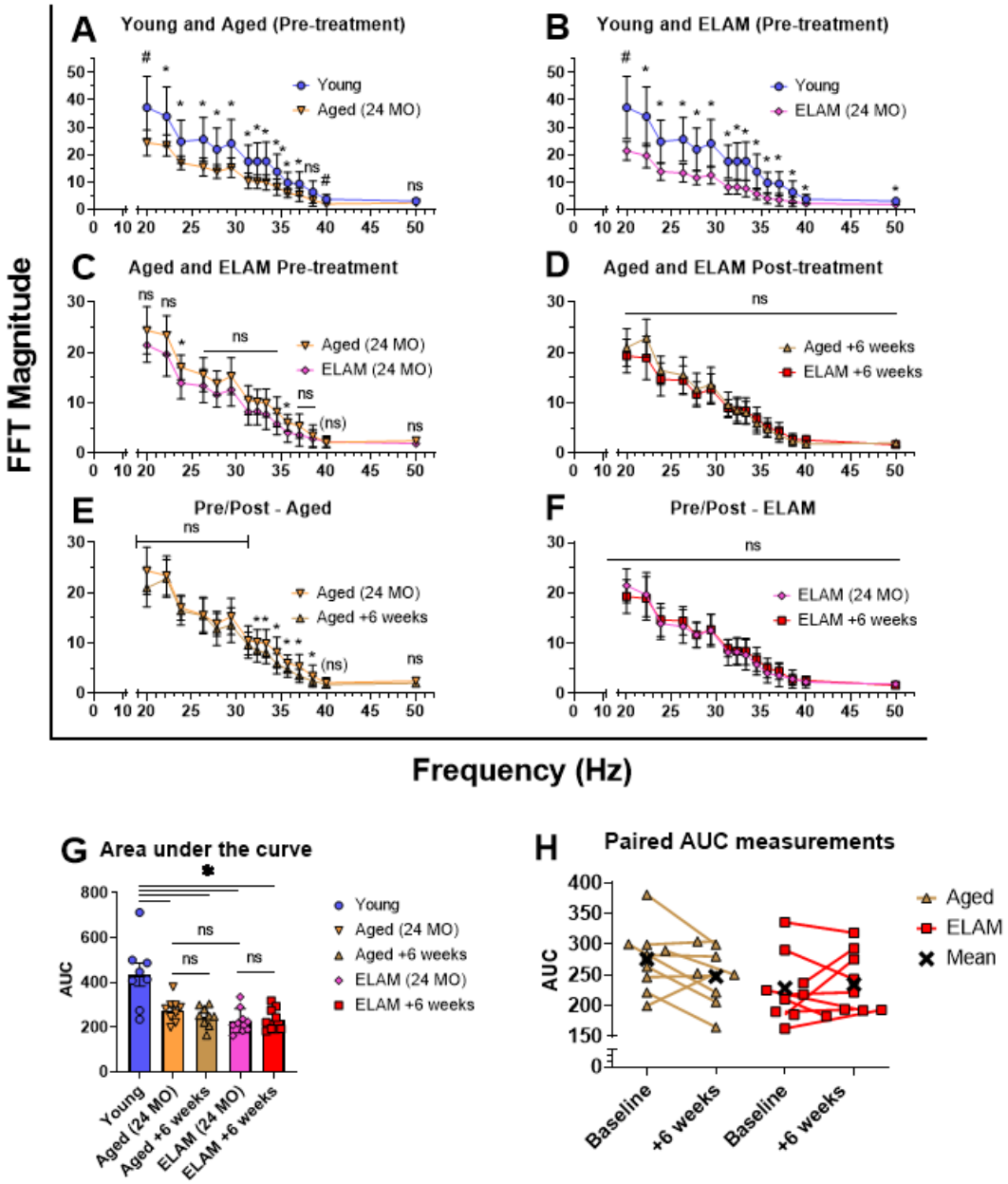

Figure 6.12: The magnitude of responses to flicker-fusion ERGs differed with ELAM.

The magnitude of the response to flickering light was calculated using Fast Fourier Transform on the individual raw responses that were shown as averages for each group in Figure 6.9, Figure 6.10, and Figure 6.11. The magnitude of response to flickering light between 20-50 Hz was plotted in Panels A-F. By 24 MO, the magnitude had declined significantly from 20-37 and 40 Hz (A). Relative to young mice, vision had declined at all measured frequencies by 26 MO (B). At their baseline measurement and 24 MO, the control and ELAM group mice were not significantly different outside of 23.8 and 35.7 Hz (C). After 6 weeks, there was no discernable difference between the control and ELAM group (D). The magnitude after 6 weeks in the control group declines relative to baseline at intermediate frequencies between 32.3-38.5 Hz (E). Surprisingly, no significant decline was seen in the magnitude of the response in the ELAM treated group (F) despite the group beginning treatment with responses that trended lower relative to the control group. The area under the curve (AUC) was taken from 20-50 Hz for each individual

mouse and then averaged (F) to serve as a means of comparing how the response changed overall. The AUC declined in all aged groups, but did not vary significantly on average with ELAM treatment. When we examined the paired pre-treatment AUC in the same mouse 6 weeks later, untreated mice often had declined from their baseline, while ELAM-treated mice often improved or remained stable. All values are plotted as the mean ± SD. The sample size is 8 for young, 9 for aged controls, and 9 for the ELAM group. Normality of the data was tested using the Shapiro-Wilk test ($\alpha = 0.05$). Statistical significance in panels A-F was examined using unpaired t-tests (* = $p < 0.05$) or Mann-Whitney tests (# = $p < 0.05$, marker of non-significance enclosed in parentheses). Differences in Panel E were tested using 1-way ANOVA followed by Tukey's multiple comparisons (* = $p < 0.05$).

We compared the response of the same young animals to the control group at baseline (A) and the ELAM group at baseline (B). The aged baseline was not significantly different at all frequencies except 38.5 and 50 Hz, while the ELAM baseline had declined relative to the young mice at all frequencies examined. Given this difference, we considered whether our control and ELAM cohorts looked differently at baseline (Figure 6.12C). The ELAM group trended slightly lower at several frequencies, but was only significantly different at 23.8 and 35.7 Hz. After 6 weeks, the control group and ELAM-treated groups were not significantly different at any frequency considered. However, when the average measurements are compared in the same groups pre- and post-treatment the aged group had declined from baseline at 32.3-38.5 Hz (Figure 6.12E), while there was no significant drop in the magnitude at any frequency we examined in the ELAM group (Figure 6.12F).

As a proxy for overall temporal resolution, we took the area under the curve (AUC) formed by the magnitudes at each frequency we measured in each animal at baseline and after treatment. On average, the temporal resolution declined in all aged groups relative to young animals, although no significant difference was found between the aged groups regardless of treatment status (Figure 6.12G). If the AUC is compared in the same animals at baseline and after 6 weeks of ELAM or in matched controls, controls tended to decline whereas ELAM-treated mice remained stable or increased (Figure 6.12**H**). We postulate that ELAM slows age-related loss of temporal resolution.

ELAM and NMN have little impact on retinal and eyecup explant metabolism

Both of these therapeutics have been implicated in mitochondrial function through different mechanisms (Birk et al., 2013; Di Stefano and Conforti, 2013; Koch-Nolte et

al., 2011; Mitchell et al., 2020). To probe cellular processes in the eye, two explants were isolated: the retina and the eyecup (Figure 6.13). Both contain a mixture of different cell types. As summarized in Figure 6.1, we examined metabolism in retina and eyecup explants isolated from 25-26 MO mice.

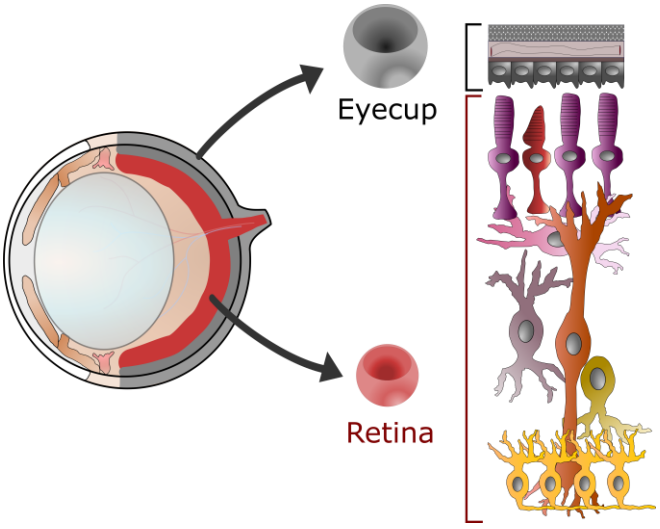

Figure 6.13: Summary of explant composition.

Retina and RPE-choroid-sclera (Eyecup) explants were isolated from untreated young and from aged mice – with or without ELAM or NMN treatment. The retina contains numerous types of neurons and glia. The eyecup includes the monolayer of RPE cells, retinal blood vessels (choroid), and the collagenous and metabolically inert sclera.

The treatment groups included both sexes after 8 weeks of ELAM or NMN treatment alongside controls. No female-treated NMN mice were included in this study. Metabolism was characterized using glucose uptake, glucose flux, and oxygen consumption rate (OCR) with mitochondrial fuels.

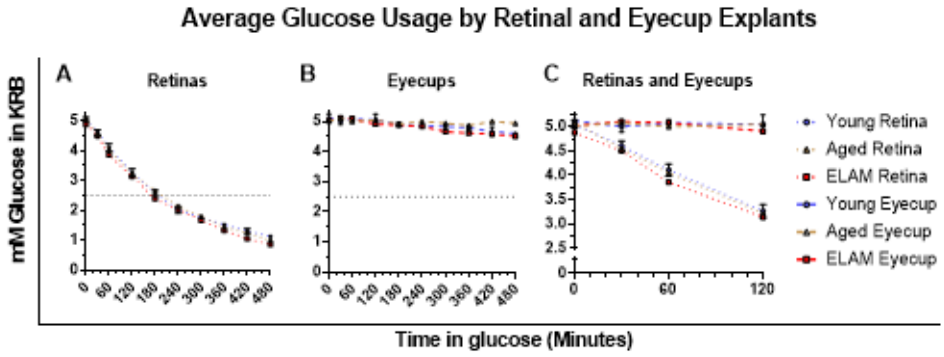

Figure 6.14: Glucose usage by young, aged, and ELAM-treated retinas and eyecups.

Glucose uptake was monitored in retina and eyecup explants *ex vivo* by pooling four of each tissue, incubating in 5 mM glucose, and measuring the concentration with a glucometer across 8 hours. The retinal explants (A) consumed glucose more quickly than eyecups (B), and the difference is visible after

30 minutes (C). There was no significant effect of age or ELAM treatment in either tissue. There were 3 young replicates of each tissue, but only a single attempt at the aged and ELAM-treated groups.

Glucose uptake by pooled samples of retinas or eyecups was measured by monitoring the depletion of glucose with a glucometer over 8 hours (Figure 6.14). Young retinas (A) utilized significantly more glucose - and significantly faster - than their matched eyecups over the same period (B). Half of the glucose in 1 mL of 5 mM glucose was depleted by 4 retinas after 3 hours. The difference between tissues was evident at the 30-minute timepoint (C). After 8 hours, 4 young eyecups had depleted only about 10% of the glucose in the same starting volume. Tissues were isolated from ELAM-treated mice and their controls. There was no obvious differences between young, aged, and ELAM-treated retinas (A). Although aged eyecups appeared to use less glucose by 8 hours (2%) compared to young and ELAM-treated eyecups (about 10% used for both groups), replication of this experiment is necessary. The results in Figure 6.14 are underpowered with samples sizes of 3 for young and 1 for aged and ELAM-treated tissues.

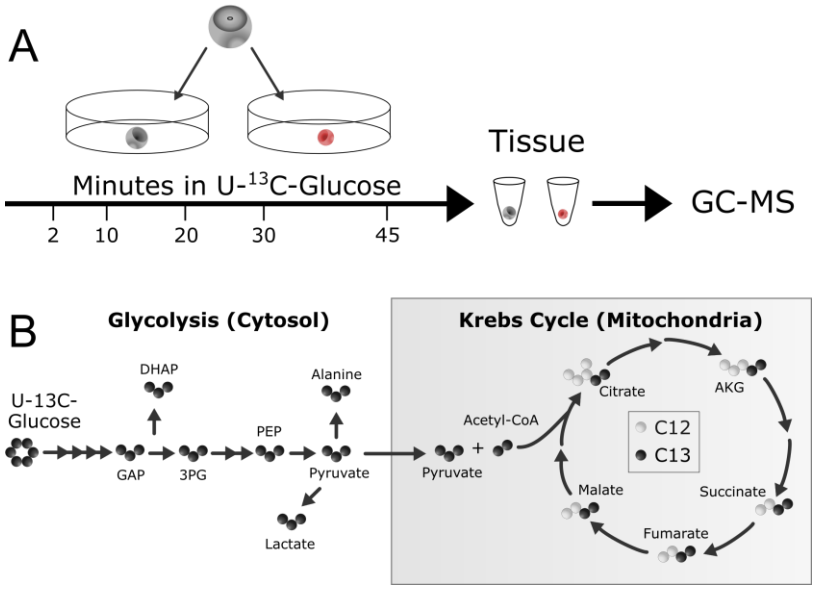

Figure 6.15: Metabolic flux experimental design and paths of ^{13}C tracer

The approach to characterizing glucose metabolism in the retina and eyecup included five incubation times and quantitation of glycolytic and Krebs cycle intermediates by GC-MS (A). The dominant path that carbons from U-^{13}C-glucose may take through glycolysis and the Krebs Cycle are summarized in Panel B. Only the main metabolites and their reactions are listed here.

Glucose metabolism is critical to the function of the eye. While we observed no significant difference in the uptake of glucose in a pilot study, we wanted to determine if the way these tissues utilized the glucose they consumed changed with age or ELAM-treatment. Retinal and eyecup explants were incubated with a heavy labeled tracer

(Figure 6.15A). The tracer, U-^{13}C-glucose, contains ^{13}C rather than ^{12}C in all 6 carbons of glucose that can be tracked upon incorporation into downstream molecules (Figure 6.15B). By quantifying these isotopologues containing ^{13}C using GC-MS, differences in metabolism can be quantified across treatment groups and compared between tissues. The incubation duration was varied to examine flux over time and included 2, 10, 20, 30, and 45 minutes in males, and only 2 minutes in females. We considered the pool size and quantity of labeled isotopologue at each timepoint in young, aged, and ELAM or NMN-treated animals.

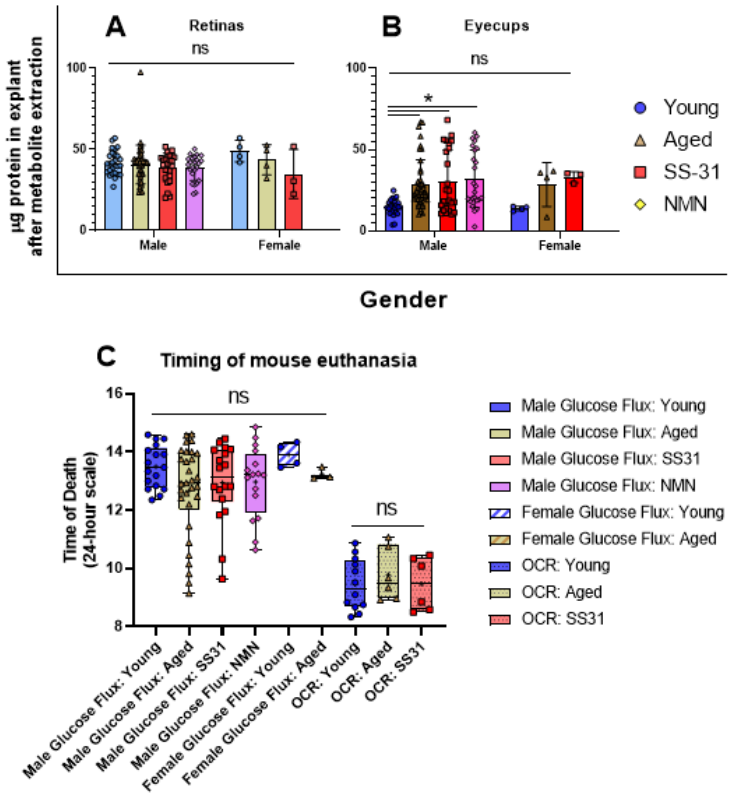

Figure 6.16: Quality control in flux and OCR experiments.

Timing of euthanasia and quantity of tissue were considered. In retinal explants for flux, there was no change in total protein content (A). In eyecups, there was a significant increase in protein with age (B). This was found to be due to differences between the individuals isolating tissues and controlled for by normalizing to protein. No difference was seen in female tissues. Time of death was different for mice used in flux and OCR (not shown), but there was no age-related effect (C). All values are plotted as the mean ± SD. Sample size varies from 3 to 43 depending on treatment group, assay, and sex of the mouse. Normality of the data was tested using the Shapiro-Wilk test ($\alpha = 0.05$). Statistical significance was examined using Kruskal-Wallis test followed by Dunn's multiple comparisons test (* = $p < 0.05$).

As a loss of proteostasis is a known hallmark of aging, we normalized all metabolite measurements to the total protein content in each explant. Although we found no age-related differences in retinal explants (Figure 6.16A), there was an increase in the aged, ELAM-treated and NMN-treated eyecup explants relative to the young (Figure 6.16B). A subset of eyecup samples with higher protein content were isolated by a different individual, and likely reflect a difference in mechanical isolation of the tissue rather than

an age-related change. Most samples were collected during the same approximately two-hour window on different days, but there was no change in the average collection time of samples between groups for each approach (Figure 6.16).

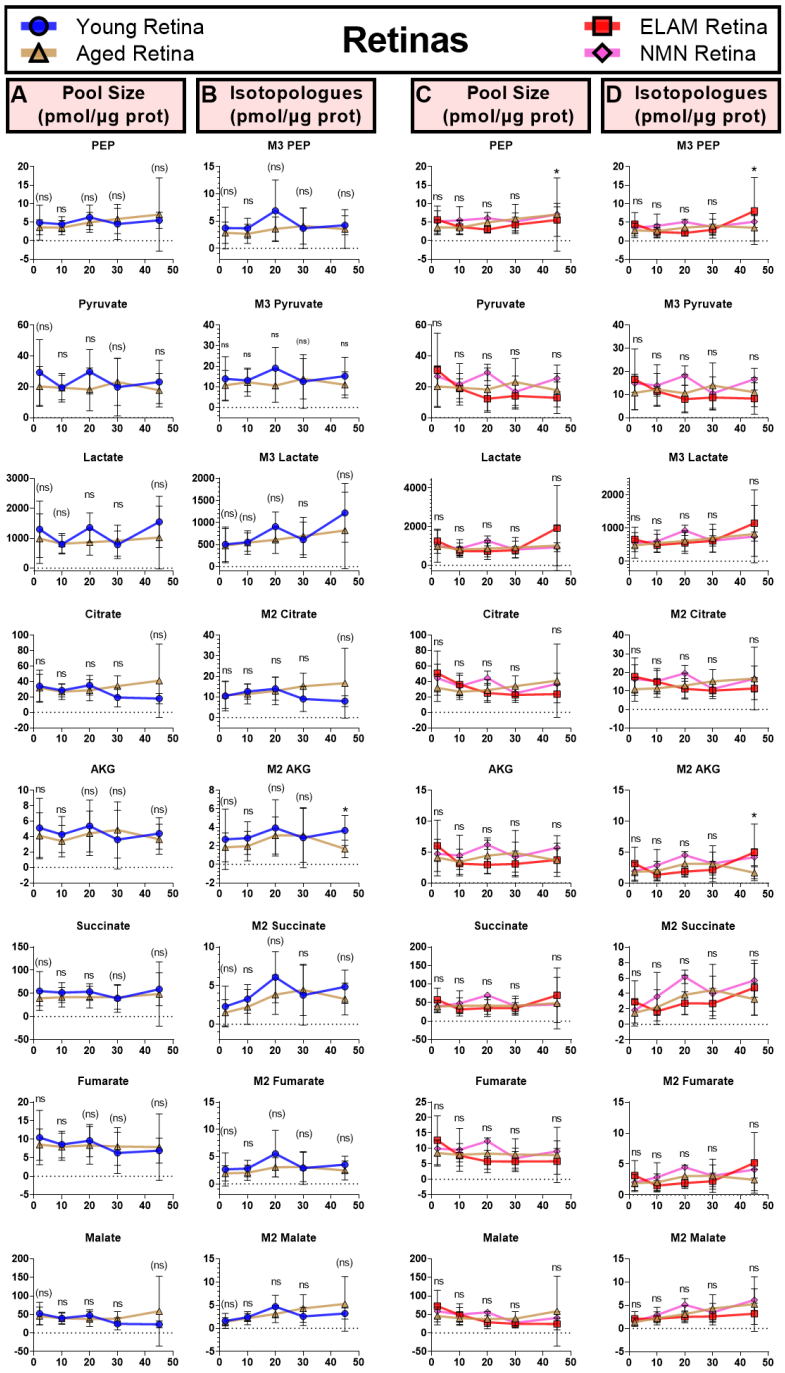

Figure 6.17: Measuring glucose flux in retinas.

Retina glucose flux in glycolysis and the Krebs cycle was quantified by measuring the incorporation of ^{13}C from U-^{13}C-glucose by GC-MS. The difference between young and aged retinas was minimal in terms of pool size (A) and labeled isotopologues (B). When aged mice were treated with ELAM or NMN, there was no consistent and significant alteration in pool size (C) or labeled isotopologues (D) relative to controls. All values are plotted as the mean ± SD. The sample size varied from 3-9 depending on the timepoint, age, and treatment group. These sample sizes and results take into account outliers that were removed from some metabolites using Grubb's test ($p < 0.05$). One sample was removed from young retinas at 20 minutes, and one from ELAM-treated retinas at 45 minutes. Normality of the data was tested using the Shapiro-Wilk test ($\alpha = 0.05$). Statistical significance in columns A and B was examined using unpaired t-tests (* = $p < 0.05$) or Mann-Whitney tests (# = $p < 0.05$, marker of non-significance enclosed in parentheses). Differences between aged controls and NMN (★ = $p < 0.05$), or between aged controls and ELAM (* = $p < 0.05$) in columns C and D were tested using 2-way ANOVA followed by Dunnett's multiple comparisons test.

The metabolism of the neural retina as measured by our *ex vivo* approach was essentially unaffected by the age of the mouse. We could not identify any consistent and significant changes in pool size Figure 6.17A) or the quantity of ^{13}C-labeled isotopologues (Figure 6.17B) of glycolytic and Krebs cycle intermediates. The aged retina retained a surprising degree of metabolic capability with age as measured in this *ex vivo* approach. Given their proposed impacts on vision and metabolism, retinas were also isolated from aged animals treated for 8 weeks with ELAM or NMN. Both drugs had negligible impact on metabolism in terms of pool size and the quantity of ^{13}C-labeled isotopologues (Figure 6.17C and D) in glycolytic and the Krebs cycle.

Surprisingly, similar trends were observed in eyecups. There were no consistent age-related changes in glycolytic or Krebs cycle intermediate pool sizes (Figure 6.18A) or ^{13}C-labeled isotopologues (Figure 6.18B) in eyecups. Despite a generally increased reliance on their mitochondria relative to the retina in young animals, ELAM and NMN did not induce any consistent and significant metabolic alteration in aged eyecups (Figure 6.18C and D).

Although sample size was limited, we also considered whether sex could differentially impact the metabolic processes in aging and whether ELAM would have any effect. A 2-minute incubation time thought to reflect *in vivo* metabolism most closely was used Figure **6.19**). Similar to our findings in males, we did not observe any age-related changes in female pool size in retinas (A) or eyecups (C). The same trend held in the resulting ^{13}C-labeled isotopologues in retinas (B) and eyecups (D). There was also no significant sex-related difference between young and aged mice in glycolysis or the Krebs cycle. The only statistically significant differences we observed were between male and female ELAM-treated mice in pyruvate, citrate, and malate. It will be critical in future studies to increase the sampling of female mice to determine if the trends observed with ELAM treatment are consistent or due to under-sampling.

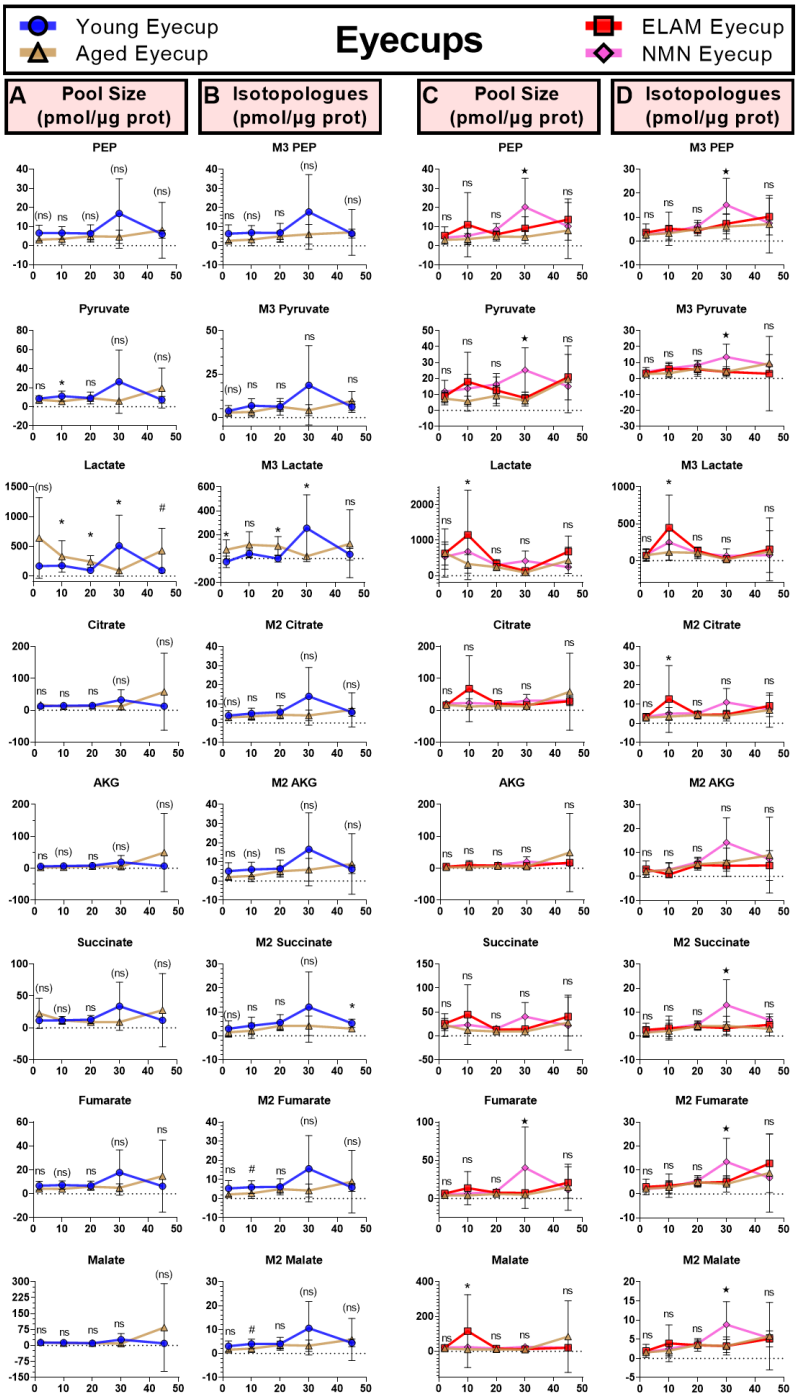

Figure 6.18: Measuring glucose flux in eyecups.

Eyecup glucose flux in glycolysis and the Krebs cycle was quantified by measuring the incorporation of ^{13}C from U-^{13}C-glucose by GC-MS. The difference between young and aged retinas was minimal in terms of pool size (A) and labeled isotopologues (B). When aged mice were treated with ELAM or NMN, there was no consistent and significant alteration in pool size (C) or labeled isotopologues (D) relative to controls. All values are plotted as the mean ± SD. Sample size varied from 3-9 depending on timepoint, age, and treatment group. These sample sizes and results take into account outliers that were removed from some metabolites using Grubb's test ($p < 0.05$). One sample was removed from aged eyecups at 30 minutes, and two total from ELAM-treated eyecups - one at 30 and one at 45 minutes. Normality was tested using the Shapiro-Wilk test. Statistical significance in columns A and B was examined using unpaired t-tests (* = $p < 0.05$) or Mann-Whitney tests (# = $p < 0.05$, marker of non-significance enclosed in parentheses). Differences between aged controls and NMN (★ = $p < 0.05$), or between aged controls and ELAM (* = $p < 0.05$) in columns C and D were tested using 2-way ANOVA followed by Dunnett's multiple comparisons test.

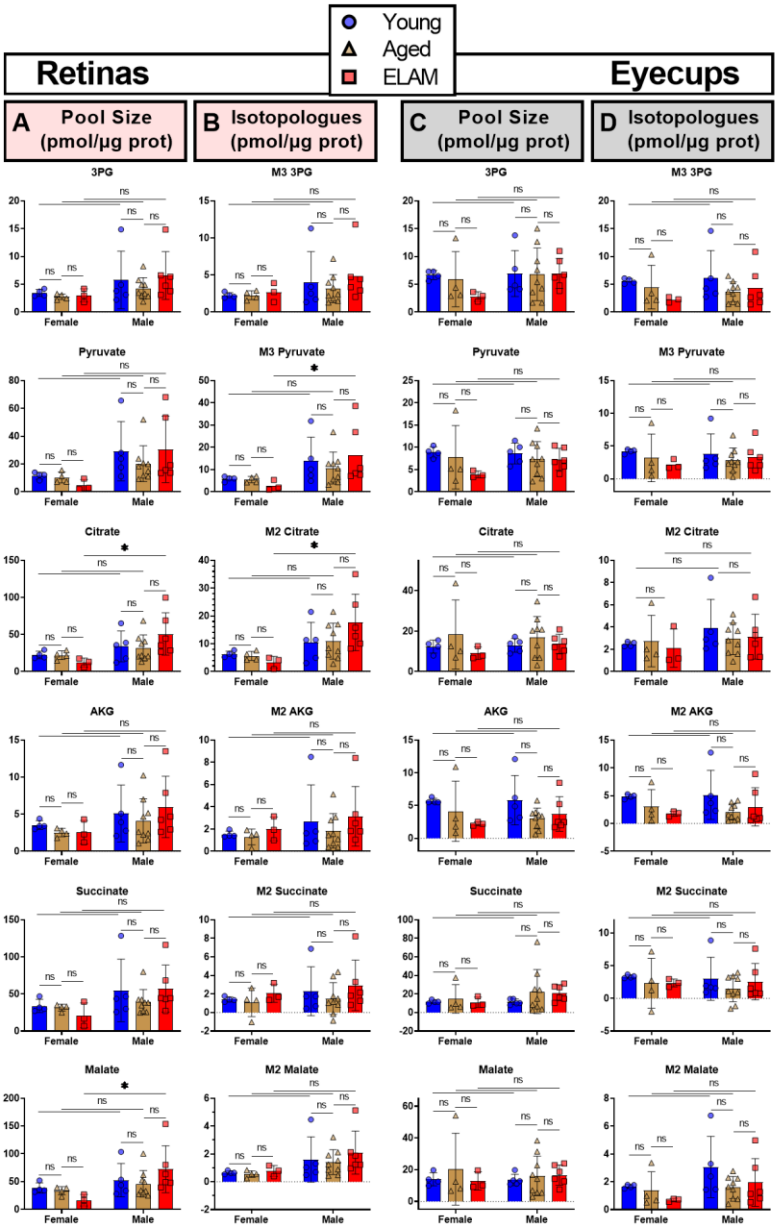

Figure 6.19: Impact of sex on glucose metabolism.

Sex-related changes were examined using a U-^{13}C-glucose tracer in female mice. Samples were collected at different times but were processed in tandem with the male samples. Note that the male data in this figure is the same young, aged, and ELAM data included in Figure 6.17 and Figure 6.18. All values are plotted as the mean ± SD. The sample size varied from 3-9 depending on the timepoint, age, and treatment group. Normality of the data was tested using the Shapiro-Wilk test ($\alpha = 0.05$). Statistical significance was examined using Kruskal-Wallis test followed by Dunn's multiple comparisons test.

Since ELAM is thought to impact the mitochondria, we measured mitochondrial function more directly using glutamine and succinate. Both are mitochondrial fuels metabolized by the RPE (Bisbach et al., 2020; Du et al., 2016b). We measured the OCR of live retinas and eyecups in a continuous perifusion system (Figure 6.20). The tissues were isolated from young, aged, and ELAM-treated male mice in tandem during three experiments run on three different days. The explants were provided 5 mM glucose, glucose with 5 mM succinate, glucose alone, glucose with 5 mM glutamine, and finally

returned to glucose alone (A). The trace over the entire experiment is presented as the nmol O_2/explant/minute after subtraction of the baseline glucose OCR (measured from -30 to 0 minutes) in Figure 6.20A, D, and G. The maximum OCR in Figure 6.20B-C, E-F, and H-I after subtraction of the basal glucose OCR in the preceding glucose-only gradient. The basal OCR values are listed in Table 6.1 before baseline subtraction.

Table 6.1: Average basal *ex vivo* O_2 consumption in young, aged and ELAM-treated retina and eyecups

Tissue	Age	n	Basal O_2 consumption*	Max O_2 consumption with succinate†	Basal O_2 after succinate #	Max O_2 consumption with glutamine‡
Retina	Young	6	1.90 ± 0.4	2.04 ± 0.4	1.9 ± 0.5	1.99 ± 0.5
	Aged	3	2.14 ± 0.4	2.34 ± 0.4	2.15 ± 0.5	2.27 ± 0.5
	ELAM	3	1.89 ± 0.6	2.02 ± 0.5	1.83 ± 0.5	1.83 ± 0.5
Eyecup	Young	6	0.52 ± 0.3	1.62 ± 0.3	0.47 ± 0.3	0.57 ± 0.4
	Aged	3	0.56 ± 0.2	1.85 ± 0.2	0.50 ± 0.2	0.55 ± 0.2
	ELAM	3	0.61 ± 0.3	1.92 ± 0.2	0.56 ± 0.3	0.68 ± 0.3

* Basal nmol O_2/min ± SD in glucose alone measured between -30 and 0 minutes

† Maximum basal nmol O_2/min ± SD with succinate was measured between 20 and 45 minutes

Basal nmol O_2/min ± SD in glucose alone between 80 and 90 minutes after succinate, but before addition of glutamine where OCR was stable

‡ Maximum basal nmol O_2/min ± SD with glutamine was measured between 120 and 135 minutes

There were clear differences between the retina and eyecup response to succinate. The eyecup OCR was increased relative to the retina, which has been described previously (Bisbach et al., 2020). To quantify any age-related changes, we took the average maximum OCR of the tissue with either mitochondrial fuel. No significant effect of age was seen in OCR with succinate or glutamine (C).

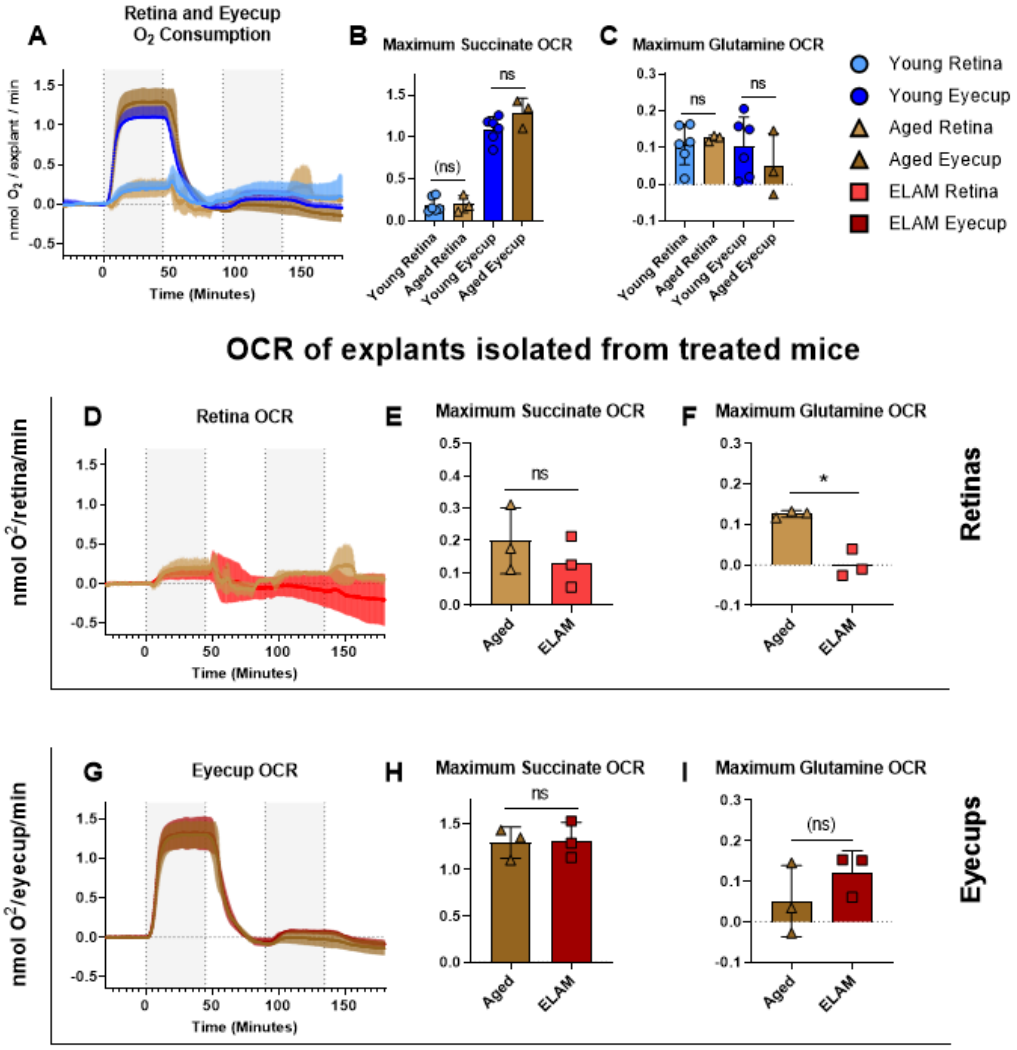

Figure 6.20: Oxygen consumption measurements in young, aged, and ELAM-treated retinas and eyecups.

The effect of age on oxygen consumption rate (OCR) in retinas and eyecups was measured in 5 mM glucose upon addition of 5 mM succinate (first gray section), and 5 mM glutamine (second gray section) in a perifusion apparatus (A). Young, aged, and ELAM groups were run in parallel, but are plotted separately for clarity. The maximum OCR with either mitochondrial fuel was calculated by subtracting the glucose-only OCR preceding it. There was no effect of age in either tissue on maximum succinate OCR (B), nor in maximum glutamine OCR (C). Retina (D) and eyecup (G) explants were isolated from 26 MO controls and after 8 weeks of ELAM treatment, OCR was measured with succinate and glutamine. No significant effect on maximum succinate OCR (E) was seen, although maximum glutamine OCR (F) declined with ELAM treatment. Maximum succinate (H) and glutamine (I) maximum OCR were not significantly impacted by ELAM. All values are plotted as the mean ± SD. The sample size is 6 for young, 3 for aged controls, and 3 for the ELAM group. Normality of the data was tested using the Shapiro-Wilk test (α = 0.05). Statistical significance was examined between ages and treatments using unpaired t-tests (* = p <0.05) or Mann-Whitney tests (# = p < 0.05, marker of non-significance enclosed in parentheses).

In tissues isolated from ELAM-treated mice, we did not observe any statistically significant age-related change in OCR in response to succinate or glutamine in eyecups (Figure 6.20G, H and I). In retinas, although we observed no significant change in succinate-driven OCR (Figure 6.20D and E), the maximum OCR with glutamine supplementation was significantly declined relative to aged controls (Figure 6.20F). One limitation to this result is that the tissues were not allowed to fully equilibrate in 5 mM glucose after succinate removal prior to the addition of glutamine.

Discussion

ELAM and ELAM+NMN may slow age-related vision loss

Previous studies of ELAM and NMN suggest these therapeutics can reduce the progression of vision loss in aging or models of degeneration (Alam et al., 2015; Lin et al., 2016; Mills et al., 2016; Wu et al., 2019). ELAM has been considered as a treatment for AMD (Samanta et al., 2021), which has few treatment options that are highly dependent upon the form and stage of the disease (Ambati and Fowler, 2012). In this study, we considered how ELAM alone or ELAM+NMN impacted age-related decline of the visual system.

Scotopic and photopic electroretinograms (ERGs) have been shown to decline with age in mice and humans (Freund et al., 2011; Kergoat et al., 2001; Kolesnikov et al., 2010; Wang et al., 2018). We found small improvements by ERG in temporal resolution, scotopic function, and photopic function. ELAM alone could maintain or modestly improve the a-wave and b-wave amplitude after 6 weeks. Temporal resolution was maintained relative to age-matched controls that tended to decline during the same time period. We were only able to measure the impact of 6 weeks of ELAM+NMN on scotopic vision, where we found that the a-wave amplitude was increased on average relative to controls. Interestingly, in the pre-treatment and post-treatment measurements used for both ELAM+NMN and ELAM, there seemed to be mice that responded positively to treatment, while others did not. Increasing the sample size of these ERG

assays will be crucial to determine if the observed effects reflect a consistent result of ELAM+NMN or ELAM treatment.

ELAM and NMN have negligible impact on retina and eyecup metabolism

Despite a modest reduction in age-related visual decline, the metabolism of two ocular tissues directly required for phototransduction (retina and eyecup containing RPE) was almost entirely unaffected by the mitochondrially-targeted NMN or ELAM.

Early characterizations of ELAM in the context of mitochondria suggested that the tetrapeptide has antioxidant activity and can interact with cardiolipin (Birk et al., 2014; Zhao et al., 2004). Mitochondrial function and metabolism are critical for a functional visual response (Eells, 2019; Winkler, 1981). The only significant metabolic change with 8 weeks of ELAM was seen in the OCR of retinas provided glutamine. Relative to aged controls, OCR of retinas isolated from ELAM-treated mice was lower in response to glutamine supplementation. Characterizing this drop in glutamine metabolism caused by ELAM will require increasing sample size and expanding our experimental approach. To clarify where this metabolic change has happened in glutamine metabolism, the metabolic flux approach we employed to study glucose can also be used to characterize glutamine anaplerosis and reductive carboxylation (Du et al., 2016b) Additionally, the activity of specific enzymes in glutamine metabolism such as glutaminase, glutamine synthetase, and branched-chain amino acid aminotransferases can be probed with activity assays (Mongin et al., 2011; Shinnick and Harper, 1976). While these results may suggest that glutamine metabolism is altered with ELAM treatment, it may also be indicative of non-mitochondrial effects. Synaptic transmission in neurons is linked to glutamine metabolism through the neurotransmitter glutamate (Hamberger et al., 1979), which can be synthesized from glutamine (Chaudhry et al., 2002). It is possible that neurotransmitter cycling may be impacted by ELAM, which could explain the small improvement in vision with minimal effects on mitochondria and metabolism.

The generally null metabolic finding of NMN and ELAM administration this study could be due to a combination of several factors. This group has found that retina and

eyecups are metabolically stable with age when examined *ex vivo*. This could be an artifact of our *ex vivo* approach. An *in vivo* infusion of labeled tracer into the damaged environment of the eye may highlight age-related deficiencies. However, it could also indicate that metabolism may not be the ideal target for improving age-related dysfunction in the eye. Specific cell types in the retina could be differentially impacted by NMN and ELAM. The approaches taken here do not allow us to distinguish cell-type metabolic state. In particular, cones comprise about 3% of the total photoreceptors in mouse retina (Carter-Dawson and LaVail, 1979) which contains numerous other cell types. Thus, these cells are uniquely challenging to examine in a wild-type, non-transgenic, aged mouse model. If cone metabolism were impacted by either drug and led to the modest improvement in photopic function seen here, our approach lacks cell-type-specific resolution. The steady-state metabolism of other tissues in the eye are altered with aging (Wang et al., 2018) and may better reflect the activities of NMN and ELAM. Finally, although the majority of metabolomics samples were collected during the early to mid-afternoon, it will be important to consider whether a particular time of day – when RPE phagocytoses photoreceptor outer segments at light onset (Strauss, 2005) – may reveal age-related differences in metabolism.

Considerations for future studies with NMN

NAD+ metabolism is entwined with mitochondrial function. Although NAD+ levels tend to decline with age, restoration with NMN has been shown to improve vision (McReynolds et al., 2020; Mills et al., 2016; Prolla and Denu, 2014; Son et al., 2016; Verdin, 2015; Whitson et al., 2020). Unfortunately, we were unable to characterize visual function of aged mice after NMN administration, and we observed no change in retina and eyecup glucose metabolism. However, it is important to note that the glucose metabolism of these tissues appear to be nearly unaffected by aging. Although glucose metabolism represents an important but limited view of metabolism, that is not the primary target of NMN and NAD+ metabolism. NMN administration can impact redox state, which is known to be altered in the aging eye (Rebrin et al., 2003). Future studies considering how redox state in the eye impacts visual function – and whether NMN can ameliorate that defect – will be crucial.

Considerations for future studies with ELAM

Alternative mechanisms of ELAM outside of metabolism should be considered. Under the conditions we tested, we saw no changes in glucose uptake, glycolysis, the Krebs cycle, or OCR with succinate. Recent publications have found very diverse phenotypic changes in ELAM treated mice. In 26 MO mouse kidneys treated late in life with ELAM, levels of senescence markers were decreased, and cellular integrity was improved (Sweetwyne et al., 2017). In a model of hypertension treated by ELAM, changes in the transcription factor PGC-1α and its downstream effectors were down-regulated (Dai et al., 2011). This could speak to substantial changes in cellular signaling. After two weeks of ELAM treatment, cerebral microvasculature and neurovascular coupling responses were improved in aged mice by dilation of microvessels (Tarantini et al., 2018).

ELAM and the other SS peptides were derived after many synthetic iterations from dermorphin, a heptapeptide with potent opioid activity first isolated in Phyllomedusa sauvagei (Schiller et al., 1989). A more recent precursor to the SS peptides, DALDA, exhibited stable, specific μ-opioid receptor activity with low blood-brain barrier (BBB) permeability (Schiller et al., 2000; Zhao et al., 2003). ELAM can cross the BBB after intraperitoneal injection (Hemachandra Reddy et al., 2017). If ELAM retained μ-opioid activity, that interaction could play a role in the changes observed by our group and by others. In the visual system, ELAM can alter ganglion cell function (Cleymaet et al., 2019) and improved outcomes after ischemia (Husain et al., 2012, 2009). Administration of μ-opioids impacted vasodilation in the eye (Someya et al., 2018, 2017). It has been shown that blood vessel function around the retina degrades (Lin et al., 2019; Orlov et al., 2019; Wei et al., 2017) and oxygen penetrance is lower (Bata et al., 2019) in aging people. Improvement of the vasculature around the retina would improve nutrient availability and could explain our finding of improved outcomes in the function of the aging visual system without an obvious *ex vivo* metabolic phenotype.

Materials & Methods

Mouse husbandry

C57Bl/6J mice of both genders were used in metabolic flux studies, but only males were used for ERGs. Young male mice were either purchased from Jackson Laboratories (Bar Harbor, ME) or acquired from the NIA aged rodent colony housed at Charles River Laboratories. Aged male mice were sourced from the NIA colony as part of existing aging studies (Whitson et al., 2020). Young female mice were purchased from Jackson Laboratories. Aged female mice were either purchased from Jackson Laboratories and aged to 23 MO or older, or acquired from the NIA colony as part of existing aging studies (Campbell et al., 2019; Zhang et al., 2020).

Administration of NMN and Elamipretide

The mice used in this study dosed with nicotinamide mononucleotide (NMN), Elamipretide (ELAM), the two drugs in combination, or their respective controls were part of other studies (Campbell et al., 2019; Whitson et al., 2020; Zhang et al., 2020). All treatments were 8 weeks in duration beginning at 24 MO and concluding at 26 MO with euthanasia by cervical dislocation (Figure 6.1).

As part of this another study (Whitson et al., 2020), the Imai laboratory at Washington University in St. Louis, MO provided the NMN. Administration was performed through ad libitum access to only NMN-spiked drinking water with a dose of 300 mg/kg body weight/day. This dosing was tailored to each cage by varying the concentration of NMN in water based on an individual cage's measured water consumption rate and the mean body weight of the mice. NMN has been found to be stable in room temperature water for at least 1 week (Mills et al., 2016). Thus, the NMN-dosed water was replaced every 3-7 days.

Mice treated with ELAM were used in other studies (Campbell et al., 2019; Whitson et al., 2020; Zhang et al., 2020), but all 3 applied the same dosing scheme and length. Stealth BioTherapeutics (Newton, MA) provided the ELAM for this work free of charge,

and played no role in the funding, experimental design, data collection or authorship of the research. The ELAM dose was 3 mg/kg body weight/day through AZLET osmotic minipumps (Cupertino, CA) for a total of 8 weeks. After 4 weeks, the first minipump was surgically removed and a second, new minipump was implanted to complete ELAM administration for the final 4 weeks. Due to experiments unrelated to the eye that necessitated compatibility with magnetic resonance spectroscopy, some of the osmotic minipumps were modified by replacing the metal stems with PEEK tubing according to the manufacturer's instructions.

Animals treated with a combination of NMN and ELAM (ELAM+NMN) were simultaneously provided NMN by water bottle as described above, and ELAM was administered by osmotic minipumps.

The single control group described in this work represents three different controls where no significant differences were found: untreated mice, mice treated with osmotic minipumps containing saline to control for ELAM, and mice who were provided ad libitum access to water in a bottle instead of system water to control for NMN. No significant differences were found between mice treated with osmotic minipumps containing saline and mice who were provided ad libitum access to water in a bottle when cardiac function was examined (Whitson et al., 2020). We also found no differences in glucose metabolism (Figure 6.2).

Scotopic ERGs

Prior to any scotopic experiments, mice were dark-adapted overnight, and electrodes placed with night vision goggles under infrared light. Mice were anesthetized with isoflurane, and eyes dilated with 2.5 % phenylephrine (Akorn, Inc; NDC 174780201-15) and 1% tropicamide (Bauch + Lomb; NDC 24208-585-64). Gold electrodes were placed on each cornea. A reference and ground electrode were positioned on the back of the head. Mice were placed inside a UTAS Visual Diagnostic System with BigShot Ganzfeld with UBA-4200 amplifier (LKC Technologies; Gaithersburg, MD). Recordings were elicited using flashes of LED white light at increasing flash intensities with two-minute

pauses between individual flashes under scotopic (-50 to 50 dB) conditions. Readings were calibrated such that 0 db = 2.5 cd*s/m^2. The a-wave amplitude was measured 8 ms after flash stimulus. Readings were taken from both eyes whenever possible and examined as an average of both eyes. If the reading from one eye was not viable due to difficulty with electrode placement, the eye with the best response was analyzed.

Photopic ERGs

In photopic experiments that followed scotopic experiments, mice were permitted to acclimate to light prior to beginning measurements. Mice were anesthetized with isoflurane, and eyes dilated with 2.5 % phenylephrine (Akorn, Inc; NDC 174780201-15) and 1% tropicamide (Bauch + Lomb; NDC 24208-585-64). Gold electrodes were placed on each cornea. A reference and ground electrode were positioned on the back of the head either with night vision goggles under infrared light when done following a scotopic experiment, or in ambient light. Mice were placed inside a UTAS Visual Diagnostic System with BigShot Ganzfeld with UBA-4200 amplifier (LKC Technologies; Gaithersburg, MD). Recordings were elicited using flashes of LED white light at increasing flash intensities with two-minute pauses between individual flashes under photopic (0 to 100 dB flashes, 30 cd/m^2 background light) conditions. Readings were calibrated such that 0 db = 2.5 cd*s/m^2. b-wave amplitude was measured as the magnitude from the a-wave minimum to the b-wave maximum. Readings were taken from both eyes whenever possible and examined as an average of both eyes. If the reading from one eye was not viable due to difficulty with electrode placement, the eye with the best response was analyzed.

Flicker-Fusion ERGs

In photopic experiments that followed scotopic experiments, mice were permitted to acclimate to light prior to beginning measurements. Mice were anesthetized with isoflurane, and eyes dilated with 2.5 % phenylephrine (Akorn, Inc; NDC 174780201-15) and 1% tropicamide (Bauch + Lomb; NDC 24208-585-64). Gold electrodes were placed on each cornea. A reference and ground electrode were positioned on the back of the head either with night vision goggles under infrared light when done following a scotopic

experiment, or in ambient light. Mice were placed inside a UTAS Visual Diagnostic System with BigShot Ganzfeld with UBA-4200 amplifier (LKC Technologies; Gaithersburg, MD). Readings were calibrated such that 0 db = 2.5 cd*s/m^2.

Temporal resolution was measured using a 5 db flash of varied frequencies (20-50 Hz) under photopic conditions. Ten second pauses were taken between frequencies and repeated 9 times each. Measurements were taken at 0.5 s intervals for a total of 512 points in 0.255 s (sampling frequency = 2003.91 samples/s). Readings were taken from both eyes whenever possible and examined as an average of both eyes. If the reading from one eye was not viable due to difficulty with electrode placement, the eye with the best response was analyzed. At each frequency, replicates were averaged. Figure 6.9, Figure 6.10, and Figure 6.11 show examples of these raw values at 33.3 and 37 Hz. A waveform was generated, and the magnitude calculated using Fast Fourier Transform (Microsoft Excel Data Analysis ToolPak). The sampling frequency was 2003.9 samples/s and the step value was 3.91.

Isolation of retinas and eyecups

Animals were euthanized by awake cervical dislocation. Eyes were enucleated with curved forceps and cleared of attached hair, muscle, connective and adipose tissue. The globe was punctured with a 20-24 gauge needle just above the ora serrata. The cornea, iris and lens were removed. The opened globe was placed back into fresh HBSS. The retina was carefully separated from the RPE-choroid-sclera complex (eyecup). The inside of the eyecup was verified to be free of visible pieces of retina. If still attached, the optic nerve was removed from the eyecup. The separated tissues were then placed in metabolic flux medium (Krebs Ringer Buffer plus added metabolites) for metabolic flux experiments or left in HBSS to process for OCR.

Metabolic flux incubations

Metabolite standards and buffer components were purchased from Sigma-Aldrich (MilliporeSigma; St. Louis, MO). Incubation medium was formulated as follows:

- Krebs's Ringer Buffer (KRB): 98.5 mM NaCl, 4.9 mM KCl, 1.2 mM KH_2PO_4, 1.2 mM $MgSO_4$, 20 mM HEPES, 2.6 mM CaCl, 25.9 mM $NaHCO_3$
- 5 mM U-^{13}C-D-glucose (99% isotopic purity) from Cambridge Isotope Laboratories, Inc (Tewksbury, MA).

Individual dishes of 2 mL of incubation medium was equilibrated in a humidified incubator at 37°C and 5% CO_2 for 1 hour prior to running experiments. Tissues were incubated for 2, 10, 20, 30, or 45 minutes in incubation medium. At time, tissues were removed from incubation medium, quickly washed in HBSS, and snap frozen. The incubation medium was mixed in the dish, aliquoted, and snap frozen. All samples were stored at -80°C until extraction.

Metabolite extraction of retina and eyecup explants

All extractions were performed in batches over numerous days. Samples each day included matched retinas and eyecups or their media from random treatment groups and random timepoints. Tissue was extracted in 80% methanol, 100 µM methylsuccinate chilled over dry ice. Tissues were homogenized and sonicated (Duty cycle: 90, output control: 2, 10 pulses) over wet ice. Proteins were precipitated on dry ice for 45 minutes, and 70% (by volume) of supernatant was collected after a 25-minute 17,000 x g spin at 4°C. Additional 80% methanol (75% of starting volume) was added to the protein pellet, precipitated for 20 minutes, and spun down to collect additional volume (70% of original volume). Sample supernatant was spiked with 10 µL of 100 µM L-norvaline and half the volume was removed and added to a new tube. Each split sample was spiked with 5 µL of 100 µM L-norleucine as an instrument control. All were lyophilized to dryness the same day and stored at -80°C until analysis by GC-MS.

Exported metabolite isolation

Media was processed by spiking a 20 µL aliquot with 5 µL of 100 µM methylsuccinate and adding chilled methanol to a concentration of 80% (100 µL). Samples were allowed to precipitate on dry ice for 45 minutes and the supernatant was collected after a 25 minute 17,000 x g spin at 4°C. Clarified supernatant was spiked with 5 µL each of 100

μM L-norvaline and L-norleucine, respectively, to serve as instrument controls. Samples were lyophilized to dryness and stored at -80°C until analysis by GC-MS

Analysis of metabolites by GC-MS

Metabolite standards between 1.25-35 μM in a final derivatization volume of 20 μL were used to generate calibration curves. One half of each split tissue sample or the full media aliquot were derivatized in batches over numerous days. Each batch included matched retinas and eyecups or their media from random treatment groups and random timepoints. Samples were incubated at 37°C for 90 minutes in 10 μL of 20 mg/mL methoxyamine (MilliporeSigma) in pyridine (MilliporeSigma). 10 μL of neat N-tertbutyldimethylsilyl-N-methyltrifluoroacetamide (MilliporeSigma) was added and the samples incubated for one hour at 70°C. Derivatized samples were transferred from Eppendorf tubes to 2 mL vials (Agilent - 5182-0715) containing high recovery glass inlets (Agilent - 5183-2085). Samples were sealed with lids containing PTFE silicone septa (Agilent - 5182-0717).

Each sample was analyzed using a splitless injection of 1 μL within 24 hours of derivatization via a 49 minute gradient on an Agilent 7890/5975C GC-MS system (Agilent Technologies; Santa Clara, CA). Two Agilent columns with differing stationary phases were used: a 5% Diphenyl / 95% Dimethylpolysiloxan (DB-5MS:128-5522) with a flow rate of 0.8 mL/min, and a phenyl methyl silox film (HP-5MS: 19091S-433I) with a flow rate of 1 mL/min. For all derivatized metabolites, we used target ions for quantification and isotopologue distribution determination, and a qualifier ion for identity confirmation. Peak areas for SIM ions were obtained in MSD ChemStation (Agilent Technologies; Santa Clara, CA) with manual verification of automated peak integrations. IsoCor v2 (Millard 2012 and 2019) was used to correct for natural ^{13}C abundance and determine percent enrichment of ^{13}C. In individual metabolite isotopologues, the number of incorporated ^{13}C is represented shorthand by “Mx”, where x is the number of ^{13}C (M0, M1, M2, etc.).

Oxygen consumption

For each replicate, two retinas or four eyecups were quartered and loaded into a perifusion system that assesses oxygen consumption as described (Sweet et al., 2002a, 2002b) with minimal changes. Tissue was perifused with Krebs-Ringer buffer maintained at equilibrium with 21% O2, 5% CO2, and 74% N2 by an artificial lung and supplemented with 0.1 g/100mL BSA, 1X antibiotic-antimycotic (Gibco; Grand Island, NY), and 5 mM glucose. Succinate or glutamine (5 mM) was added when testing mitochondrial function. Flow rate over live tissue averaged 61.9 ± 5 µL/minute. OCR was calculated as the product of flow rate times the difference in outflow and inflow oxygen levels. Data was reported as a change in OCR after subtracting off the baseline OCR measured in 5 mM glucose alone.

Glucose uptake

For each replicate, four retinas or four eyecups were pooled. Incubation buffer was formulated with 5 mM glucose and KRB at an initial volume of 1 mL. Incubations were performed in a humidified incubator at 37°C and 5% CO_2 for a total of 8 hours. At each timepoint, the dish was moved out of the incubator, a 12 µL aliquot pulled, and the dish immediately placed back into the incubator. From that aliquot, at least 2 µL was used to measure glucose in duplicate measurements of 1 µL with a commercial glucometer (Accu Chek Performa, Roche Diagnostics). The precision of the glucometer was confirmed with a calibration curve of glucose standards prior to running the experiment. Values were converted to mM after measurement by the glucometer in mg/dL.

Protein concentration for normalization

Protein pellets were solubilized in RIPA buffer (150 mM NaCl, 1% Triton X-100, 0.5% sodium deoxycholate, 0.1% SDS, 50 mM Tris pH 8.0, 1X HALT protease/phosphatase inhibitor), sonicated, and the supernatant quantified using the Pierce™ BCA Protein Assay Kit per manufacturer's instructions.

Grouping and statistics

Sample collection from young and aged groups occurred at different times. Sample

sizes represent biological replicates. Extractions, derivatization, and sample runs were processed in batches including both ages, genders, matched retinas, eyecups, and/or their media, and random timepoints. To account for circadian contributions, the time of death for animals used in glucose flux, glutamine flux, and OCR are plotted in Supplementary Figure 1.

Statistical tests used are included in each figure legend. Broadly, the normality of the data was tested using the Shapiro-Wilk test ($\alpha = 0.05$). Comparisons between two groups were made using either unpaired t-tests (Marked with * for $p < 0.05$) or Mann-Whitney tests (Marked with # for $p < 0.05$, or (ns) is not statistically significant). Comparisons between three or more groups ($p < 0.05$) were performed using one-way ANOVA followed by Tukey's multiple comparisons test, two-way ANOVA followed by Dunnett's multiple comparisons test, or the nonparametric Kruskal-Wallis test followed by Dunn's multiple comparisons test. The comparison of pre- and post-treatment conditions in the same animal were made using either paired t-tests (Marked with * for $p < 0.05$) or Wilcoxon matched-pairs signed rank tests (Marked with # for $p < 0.05$, or (ns) is not statistically significant).

Acknowledgments

The work in this chapter represents the combined efforts of several laboratories and many dedicated individuals who contributed experimentation, time, and thoughtful discussions. In the laboratories of James B. Hurley and of Susan E. Brockerhoff, we wish to thank Whitney M. Cleghorn, Celia M. Bisbach, Daniel T. Hass, Brian M. Robbings, Jonathan D. Linton, Connor S.R. Jankowski, Michelle M. Giarmarco, Mark A. Kanow, Kelie Gonzalez, Benjamin H. Baur, and Chris C. Farnsworth. Martin Sadilek was instrumental in developing the mass spectrometry methods detailed here. Mice, NMN and ELAM dosing, expertise in the biology of aging, and thoughtful discussion were provided by the laboratories of Peter S. Rabinovitch and David J. Marcinek. In particular, we are grateful for the work of Jeremy A. Whitson, Mariya T. Sweetwyne, Matthew D. Campbell, Ana P. Valencia, Huiliang Zhang, and Jeanne Fredrickson.

Finally, Austin M. Rountree in the laboratory of Ian R. Sweet performed the OCR experiments. Clara Suelen, Anthony Scott, and Csaba Nagy provided care for the mice in this study. The Imai laboratory at Washington University in St. Louis, MO provided the NMN. Stealth BioTherapeutics (Newton, MA) provided the ELAM for this work free of charge, and played no role in the funding, experimental design, data collection or authorship of the research. Funding for this work was provided by the NIA, NEI, and NIDDK:

NIH/NIA

- Peter S. Rabinovitch and David J. Marcinek - Mitochondrial Protective Interventions, Aging and Healthspan: 5P01AG001751
- Kristine A. Tsantilas T32 - Genetic Approaches to Aging Training Grant T32 AG000057
- Kristine A. Tsantilas T32 - Biological Mechanisms for Healthy Aging Training Grant T32 AG066574
- Mariya T. Sweetwyne K01 - Mitochondrial Protection to Derive Expanded Aged Renal Glomerular Progenitor Cells: K01 AG062757-02

NIH/NEI

- James B. Hurley R01 - Determinants of Rod and Cone Response Characteristics: 5R01EY006641
- James B. Hurley R01 - Control of Photoreceptor Metabolism: 5R01EY017863
- Celia M. Bisbach F31 - Understanding the role of cytosolic NADH production in maintaining aerobic glycolysis in the retina: F31EY031165
- Daniel T. Hass T32 - Vision Training Grant: T32EY007031

- **NIH/NIDDK**
- Ian R, Sweet - Cell Function Analysis Core of the Diabetes Research Center: P30 DK017047

Chapter 7 - Analysis of metabolites in vertebrate retina and RPE-choroid complex using gas chromatography-mass spectrometry

Introduction

Metabolism effectively represents the final output of the crosstalk between the epigenome, genome, transcriptome, and proteome. The health of an organism or organ system is reflected in the identity and quantity of metabolites. Examining the flux of metabolites – the paths they take and to what extent they do so – has diverse applications. With the discovery of isotopes and radioactivity, biology would subsequently experience a revolution. Radioisotope tracers were used to illuminate concepts we now see as dogma – particularly that living organisms exist in a constant state of dynamic change (Lappin, 2015; Lehmann, 2017; Wilson and Saiardi, 2017). As organisms, we are continuously battling to remain at an equilibrium, but to never truly reach equilibrium. Today, the field has moved towards non-radioactive isotopic tracers including ^{13}C, ^{15}N, ^{18}O, and ^{2}H.

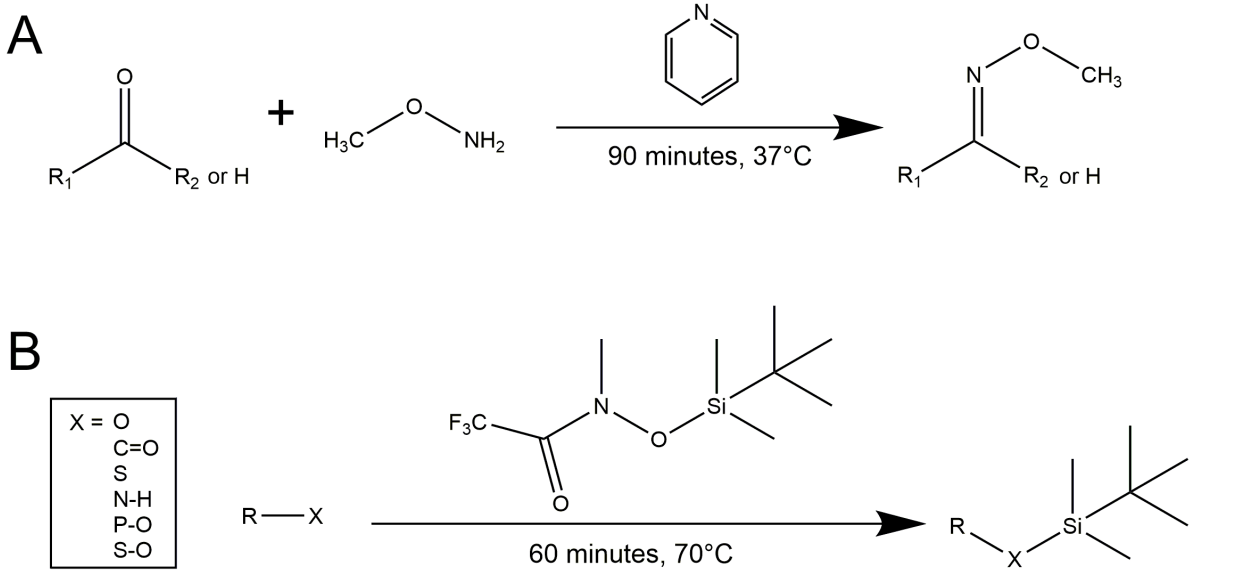

Figure 7.1: Two-step methoximation and *tert*-butyldimethylsilylation derivatization.

In Reaction A, methoxyamine HCl is dissolved in dry pyridine, which serves as a catalyst. The samples are incubated in the methoxyamine-pyridine solution for 90 minutes at 37°C to protect carbonyl groups. In the second step, Reaction B, the silylation reaction is facilitated by the addition of neat N-tertbutyldimethylsilyl-N-methyltrifluoroacetamide followed by a 60 minute incubation at 70°C. Amines, alcohols, amides, carboxylic acids, phosphates, and thiols are targeted.

Mass spectrometry permits thorough quantitation of a diverse number of biological molecules. In particular, gas chromatography-mass spectrometry permits the reliable identification and quantitation of many metabolites in a single sample run. The use of electron ionization generates a reliable fragmentation pattern (Fiehn, 2016; Kitson et al., 1996). This chapter describes how GC-MS can be used to characterize isotopologues in retinas and RPE-choroid-sclera complexes (eyecup).

GC-MS requires volatile molecules for effective chromatographic separation. Many biological molecules of interest include polar groups and have hydrogen bonding capabilities, which lead to a high boiling point. This is problematic in GC-MS, as these molecules are not volatile, can interact with the solid phase, and result in sub-par detectability. However, replacement of polar groups containing acidic hydrogens with aliphatic groups is widely used to render molecules more amenable to analysis by GC-MS (Fiehn, 2016; Kashutina et al., 1975; Schummer et al., 2009).

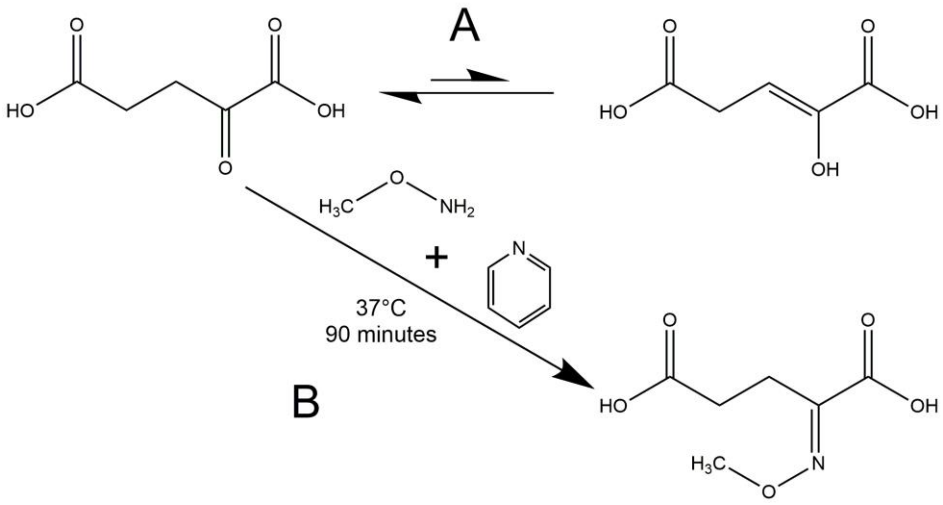

Figure 7.2: Methoximation is used to protect carbonyl groups.

An example case where methoximation can be useful for quantifying a molecule where tautomerization between a keto/enol form (A) may result in two different molecules measured by GC-MS. The structures in Reaction A are two forms of alpha-ketoglutarate. In reaction B, alpha-ketoglutarate is shown before and after methoximation, but before silylation.

The derivatization employed in this study uses two steps: methoximation and *tert*-butyldimethylsilylation (Figure 7.1). Methoximation protects carbonyl groups and also has the advantage of “locking” molecules with the ability to tautomerize into a single

consistent conformation for subsequent silylation (Figure 7.2). Amines, alcohols, amides, carboxylic acids, phosphates, and thiols are protected with *tert*-butyldimethylsilyl (TBDMS) groups with the addition of neat N-tertbutyldimethylsilyl-N-methyltrifluoroacetamide (MTBSTFA).

The electron ionization of *tert*-butylsilyl metabolites generates a reliable array of fragments including $[M-1]^+$, $[M-15]^+$, $[M-57]^+$, $[M-85]^+$, $[M-131]^+$, and $[M-159]^+$ ions (Kitson et al., 1996; Schummer et al., 2009) that can be detected in full scan mode. We confirmed that $[M-57]^+$ fragments are consistently higher abundance than the other types of fragments (Schummer et al., 2009), although $[M-159]^+$ and $[M-85]^+$ were also common. To examine the isotopic distribution of each metabolite

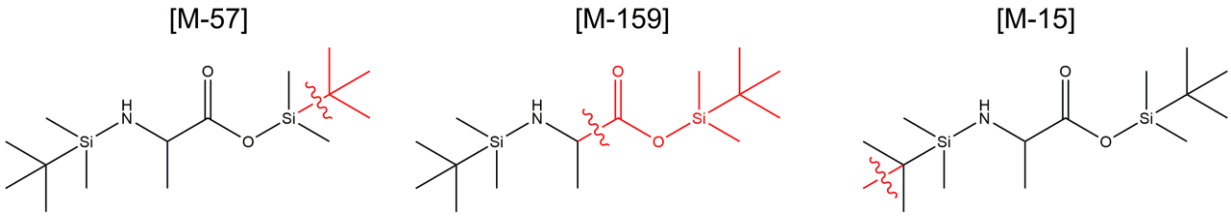

Figure 7.3: Fragmentation examples after electron ionization of TBDMS-derivatized alanine.
The $[M-57]^+$, $[M-159]^+$ and $[M-15]^+$ fragments generated by electron ionization on a molecule of derivatized alanine. The lost atoms of the molecule are highlighted in red, and the hypothetical location of the bond break is indicated with a wavy red line.

Once the optimum fragments are determined for individual unlabeled molecules, a targeted approach can be developed that tracks all isotopologues of a given element. In this method, the focus was placed on carbon atoms and tracing ^{13}C. Selected Ion Monitoring (SIM) mode can be used to improve sensitivity (Kitson et al., 1996), although selectivity is reduced as only the ions of interest are measured by the detector. Designing experiments with specific hypotheses in mind is necessary to perform a targeted metabolomics experiment using the approach we describe here. Thus, if the retention time and best fragments to quantify of the analytes of interest are unknown, it is necessary to first use full scan mode with internal standards to acquire this information to set-up a quantitative SIM method.

Protocol

The metabolic characterization of retina and RPE-choroid-sclera complexes (eyecups) by GC-MS can be completed within approximately 4 days – depending on the sample number. It is advisable when working with large numbers of samples, numerous days of extraction and derivatization may be required. A recommended approach for fewer than 30 samples is as follows:

Day 1

- Section 7.1: Preparing Krebs-Ringer Buffer (KRB)
- Section 7.2: Prepare mix of standard metabolites for normalization

Day 2

- Section 7.3: Preparing complete incubation medium for flux experiments
- Collect samples
    - Section 7.4: Tissue isolation from mice
    - Section 7.5: Tissue isolation from zebrafish
    - Section 7.6: Metabolic Flux Incubations

Day 3

- Section 7.7: Metabolite extraction of retinas and eyecups

Day 4

- Section 7.8: Methoximation and tert-butylsilylation derivatization
- Section 7.9: Analysis of metabolites by GC-MS
    - Section 7.10: Metabolite information

Section 7.1: Preparing Krebs-Ringer Buffer (KRB)

1. Assemble 15 mL conical vials, a large Erlenmeyer flask (or bottle), and disposable PVDF filter

2. Assemble all compounds

Table 7.1: Quantity of reagents required to prepare Krebs-Ringer Buffer

Solute	MW (g/mol)	Final Molarity (mM)	Solute per 1 L required for concentrated KRB* (g)	Solute per 1 L required for concentrated KRB† (g)	Solute per 500 mL required for concentrated KRB† (g)
NaCl	58.44	98.5	5.75634	**5.996**	2.998
KCl	74.55	4.9	0.365295	**0.381**	0.1905
KH_2PO_4	136.09	1.2	0.163308	**0.170**	0.085
$MgSO_4$-$7H_2O$	246.47	1.2	0.295764	**0.308**	0.154
HEPES	238.30	20	4.766	**4.965**	2.4825
$CaCl$-$2H_2O$‡	147.01	2.6	0.382226	**0.398**	0.199
$NaHCO_3$	84.01	25.9	2.175859	**2.267**	1.1335

* Desired if NO dilution of KRB with a dissolved metabolite stock.
† Hurley lab prepares incubation media by diluting this higher concentration KRB stock down to final molarity with metabolite stock(s) & water
‡ Hygroscopic compound. Measure quickly and keep stock lid closed to reduce moisture exposure.

3. Use the large graduated cylinder and fill with MilliQ water to desired FINAL volume
    a. Turn on MilliQ system: Run for ~10 seconds before filling graduated cylinder to 500 mL or 1000 mL mark.
    b. Keep covered with foil until use
4. Label 15 mL conical vial with each compound's name
5. Weigh out as close to exact mass as possible by hand (General tolerance of ±0.005 g) and add to conical vial
6. Repeat for all compounds
7. Add MilliQ water from cylinder to all falcon tubes and solubilize by vortexing
8. Once buffers solubilized, carefully pour into large autoclaved Erlenmeyer flask
    a. Added in order listed in
    b. Table 7.1 to avoid precipitation.
9. Swirl and add about half of MilliQ water from graduated cylinder
10. Solubilize remaining compounds and add to Erlenmeyer

11. Add remaining water from graduated cylinder to Erlenmeyer
12. Visibly ensure all compounds are fully solubilized.
    a. If yes, proceed to filtration step
    b. If no, add the magnetic stir bar and mix for ~1 hour. Check again and filter
13. Pull vacuum through the PVDF membrane and pour in KRB medium until all of it has passed through the filter.
14. Label container with contents and date.
15. Store prepared KRB at 4°C for up to 4 weeks.

Section 7.2: Prepare mix of standard metabolites for normalization

To reduce freeze-thaw cycles and simplify preparation later, a standard mix containing equivalent concentrations of metabolites of interest should be prepared. One approach is as follows:

1. Prepare all metabolites at stock solutions of 1 mM or higher – to simplify pipetting, the same concentration is advised - and snap freeze aliquots.
2. Thaw an aliquot of each metabolite and pool equivalent volumes of all metabolites
3. Dilute standard mix to desired concentration. A concentration of 50 or 100 µM are ideal for final concentrations of 50-2.5 µM at a final derivatization volume of 20 µL.

Section 7.3: Preparing complete incubation medium for flux experiments

Prepare fresh metabolite-KRB medium in 15-50 mL conical tubes according to the total sample size with at least one spare dish to allow for thorough mixing.

1. Prepare complete incubation medium using KRB, milliQ or MS-grade water, and stock solution of your metabolite(s) of choice. Vortex thoroughly.
    a. Ensure the isotopic purity of the tracer is noted for subsequent isotope correction!
    b. Sample calculations for the preparation of 5 mM U-^{13}C glucose are shown

in Table 7.2.

Table 7.2: Sample calculations for prepared 5 mM U-^{13}C-glucose in KRB

Volume of prepared KRB Medium (mL)	KRB Stock* (mL)	0.5M U-^{13}C-glucose stock (mL)	ddH_2O (mL)
10 ml	9.6 ml	0.1 ml	0.3 ml
20 ml	19.2 ml	0.2 ml	0.6 ml
40 ml	38.4 ml	0.4 ml	1.2 ml

*NOTE: These values result in the final molarity in Table 7.1 for incubations.

2. Add 2 mL of final metabolite-KRB buffer to each dish using a 1 mL pipette
    a. **NOTE:** Precise addition of same volume of buffer to each dish is important for consistency regarding gas exchange and if pulling aliquots of incubation medium for GC-MS analysis of exported metabolites.
    b. **NOTE:** Less volume can be used if the dishes are canted to conserve more expensive reagents. The different depth of medium may impact oxygen levels, but this has not been tested.
3. Pre-incubate the dishes with complete incubation medium in a humidified 37^{o}C, 5% CO_2 tissue culture incubator for 1 hour prior to flux experiment.
    c. The pH of the final solution after incubation should be ~7.4 after 1 hour.

Section 7.4: Tissue isolation from mice

1. If performing metabolic flux, prepare complete medium from KRB and metabolites. Ensure the medium aliquots have incubated as described above prior to euthanizing zebrafish.
2. Set aside fresh HBSS (formulated with glucose and without Mg^{2+} and Ca^{2+}) in 35 mm (non-treated) culture dishes for use during tissue isolation.
3. Euthanize mice by awake cervical dislocation.
    a. Mice for metabolic flux should be euthanized by awake cervical dislocation and processed quickly postmortem to reduce metabolic changes in tissues. CO_2 asphyxiation was found to differentially alter metabolite abundance in retinas and eyecups (Zhu et al., 2018).

4. Enucleate eyes with curved forceps and place into dish of HBSS.
5. If collecting eyecups, place the globe on a damp paper towel soaked in HBSS and remove attached hair, muscle, connective, and adipose tissue from the globe. If only isolating retina, proceed to Step 4 immediately.
    a. This can be done with a combination of microscissors and microtweezers.
    b. Once punctured, the globe will be significantly more difficult to clear of excess tissue. It is advised to complete the cleaning process prior to making any cuts into the sclera.
6. Puncture the globe with a 20-24 gauge needle just above the ora serrata.
7. Using microtweezers, cut circularly around the globe to remove the cornea and iris, and lens.
    a. Frequently, the lens and vitreous will be liberated from the globe as the cornea and iris are removed.
8. The opened globe should be gently placed back into fresh HBSS. Remove the lens if it was not removed during removal of the cornea and iris.
9. Carefully separate the retina from the RPE-choroid-sclera complex (eyecup).
    a. One approach to remove the retina is to grasp the bottom of the eyecup with one set of microtweezers. Using another set of tweezers, carefully and with very little pressure squeeze perpendicular to the tweezers at the bottom of the eyecup and move towards the opening of the globe to squeeze the retina out.
        i. Too much pressure can shred it the retina or trap it in the eyecup
10. Visually confirm that the inside of the eyecup is free of visible pieces of retina.
11. If still attached, cut the optic nerve at the base of the eyecup.
12. The separated retina and eyecup can then be placed in metabolic flux medium or snap frozen.

Section 7.5: Tissue isolation from zebrafish

1. Due to the percolation of RPE apical processes into photoreceptor outer segments by retinomotor movements (Burnside et al., 1993), it is recommended

that zebrafish be dark adapted for one hour or more prior to dissections and dissections be performed under red light.

2. If performing metabolic flux, prepare complete medium from KRB and metabolites. Ensure the medium aliquots have incubated as described above prior to euthanizing zebrafish.
3. Set aside fresh HBSS (formulated with glucose and without Mg^{2+} and Ca^{2+}) in 35 mm (non-treated) culture dishes for use during tissue isolation.
4. Euthanize zebrafish in an ice bath followed by cervical dislocation.
5. Enucleate eyes with a small ring and place into dish of HBSS.
6. Using sharp tweezers or needle, puncture cornea.
7. Gently open front of the eye either with tweezers or microscissors
8. Remove the lens, remainder of the cornea, and iris
9. Separate the retina from the eyecup
    a. If the retina was still attached to the lens, separate it
10. Separated retina and eyecup can be placed in metabolic flux medium or frozen.

Section 7.6: Metabolic Flux Incubations

1. Once retina and eyecup explants are ready, place the tissues into separate dishes of equilibrated incubation medium and start timer immediately.
2. Immediately place dish containing tissues back into incubator.
3. Once time is up, remove tissue from incubation medium using microtweezers.
4. Drop tissue into 1 mL HBSS or 0.9% saline to wash away excess label.
5. Remove supernatant as fast as possible and close lid firmly.
6. Snap freeze tissues in liquid nitrogen.
7. If planning to analyze metabolites secreted into the medium, swirl dish or use a pipette to mix the solution.
8. Save ~500 µL of media in multiple aliquots to avoid freeze-thawing cycles.
9. Place samples in -80°C until shipment or extraction.

Section 7.7: Metabolite extraction of retinas and eyecups

To avoid batch effects when preparing a large set of samples, it is advisable to randomize samples according to treatment groups and timepoints prior to processing. Before beginning extraction, determine the final derivatization volume of your sample to ensure you can add the correct quantities of internal standards and dry down the correct volume of standard mix. In mice, 20 µL is recommended. In zebrafish, a volume as low as 14 µL is sufficient to increase signal about 40% and permit use of the autosampler.

Table 7.3: Product numbers and purity of metabolites measured using GC-MS.

Metabolite	Vendor/product number	Purity
L-2-Hydroxyglutarate	Sigma Aldrich; 90790	98%
(3) β-Hydroxybutyrate	Sigma Aldrich; 54965	99%
5-Hydroxydecanoic acid	Sigma Aldrich; H135	97%
2-Phosphogylcerate	Sigma Aldrich; 73885	95%
3-Phosphogylcerate	Sigma Aldrich; P7127	97%
5-oxoproline	Sigma Aldrich; 292915	99%
Acetoacetate	Millipore Sigma; A8509	90%
Alpha-ketoglutarate	Sigma Aldrich; 75890	99-101%
Alanine	Sigma Aldrich; A7627	98%
Asparagine	Sigma Aldrich ; A4284	99%
Aspartate	Sigma Aldrich; A6558	98%
Citrate	Sigma Aldrich; S4641	99%
Cysteine	Millipore Sigma; C7352	98%
Dihydroxyacetone phosphate	Sigma Aldrich; D7137	93%
Fumarate	Sigma Aldrich; F1506	99%
GABA	Sigma Aldrich; A2129	99%
Glyceraldehyde-3-phosphate	Sigma Aldrich; G5251	45-55 mg/mL
Glutamate	Sigma Aldrich; G8415	98.5-100%
Glutamine	Sigma Aldrich; G3126	99%
Glycine	Sigma Aldrich; G7126	99%
Histidine	Sigma Aldrich; H8125	98%
Hypotaurine	Millipore Sigma; H1384	98%
Isocitrate	Sigma Aldrich; I1252	93%
Isoleucine	Millipore Sigma; I2752	98%
Lactate	Sigma Aldrich; L7022	98%
Leucine	Sigma Aldrich; L8912	99%
Lysine	Millipore Sigma; L5501	98%
Malate	Sigma Aldrich; M1000	95%
Methionine	Sigma Aldrich; M5308	99%
Methylsuccinate	Sigma Aldrich; M81209	99%
N-Acetylaspartate	Fluka Analytical; 00920	99%
Norleucine	Sigma Aldrich; N6877	98%
Norvaline	Sigma Aldrich; N7627	99%
Oxaloacetate	Sigma Aldrich; O4126	97%
Palmitic Acid	Sigma Aldrich; P5585	99%
Phosphoenolpyruvate	Sigma Aldrich; P7127	97%
Phenylalanine	Sigma Aldrich; P5482	98.5-101%
Proline	Millipore Sigma; P0380	99%
Pyruvate	Sigma Aldrich; P4562	99%
Serine	Sigma Aldrich; S4500	99%
Succinate	Sigma Aldrich; 14160	98%
Taurine	Millipore Sigma; T0625	99%
Threonine	Sigma Aldrich; T8625	98%
Tyrosine	Sigma Aldrich; 93829	99%
Valine	Millipore Sigma; V0500	98%

Preparation

1. Formulate a standard mix for normalization using compounds of interest from Table 7.3 and freeze aliquots to avoid numerous freeze-thaw cycles.
2. Turn on vacuum manifold
3. Thaw aliquots of internal standards (Table 7.4).

Table 7.4: Recommended internal standard concentrations

Spike	Starting conc. (µM)	Final Volume (µL)	Volume needed per sample (µL)	Final Conc. (µM)
Methylsuccinate	100	20	5	50
Norvaline	100	20	5	25
Norleucine	100	20	5	25

4. Prepare sufficient metabolite extraction buffer according to the planned method of tissue homogenization as described in Table 7.5. If using the Tissumizer, a higher volume is needed, ad it is not recommended for retinas.
5. Store prepared extraction buffer and place 1 mL pipette tips in empty Eppendorf tubes to chill on dry ice for at least 20 minutes.
6. Using 1 mL pipette, condition chilled tip with cold buffer before beginning to add to tissue samples.
7. Add volume to all samples. Avoid sample cross-contamination, and swap to a new tip and condition if needed.
8. Proceed to homogenization and sonication.

Table 7.5: Composition of tissue extraction buffer

Extraction method	Stock	n	Extraction Volume	Total volume n*	100 µM Methylsucc.†	Methanol (µL)	Water (µL)	Total Volume Needed
Dounce homogenizer & sonication	Retinas or Eyecups	10	150	14	140	1680	280	2100
Tissumizer & sonication	Eyecups	10	350	14	140	3920	840	4900

* Prepare excess volume to ensure stock is not depleted prematurely.

† Volume (µL) of 100 µM methylsuccinate to add to 50 µM final concentration

Dounce homogenizer & sonication (<5 minutes per sample)

1. Homogenize retina or eyecup over wet ice until broken down well.
2. Vortex and return sample to dry ice.
3. Sonicate sample as follows
    a. Run sonicator for 5 pulses in a 2 mL tube full of methanol to clean probe
    b. Run sonicator for 5 pulses in a 2 mL tube full of water to clean probe
    c. Spray probe with methanol
    d. Wipe clean with kimwipe to remove excess methanol
    e. Sonicate sample over ice for 10 pulses using the following settings:

Timer	Hold
Duty Cycle	90
Output Control	2

4. Vortex and return sample to dry ice
5. If running additional samples, repeat steps c-e for each sample
6. Proceed to precipitation and clarification in later section

Tissumizer & sonication (>5 minutes per sample)

1. Turn homogenizer output to lowest setting.
2. Open sample tube, insert homogenizer and turn the power on to start homogenizing slowly.
3. Move the output up to 50 and then from 60 to 70 to begin homogenizing the eyecup.
4. Increase speed up to 80-90 if not being broken down well at 70.
5. Once eyecup is fully homogenized, vortex and return to dry ice immediately
6. Wash homogenizer with 500 µL water in 2 mL Eppendorf on full speed
7. Wash homogenizer with 500 µL methanol in 2 mL Eppendorf on full speed
8. Continue onto the next sample, or proceed to sonication as described in previous section
9. After sonication, proceed to precipitation and clarification

Precipitation, Clarification and Extraction

1. If GC-MS method can track norvaline and norleucine in single run, can spike either compound at this step, vortex, and spin down tabletop as a process control

2. Allow samples to stand for 45 minutes on dry ice to precipitate proteins
3. Spin the samples down for 25 minutes at 17,000 x g at 4°C to pellet proteins and cellular debris
4. Keep tube canted after removal from centrifuge to prevent disruption of pellet
5. Transfer the supernatant into new labeled microfuge tube
    a. Recommend sabing protein pellets and storing at -80°C to normalize to protein content in tissues later.
6. Spike each sample with 5 µL of 100 µM norvaline and 5 µL of 100 µM norleucine
    a. At this step, these will serve as instrument/injection controls.
7. Vortex and spin tube down table-top
8. Dry samples completely
    a. Recommend drying samples the day-of. Extracted metabolites in 80% methanol can be stored at -80°C if necessary.
9. Store dried metabolites in -80°C freezer until ready for GC-MS.

Section 7.8: Methoximation and tert-butylsilylation derivatization

To avoid batch effects when preparing a large set of samples, it is advisable to randomize samples according to treatment groups and timepoints prior to processing. Final derivatized volume of standards and samples must have been determined before drying extracted metabolites. Deviating from the pre-determined value upon which internal standard concentrations were based will skew quantitation values of the standard mixes and spiked metabolite standards. Finally, it is critical that samples were fully dried before beginning the derivatization or the efficiency of the reaction will suffer immensely.

Preparation

1. Set the dry heating block to 70°C and ensure that the correct size blocks are installed in the heating apparatus at this stage.
2. Verify that the oven is set to 37°C.
3. Remove samples from freezer and place in speed vac.

4. Dry for a minimum of 20 minutes to ensure samples are dry before beginning reaction with methoxyamine.

Derivatization

1. Prepare a 20 mg/mL methoxyamine HCl solution by weighing out sufficient methoxyamine HCl and dissolving in dry pyridine. Mix thoroughly by vortexing
    a. **NOTE:** Prepare enough 20 mg/mL solution to account for 7-10 µL per sample. Can weigh 5-10 mg and dilute to 20 mg/mL for more rapid weighing. Must minimize time exposed to atmosphere before beginning reaction!
2. As soon as the methoxyamine solution is prepared, add 10 µL to each Eppendorf tube and thoroughly vortex to dissolve. Spin down to collect solution.
3. Place the samples in a 37°C incubator for 90 minutes.
4. Verify the heating block has reached 70°C and adjust as needed.
5. After incubation, cool in the hood for approximately 5 minutes.
6. Add 10 µL of the neat N-tertbutyldimethylsilyl-N-methyltrifluoroacetamide to each Eppendorf tube and thoroughly vortex to dissolve. Spin down to collect solution.
    a. **NOTE:** The solution will become cloudy upon addition of the TBDMS.
7. Place the samples in the 70°C heating block and incubate for 60 minutes.
8. Carefully remove the samples from the heating block and allow to come to room temperature for easier handling.
9. At this stage, transfer solution from Eppendorf tubes into corresponding labeled high recovery glass inlets (Agilent - 5183-2085) placed in autosampler vials (Agilent - 5182-0715).
10. Seal vials with lids containing PTFE silicone septa (Agilent - 5182-0717).
11. Samples should be run on GC-MS as soon as possible. Recommend leaving samples at room temperature for short-term storage rather than freezing based on stability results detailed in Figure 7.8.

Section 7.9: Analysis of metabolites by GC-MS

Samples were analyzed using 49 minute gradients on an Agilent 7890/5975C GC-MS system (Agilent Technologies; Santa Clara, CA). Each sample was analyzed using a splitless injection of 1 µL within 24 hours of derivatization. Two approaches were used to accommodate two different Agilent columns: Method 1 (DB-5MS (128-5522), flow rate of 0.8 mL/min) and Method 2 (HP-5MS column (19091S-433I), flow rate of 1 mL/min). For all derivatized metabolites, target ions were used for quantification and isotopologue distribution determination. One or two qualifier ions were matched to M0 for identity confirmation. The retention times of the metabolites examined are listed in Table 7.6: Methoxime and tert-butylsilyl derivatized metabolite retention times in Table 7.6, and the ions tracked in Table 7.7. The peak areas for SIM ions were obtained in MSD Chemstation (Agilent Technologies; Santa Clara, CA) with manual verification of automated peak integrations. IsoCor v2 (Millard 2012 and 2019) was used to correct for natural ^{13}C abundance and determine percent enrichment of ^{13}C.

Section 7.10: Metabolite information

Metabolite retention times and column information

Targeted SIM approach by GC-MS was performed using a single (Method 1) or two sequential (Method 2) splitless injections of 1 µL of derivatized sample. These differing approaches were taken when amino acid characterization was desired, but the 25 m (DB-5MS) column was swapped to a 30 m (HP-5MS) column. This was due to a loss of peak separation among metabolites with similar elution times.

Table 7.6: Methoxime and tert-butylsilyl derivatized metabolite retention times

Metabolite	Retention Time #1 †	Retention Time #2 ‡	Metabolite mass◊	Chemical Formula◊
L-2-Hydroxyglutarate	30.7	29.65	148	C5H5O5
(3) β-Hydroxybutyrate	18.24	17.3	104	C4H6O3
5-Hydroxydecanoic acid	29.07	27.8	188	C10H18O3
2-Phosphogylcerate	36.45	N/A	186	C3H3O7P
3-Phosphogylcerate	37.2	36.27	186	C3H3O7P
5-oxoproline	25.87	N/A	129	C5H5NO3
Acetoacetate	12.15	12.02	102	C4H5O2
Alpha-ketoglutarate	26.99	25.97	146	C5H4O4
Alanine	16.86	15.93	89	C3H5NO2
Asparagine	32.3	31.13	132	C4H5N2O3
Aspartate	29.66	28.56	133	C4H4NO4
Citrate	37.1	36.12	192	C6H4O7
Cysteine	30.5	29.45	121	C3H4NO2S
Dihydroxyacetone phosphate	32.84	32.15	170	C3H4O5P
Fumarate	22.8	21.53	116	C4H2O4
GABA	22.01	20.86	103	C4H7NO2
Glyceraldehyde-3-phosphate	32.45	31.75	170	C3H3O5P
Glutamate	31.71	30.6	147	C5H6NO4
Glutamine	34.23	33.06	146	C5H7N2O3
Glycine	17.53	16.46	75	C2H3NO2
Histidine	36.75	35.6	155	C6H6N3O2
Hypotaurine	23.78	22.58	109	C2H5NO2S
Isocitrate	37.25	36.31	192	C6H4O7
Isoleucine	21.21	20.26	131	C6H11NO2
Lactate	15.51	12.8	90	C3H4O3
Leucine	20.5	19.6	131	C6H11NO2
Lysine	33.55	32.38	146	C6H11N2O2
Malate	28.82	27.83	134	C4H3O5
Methionine	26.14	25.09	149	C5H9NO2S
Methylsuccinate*	22.17	21.09	132	C5H6O4
N-Acetylaspartate	32.35	N/A	175	C6H6NO5
Norleucine*	21.51	20.66	131	C6H11NO2
Norvaline*	19.88	18.95	117	C5H9NO2
Oxaloacetate	24.51	N/A	132	C4H2O4
Palmitic Acid	32.26	N/A	256	C16H31O2
Phosphoenolpyruvate	30.85	29.9	168	C3H2O6P
Phenylalanine	28.45	27.36	165	C9H9NO2
Proline	22.05	N/A	115	C5H7NO2
Pyruvate	9.58	8.87	88	C3H3O2
Serine	26.49	25.56	105	C3H4NO3
Succinate	22.04	20.89	118	C4H4O4
Taurine	25.14	24.1	125	C2H5NO3S
Threonine	26.98	26.14	119	C4H6NO3
Tyrosine	37.5	36.36	181	C9H8NO3
Valine	19.53	18.65	117	C5H9NO2

* Denotes an internal standard

† In method 1, a DB-5MS column with a flow rate of 0.8 mL/min was used. Column length was 25 m with an inner diameter of 200 µm, and a 0.33 µm nonpolar phenyl arylene polymer film.

‡ In method 2, a HP-5MS with a flow rate of 1 mL/min was used. Column length was 30 m with an inner diameter of 250 µm, and a 0.25 µm 5% phenyl methyl silox film.

◊ Assuming neutral molecule and full protonation.

Metabolite fragmentation

A series of target ions were used for quantitation and qualifier ions were used to verify the target ion originated from the compound of interest. These ions and the number of derivatized moieties are listed in Table 7.7.

Table 7.7: Fragmentation of methoxime and tert-butylsilyl derivatized metabolites

Metabolite	# TBDMS	# MeOxAm	Deriv. Mass	Target Fragment	Target Ions	Qualifier Fragment	Qualifier Ion	Secondary Qualifier Ion
L-2-Hydroxyglutarate	3	0	490	M-57	433-438	M-15	475	N/A
(3) β-Hydroxybutyrate	2	0	332	M-57	275-279	M-173	159*	N/A
5-Hydroxydecanoic acid	2	0	416	M-57	359	M-15	401	N/A
2-Phosphogylcerate	4	0	642	M-57	585	Other	453	N/A
3-Phosphogylcerate	4	0	642	M-57	585-588	M-159	483	N/A
5-oxoproline	2	0	357	M-57	300	M-85	272	N/A
Acetoacetate	1	1	245	M-57	188-192	M-15	230	N/A
Alpha-ketoglutarate	2	1	403	M-57	346-351	M-15	388	N/A
Alanine	2	0	317	M-57	260-263	M-85	232	N/A
Asparagine	3	0	474	M-57	417-421	M-159	315	N/A
Aspartate	3	0	475	M-57	418-422	M-85	316	N/A
Citrate	4	0	648	M-57	591-597	M-189	459	N/A
Cysteine	3	0	463	M-57	406-409	M-159	378	N/A
Dihydroxyacetone phosphate	3	1	541	M-57	484-487	M-85	526	N/A
Fumarate	2	0	344	M-57	287-291	M-15	329	N/A
GABA	2	0	331	M-57	274-278	M-15	316	N/A
Glyceraldehyde-3-phosphate	3	1	541	M-57	484-487	M-85	456	N/A
Glutamate	3	0	489	M-57	432-437	M-159	330	N/A
Glutamine	3	0	488	M-57	431-436	M-159	329	N/A
Glycine	2	0	303	M-57	246-248	M-85	218	N/A
Histidine	3	0	497	M-57	440-446	M-159	338	N/A
Hypotaurine	2	0	337	M-57	280-282	M-15	322	N/A
Isocitrate	4	0	648	M-57	591-597	M-189	459	N/A
Isoleucine	2	0	359	M-57	302-308	M-85 and M-159	274	200
Lactate	2	0	318	M-57	261-264	M-85 and M-159	233	159
Leucine	2	0	359	M-57	302-308	M-85 and M-159	274	200
Lysine	3	0	488	M-57	431-437	M-159	329	N/A
Malate	3	0	476	M-57	419-423	M-15	461	N/A
Methionine	2	0	377	M-57	320-325	M-85	292	N/A
Methylsuccinate	2	0	360	M-57	303	M-15	345	N/A
N-Acetylaspartate	3	0	517	M-57	460	M-159	358	N/A
Norleucine	2	0	359	M-57	302-308	M-85 and M-159	274	200
Norvaline	2	0	345	M-57	288-293	M-85 and M-159	260	186
Oxaloacetate	2	1	389	M-57	332	M-15	374	N/A
Palmitic Acid	1	0	370	M-57	313	N/A	N/A	N/A
Phosphoenolpyruvate	3	0	510	M-57	453-456	M-15	495	N/A
Phenylalanine	2	0	393	M-57	336-345	M-85	308	N/A
Proline	2	0	343	M-57	286-291	M-85	258	N/A
Pyruvate	1	1	231	M-57	174-177	M-131	100	N/A
Serine	3	0	447	M-57	390-393	M-159	288	N/A
Succinate	2	0	346	M-57	289-293	M-15	331	N/A
Taurine	2	0	353	M-15	296-298	M-57	338	N/A
Threonine	3	0	461	M-57	404-408	M-85	376	N/A
Tyrosine	3	0	523	M-57	466-475	M-85	438	N/A
Valine	2	0	345	M-57	288-293	M-85 and M-159	260	186

* $[M-159]^+$ in β-Hydroxybutyrate found to be due to loss of carbons 3 and 4 (Des Rosiers et al., 1991)

Challenges with specific metabolites

The metabolites listed in Tables 7.6 and 7.7 are not inclusive of every metabolite examined in this work. The stability of a subset of these molecules was considered and summarized in Figure 7.7 and Figure 7.8. Other more metabolite-specific challenges associated with quantitation are listed below:

- **5-oxoproline:** Likely cannot quantify reliably due to contribution of degraded glutamine to signal.
- **2-PG: 3**-PG may interfere with quantitation. 2- PG has two peaks - one higher abundance that overlaps with 3-PG and one that is unique to 2-PG with a RT about 0.6 minutes earlier (Method 1). Low abundance.
- **Acetoacetate:** Standard can be detected, but not reliably in retina or eyecup. Pooling did not improve sensitivity. Suggest alternate derivatization or stability study.
- **Alanine:** Proximity to large peak at 17.1 minutes (Method 1, thought to be carbonate) frequently interfere with automated quantitation in MSD ChemStation. Can change range of integration in software to reduce frequency of inaccurate integration.
- **Arginine:** Previous work has shown that arginine, after TBDMS-derivatization, transforms into ornithine (Corso et al., 1993). It is effectively impossible to quantify with our approach.
- **Lactate:** Significant and unpredictable background levels.
- **GABA:** Co-elutes partially with proline and succinate.
- **Glycine:** Frequently observe a significantly larger peak with no discernable explanation.
- **Glutamine:** Glutamine is unstable and signal declines with time. Hypothesized that it cyclizes into 5-oxo-proline. A peak at 25.87 minutes (Method 1) containing the $[M-57]^+$, $[M-15]^+$, $[M-85]^+$, and $[M-159]^+$ ions that correlate with 5-oxoproline were observed in a full scan spectra of glutamine standard.

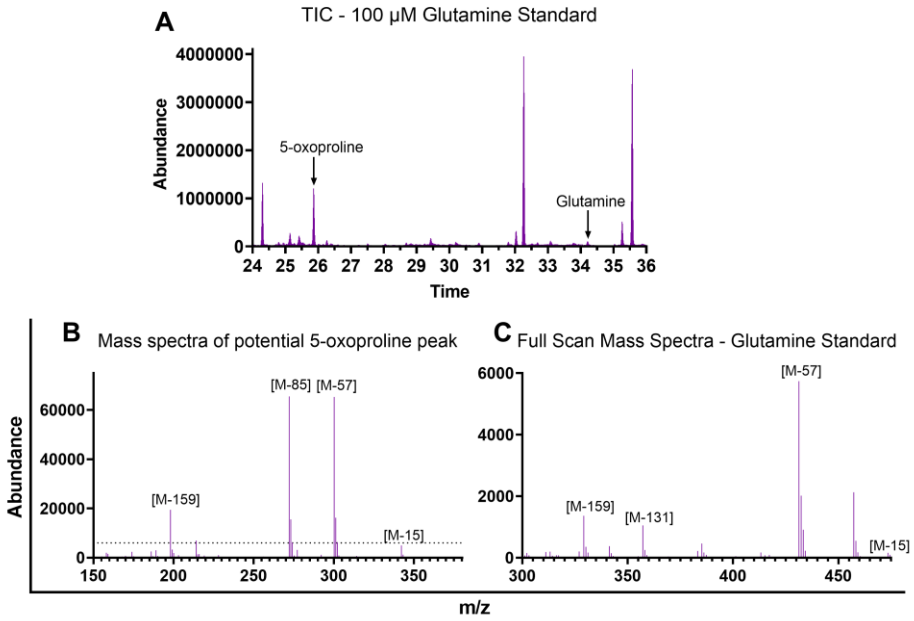

Figure 7.4: Glutamine appears to degrade into 5-oxoproline.

Upon injection of a 100 µM standard of pure glutamine (99% purity), we identified two peaks of interest in the total ion chromatogram (TIC) that were not as abundant in a process blank (A): a peak for glutamine at about 34.2 minutes and a proposed peak representing a cyclized derivative of glutamine, 5-oxproline, at about 25.8 minutes. Common fragments in TBDMS-derivatized molecules including $[M-57]^+$, $[M-15]^+$, $[M-85]^+$, $[M-131]^+$, and $[M-159]^+$ are labeled in the mass spectra of proposed 5-oxoproline (B) and glutamine (C). Note the significantly higher signal from 5-oxoproline (B) compared to glutamine (C), with the y-axis maximum in C shown as a dotted line in B.

- **Histidine:** Low quantities in tissues. Need to pool retinas or eyecups for reliable quantitation. M0 signal valid for unlabeled quantitation, but there is background signal in isotopologues. If considering ^{13}C-flux measurements, unlabeled matched tissues will be necessary for correction.
- **Isoleucine:** M0 signal valid for unlabeled quantitation, but there is background signal in isotopologues. If considering ^{13}C-flux measurements, unlabeled matched tissues will be necessary for correction.
- **Leucine:** M0 signal valid for unlabeled quantitation, but there is background signal in isotopologues. If considering ^{13}C-flux measurements, unlabeled matched tissues will be necessary for correction.
- **Oxaloacetate:** Standard can be detected, but not reliably found in retina or eyecup.

- **Palmitic acid:** Significant background levels. Important consideration if considering ^{13}C-flux measurements in fatty acids.
- **Phenylalanine:** M0 signal valid for unlabeled quantitation, but there is background signal in isotopologues. If considering ^{13}C-flux measurements, unlabeled matched tissues will be necessary for correction.
- **Proline:** Co-elutes partially with GABA and succinate. Possible interference with ^{13}C-flux measurements due to shared ions.
- **Succinate:** Co-elutes partially with GABA and proline. Possible interference with ^{13}C-flux measurements due to shared ions. Observed background in some isotopologues.
- **Taurine:** Shared peaks with phosphoric acid. Molecule is unstable in a standard mix – must be prepared fresh for accurate quantitation.
- **Tyrosine:** M0 signal valid for unlabeled quantitation, but there is background signal in isotopologues. If considering ^{13}C-flux measurements, unlabeled matched tissues will be necessary for correction.

Representative Results and Method Optimization

Mouse retina and eyecup in full scan and SIM modes

The metabolites extracted from a single young mouse retina and a single eyecup were derivatized in a final volume of 20 µL. After splitless injection of 1 µL run in SIM and a second splitless injection of 1 µL in full scan, there are significant differences in background signal and the final results (Figure 7.5). The full scan TICs (A and C) tend to have a more intense base peak and higher background signal, although even in SIM mode the mouse retina (B) has a very intense base peak (most often Taurine at 25.1 minutes). In SIM mode, the base peak and overall complexity of the eyecup TIC declines (D) where the peak at about 17 minutes (likely derivatized carbonate) tends to be the most intense ion.

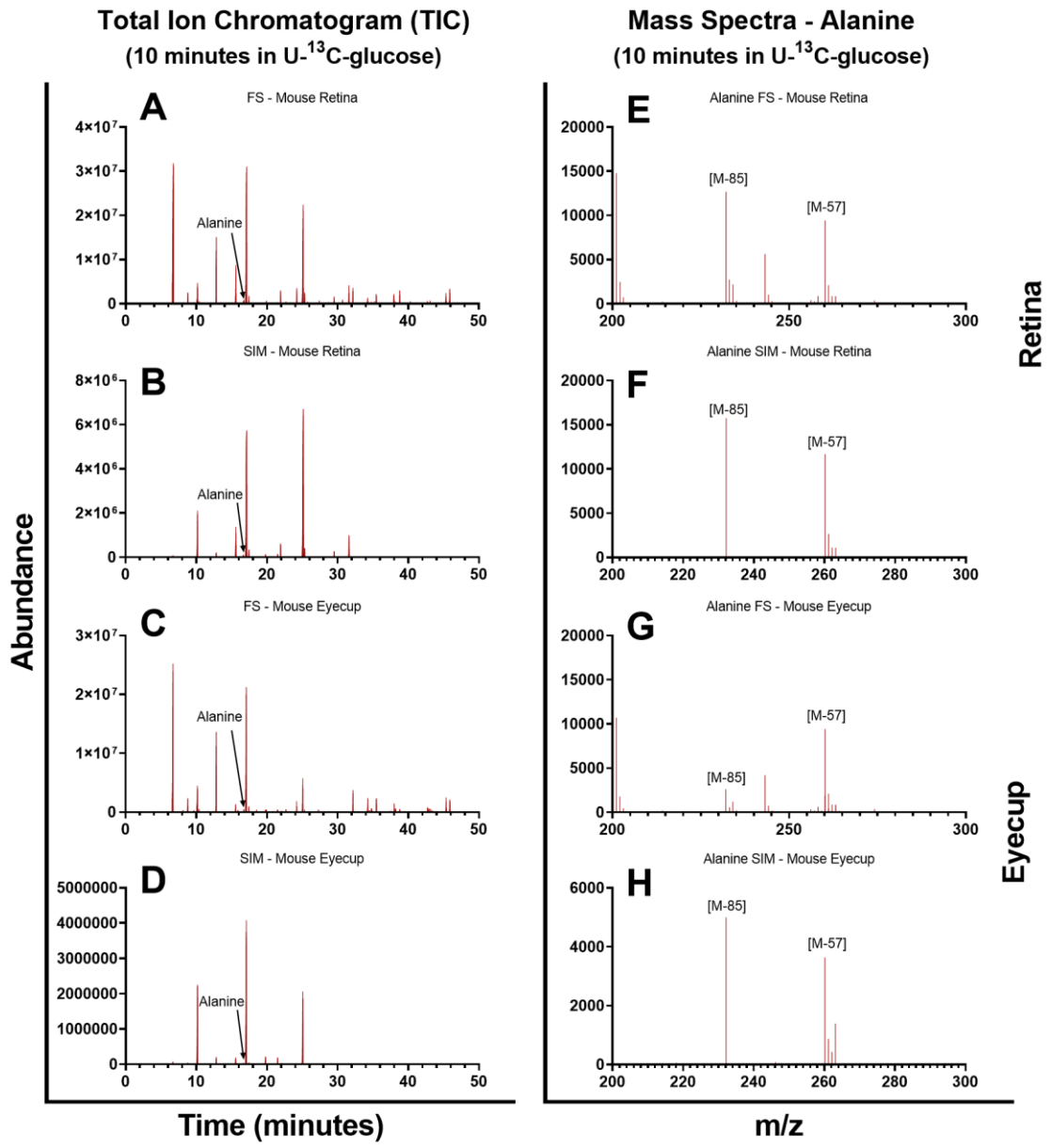

Figure 7.5: Comparing SIM and full scan mode.

Comparison of the total ion chromatograms (A-D) and mass spectra (E-H) in both SIM and full scan modes. After a 10 minute incubation in U-^{13}C-glucose, a retina (A, B, E, and F) and eyecup (C, D, G, and H) are shown here.

In the TICs shown (**Figure 7.5A-D**), the metabolite alanine has a slightly shorter retention time than the large peak at 17 minutes. The location of the alanine peak is indicated with an arrow in each panel. When the mass spectrum is extracted from each alanine peak, additional differences in the full scan and SIM modes emerge. The isotopic distribution improves in eyecups in SIM mode (H) relative to full scan mode (G).

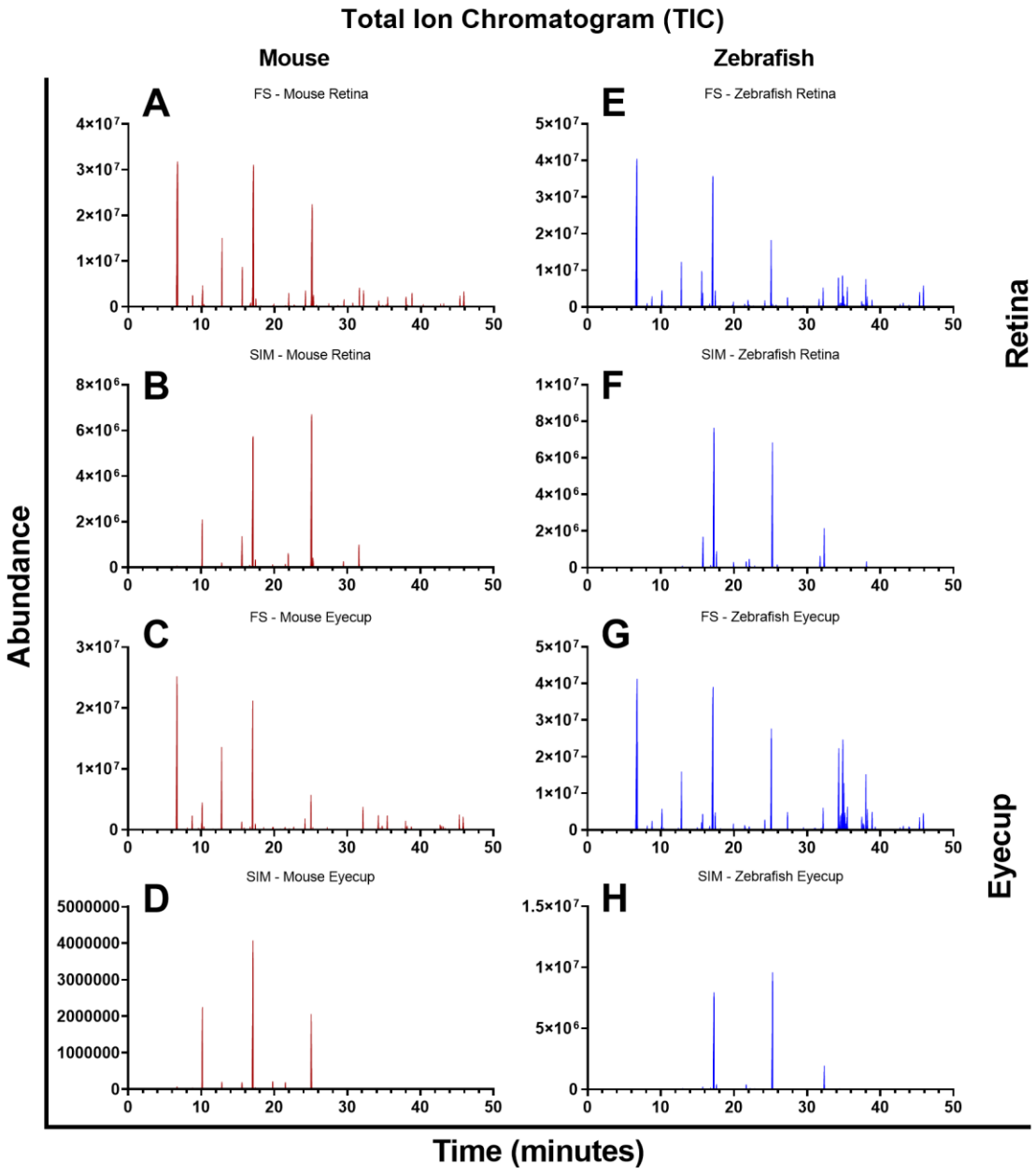

Figure 7.6: Comparing mouse and zebrafish retinas by GC-MS.

The total ion chromatograms in full scan and SIM mode are shown for retinas and eyecups from mice and zebrafish.

Comparison between mouse and zebrafish retina and eyecup

Mice and zebrafish can provide complementary insight into the study of vision. Although sensitivity for the majority of analytes considered in mice is adequate, the lower quantity of tissue in a single zebrafish eye was important to consider (Figure 7.6). Rather than

the standardized 20 µL volume in murine tissues, the metabolites extracted from a single young zebrafish retina and a single eyecup were derivatized in a final volume of 16 µL. The base peak intensities were maintained or improved in zebrafish relative to mice with the lower derivatization volume, although the total starting material is lower. We found that a single zebrafish retina and eyecup provide sufficient material in a slightly reduced volume to still facilitate multiple injections of analyte with peak intensities comparable to mice.

Eyecup homogenization approach

The yield and variability of metabolite extraction in eyecups were compared using the Tissumizer to Dounce homogenizer. There was not a significant change in yield, but a noticeable decrease in variability. Due to the potential for sample loss and increased variability associated with the Tissumizer, it is recommended that the Dounce homogenizer be used for eyecup metabolite extraction.

Metabolite stability

Other work described in this volume included high-throughput datasets. In addition to concerns with batch effects, analyte stability is critical for a successful experiment. In the approach detailed here, the 49 minute gradient of each run extends to a total of approximately 53 minutes per sample when needle washes and the injection are accounted for.

To test the stability of TBDMS-derivatized metabolites under the conditions this protocol has been optimized for, a pooled sample was generated using retinas from six mice. The 12 retinas were processed individually from homogenization, sonication, protein precipitation, and supernatant isolation after clarification. The supernatant from the 12 retinas were pooled and mixed to generate a pooled sample. This pooled sample was equally split into a total of 9 vials and all aliquoted samples were dried down together.

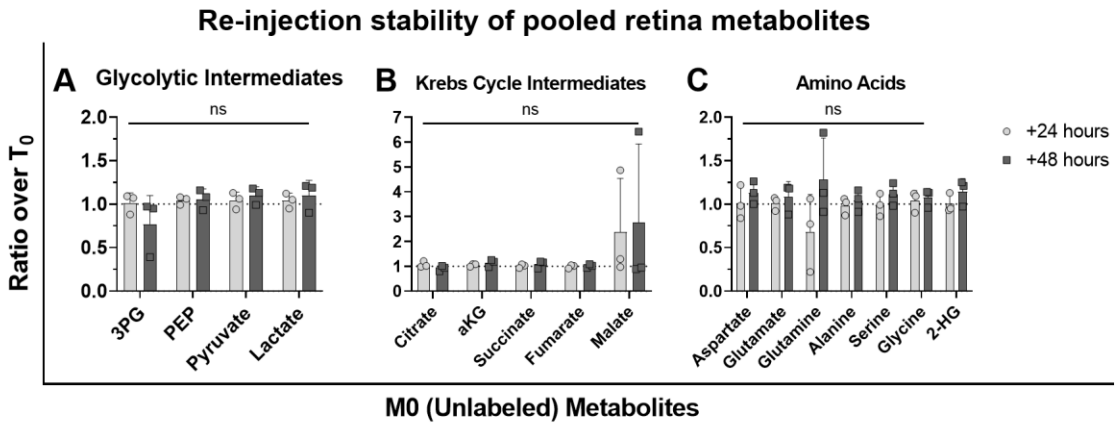

Figure 7.7: Metabolite ratios in the same sample after re-injection 24 and 48 hours later.

Three aliquots from a single pool of retinal metabolites were re-injected after 24 and 48-hours. For individuals vials, the ratios of the 24-hour timepoint over baseline and 48 hour- timepoint over baseline showed that overall, the metabolites we examined were stable up to 48 hours. An additional set of three replicates at 24 hours is shown in **Figure 7.8**.

Of the 9 samples, three were injected immediately after derivatization (T_0) to acquire baseline values for the pooled sample. The samples were re-capped immediately after injection to reduced evaporation. The samples were re-injected after 24 hours, re-capped, and injected again at 48 hours. When the ratio of the 24-hour or 48-hour IsoCor-corrected M0 metabolite intensities were taken as a ratio over T_0 (**Figure 7.7**), there were no statistically significant differences in the quantity of metabolites over time. This spanned glycolytic intermediates (A), Krebs cycle intermediates (B), and amino acids (C). However, it is important to emphasize that this study of TBDMS-metabolite stability only spanned a subset of the potential metabolites we measured. Future examinations of stability in eyecups and other tissues would be beneficial to rule out any effect of the sample matrix on analyte stability.

The slight differences in glutamine and 3PG after 24 hours were further tested using three additional aliquoted samples that had derivatized at the same time as the baseline vials described in **Figure 7.7**, but had been allowed to remain sealed on the autosampler until 24 hours later. These samples values were pooled with those from the re-injected baseline samples 24 hours later. There were no statistically significant

differences in metabolite abundance associated with 24 hours on the autosampler in metabolites with lower (A) or higher intensity (B) responses.

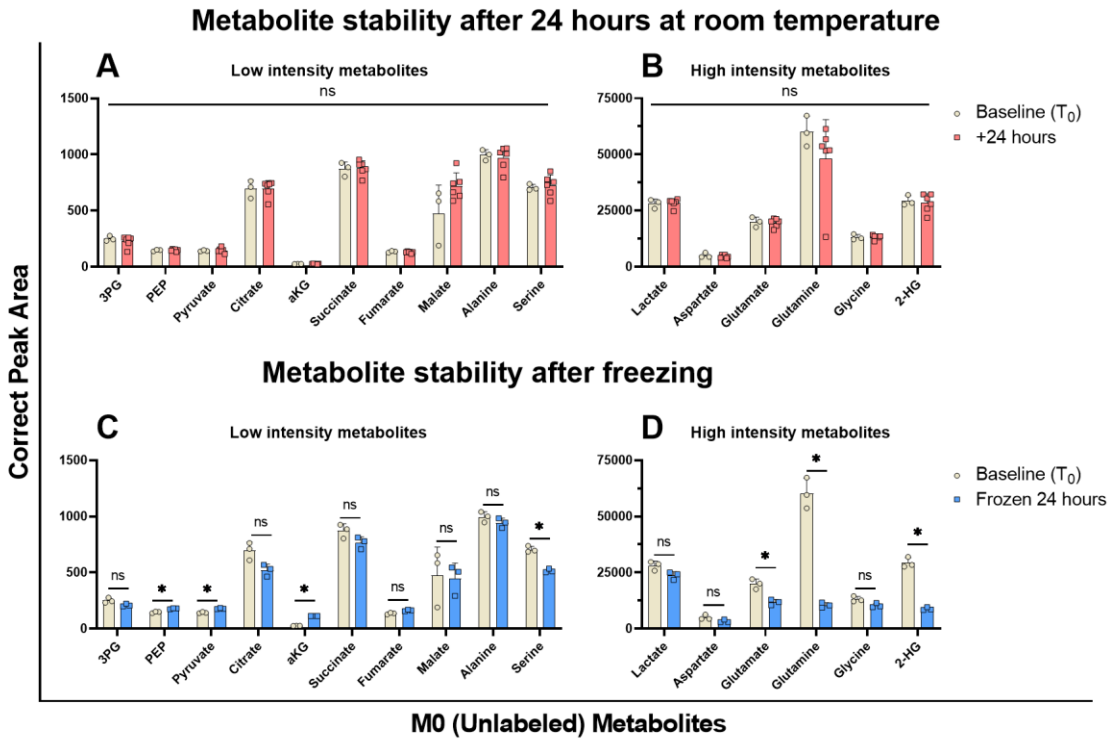

Figure 7.8: Quantifying levels of derivatized metabolites after 24 hours at room temperature and 24 hours frozen at -80°C.

Metabolites were grouped as “low intensity” and “high intensity” for ease of viewing the data based on the AUC. The 24 hours post-derivatization group includes three baseline replicates after 24 hours and three vials that had not been injected previously. After 24 hours (A-B), there were no significant alterations in the glycolytic intermediates, Krebs cycle intermediates, or amino acids measured. 24 hours of freezing caused significant changes in 7 of the 16 metabolites considered in this study. Increases were seen in PEP, pyruvate, and alpha-ketoglutarate. A decline in abundance was seen in serine, glutamate, glutamine, and 2-hydroxyglutarate. Note that the baseline values in A and C, and B and D, are the same samples plotted with a different dataset for comparison.

When preparing derivatized samples, unanticipated problems with instrumentation may necessitate storage of derivatized samples. For example, a leak in the septum, reaching the end of a helium tank, or the demise of a filament can set the timing of an experiment back at least 24 hours. Thus, to determine whether samples were salvageable after freezing, the stability of the derivatized metabolites after freezing for 24 hours were tested using the pooled samples. These 3 vials were derivatized at the same time as the baseline vials described in Figure 7.7, but rather than being run immediately were

stored at -80°C for 24 hours. The metabolites were grouped as lower intensity peaks in Figure 7.8**C** and higher intensity peaks in Figure 7.8**D** for easier visualization. We identified several metabolites with differences in abundance. PEP, pyruvate, and alpha-ketoglutarate were increased in abundance (Figure 7.8**C**) while serine (Figure 7.8**C**), glutamate, glutamine, and 2-hydroxyglutarate (Figure 7.8**D**) were decreased with freezing. Glutamine and 2-hydroxyglutarate were particularly impacted with approximately 5.7 and 3.3-fold decreases.

Discussion

In order to acquire the most metabolites in a single 49 minute gradient, the SIM organization and chromatography detailed for Method 1 are suggested as a baseline. However, it is important to acknowledge that there are several approaches which may improve the sensitivity of the assay, which currently suffers from unresolved interfering signals that can make isotopologue quantitation challenging for some metabolites. Altering the solvents use for metabolite extraction may permit the continued isolation of the hydroxyl acids and amino acids of interest while reducing the current approach utilizes only water and methanol. Recent work has examined the performance of a ternary combination of water, isopropanol, and acetonitrile to extract metabolites in plasma, tissues, urine, and cells (Fiehn, 2016; Yerges-Armstrong, Laura M. Ellero-Simatos et al., 2013). Although a lipid clean-up step was recommended by both groups, it may be unnecessary due to the small quantity of tissue being examined in our approach. It is currently recommended that operators utilize 2-3 process blank injections at the start of every set of sample runs to account for a consistent shift in retention time seen in the first couple injections. Expanding this to include biological samples to “condition” the sample pipeline could reduce the risk of the samples of interest interacting with catalytic sites (Fiehn, 2016) and thus improve sample signal. This could be of particular importance when new injection components or columns have been installed on the instrument.

In addition to changing the metabolite extraction and GC-MS workflow, the data processing pipeline can be improved to increase throughput, transparency, and In the analysis of isotopologue distributions, caution in interpreting results is necessary due to the frequency of artifacts related to unresolved interfering signals. Section 7.10 details specific examples of concerns, including metabolites with high background in M0 (lactate, succinate, palmitate) or in isotopologues (Leucine, isoleucine, tyrosine, etc.). The current workflow of MSD ChemStation with correction in IsoCor is not sufficient to disentangle what signal in these M1 or higher isotopologues is due to interfering background of the molecule. A newer tool called FluxFix (Trefely et al., 2016)may be useful to overcome these issues. To remove background in lactate, unlabeled snap-frozen tissues could be extracted and run alongside labeled tissues. The resulting responses acquired through MSD ChemStation can be plugged into the program to use the natural isotopologue distribution for a chosen analyte in the unlabeled tissues and use that to correct the labeled tissues. To make analysis more transparent and reproducible without requiring the financial investment of proprietary software, swapping to a new program for the interpretation of chromatograms and mass spectra would be beneficial. There are two open-source, cross-platform programs that show promise: OpenChrom (Wenig and Odermatt, 2010) and Skyline (Adams et al., 2020; Pino et al., 2020).

Finally, confirmation of the stability of the metabolites is advisable. We found that the introduction of a freeze-thaw cycle could drastically reduce the resolved intensities of numerous molecules. Despite the notion that cold temperatures Is best for preservation, that does not appear to be the case for TBDMS-derivatized metabolites. Short-term storage at room temperature is preferrable in this case. Additionally, a similar study should be performed on all metabolites of interest in each tissue being analyzed to ensure all changes observed relate to biological changes between groups rather than differences associated with sample preparation. In particular, the degradation of glutamine in standards and biological samples will be critical in future work. Testing the stability of glutamine standards alongside a standard solution of pure 5-oxoproline can quickly confirm these anecdotal observations.

Materials and Reagents

Materials to prepare KRB buffer

- Large graduated cylinder (500 mL+)
- 15 mL conical vials
- 50 mL conical vials
- Large autoclaved Erlenmeyer flask or glass bottle to mix solution
- Magnetic stir bar and hot plate if needed
- One filter (Select size based on volume being prepared):
    - PVDF Membrane 1000mL, 0.22 µM GV (MilliporeSigma - SCGVU11RE)
    - PVDF Membrane 500mL, 0.22 µM GV (MilliporeSigma - SCGVU05RE)

Reagents to prepare KRB buffer

- Milli-Q or LC-grade water
- Solids*
    - NaCl (S5886-1KG)
    - KCl (P5405-250G)
    - KH_2PO_4 (P5655-100G)
    - $MgSO_4$-$7H_2O$ (M1880-500G)
    - HEPES (H4034-100G)
    - $CaCl$-$2H_2O$ (C7902-500G)
    - $NaHCO_3$ (S5761-500G)

    *Product numbers from MilliporeSigma

Materials required for flux experiments

- Dissection instruments†
    - Larger curved tweezers (14188)
    - Two sets of tweezers (500342)
    - Microscissors (501777)
    - 20, 22 or 24 gauge needle

- 35 mM tissue culture dishes
- Labeled tubes for tissues
    - 1.5 mL tubes if using Dounce homogenizer and sonicator for extraction
    - 2 mL tubes if using Tissumizer and sonicator for extraction
- Liquid nitrogen dewar

† Product numbers from World Precision Instruments

Reagents required for flux experiments

- Prepared KRB buffer
- Labeled metabolite stock solutions (Cambridge Isotope Laboratories)
    - D-Glucose (U-^{13}C6, 99%) (CLM-1396-PK)
    - L-Glutamine (U-^{13}C5, 99%) (CLM-1822-H-PK)
- Unlabeled metabolite stock solutions
- Hanks Buffered Salt Solution (HBSS) (ThermoFisher - 14175095)
- Wet ice (To chill HBSS to rinse before snap freezing)
- Liquid nitrogen

Materials required for metabolite extraction

- Dounce homogenizer (Sigma Aldrich - Z359971-1EA)
- Disposable pestles (USA Scientific Plastics - 1415-5390)
- Ultra-Turrax Tissumizer (Tekmar Company - #SDT 1810)
    - Fitted with 8 mm dispersing tool number S25N-8G
- Microcentrifuge set to or stored at 4°C
- 5.0 mL or higher capped vials
- Spare 1.5 mL or 2.0 mL Eppendorf tubes for buffers
    - Store 3-6 over dry ice with caps removed to chill pipette tips

Reagents required for metabolite extraction

- Dry ice
- Wet ice

- MS-grade ethanol
- MS-grade methanol
- Internal standards:
    - Methylsuccinate (100 µM in MS-grade water)
    - L-norvaline (100 µM in MS-grade water)
    - L-norleucine (100 µM in MS-grade water)

Materials required for derivatization

- Lyophilizer to dry samples
- Oven set to 37°C
- Heating block set to 70°C
- Microcentrifuge
- Fume hood to handle pyridine
- High-recovery glass inserts (Agilent - 5183-2085)
- Autosampler vials (Agilent - 5182-0715).
- Lids containing PTFE silicone septa (Agilent - 5182-0717)

Reagents required for derivatization

- Dry ice
- Solid methoxyamine HCl (MilliporeSigma - 226904-1G)
- N-tertbutyldimethylsilyl-N-methyltrifluoroacetamide (MTBSFA) (MilliporeSigma - 394882-10X1ML)
- Dry pyridine (MilliporeSigma - 270970-4X25ML)
    - Recommend storing in desiccator up to two months

Acknowledgments

The work described in this chapter was used to generate results in Chapter 3, Chapter 4, Chapter 5 and Chapter 6. Martin Sadilek was instrumental in developing these

methodologies and training the other individuals who contributed to this work. Brian Robbings assisted in much of the method development and the stability study. Mark A. Kanow, Celia M. Bisbach, Connor S.R. Jankowski, and Christopher C. Farnsworth also gave of their time for experiments and thoughtful discussion. The optimized approach detailed here was built upon the foundations laid by Jianhai Du and Andrei O. Chertov.

This work was supported by NIH funding to Kristine Tsantilas (Genetic Approaches to Aging Training Grant T32 AG000057 and Biological Mechanisms for Healthy Aging Training Grant T32 AG066574), James B. Hurley (Determinants of Rod and Cone Response Characteristics 5R01EY006641, and Control of Photoreceptor Metabolism 5R01EY017863), and Susan E. Brockerhoff (2R01EY026020).

Chapter 8 - Conclusions and Future Directions

The retina, RPE, and choroid form a dynamic and highly specialized ecosystem

The work in Chapter 2 (Kanow et al., 2017) provided further evidence to suggest that the ANLS approach described in Chapter 1 likely does not hold true in the retina. Photoreceptors express GLUT1, whereas glia do not, making it challenging to accept that glia in the retina are performing the bulk of glycolytic reactions in the eye (Figure 2.1). To show that photoreceptors use glucose they are capable of transporting, we fed a fluorescent glucose analog, 2-NBDG (Yoshioka et al., 1996), to mice and zebrafish and used a retinal slice preparation (Giarmarco et al., 2018) to image glucose uptake in live photoreceptors and the inner neuron. Photoreceptors preferentially took up glucose with only sporadic and low intensity uptake in other neurons or glia (Figure 2.2). The location of the RPE - situated directly between the choroid and retina – was hypothesized to contribute to the metabolic exchanges between choroid and the retina. However, given its proximity to the vasculature, what incentive do RPE cells have to pass along glucose? We found that retinas generate large amounts of lactate *ex vivo*, while eyecups containing RPE generated significantly less (Figure 2.4). Additionally, the RPE appears to prefer lactate as a substrate (Figure 2.5, Figure 2.6, Figure 2.7, and Figure 2.9). We postulate that the glycolytic retina consumes large quantities of glucose, generates lactate that it exports to the extracellular space, where it can be taken up the RPE and used to feed its mitochondria (Figure 2.10)

Zebrafish have a cone-dominant retina which makes them uniquely suited to the study of cone photoreceptor. In Chapter 3, we considered the dynamics of cone mitochondria and metabolism in circadian rhythm (Giarmarco et al., 2020). The zebrafish retina is motile, with retinomotor movements that change the structure of the retina depending on the light and circadian rhythm (Burnside et al., 1993; Menger et al., 2005). We discovered that zebrafish cone mitochondria in the ellipsoid reason are highly dynamic. This study serves well to remind the reader that mitochondria are so much more than just a means of ATP-generation (Hoppins, 2014). The size, distribution, complexity, and quantity of mitochondria change with circadian time in different ways depending on the cone subtype (Figure 3.1, Figure 3.2, and Figure 3.3). While the fish sleeps, retinal mitochondria are quite active. Mitogenesis genes appear to peak in the evening in

tandem with a decline in autophagosomes and mitochondrial metabolism is increased due to increased succinate dehydrogenase activity (Figure 3.4 and Figure 3.6). Of all the discoveries in this research, chasing down the origin of the dark deposits that had been seen regularly in SBFSEM images of cone mitochondria was perhaps the most mysterious. These dark deposits were found to distort mitochondrial and plasma membranes, and even be extruded from the photoreceptor (Figure 3.5A and B). Stranger still, we found branched networks that connected these mitochondrial-associated deposits in between different photoreceptors (Figure 3.5C-E). These remarkable structures were found to occur more frequently at night. Future work will be needed to determine the composition of these mitochondria-connecting networks and their precise purpose.

NNT is likely not essential in the eye

The dominant model of vision in the field is far and away the C57Bl/6 substrains (Bryant, 2011). The C57Bl/6J mouse strain has a large deletion in NNT that renders it non-functional (Toye et al., 2005). This mutation impacts causes disease (Rydström, 2006), and we hypothesized that its loss would impact vision and the process of reductive carboxylation which is used by RPE cells in culture (Du et al., 2016b). We considered these possibilities in Chapter 4.

Vision was found to be preserved relative to a non-degenerative control (129S1/SvImJ). While RPE cells were found to be able perform reductive carboxylation outside of culture, the significance of the pathway *in vivo* remains to be seen. Based on our findings (Figure 4.6 and Figure 4.8), NNT is not necessary for reductive carboxylation. We observed no change in the rate of flux in the pathway when NNT is non-functional in C57Bl/6J mice relative to mice with functional NNT (C57Bl/6N and 129S1/SvImJ). However, withholding glucose was sufficient to increase flux in 6N mice (Figure 4.7). Young C57Bl/6N mice carrying the Rd8 mutation appeared to be metabolically stable *ex vivo* relative to a non-degenerative control (129S1/SvImJ).

The aging ocular ecosystem is surprisingly robust despite functional decline

We used targeted GC-MS (Chapter 7), a continuous perfusion apparatus, enzymatic assays, and ERGs to characterize the function of the visual system and how metabolic capacity is altered in aging (Chapter 5). Additionally, we utilized two mitochondrial therapeutic interventions – NMN and Elamipretide – to discern whether age-related vision loss could be slowed and if metabolism was impacted (Chapter 6). In this work we focused on the interplay of the retina and the RPE-choroid-sclera complex (eyecups).

We confirmed previous reports that have shown the ERG response in mice declines with age (Kolesnikov et al., 2010; Wang et al., 2018). Both rod and cone-derived vision (Figure 5.2) were shown to decline in C57Bl/6J mice by 26 months of age. We also found that temporal resolution in these animals was reduced (Figure 5.2), suggesting the ability of the mouse to identify and track moving objects (Fleishman et al., 2019; McComb et al., 2010) had declined.

Retinas were remarkably stable *ex vivo*. Glucose uptake, glucose flux through glycolysis and the Krebs cycle, amino acid pool size, anaplerotic flux from glucose or glutamine, and mitochondrial function measured in terms of ATP pools and the OCR in response to succinate or glutamine were unaltered by age (Figure 5.5, Figure 5.9, Figure 5.10, Figure 5.12, and Figure 5.13). Limited alterations were seen in oxidative glutamine metabolism, however none of these changes reached significance (Supplementary Figure 5.4).

Eyecup glucose metabolism mirrored the retina in that it was broadly unchanged by age in terms of uptake and flux into glycolysis and the Krebs cycle (Figure 5.3 and Figure 5.5). There were no significant age-related change in amino acid pools or anaplerotic pathways (Figure 5.10, Figure 5.12, and Figure 5.13). However, Krebs cycle intermediates derived from glutamine were found to reach a lower threshold more quickly than in younger animals which generated increased quantities of M4 intermediates by 90 minutes (Figure 5.8Supplementary Figure 5.5: Pool sizes and

product:reactant ratios in young and aged eyecups indicate an age-related decline in glutamine flux. and Supplementary Figure 5.5). This decreased flux through glutamine metabolism was supported by a modest drop in the glutamine-driven OCR in a perifusion device (Figure 5.9). However, this experiment was performed with a low sample number (n=3). We believe that these data suggest we have identified a defect in glutamine metabolism in aged eyecups. Future experiments will be necessary to determine where the deficiency originates.

Both NMN and ELAM had negligible impact on glucose metabolism of retinas and eyecups. Given the limited metabolic change with age, this is not particular surprising. However, we found modest improvements with ELAM alone and ELAM+NMN. Both regiments on tended to improve scotopic, rod-mediated vision (Figure 6.5). ELAM-alone may also have prevented vision loss in photopic circuits as measured with single-flash ERGs and the temporal response (Figure 6.8 and Figure 6.12). We frequently found that a sub-set of mice responded quite well to treatment, while others did not or simply retained baseline visual function. Future work with these interventions would likely best be served beginning with an earlier start time for dosing to maximize their efficiency in salvaging existing cellular function.

This relative metabolic stability of these tissues could be perplexing given that other reports have provided strong evidence of physical and functional alterations with aging in the retina and RPE (Bonilha, 2008; Cavallotti et al., 2004; Gu et al., 2012; Kolesnikov et al., 2010; Samuel et al., 2011; Wang et al., 2018). Additionally, there is previous evidence of that tissues in the eye (Kam et al., 2019b; Wang et al., 2018) and other organs experience metabolic changes with aging (Angelin et al., 2017; Camandola and Mattson, 2017; Chiao and Rabinovitch, 2015; Demontis et al., 2013; Garvey et al., 2014; Goyal et al., 2017; Nishikawa et al., 2014; Ohlendieck, 2011; Ritterhoff and Tian, 2017; Vitorica et al., 1981; Weyand and Goronzy, 2016). However, the majority of these experiments were examining either function *in vivo,* protein localization, or steady-state metabolite abundance. The *ex vivo* approach we used allows us to directly probe the tissue's metabolic capacity free of damaged vasculature or other malfunctioning

neighbors. In this way, we can effectively ask whether a tissue has any intrinsic alterations that will still be observable despite sufficient nutrition. In eyecups, we observed an intrinsic change in oxidative glutamine metabolism. However, the retina was effectively unaffected by age. We propose the use of a corresponding *in vivo* approach wherein a labeled intermediate is injected directly into the bloodstream, permitted to circulate, and the tissue collected rapidly (TeSlaa et al., 2021) to obtain as close to a physiological response as possible. Using a paired *ex vivo* and *in vivo* approach in subsequent studies of metabolic capacity may permit the researcher to discern what changes are intrinsic to the tissue of interest and what changes are due to neighboring tissues failures. Our research suggests that declining blood vessel health vessel and lowered oxygen penetrance (Bata et al., 2019; Lin et al., 2019; Orlov et al., 2019; Wei et al., 2017) could be indicative of a nutritional bottleneck that we simply can't observe *ex vivo.* Should this hypothesis gain additional support, it is possible then that many of the age-related metabolic dysfunction we observe may be due in large part to degradation of the vasculature rather than solely damage to the organ itself.

GC-MS is broadly applicable to the study of metabolism in the eye

We utilized a GC-MS approach to examine the metabolome in retinal and eyecup explants in several capacities. Extracted metabolites were derivatized with methoximation and tert-butyldimethylsilylation reactions to increase their volatility and facilitate the use of GC-MS and Selected Ion Monitoring (SIM) mode to track specific analytes of interest (Fiehn, 2016; Kashutina et al., 1975; Kitson et al., 1996; Schummer et al., 2009). This assay can be re-tooled to target new analytes quickly and with high sensitivity. In this work, the number of metabolites tracked for isotopic tracing in a single injection across a 49 minute gradient was expanded to 40 which included 3 internal standards. In future iterations of this approach, the inclusion of an 4th internal standard with a retention time later in the gradient (>30 minutes) is advised to improve QC.

Variations of the assay were used to: characterize the ocular ecosystem (Chapter 2), study the circadian rhythm of metabolism (Chapter 3), find that the loss of NNT does not alter reductive carboxylation in the eye (Chapter 4), examine how the ocular metabolic

ecosystem is impacted by age (Chapter 5), and finally discern how elamipretide effects aged metabolism (Chapter 6).

Coupling the GC-MS approach outlined here with cellular enrichment could provide more cell-type specific information that is currently lacking. For example, serial sectioning of the retina (Reidel et al., 2011) could parse differences in metabolism relate to photoreceptors or the inner neuron. The removal of the RPE cells from the eyecup by altering a rapid, brush-based protocol (Wei et al., 2016) with cold 80% methanol could isolate choroidal signal from RPE.

Epigenetics in the eye is a promising new direction

Of the multitude of "-omics" technologies being broadly applied across biological studies, characterization of the epigenome represents an as yet understudied view of the ocular ecosystem. The structure of chromatin appears to follow a diurnal rhythm in photoreceptors (Hoppe et al., 2007). The epigenetic landscape of rods and cones in mice have been found to differ significantly (Hughes et al., 2017; Mo et al., 2016). The chromatin structure in rods depends on the preferred time of activity, with substantial differences between nocturnal and diurnal organisms (Solovei et al., 2009). For example, nocturnal mouse rod photoreceptors contain a large heterochromatic region in the interior of the nucleus (Eberhart et al., 2013; Kizilyaprak et al., 2010) compared to diurnal rods that have a heterochromatic region on the nuclear periphery (Solovei et al., 2009). Recent work suggests this structural peculiarity of inverted heterochromatin in photoreceptors may relate to improving contrast sensitivity by reducing light scatter (Subramanian et al., 2019). Interestingly, aberrant chromatin structure and DNA methylation have been found in models of retinitis pigmentosa (Farinelli et al., 2014). Characterizing the epigenome may help fill the gaps in the field's understanding of the various blinding diseases we currently lack effective treatments for including AMD, glaucoma, and diabetic retinopathy which appear to have epigenetic links (He et al., 2013; Li et al., 2016; Pennington and DeAngelis, 2015).

Expanding the breadth of model organisms in aging and vision research

Vision research is known for utilizing an array of different model organisms (Chapter 1). Geroscience is expanding beyond the common models that include the laboratory mouse, fruit flies (*Drosophila melanogaster*), worms (C*aenorhabditis elegans*), and yeast (*Saccharomyces cerevisiae*) (Taormina et al., 2019). Recent work has expanded to consider novel organisms (Mikuła-Pietrasik et al., 2021) such as naked mole rats (Buffenstein and Ruby, 2021), hydra (Tomczyk et al., 2015), ocean quahog bivalves (Butler et al., 2013; Gruber et al., 2015), zebrafish (Gilbert et al., 2013; Kishi et al., 2003; Van houcke et al., 2015), and the Greenland shark (Nielsen et al., 2016). All of these species have unique adaptations that render them uniquely suited to a biological question. For example, naked mole rats are significantly longer lived (>30 years) than laboratory mice (about 2 years). Examining what makes these organisms uniquely long-lived may shed light on biological approaches that could extend human lifespan.

One of the largest limitations in aging research – and certainly in vision science – is that experiments are frequently done in a single strain of a single species. While this certainly can help with decreasing variability in results, it does not increase the odds for the researcher that what they are seeing is not related to a strain-specific artifact. As was summarized in Chapter 4, even within a single mouse lineage different substrains can have deleterious mutations that may influence the outcome of an experiment. Employing multiple organisms to study a single process may improve our ability to identify truly conserved biological processes. For example, in an otherwise immaculate study on the use of NMN to mitigate age-related decline across a broad set of organs, the author's ability to interpret the improved ERG responses in aged mice was limited due to the Rd8 mutation being present in their line (Mills et al., 2016). The use of multiple organisms would serve to validate whether the impacts a researcher is seeing are describing a broadly physiological biological phenomenon or an artifact of the model of choice. This could make basic science approaches to research even more valuable when considering a translationally relevant system.

A new organism of particular relevance to aging vision is the turquoise killifish (*Nothobranchius furzeri*). This small, annual teleost is unique due to its reliance on diapause to survive their habitat drying completely for a significant part of the year and for their median lifespan of only 4 months (Hu and Brunet, 2018; Poeschla and Valenzano, 2020). This organism may represent one of the most efficient ways to study aging vision before moving into longer-lived organisms. Mouse lifespan is typically around two years (Taormina et al., 2019) and the lifespan in zebrafish is closer to three years (Gilbert et al., 2013; Kishi et al., 2003; Van houcke et al., 2015). Early work on the eye of has begun. The general structure of killifish retina shows it shares many features with other teleost fish like zebrafish (Gatta et al., 2014). With aging, the relative content of mitochondrial DAN appears stable (Hartmann et al., 2011). Now that the killifish genome has been sequenced (Valenzano et al., 2015), husbandry is being standardized (Dodzian et al., 2018; Žák et al., 2020), and novel tools are being developed (Harel et al., 2016), these little fish may become a revolutionary model to accelerate studies in aging vision.

References

Abate M, Festa A, Falco M, Lombardi A, Luce A, Grimaldi A, Zappavigna S, Sperlongano P, Irace C, Caraglia M, Misso G. 2020. Mitochondria as playmakers of apoptosis, autophagy and senescence. *Semin Cell Dev Biol* **98**:139–153. doi:10.1016/j.semcdb.2019.05.022

Ablonczy Z, Dahrouj M, Tang PH, Liu Y, Sambamurti K, Marmorstein AD, Crosson CE. 2011. Human retinal pigment epithelium cells as functional models for the RPE in vivo. *Investig Ophthalmol Vis Sci* **52**:8614–8620. doi:10.1167/iovs.11-8021

Abou-Hanna JJ, Leggett AN, Andrews CA, Ehrlich JR. 2021. Vision impairment and depression among older adults in low- and middle-income countries. *Int J Geriatr Psychiatry* **36**:64–75. doi:10.1002/gps.5394

Acín-Pérez R, Carrascoso I, Baixauli F, Roche-Molina M, Latorre-Pellicer A, Fernández-Silva P, Mittelbrunn M, Sanchez-Madrid F, Pérez-Martos A, Lowell CA, Manfredi G, Enríquez JA. 2014. ROS-triggered phosphorylation of complex II by Fgr kinase regulates cellular adaptation to fuel use. *Cell Metab* **19**:1020–1033. doi:10.1016/j.cmet.2014.04.015

Ackrell BA, Kearney EB, Mayr M. 1974. Role 3f oxalacetate in the regulation of mammalian succinate dehydrogenase. *J Biol Chem* **249**:2021–2027.

Adams KJ, Pratt B, Bose N, Dubois LG, St. John-Williams L, Perrott KM, Ky K, Kapahi P, Sharma V, Maccoss MJ, Moseley MA, Colton CA, Maclean BX, Schilling B, Thompson JW, Consortium ADM. 2020. Skyline for Small Molecules: A Unifying Software Package for Quantitative Metabolomics. *J Proteome Res* **19**:1447–1458. doi:10.1021/acs.jproteome.9b00640

Adijanto J, Du J, Moffat C, Seifert EL, Hurley JB, Philp NJ. 2014. The retinal pigment epithelium utilizes fatty acids for ketogenesis. *J Biol Chem* **289**:20570–20582. doi:10.1074/jbc.M114.565457

Adijanto J, Philp NJ. 2014. Cultured primary human fetal retinal pigment epithelium (hfRPE) as a model for evaluating RPE metabolism. *Exp Eye Res* **126**:77–84. doi:10.1016/j.exer.2014.01.015

Adler AJ, Southwick RE. 1992. Distribution of glucose and lactate in the interphotoreceptor matrix. *Ophthalmic Res* **24**:243–252. doi:10.1159/000267174

Aït-Ali N, Fridlich R, Millet-Puel G, Clérin E, Delalande F, Jaillard C, Blond F, Perrocheau L, Reichman S, Byrne LC, Olivier-Bandini A, Bellalou J, Moyse E, Bouillaud F, Nicol X, Dalkara D, Van Dorsselaer A, Sahel JA, Léveillard T. 2015. Rod-derived cone viability factor promotes cone survival by stimulating aerobic glycolysis. *Cell* **161**:817–832. doi:10.1016/j.cell.2015.03.023

Akimoto H, Kinumi T, Ohmiya Y. 2005. Circadian Rhythm of a TCA Cycle Enzyme Is Apparently Regulated at the Translational Level in the Dinoflagellate Lingulodinium polyedrum. *J Biol Rhythms* **20**:479–489. doi:10.1177/0748730405280811

Akimoto M, Cheng H, Zhu D, Brzezinski JA, Khanna R, Filippova E, Oh ECT, Jing Y, Linares JL, Brooks M, Zareparsi S, Mears AJ, Hero A, Glaser T, Swaroop A. 2006. Targeting of GFP to newborn rods by Nrl promoter and temporal expression profiling of flow-sorted photoreceptors. *Proc Natl Acad Sci U S A* **103**:3890–3895. doi:10.1073/pnas.0508214103

Alam NM, Iv WCM, Wong AA, Douglas RM, Szeto HH, Prusky GT. 2015. A mitochondrial therapeutic reverses visual decline in mouse models of diabetes. *DMM Dis Model Mech* **8**:701–710. doi:10.1242/dmm.020248

Alavi M V. 2016. Aging and Vision In: Bowes Rickman C, LaVail MM, Anderson RE, Grimm C, Hollyfield J, Ash J, editors. Retinal Degenerative Diseases. Basingstoke: Springer Nature. pp. 393–399. doi:10.1007/978-3-319-17121-0_52

Altimus CM, Güler AD, Alam NM, Arman AC, Prusky GT, Sampath AP, Hattar S. 2010. Rod photoreceptors drive circadian photoentrainment across a wide range of light intensities. *Nat Neurosci* **13**:1107–1112. doi:10.1038/nn.2617

Ambati J, Fowler BJ. 2012. Mechanisms of age-related macular degeneration. *Neuron* **75**:26–39. doi:10.1016/j.neuron.2012.06.018

Ames A, Li Y, Heher EC, Kimble CR. 1992. Energy metabolism of rabbit retina as related to function: High cost of Na+ transport. *J Neurosci* **12**:840–853. doi:10.1523/jneurosci.12-03-00840.1992

Amiri M, Hollenbeck PJ. 2008. Mitochondrial biogenesis in the axons of vertebrate peripheral neurons. *Dev Neurobiol* **68**:1348–1361. doi:10.1002/dneu.20668

Andersen B. 1980. Lack of deviation from Michaelis--Menten kinetics for pig heart fumarase. *Biochem J* **189**:653–654. doi:10.1042/bj1890653

Andrews RM, Griffiths PG, Johnson MA, Turnbull DM. 1999. Histochemical localisation of mitochondrial enzyme activity in human optic nerve and retina. *Br J Ophthalmol* **83**:231–235. doi:10.1136/bjo.83.2.231

Angelin A, Gil-de-Gómez L, Dahiya S, Jiao J, Guo L, Levine MH, Wang Z, Quinn III WJ, Kopinski PK, Wang L, Akimova T, Liu Y, Bhatti TR, Han R, Laskin BL, Baur JA, Blair IA, Wallace DC, Hancock WW, Beier UH. 2017. Foxp3 Reprograms T Cell Metabolism to Function in Low-Glucose, High-Lactate Environments. *Cell Metab* **25**:1282–1293. doi:10.1016/j.cmet.2016.12.018

Aredo B, Zhang K, Chen X, Wang CX-Z, Li T, Ufret-Vincenty RL. 2015. Differences in the distribution, phenotype and gene expression of subretinal microglia/macrophages in C57BL/6N (Crb1rd8/rd8) versus C57BL6/J (Crb1wt/wt) mice. *J Neuroinflammation* **12**:6. doi:10.1186/s12974-014-0221-4

Arshavsky VY, Lamb TD, Pugh EN. 2002. G proteins and phototransduction. *Annu Rev Physiol* **64**:153–187. doi:10.1146/annurev.physiol.64.082701.102229

Artuso L, Romano A, Verri T, Domenichini A, Argenton F, Santorelli FM, Petruzzella V. 2012. Mitochondrial DNA metabolism in early development of zebrafish (Danio rerio). *Biochim Biophys Acta* **1817**:1002–1011. doi:10.1016/j.bbabio.2012.03.019

Badr GA, Tang J, Ismail-Beigi F, Kern TS. 2000. Diabetes downregulates GLUT1 expression in the retina and its microvessels but not in the cerebral cortex or its microvessels. *Diabetes* **49**:1016–1021. doi:10.2337/diabetes.49.6.1016

Bainbridge MN, Davis EE, Choi WY, Dickson A, Martinez HR, Wang M, Dinh H, Muzny DM, Pignatelli R, Katsanis N, Boerwinkle E, Gibbs RA, Jefferies JL. 2015. Loss of Function Mutations in NNT Are Associated with Left Ventricular Noncompaction. *Circ Cardiovasc Genet* **8**:544–552. doi:10.1161/CIRCGENETICS.115.001026

Banks G, Heise I, Starbuck B, Osborne T, Wisby L, Potter P, Jackson IJ, Foster RG, Peirson SN, Nolan PM. 2015. Genetic background influences age-related decline in visual and nonvisual responses, circadian rhythms, and sleep. *Neurobiol Aging* **36**:380–393.

Barlow HB, Levick WR. 1965. The mechanism of directionally selective units in rabbit's

retina. *J Physiol* **178**:477–504. doi:10.1113/jphysiol.1965.sp007638

Barron MJ, Johnson MA, Andrews RM, Clarke MP, Griffiths PG, Bristow E, He LP, Durham S, Turnbull DM. 2001. Mitochondrial abnormalities in ageing macular photoreceptors. *Invest Ophthalmol Vis Sci* **42**:3016–3022.

Bata AM, Fondi K, Szegedi S, Aschinger GC, Hommer A, Schmidl D, Chua J, Werkmeister RM, Garhöfer G, Schmettere L. 2019. Age-Related Decline of Retinal Oxygen Extraction in Healthy Subjects. *Investig Ophthalmol Vis Sci* **60**:3162–3169. doi:10.1167/iovs.18-26234

Bélanger M, Allaman I, Magistretti PJ. 2011. Brain energy metabolism: Focus on Astrocyte-neuron metabolic cooperation. *Cell Metab* **14**:724–738. doi:10.1016/j.cmet.2011.08.016

Bénit P, Letouzé E, Rak M, Aubry L, Burnichon N, Favier J, Gimenez-Roqueplo AP, Rustin P. 2014. Unsuspected task for an old team: Succinate, fumarate and other Krebs cycle acids in metabolic remodeling. *Biochim Biophys Acta - Bioenerg* **1837**:1330–1337. doi:10.1016/j.bbabio.2014.03.013

Bentmann A, Schmidt M, Reuss S, Wolfrum U, Hankeln T, Burmester T. 2005. Divergent distribution in vascular and avascular mammalian retinae links neuroglobin to cellular respiration. *J Biol Chem* **280**:20660–20665. doi:10.1074/jbc.M501338200

Berezowska I, Chung NN, Lemieux C, Zelent B, Szeto HH, Schiller PW. 2003. Highly potent fluorescent analogues of the opioid peptide [Dmt 1]DALDA. *Peptides* **24**:1195–1200. doi:10.1016/j.peptides.2003.07.004

Bhutto I, Lutty G. 2012. Understanding age-related macular degeneration (AMD): Relationships between the photoreceptor/retinal pigment epithelium/Bruch's membrane/choriocapillaris complex. *Mol Aspects Med* **33**:295–317. doi:10.1016/j.mam.2012.04.005.

Birk A V., Chao WM, Bracken C, Warren JD, Szeto HH. 2014. Targeting mitochondrial cardiolipin and the cytochrome c/cardiolipin complex to promote electron transport and optimize mitochondrial ATP synthesis. *Br J Pharmacol* **171**:2017–2028. doi:10.1111/bph.12468

Birk A V., Liu S, Soong Y, Mills W, Singh P, Warren JD, Seshan S V., Pardee JD, Szeto

HH. 2013. The mitochondrial-targeted compound SS-31 re-energizes ischemic mitochondria by interacting with cardiolipin. *J Am Soc Nephrol* **24**:1250–1261. doi:10.1681/ASN.2012121216

Bisbach CM, Hass DT, Robbings BM, Rountree AM, Sadilek M, Sweet IR, Hurley JB. 2020. Succinate Can Shuttle Reducing Power from the Hypoxic Retina to the O2-Rich Pigment Epithelium. *Cell Rep* **31**:107606. doi:10.1016/j.celrep.2020.107606

Blanchette-Mackie EJ, Scow RO. 1983. Movement of lipolytic products to mitochondria in brown adipose tissue of young rats: an electron microscope study. *J Lipid Res* **24**:229–244.

Blasiak J, Glowacki S, Kauppinen A, Kaarniranta K. 2013. Mitochondrial and nuclear DNA damage and repair in age-related macular degeneration. *Int J Mol Sci* **14**:2996–3010. doi:10.3390/ijms14022996

Bleck CKE, Kim Y, Willingham TB, Glancy B. 2018. Subcellular connectomic analyses of energy networks in striated muscle. *Nat Commun* **9**:5111. doi:10.1038/s41467-018-07676-y

Blenkinsop TA, Saini JS, Maminishkis A, Bharti K, Wan Q, Banzon T, Lotfi M, Davis J, Singh D, Rizzolo LJ, Miller S, Temple S, Stern JH. 2015. Human adult retinal pigment epithelial stem cell-derived RPE monolayers exhibit key physiological characteristics of native tissue. *Investig Ophthalmol Vis Sci* **56**:7085–7099. doi:10.1167/iovs.14-16246

Bonilha VL. 2008. Age and disease-related structural changes in the retinal pigment epithelium. *Clin Ophthalmol* **2**:413–424. doi:10.2147/opth.s2151

Booth LN, Brunet A. 2016. The Aging Epigenome. *Mol Cell* **62**:728–744. doi:10.1016/j.molcel.2016.05.013

Bramall AN, Wright AF, Jacobson SG, McInnes RR. 2010. The genomic, biochemical, and cellular responses of the retina in inherited photoreceptor degenerations and prospects for the treatment of these disorders. *Annu Rev Neurosci* **33**:441–472. doi:10.1146/annurev-neuro-060909-153227

Bratic A, Larsson NG. 2013. The role of mitochondria in aging. *J Clin Invest* **123**:951–957. doi:10.1172/JCI64125

Bratic I, Trifunovic A. 2010. Mitochondrial energy metabolism and ageing. *Biochim*

Biophys Acta - Bioenerg **1797**:961–967. doi:10.1016/j.bbabio.2010.01.004

Brockerhoff SE, Dowling JE, Hurley JB. 1998. Zebrafish retinal mutants. *Vision Res* **38**:1335–1339. doi:10.1016/S0042-6989(97)00227-7

Brunk UT, Terman A. 2002. Lipofuscin: Mechanisms of age-related accumulation and influence on cell function. *Free Radic Biol Med* **33**:611–619. doi:10.1016/S0891-5849(02)00959-0

Bryant CD. 2011. The blessings and curses of C57BL/6 substrains in mouse genetic studies. *Ann N Y Acad Sci* **1245**:31–33. doi:10.1111/j.1749-6632.2011.06325.x.The

Bryant CD, Zhang NN, Sokoloff G, Fanselow MS, Ennes HS, Palmer AA, McRoberts JA. 2008. Behavioral differences among C57BL/6 substrains: Implications for transgenic and knockout studies. *J Neurogenet* **22**:315–331. doi:10.1080/01677060802357388

Buffenstein R, Ruby JG. 2021. Opportunities for new insight into aging from the naked mole-rat and other non-traditional models. *Nat Aging* **1**:3–4. doi:10.1038/s43587-020-00012-4

Burgess EA, Sylvén B. 1962. Glucose, Lactate, and Lactic Dehydrogenase Activity in Normal Interstitial Fluid and That of Solid Mouse Tumors. *Cancer Res* **22**:581–588.

Burnside B, Wang E, Pagh-Roehl K, Rey H. 1993. Retinomotor movements in isolated teleost retinal cone inner-outer segment preparations (CIS-COS): Effects of light, dark and dopamine. *Exp Eye Res*. doi:10.1006/exer.1993.1179

Butler PG, Wanamaker AD, Scourse JD, Richardson CA, Reynolds DJ. 2013. Variability of marine climate on the North Icelandic Shelf in a 1357-year proxy archive based on growth increments in the bivalve Arctica islandica. *Palaeogeogr Palaeoclimatol Palaeoecol* **373**:141–151. doi:10.1016/j.palaeo.2012.01.016

Cabral-Costa J V., Kowaltowski AJ. 2020. Neurological disorders and mitochondria. *Mol Aspects Med* **71**:100826. doi:10.1016/j.mam.2019.10.003

Cahill GM. 2002. Clock mechanisms in zebrafish. *Cell Tissue Res* **309**:27–34. doi:10.1007/s00441-002-0570-7

Cai T, Hua B, Luo D, Xu L, Cheng Q, Yuan G, Yan Z, Sun N, Hua L, Lu C. 2019. The circadian protein CLOCK regulates cell metabolism via the mitochondrial carrier SLC25A10. *Biochim Biophys acta Mol cell Res* **1866**:1310–1321.

doi:10.1016/j.bbamcr.2019.03.016

Camandola S, Mattson MP. 2017. Brain metabolism in health, aging, and neurodegeneration. *EMBO J* **36**:1474–1492. doi:10.15252/embj.201695810

Campbell MD, Duan J, Samuelson AT, Gaffrey MJ, Merrihew GE, Egertson JD, Wang L, Bammler TK, Moore RJ, White CC, Kavanagh TJ, Voss JG, Szeto HH, Rabinovitch PS, MacCoss MJ, Qian WJ, Marcinek DJ. 2019. Improving mitochondrial function with SS-31 reverses age-related redox stress and improves exercise tolerance in aged mice. *Free Radic Biol Med* **134**:268–281. doi:10.1016/j.freeradbiomed.2018.12.031

Carter-Dawson LD, LaVail MM. 1979. Rods and cones in the mouse retina. II. Autoradiographic analysis of cell generation using tritiated thymidine. *J Comp Neurol* **188**:263–272. doi:10.1002/cne.901880205

Casson RJ, Wood JPM, Han G, Kittipassorn T, Peet DJ, Chidlow G. 2016. M-type pyruvate kinase isoforms and lactate dehydrogenase a in the mammalian retina: Metabolic implications. *Investig Ophthalmol Vis Sci* **57**:66–80. doi:10.1167/iovs.15-17962

Castillo-Quan JI, Tain LS, Kinghorn KJ, Li L, Grönke S, Hinze Y, Blackwell TK, Bjedov I, Partridge L. 2019. A triple drug combination targeting components of the nutrient-sensing network maximizes longevity. *Proc Natl Acad Sci U S A* **116**:20817–20819. doi:10.1073/pnas.1913212116

Cavallotti C, Artico M, Pescosolido N, Tranquilli Leali FM, Feher J. 2004. Age-related changes in the human retina. *Can J Ophthalmol* **39**:61–68. doi:10.1016/S0008-4182(04)80054-1

Chang B, Hawes NL, Hurd RE, Davisson MT, Nusinowitz S, Heckenlively JR. 2002. Retinal degeneration mutants in the mouse. *Vision Res* **42**:517–525. doi:10.1016/S0042-6989(01)00146-8

Chang JYA, Shi L, Ko ML, Ko GYP. 2018. Circadian Regulation of Mitochondrial Dynamics in Retinal Photoreceptors. *J Biol Rhythms* **33**:151–165. doi:10.1177/0748730418762152

Chao JR, Knight K, Engel AL, Jankowski C, Wang Y, Manson MA, Gu H, Djukovic D, Raftery D, Hurley JB, Du J. 2017. Human retinal pigment epithelial cells prefer

proline as a nutrient and transport metabolic intermediates to the retinal side. *J Biol Chem* **292**:12895–12905. doi:10.1074/jbc.M117.788422

Chaudhry FA, Reimer RJ, Edwards RH. 2002. The glutamine commute: Take the N line and transfer to the A. *J Cell Biol* **157**:349–355. doi:10.1083/jcb.200201070

Chavez JD, Tang X, Campbell MD, Reyes G, Kramer PA, Stuppard R, Keller A, Zhang H, Rabinovitch PS, Marcinek DJ, Bruce JE. 2020. Mitochondrial protein interaction landscape of SS-31. *Proc Natl Acad Sci U S A* **117**:15363–15373. doi:10.1073/pnas.2002250117

Chen H, Chan DC. 2009. Mitochondrial dynamics--fusion, fission, movement, and mitophagy--in neurodegenerative diseases. *Hum Mol Genet* **18**:R169-76. doi:10.1093/hmg/ddp326

Chen H, Chomyn A, Chan DC. 2005. Disruption of fusion results in mitochondrial heterogeneity and dysfunction. *J Biol Chem* **280**:26185–26192. doi:10.1074/jbc.M503062200

Chen M, Rajapakse D, Fraczek M, Luo C, Forrester J V., Xu H. 2016. Retinal pigment epithelial cell multinucleation in the aging eye - a mechanism to repair damage and maintain homoeostasis. *Aging Cell* **15**:436–445. doi:10.1111/acel.12447

Chhetri J, Jacobson G, Gueven N. 2014. Zebrafish-on the move towards ophthalmological research. *Eye* **28**:367–380. doi:10.1038/eye.2014.19

Chiao YA, Rabinovitch PS. 2015. The aging heart. *Cold Spring Harb Perspect Med* **5**:a025148. doi:10.1101/cshperspect.a025148

Chiao YA, Zhang H, Sweetwyne M, Whitson J, Ting YS, Basisty N, Pino L, Quarles E, Thi Nguyen NH, Campbell MD, Zhang T, Gaffrey MJ, Merrihew G, Wang L, Yue Y, Duan D, Granzier H, Szeto HH, Qian WJ, Marcinek D, MacCoss MJ, Rabinovitch PS. 2020. Late-life restoration of mitochondrial function reverses cardiac dysfunction in old mice. *bioRxiv* **9**:e55513. doi:10.1101/2020.01.02.893008

Chinchore Y, Begaj T, Wu D, Drokhlyansky E, Cepko CL. 2017. Glycolytic reliance promotes anabolism in photoreceptors. *Elife* **6**:e25946. doi:10.7554/eLife.25946

Chinen A, Hamaoka T, Yamada Y, Kawamura S. 2003. Gene duplication and spectral diversification of cone visual pigments of zebrafish. *Genetics* **163**:663–675.

Cieri D, Brini M, Calì T. 2017. Emerging (and converging) pathways in Parkinson’s

disease: keeping mitochondrial wellness. *Biochem Biophys Res Commun* **483**:1020–1030. doi:10.1016/j.bbrc.2016.08.153

Cimen H, Han M-J, Yang Y, Tong Q, Koc H, Koc EC. 2010. Regulation of succinate dehydrogenase activity by SIRT3 in mammalian mitochondria. *Biochemistry* **49**:304–311. doi:10.1021/bi901627u

Clapcote SJ, Roder JC. 2006. Deletion polymorphism of Disc1 is common to all 129 mouse substrains: Implications for gene-targeting studies of brain function. *Genetics* **173**:2407–2410. doi:10.1534/genetics.106.060749

Cleymaet AM, Gallagher SK, Tooker RE, Lipin MY, Renna JM, Sodhi P, Berg D, Hartwick ATE, Berson DM, Vigh J. 2019. μ-Opioid Receptor Activation Directly Modulates Intrinsically Photosensitive Retinal Ganglion Cells. *Neuroscience* **408**:400–417. doi:10.1016/j.neuroscience.2019.04.005

Cogliati S, Enriquez JA, Scorrano L. 2016. Mitochondrial Cristae: Where Beauty Meets Functionality. *Trends Biochem Sci* **41**:261–273. doi:10.1016/j.tibs.2016.01.001

Collymore C, Rasmussen S, Tolwani RJ. 2013. Gavaging Adult Zebrafish. *JoVE* e50691. doi:doi:10.3791/50691

Corso G, Esposito M, Gallo M, Russo A Dello, Antonio M. 1993. Transformation of arginine into ornithine during the preparation of its tert-butyldimethylsilyl derivative for analysis by gas chromatography/mass spectrometry. *Biol Mass Spectrom* **22**:698–702. doi:10.1002/bms.1200221205

Crabb JW. 2014. The proteomics of drusen. *Cold Spring Harb Perspect Med* **4**:a017194. doi:10.1101/cshperspect.a017194

Crews JE, Chou C-F, Sekar S, Saaddine JB. 2017. The Prevalence of Chronic Conditions and Poor Health Among People With and Without Vision Impairment, Aged ≥65 Years, 2010–2014. *Am J Ophthalmol* **182**:18–30. doi:10.1016/j.ajo.2017.06.038

Dai DF, Chen T, Szeto H, Nieves-Cintrón M, Kutyavin V, Santana LF, Rabinovitch PS. 2011. Mitochondrial targeted antioxidant peptide ameliorates hypertensive cardiomyopathy. *J Am Coll Cardiol* **58**:73–82. doi:10.1016/j.jacc.2010.12.044

Davis CHO, Kim KY, Bushong EA, Mills EA, Boassa D, Shih T, Kinebuchi M, Phan S, Zhou Y, Bihlmeyer NA, Nguyen J V., Jin Y, Ellisman MH, Marsh-Armstrong N.

2014. Transcellular degradation of axonal mitochondria. *Proc Natl Acad Sci U S A* **111**:9633–9638. doi:10.1073/pnas.1404651111

De Goede P, Wefers J, Brombacher EC, Schrauwen P, Kalsbeek A. 2018. Circadian rhythms in mitochondrial respiration. *J Mol Endocrinol* **60**:R115–R130. doi:10.1530/JME-17-0196

Demontis F, Piccirillo R, Goldberg AL, Perrimon N. 2013. Mechanisms of skeletal muscle aging: Insights from Drosophila and mammalian models. *DMM Dis Model Mech* **6**:1339–1352. doi:10.1242/dmm.012559

Den Hollander AI, Ten Brink JB, De Kok YJM, Van Soest S, Van Den Born LI, Van Driel MA, Van De Pol DJR, Payne AM, Bhattacharya SS, Kellner U, Hoyng CB, Westerveld A, Brunner HG, Bleeker-Wagemakers EM, Deutman AF, Heckenlively JR, Cremers FPM, Bergen AAB. 1999. Mutations in a human homologue of Drosophila crumbs cause retinitis pigmentosa (RP12). *Nat Genet* **23**:217–221. doi:10.1038/13848

Des Rosiers C, David F, Garneau M, Brunengraber H. 1991. Nonhomogeneous labeling of liver mitochondrial acetyl-CoA*. *J Biol Chem* **266**:1574–1578. doi:10.1016/s0021-9258(18)52332-2

Desaulniers N, Moerland TS, Sidell BD. 1996. High lipid content enhances the rate of oxygen diffusion through fish skeletal muscle. *Am J Physiol Integr Comp Physiol* **271**:R42–R47. doi:10.1152/ajpregu.1996.271.1.R42

DeVera C, Tosini G. 2020. Circadian analysis of the mouse retinal pigment epithelium transcriptome. *Exp Eye Res* **193**:107988. doi:10.1016/j.exer.2020.107988

Di Stefano M, Conforti L. 2013. Diversification of NAD biological role: The importance of location. *FEBS J* **280**:4711–4728. doi:10.1111/febs.12433

Dmitriev A V., Mangel SC. 2000. A circadian clock regulates the pH of the fish retina. *J Physiol* **522**:77–82. doi:10.1111/j.1469-7793.2000.0077m.x

Dodzian J, Kean S, Seidel J, Valenzano DR. 2018. A Protocol for Laboratory Housing of Turquoise Killifish (Nothobranchius furzeri). *JoVE* e57073. doi:doi:10.3791/57073

Dowling JE. 1987. The Retina: An Approachable Part of the Brain. Cambridge, Mass.: Belknap Press of Harvard University Press.

Du J, Cleghorn W, Contreras L, Linton JD, Chan GCK, Chertov AO, Saheki T,

Govindaraju V, Sadilek M, Satrústegui J, Hurley JB. 2013a. Cytosolic reducing power preserves glutamate in retina. *Proc Natl Acad Sci U S A* **110**:18501–18506. doi:10.1073/pnas.1311193110

Du J, Cleghorn WM, Contreras L, Lindsay K, Rountree AM, Chertov AO, Turner SJ, Sahaboglu A, Linton J, Sadilek M, Satruśtegui J, Sweet IR, Paquet-Durand F, Hurley JB. 2013b. Inhibition of mitochondrial pyruvate transport by Zaprinast causes massive accumulation of aspartate at the expense of glutamate in the retina. *J Biol Chem* **288**:36129–36140. doi:10.1074/jbc.M113.507285

Du J, Linton JD, Hurley JB. 2015. Probing Metabolism in the Intact Retina Using Stable Isotope Tracers Jianhai. *Methods Enzymol* **561**:149–170. doi:doi:10.1016/bs.mie.2015.04.002

Du J, Rountree A, Cleghorn WM, Contreras L, Lindsay KJ, Sadilek M, Gu H, Djukovic D, Raftery D, Satrústegui J, Kanow M, Chan L, Tsang SH, Sweet IR, Hurley JB. 2016a. Phototransduction influences metabolic flux and nucleotide metabolism in mouse retina. *J Biol Chem* **291**:4698–4710. doi:10.1074/jbc.M115.698985

Du J, Yanagida A, Knight K, Engel AL, Vo AH, Jankowski C, Sadilek M, Tran VTB, Manson MA, Ramakrishnan A, Hurley JB, Chao JR. 2016b. Reductive carboxylation is a major metabolic pathway in the retinal pigment epithelium. *Proc Natl Acad Sci U S A* **113**:14710–14715. doi:10.1073/pnas.1604572113

Du M, Mangold CA, Bixler G V., Brucklacher RM, Masser DR, Stout MB, Elliott MH, Freeman WM. 2017. Retinal gene expression responses to aging are sexually divergent. *Mol Vis* **23**:707–717.

Duncan G, Michael Wormstone I, Davies PD. 1997. The aging human lens: Structure, growth, and physiological behaviour. *Br J Ophthalmol* **81**:818–823. doi:10.1136/bjo.81.10.818

Duong JK, Hsu C-W, Tsai Y-T, Lin C-S, Wahl-schott CA, Tsang SH. 2017. Genetic rescue models refute nonautonomous rod cell death in retinitis pigmentosa. *Proc Natl Acad Sci U S A* **114**:E5484. doi:10.1073/pnas.1708940114

Eberhart A, Feodorova Y, Song C, Wanner G, Kiseleva E, Furukawa T, Kimura H, Schotta G, Leonhardt H, Joffe B, Solovei I. 2013. Epigenetics of eu- and heterochromatin in inverted and conventional nuclei from mouse retina.

Chromosom Res **21**:535–554. doi:10.1007/s10577-013-9375-7

Eells JT. 2019. Mitochondrial dysfunction in the aging retina. *Biology (Basel)* **8**:31. doi:10.3390/biology8020031

Farinelli P, Perera A, Arango-Gonzalez B, Trifunovic D, Wagner M, Carell T, Biel M, Zrenner E, Michalakis S, Paquet-Durand F, Ekström PAR. 2014. DNA methylation and differential gene regulation in photoreceptor cell death. *Cell Death Dis* **5**:e1558. doi:10.1038/cddis.2014.512

Ferrington DA, Kapphahn RJ, Leary MM, Atilano SR, Terluk MR, Karunadharma P, Chen GKJ, Ratnapriya R, Swaroop A, Montezuma SR, Kenney MC. 2016. Increased retinal mtDNA damage in the CFH variant associated with age-related macular degeneration. *Exp Eye Res* **145**:269–277. doi:10.1016/j.exer.2016.01.018

Fiehn O. 2016. Metabolomics by gas chromatography-mass spectrometry: Combined targeted and untargeted profiling, Current Protocols in Molecular Biology. doi:10.1002/0471142727.mb3004s114

Fleishman LJ, Marshall CJ, Hertz PE, Fleishman LEOJ, Marshall CJ, Hertz PE. 2019. Comparative Study of Temporal Response Properties of the Visual System of Three Species of Anoline Lizards Published by : American Society of Ichthyologists and Herpetologists (ASIH) Stable URL : https://www.jstor.org/stable/1446905 Comparative Study of **1995**:422–431.

Fontana L, Partridge L, Longo VD. 2010. Dietary Restriction, Growth Factors and Aging: from yeast to humans. *Science (80-)* **328**:321–6. doi:10.1126/science.1172539.Dietary

Freund PR, Watson J, Gilmour GS, Gaillard F, Sauvé Y. 2011. Differential changes in retina function with normal aging in humans. *Doc Ophthalmol* **122**:177–190. doi:10.1007/s10633-011-9273-2

Friedman JR, Lackner LL, West M, Dibenedetto JR, Nunnari J, Voeltz GK. 2011. ER Tubules Mark Sites of Mitochondrial Division Published by : American Association for the Advancement of Science Linked references are available on JSTOR for this article : ER Tubules Mark Sites of Mitochondrial Division. *Science (80-)* **334**:358–362.

Fujisawa Y, Napoli E, Wong S, Song G, Yamaguchi R, Matsui T, Nagasaki K, Ogata T,

Giulivi C. 2015. Impact of a novel homozygous mutation in nicotinamide nucleotide transhydrogenase on mitochondrial DNA integrity in a case of familial glucocorticoid deficiency. *BBA Clin* **3**:70–78. doi:10.1016/j.bbacli.2014.12.003

Gameiro PA, Laviolette LA, Kelleher JK, Iliopoulos O, Stephanopoulos G. 2013. Cofactor balance by nicotinamide nucleotide transhydrogenase (NNT) coordinates reductive carboxylation and glucose catabolism in the tricarboxylic acid (TCA) cycle. *J Biol Chem* **288**:12967–12977. doi:10.1074/jbc.M112.396796

Garvey SM, Dugle JE, Kennedy AD, McDunn JE, Kline W, Guo L, Guttridge DC, Pereira SL, Edens NK. 2014. Metabolomic profiling reveals severe skeletal muscle group-specific perturbations of metabolism in aged FBN rats. *Biogerontology* **15**:217–232. doi:10.1007/s10522-014-9492-5

Gasko O, Danon D. 1972. Deterioration and disappearance of mitochondria during reticulocyte maturation. *Exp Cell Res* **75**:159–169. doi:10.1016/0014-4827(72)90532-0

Gatta C, Castaldo L, Cellerino A, de Girolamo P, Lucini C, D'Angelo L. 2014. Brain derived neurotrophic factor in the retina of the teleost N. furzeri. *Ann Anat* **196**:192–196. doi:10.1016/j.aanat.2014.01.002

Géminard C, de Gassart A, Vidal M. 2002. Reticulocyte maturation: mitoptosis and exosome release. *Biocell* **26**:205—215.

George AA, Hayden S, Holzhausen LC, Ma EY, Suzuki SC, Brockerhoff SE. 2014. Synaptojanin 1 is required for endolysosomal trafficking of synaptic proteins in cone photoreceptor inner segments. *PLoS One* **9**:e84394. doi:10.1371/journal.pone.0084394

Gerdes H-H, Carvalho RN. 2008. Intercellular transfer mediated by tunneling nanotubes. *Curr Opin Cell Biol* **20**:470–475. doi:10.1016/j.ceb.2008.03.005

Gestri G, Link BA, Neuhauss SC. 2012. The visual system of zebrafish and its use to model human ocular diseases. *Dev Neurobiolgy* **72**:302–327. doi:10.1002/dneu.20919.The

Giarmarco MM. 2020. Giarmarco_PNAS_2020_rawdata. *Open Sci Framew*. https://osf.io/qaed8

Giarmarco MM, Brock DC, Robbings BM, Cleghorn WM, Tsantilas KA, Kuch KC, Ge W,

Rutter KM, Parker ED, Hurley JB, Brockerhoff SE. 2020. Daily mitochondrial dynamics in cone photoreceptors. *Proc Natl Acad Sci U S A* **117**:28816–28827. doi:10.1073/pnas.2007827117

Giarmarco MM, Cleghorn WM, Hurley JB, Brockerhoff SE. 2018. Preparing Fresh Retinal Slices from Adult Zebrafish for Ex Vivo Imaging Experiments. *J Vis Exp*. doi:10.3791/56977

Giarmarco MM, Cleghorn WM, Sloat SR, Hurley JB, Brockerhoff SE. 2017. Mitochondria maintain distinct Ca2+ pools in cone photoreceptors. *J Neurosci* **37**:2061–2072. doi:10.1523/JNEUROSCI.2689-16.2017

Gilbert MJH, Zerulla TC, Tierney KB. 2013. Zebrafish (Danio rerio) as a model for the study of aging and exercise: Physical ability and trainability decrease with age. *Exp Gerontol* **50**:106–113. doi:10.1016/j.exger.2013.11.013

Gómez-Sintes R, Kvajo M, Gogos JA, Lucas JJ. 2014. Mice with a naturally occurring DISC1 mutation display a broad spectrum of behaviors associated to psychiatric disorders. *Front Behav Neurosci* **8**:253. doi:10.3389/fnbeh.2014.00253

Gonzalez-Freire M, De Cabo R, Bernier M, Sollott SJ, Fabbri E, Navas P, Ferrucci L. 2015. Reconsidering the Role of Mitochondria in Aging. *Journals Gerontol - Ser A Biol Sci Med Sci* **70**:1334–1342. doi:10.1093/gerona/glv070

Gospe SM, Baker SA, Arshavsky VY. 2010. Facilitative glucose transporter Glut1 is actively excluded from rod outer segments. *J Cell Sci* **123**:3639–3644. doi:10.1242/jcs.072389

Goyal MS, Vlassenko AG, Blazey TM, Su Y, Couture LE, Durbin TJ, Bateman RJ, Benzinger TLS, Morris JC, Raichle ME. 2017. Loss of Brain Aerobic Glycolysis in Normal Human Aging. *Cell Metab* **26**:353–360. doi:10.1016/j.cmet.2017.07.010

Gruber H, Wessels W, Boynton P, Xu J, Wohlgemuth S, Leeuwenburgh C, Qi W, Austad SN, Schaible R, Philipp EER. 2015. Age-related cellular changes in the long-lived bivalve A. islandica. *Age (Omaha)* **37**:90. doi:10.1007/s11357-015-9831-8

Gu F, Chen L, Ni B, Zhang X. 2002. A comparative study on the electron microscopic enzymo-cytochemistry of Paramecium bursaria from light and dark cultures. *Eur J Protistol* **38**:267–278. doi:https://doi.org/10.1078/0932-4739-00875

Gu X, Neric NJ, Crabb JS, Crabb JW, Bhattacharya SK, Rayborn ME, Hollyfield JG, Bonilha VL. 2012. Age-related changes in the retinal pigment epithelium (RPE). *PLoS One* **7**:e38673. doi:10.1371/journal.pone.0038673

Guillon M, Dumbleton K, Theodoratos P, Gobbe M, Wooley CB, Moody K. 2016. The effects of age, refractive status, and luminance on pupil size. *Optom Vis Sci* **93**:1093–1100. doi:10.1097/OPX.0000000000000893

Guo R, Gu J, Zong S, Wu M, Yang M. 2018. Structure and mechanism of mitochondrial electron transport chain. *Biomed J* **41**:9–20. doi:10.1016/j.bj.2017.12.001

Hamasaki M, Furuta N, Matsuda A, Nezu A, Yamamoto A, Fujita N, Oomori H, Noda T, Haraguchi T, Hiraoka Y, Amano A, Yoshimori T. 2013. Autophagosomes form at ER-mitochondria contact sites. *Nature* **495**:389–393. doi:10.1038/nature11910

Hamberger AC, Chiang GH, Nylén ES, Scheff SW, Cotman CW. 1979. Glutamate as a CNS transmitter. I. Evaluation of glucose and glutamine as precursors for the synthesis of preferentially released glutamate. *Brain Res* **168**:513–530. doi:10.1016/0006-8993(79)90306-8

Harel I, Valenzano DR, Brunet A. 2016. Efficient genome engineering approaches for the short-lived African turquoise killifish. *Nat Protoc* **11**:2010–2028. doi:10.1038/nprot.2016.103

Hartmann N, Reichwald K, Wittig I, Dröse S, Schmeisser S, Lück C, Hahn C, Graf M, Gausmann U, Terzibasi E, Cellerino A, Ristow M, Brandt U, Platzer M, Englert C. 2011. Mitochondrial DNA copy number and function decrease with age in the short-lived fish Nothobranchius furzeri. *Aging Cell* **10**:824–831. doi:10.1111/j.1474-9726.2011.00723.x

Haydinger CD, Kittipassorn T, Peet DJ. 2020. Power to see—Drivers of aerobic glycolysis in the mammalian retina: A review. *Clin Exp Ophthalmol* **48**:1057–1071. doi:10.1111/ceo.13833

He S, Li X, Chan N, Hinton DR. 2013. Review: Epigenetic mechanisms in ocular disease. *Mol Vis* **19**:665–674.

Heesterbeek TJ, van der Aa HPA, van Rens GHMB, Twisk JWR, van Nispen RMA. 2017. The incidence and predictors of depressive and anxiety symptoms in older adults with vision impairment: a longitudinal prospective cohort study. *Ophthalmic*

Physiol Opt **37**:385–398. doi:10.1111/opo.12388

Hemachandra Reddy P, Manczak M, Kandimalla R. 2017. Mitochondria-targeted small molecule SS31: A potential candidate for the treatment of Alzheimer's disease. *Hum Mol Genet* **26**:1483–1496. doi:10.1093/hmg/ddx052

Hitchcock PF, Raymond PA. 2004. The Teleost Retina as a Model for Developmental and Regeneration Biology. *Zebrafish* **1**:257–271. doi:10.1089/zeb.2004.1.257

Ho HY, Lin YT, Lin G, Wu PR, Cheng ML. 2017. Nicotinamide nucleotide transhydrogenase (NNT) deficiency dysregulates mitochondrial retrograde signaling and impedes proliferation. *Redox Biol* **12**:916–928. doi:10.1016/j.redox.2017.04.035

Hodel C, Neuhauss SCF, Biehlmaier O. 2006. Time course and development of light adaptation processes in the outer zebrafish retina. *Anat Rec - Part A* **288**:653–662. doi:10.1002/ar.a.20329

Hofer H, Carroll J, Neitz J, Neitz M, Williams DR. 2005. Organization of the human trichromatic cone mosaic. *J Neurosci* **25**:9669–9679. doi:10.1523/JNEUROSCI.2414-05.2005

Hollyfield JG. 1999. Hyaluronan and the Functional Organization of the Interphotoreceptor Matrix. *Invest Ophthalmol Vis Sci* **40**:2767–2769.

Hollyfield JG, Rayborn ME. 1987. Endocytosis in the inner segment of rod photoreceptors: analysis of Xenopus laevis retinas using horseradish peroxidase. *Exp Eye Res* **45**:703–719. doi:10.1016/s0014-4835(87)80119-7

Hollyfield JG, Varner HH, Rayborn ME, Liou GI, David Bridges C. 1985. Endocytosis and degradation of interstitial retinol-binding protein: Differential capabilities of cells that border the interphotoreceptor matrix. *J Cell Biol* **100**:1676–1681. doi:10.1083/jcb.100.5.1676

Hopkins AE. 1927. Vision and Retinal Structure in Mice. *Proc Natl Acad Sci* **13**:488–492. doi:10.1073/pnas.13.7.488

Hoppe G, Rayborn ME, Sears JE. 2007. Diurnal Rhythm of the Chromatin Protein Hmgb1 in Rat Photoreceptors Is Under Circadian Regulation. *J Comp Neurol* **501**:219–230. doi:10.1002/cne

Hoppins S. 2014. The regulation of mitochondrial dynamics. *Curr Opin Cell Biol* **29**:46–

52. doi:10.1016/j.ceb.2014.03.005

Hu CK, Brunet A. 2018. The African turquoise killifish: A research organism to study vertebrate aging and diapause. *Aging Cell* **17**:e12757. doi:10.1111/acel.12757

Huang Y, Yang P, Chen H, Bai X, Wang X, Vistro WA, Haseeb A, Shi Y, Chen Q. 2018. A “Lamellar structure” contributes to autophagosome biogenesis and mitophagy in zebrafish hepatocytes. *Fish Shellfish Immunol* **81**:83–91. doi:10.1016/j.fsi.2018.06.044

Hughes AEO, Enright JM, Myers CA, Shen SQ, Corbo JC. 2017. Cell Type-Specific Epigenomic Analysis Reveals a Uniquely Closed Chromatin Architecture in Mouse Rod Photoreceptors. *Sci Rep* **7**:43184. doi:10.1038/srep43184

Hung YP, Albeck JG, Tantama M, Yellen G. 2011. Imaging cytosolic NADH-NAD + redox state with a genetically encoded fluorescent biosensor. *Cell Metab* **14**:545–554. doi:10.1016/j.cmet.2011.08.012

Hurley JB, Lindsay KJ, Du J. 2015. Glucose, lactate, and shuttling of metabolites in vertebrate retinas. *J Neurosci Res* **93**:1079–1092. doi:10.1002/jnr.23583

Husain S, Abdul Y, Crosson CE. 2012. Preservation of retina ganglion cell function by morphine in a chronic ocular-hypertensive rat model. *Investig Ophthalmol Vis Sci* **53**:4289–4298. doi:10.1167/iovs.12-9467

Husain S, Potter DE, Crosson CE. 2009. Opioid receptor-activation: Retina protected from ischemic injury. *Investig Ophthalmol Vis Sci* **50**:3853–3859. doi:10.1167/iovs.08-2907

Hutto RA, Bisbach CM, Abbas F, Brock DC, Cleghorn WM, Parker ED, Bauer BH, Ge W, Vinberg F, Hurley JB, Brockerhoff SE. 2020. Increasing Ca2+ in photoreceptor mitochondria alters metabolites, accelerates photoresponse recovery, and reveals adaptations to mitochondrial stress. *Cell Death Differ* **27**:1067–1085. doi:10.1038/s41418-019-0398-2

Inana G, Murat C, An W, Yao X, Harris IR, Cao J. 2018. RPE phagocytic function declines in age-related macular degeneration and is rescued by human umbilical tissue derived cells. *J Transl Med* **16**:63. doi:10.1186/s12967-018-1434-6

Ishikawa M, Sawada Y, Yoshitomi T. 2015. Structure and function of the interphotoreceptor matrix surrounding retinal photoreceptor cells. *Exp Eye Res*

133:3–18. doi:https://doi.org/10.1016/j.exer.2015.02.017

Ishikawa T, Yamada E. 1969. Atypical mitochondria in the ellipsoid of the photoreceptor cells of vertebrate retinas. *Invest Ophthalmol* **8**:302–316.

Izuta Y, Imada T, Hisamura R, Oonishi E, Nakamura S, Inagaki E, Ito M, Soga T, Tsubota K. 2017. Ketone body 3-hydroxybutyrate mimics calorie restriction via the Nrf2 activator, fumarate, in the retina. *Aging Cell* **17**:e12699. doi:10.1111/acel.12699

Jackson Laboratory. n.d. Life span as a biomarker. https://www.jax.org/research-and-faculty/research-labs/the-harrison-lab/gerontology/life-span-as-a-biomarker

Januschka MM, Burkhardt DA, Erlandsen SL, Purple RL. 1987. The ultrastructure of cones in the walleye retina. *Vision Res* **27**:327–341. doi:https://doi.org/10.1016/0042-6989(87)90082-4

Jarrett SG, Lewin AS, Boulton ME. 2010. The importance of Mitochondria in age-related and inherited eye disorders. *Ophthalmic Res* **44**:179–190. doi:10.1159/000316480

Jazayeri O, Liu X, van Diemen CC, Bakker-van Waarde WM, Sikkema-Raddatz B, Sinke RJ, Zhang J, van Ravenswaaij-Arts CMA. 2015. A novel homozygous insertion and review of published mutations in the NNT gene causing familial glucocorticoid deficiency (FGD). *Eur J Med Genet* **58**:642–649. doi:10.1016/j.ejmg.2015.11.001

Johnson L V., Forest DL, Banna CD, Radeke CM, Maloney MA, Hu J, Spencer CN, Walker AM, Tsie MS, Bok D, Radeke MJ, Anderson DH. 2011. Cell culture model that mimics drusen formation and triggers complement activation associated with age-related macular degeneration. *Proc Natl Acad Sci U S A* **108**:18277–18282. doi:10.1073/pnas.1109703108

Johnson L V, Hageman GS, Blanks JC. 1986. Interphotoreceptor matrix domains ensheath vertebrate cone photoreceptor cells. *Invest Ophthalmol Vis Sci* **27**:129–135.

Jorstad NL, Wilken MS, Grimes WN, Wohl SG, Vandenbosch LS, Yoshimatsu T, Wong RO, Rieke F, Reh TA. 2017. Stimulation of functional neuronal regeneration from Müller glia in adult mice. *Nature* **548**:103–107. doi:10.1038/nature23283

Joyal JS, Sun Y, Gantner ML, Shao Z, Evans LP, Saba N, Fredrick T, Burnim S, Kim

JS, Patel G, Juan AM, Hurst CG, Hatton CJ, Cui Z, Pierce KA, Bherer P, Aguilar E, Powner MB, Vevis K, Boisvert M, Fu Z, Levy E, Fruttiger M, Packard A, Rezende FA, Maranda B, Sapieha P, Chen J, Friedlander M, Clish CB, Smith LEH. 2016. Retinal lipid and glucose metabolism dictates angiogenesis through the lipid sensor Ffar1. *Nat Med* **22**:439–445. doi:10.1038/nm.4059

Kam JH, Weinrich TW, Sangha H, Powner MB, Fosbury R, Jeffery G. 2019a. Mitochondrial absorption of short wavelength light drives primate blue retinal cones into glycolysis which may increase their pace of aging. *Vis Neurosci* **36**:E007. doi:DOI: 10.1017/S0952523819000063

Kam JH, Weinrich TW, Shinhmar H, Powner MB, Roberts NW, Aboelnour A, Jeffery G. 2019b. Fundamental differences in patterns of retinal ageing between primates and mice. *Sci Rep* **9**:12574. doi:10.1038/s41598-019-49121-0

Kane KL, Longo-Guess CM, Gagnon LH, Ding D, Salvi RJ, Johnson KR. 2012. Genetic background effects on age-related hearing loss associated with Cdh23 variants in mice. *Hear Res* **283**:80–88. doi:10.1016/j.heares.2011.11.007.Genetic

Kanow MA, Giarmarco MM, Jankowski C, Tsantilas K, Engel AL, Du J, Linton JD, Farnsworth CC, Sloat SR, Lindsay KJ, Parker ED, Brockerhoff SE, Sadilek M, Chao JR, Hurley JB. 2017. Biochemical adaptations of the retina and retinal pigment epithelium support a metabolic ecosystem in the vertebrate eye. *Elife* **6**:e28899. doi:10.1101/143347

Karp NA, Mason J, Beaudet AL, Benjamini Y, Bower L, Braun RE, Brown SDM, Chesler EJ, Dickinson ME, Flenniken AM, Fuchs H, de Angelis MH, Gao X, Guo S, Greenaway S, Heller R, Herault Y, Justice MJ, Kurbatova N, Lelliott CJ, Lloyd KCK, Mallon A-M, Mank JE, Masuya H, McKerlie C, Meehan TF, Mott RF, Murray SA, Parkinson H, Ramirez-Solis R, Santos L, Seavitt JR, Smedley D, Sorg T, Speak AO, Steel KP, Svenson KL, Consortium IMP, Wakana S, West D, Wells S, Westerberg H, Yaacoby S, White JK. 2017. Prevalence of sexual dimorphism in mammalian phenotypic traits. *Nat Commun* **8**:15475. doi:10.1038/ncomms15475

Karunadharma PP, Nordgaard CL, Olsen TW, Ferrington DA. 2010. Mitochondrial DNA damage as a potential mechanism for Age-Related macular Degeneration. *Investig Ophthalmol Vis Sci* **51**:5470–5479. doi:10.1167/iovs.10-5429

Kashutina M V, Ioffe SL, Tartakovskii VA. 1975. Silylation of Organic Compounds. *Russ Chem Rev* **44**:733–747. doi:10.1070/rc1975v044n09abeh002373

Kawajiri S, Saiki S, Sato S, Sato F, Hatano T, Eguchi H, Hattori N. 2010. PINK1 is recruited to mitochondria with parkin and associates with LC3 in mitophagy. *FEBS Lett* **584**:1073–1079. doi:10.1016/j.febslet.2010.02.016

Kefalov VJ. 2012. Rod and cone visual pigments and phototransduction through pharmacological, genetic, and physiological approaches. *J Biol Chem* **287**:1635–1641. doi:10.1074/jbc.R111.303008

Kergoat H, Kergoat M-J, Justino L. 2001. Age-related changes in the flash electroretinogram and oscillatory potentials in individuals age 75 and older. *J Am Geriatr Soc* **49**:1212–1217. doi:10.1046/j.1532-5415.2001.49239.x

Kim J, Lee E, Chang BS, Oh CS, Mun GH, Chung YH, Shin DH. 2005. The presence of megamitochondria in the ellipsoid of photoreceptor inner segment of the zebrafish retina. *J Vet Med Ser C Anat Histol Embryol* **34**:339–342. doi:10.1111/j.1439-0264.2005.00612.x

Kishi S, Uchiyama J, Baughman AM, Goto T, Lin MC, Tsai SB. 2003. The zebrafish as a vertebrate model of functional aging and very gradual senescence. *Exp Gerontol* **38**:777–786. doi:10.1016/S0531-5565(03)00108-6

Kitson FG, Larsen BS, McEwen CN. 1996. Chapter 1 - What Is GC/MS?Gas Chromatography and Mass Spectrometry : A Practical Guide. pp. 3–23. doi:https://doi.org/10.1016/B0-12-369397-7/00223-5

Kizilyaprak C, Spehner D, Devys D, Schultz P. 2010. In Vivo chromatin organization of mouse rod photoreceptors correlates with histone modifications. *PLoS One* **5**:e11039. doi:10.1371/journal.pone.0011039

Klein R, Klein BEK. 2013. The prevalence of age-related eye diseases and visual impairment in aging: Current estimates. *Investig Ophthalmol Vis Sci* **54**:ORSF5–ORSF13. doi:10.1167/iovs.13-12789

Knabe W, Kuhn H-J. 1996. Morphogenesis of megamitochondria in the retinal cone inner segments of Tupaia belangeri (Scandentia). *Cell Tissue Res* **285**:1–9. doi:10.1007/s004410050614

Knabe W, Skatchkov S, Kuhn H-J. 1997. “Lens mitochondria” in the retinal cones of the

tree-shrew Tupaia belangeri. *Vision Res* **37**:267–271. doi:10.1016/S0042-6989(96)00199-X

Koch-Nolte F, Fischer S, Haag F, Ziegler M. 2011. Compartmentation of NAD+-dependent signalling. *FEBS Lett* **585**:1651–1656. doi:10.1016/j.febslet.2011.03.045

Kolesnikov A V., Fan J, Crouch RK, Kefalov VJ. 2010. Age-related deterioration of rod vision in mice. *J Neurosci* **30**:11222–11231. doi:10.1523/JNEUROSCI.4239-09.2010

Kolko M, Vosborg F, Henriksen UL, Hasan-Olive MM, Diget EH, Vohra R, Gurubaran IRS, Gjedde A, Mariga ST, Skytt DM, Utheim TP, Storm-Mathisen J, Bergersen LH. 2016. Lactate Transport and Receptor Actions in Retina: Potential Roles in Retinal Function and Disease. *Neurochem Res* **41**:1229–1236. doi:10.1007/s11064-015-1792-x

Korobova F, Ramabhadran V, Higgs HN. 2013. An Actin-Dependent Step in Mitochondrial Fission Mediated by the ER-Associated Formin INF2. *Science (80-)* **25**:6118. doi:doi:10.1126/science.1228360

Krebs HA. 1927. On the metabolism of the retina. *Biochem Z* **189**:57–59.

Kurihara T, Westenskow PD, Gantner ML, Usui Y, Schultz A, Bravo S, Aguilar E, Wittgrove C, Friedlander MSH, Paris LP, Chew E, Siuzdak G, Friedlander M. 2016. Hypoxia-induced metabolic stress in retinal pigment epithelial cells is sufficient to induce photoreceptor degeneration. *Elife* **5**:e14319. doi:10.7554/eLife.14319

Labbadia J, Morimoto RI. 2015. The biology of proteostasis in aging and disease. *Annu Rev Biochem* **84**:435–464. doi:10.1146/annurev-biochem-060614-033955

Lao-On U, Attwood P V., Jitrapakdee S. 2018. Roles of pyruvate carboxylase in human diseases: from diabetes to cancers and infection. *J Mol Med* **96**:237–247. doi:10.1007/s00109-018-1622-0

Lappin G. 2015. A historical perspective on radioisotopic tracers in metabolism and biochemistry. *Bioanalysis* **7**:531–540. doi:10.4155/bio.14.286

Larison KD, Bremiller R. 1990. Early onset of phenotype and cell patterning in the embryonic zebrafish retina. *Development* **109**:567–576.

LaVail MM. 1976. Rod Outer Segment Disk Shedding in Rat Retina: Relationship to Cyclic Lighting. *Science (80-)* **194**:1071–1074.

LaVail MM, Gorrin GM, Repaci MA, Thomas LA, Ginsberg HM. 1987. Genetic regulation of light damage to photoreceptors. *Investig Ophthalmol Vis Sci* **28**:1043–1048.

Lefevere E, Toft-Kehler AK, Vohra R, Kolko M, Moons L, Van Hove I. 2017. Mitochondrial dysfunction underlying outer retinal diseases. *Mitochondrion* **36**:66–76. doi:10.1016/j.mito.2017.03.006

Lehmann GL, Benedicto I, Philp NJ, Rodriguez-Boulan E. 2014. Plasma membrane protein polarity and trafficking in RPE cells: Past, present and future. *Exp Eye Res* **126**:5–15. doi:10.1016/j.exer.2014.04.021

Lehmann WD. 2017. A timeline of stable isotopes and mass spectrometry in the life sciences. *Mass Spectrom Rev 2017* **36**:58–85. doi:10.1002/mas

Lewis A, Williams P, Lawrence O, Wong ROL, Brockerhoff SE. 2010. Wild-type cone photoreceptors persist despite neighboring mutant cone degeneration. *J Neurosci* **30**:382–389. doi:10.1523/JNEUROSCI.5019-09.2010

Li L, Dowling JE. 1998. Zebrafish visual sensitivity is regulated by a circadian clock. *Vis Neurosci* **15**:851–857. doi:10.1017/s0952523898155050

Li P, Chaurasia SS, Gao Y, Carr AL, Iuvone PM, Li L. 2008. CLOCK is required for maintaining the circadian rhythms of Opsin mRNA expression in photoreceptor cells. *J Biol Chem* **283**:31673–31678. doi:10.1074/jbc.M803875200

Li W. 2020. Ground squirrel – A cool model for a bright vision. *Semin Cell Dev Biol* **106**:127–134. doi:10.1016/j.semcdb.2020.06.005

Li W, Liu J, Galvin JA. 2016. Epigenetics and common ophthalmic diseases. *Yale J Biol Med* **89**:597–600.

Lin JB, Kubota S, Ban N, Yoshida M, Santeford A, Sene A, Nakamura R, Zapata N, Kubota M, Tsubota K, Yoshino J, Imai S ichiro, Apte RS. 2016. NAMPT-Mediated NAD+ Biosynthesis Is Essential for Vision In Mice. *Cell Rep* **17**:69–85. doi:10.1016/j.celrep.2016.08.073

Lin Y, Jiang H, Liu Y, Gameiro GR, Gregori G, Dong C, Rundek T, Wang J. 2019. Age-related alterations in retinal tissue perfusion and volumetric vessel density. *Investig Ophthalmol Vis Sci* **60**:685–693. doi:10.1167/iovs.18-25864

Lindsay KJ, Du J, Sloat SR, Contreras L, Linton JD, Turner SJ, Sadilek M, Satrústegui J, Hurley JB. 2014. Pyruvate kinase and aspartate-glutamate carrier distributions

reveal key metabolic links between neurons and glia in retina. *Proc Natl Acad Sci U S A* **111**:15579–15584. doi:10.1073/pnas.1412441111

Linton JD, Holzhausen LC, Babai N, Song H, Miyagishima KJ, Stearns GW, Lindsay K, Wei J, Chertov AO, Peters TA, Caffe R, Pluk H, Seeliger MW, Tanimoto N, Fong K, Bolton L, Kuok DLT, Sweet IR, Bartoletti TM, Radu RA, Travis GH, Zagotta WN, Townes-Anderson E, Parker E, Van Der Zee CEEM, Sampath AP, Sokolov M, Thoreson WB, Hurley JB. 2010. Flow of energy in the outer retina in darkness and in light. *Proc Natl Acad Sci U S A* **107**:8599–8604. doi:10.1073/pnas.1002471107

Litts KM, Messinger JD, Freund KB, Zhang Y, Curcio CA. 2015. Inner segment Remodeling and mitochondrial translocation in cone photoreceptors in age-related macular degeneration with outer retinal tubulation. *Investig Ophthalmol Vis Sci* **56**:2243–2253. doi:10.1167/iovs.14-15838

Lluch S, López-Fuster MJ, Ventura J. 2003. Giant mitochondria in the retina cone inner segments of shrews of genus Sorex (insectivora, soricidae). *Anat Rec - Part A Discov Mol Cell Evol Biol* **272**:484–490. doi:10.1002/ar.a.10066

López-Otín C, Blasco MA, Partridge L, Serrano M, Kroemer G. 2013. The hallmarks of aging. *Cell* **153**:1194–1217. doi:10.1016/j.cell.2013.05.039

Lotry AJ, Jacobson SG, Fishman GA, Weleber RG, Fulton AB, Namperumalsamy P, Héon E, Levin A V., Grover S, Rosenow JR, Kopp KK, Sheffield VC, Stone EM. 2001. Mutations in the CRB1 Gene Cause Leber Congenital Amaurosis Andrew. *JAMA Ophthalmol* **119**:415–420.

Lu J, Zheng X, Li F, Yu Y, Chen Z, Liu Z, Wang Z, Xu H, Yang W. 2017. Tunneling nanotubes promote intercellular mitochondria transfer followed by increased invasiveness in bladder cancer cells. *Oncotarget* **8**:15539–15552. doi:10.18632/oncotarget.14695

Lyamzaev KG, Nepryakhina OK, Saprunova VB, Bakeeva LE, Pletjushkina OY, Chernyak B V, Skulachev VP. 2008. Novel mechanism of elimination of malfunctioning mitochondria (mitoptosis): formation of mitoptotic bodies and extrusion of mitochondrial material from the cell. *Biochim Biophys Acta* **1777**:817–825. doi:10.1016/j.bbabio.2008.03.027

MacNichol EF, Kunz YW, Levine JS, Harosi FI, Collins BA. 1978. Ellipsosomes:

organelles containing a cytochrome-like pigment in the retinal cones of certain fishes. *Science (80-)* **200**:549–552. doi:10.1126/science.644317

Maryanovich M, Zaltsman Y, Ruggiero A, Goldman A, Shachnai L, Zaidman SL, Porat Z, Golan K, Lapidot T, Gross A. 2015. An MTCH2 pathway repressing mitochondria metabolism regulates haematopoietic stem cell fate. *Nat Commun* **6**:7901. doi:10.1038/ncomms8901

Masuda T, Wada Y, Kawamura S. 2016. ES1 is a mitochondrial enlarging factor contributing to form mega-mitochondria in zebrafish cones. *Sci Rep* **6**:22360. doi:10.1038/srep22360

Matschinsky FM, Passonneau JV, Lowry OH. 1968. Quantitative histochemical analysis of glycolytic intermediates and cofactors with an oil well technique. *J Histochem Cytochem* **16**:29–39.

Matsuo N, Takao K, Nakanishi K, Yamasaki N, Tanda K, Miyakawa T. 2010. Behavioral profiles of three C57BL/6 substrains. *Front Behav Neurosci* **4**:29. doi:10.3389/fnbeh.2010.00029

Mattapallil MJ, Wawrousek EF, Chan CC, Zhao H, Roychoudhury J, Ferguson TA, Caspi RR. 2012. The Rd8 mutation of the Crb1 gene is present in vendor lines of C57BL/6N mice and embryonic stem cells, and confounds ocular induced mutant phenotypes. *Invest Ophthalmol Vis Sci* **53**:2921–2927. doi:10.1167/iovs.12-9662

McComb DM, Frank TM, Hueter RE, Kajiura SM. 2010. Temporal resolution and spectral sensitivity of the visual system of three coastal shark species from different light environments. *Physiol Biochem Zool* **83**:299–307. doi:10.1086/648394

McReynolds MR, Chellappa K, Baur JA. 2020. Age-related NAD+ decline. *Exp Gerontol* **134**:110888. doi:https://doi.org/10.1016/j.exger.2020.110888

Medrano CJ, Fox DA. 1995. Oxygen consumption in the rat outer and inner retina: Light- and pharmacologically-induced inhibition. *Exp Eye Res* **61**:273–284. doi:10.1016/S0014-4835(05)80122-8

Mehalow AK, Kameya S, Smith RS, Hawes NL, Denegre JM, Young JA, Bechtold L, Haider NB, Tepass U, Heckenlively JR, Chang B, Naggert JK, Nishina PM. 2003. CRB1 is essential for external limiting membrane integrity and photoreceptor morphogenesis in the mammalian retina. *Hum Mol Genet* **12**:2179–2189.

doi:10.1093/hmg/ddg232

Mekada K, Abe K, Murakami A, Nakamura S, Nakata H, Moriwaki K, Obata Y, Yoshiki A. 2009. Genetic Differences among C57BL/6 Substrains. *Exp Anim* **58**:141–149.

Melentijevic I, Toth ML, Arnold ML, Guasp RJ, Harinath G, Nguyen KC, Taub D, Parker JA, Neri C, Gabel C, Hall DH, Driscoll M. 2017. C. elegans Neurons Jettison Protein Aggregates and Mitochondria Under Neurotoxic Stress. *Physiol Behav* **176**:139–148. doi:10.1038/nature21362

Menger GJ, Koke JR, Cahill GM. 2005. Diurnal and circadian retinomotor movements in zebrafish. *Vis Neurosci* **22**:203–209. doi:10.1017/S0952523805222083

Mercurio AM, Holtzman E. 1982. Smooth endoplasmic reticulum and other agranular reticulum in frog retinal photoreceptors. *J Neurocytol* **11**:263–293. doi:10.1007/BF01258247

Metallo CM, Walther JL, Stephanopoulos G. 2009. Evaluation of 13C isotopic tracers for metabolic flux analysis in mammalian cells. *J Biotechnol* **144**:167–174. doi:10.1016/j.jbiotec.2009.07.010

Michael R, Bron AJ. 2011. The ageing lens and cataract: A model of normal and pathological ageing. *Philos Trans R Soc B Biol Sci* **366**:1278–1292. doi:10.1098/rstb.2010.0300

Mikuła-Pietrasik J, Pakuła M, Markowska M, Uruski P, Szczepaniak-Chicheł L, Tykarski A, Książek K. 2021. Nontraditional systems in aging research: an update. *Cell Mol Life Sci* **78**:1275–1304. doi:10.1007/s00018-020-03658-w

Millard P, Delépine B, Guionnet M, Heuillet M, Bellvert F, Létisse F. 2019. IsoCor: isotope correction for high-resolution MS labeling experiments. *Bioinformatics* **35**:4484–4487. doi:10.1093/bioinformatics/btz209

Millard P, Letisse F, Sokol S, Portais JC. 2012. IsoCor: correcting MS data in isotope labeling experiments. *Bioinformatics* **28**:1294–1296. doi:10.1093/bioinformatics/bts127

Mills KF, Yoshida S, Stein LR, Grozio A, Kubota S, Sasaki Y, Redpath P, Migaud ME, Apte RS, Uchida K, Yoshino J, Imai S ichiro. 2016. Long-Term Administration of Nicotinamide Mononucleotide Mitigates Age-Associated Physiological Decline in Mice. *Cell Metab* **24**:795–806. doi:10.1016/j.cmet.2016.09.013

Mitchell W, Ng EA, Tamucci JD, Boyd KJ, Sathappa M, Coscia A, Pan M, Han X, Eddy NA, May ER, Szeto HH, Alder NN. 2020. The mitochondria-targeted peptide SS-31 binds lipid bilayers and modulates surface electrostatics as a key component of its mechanism of action. *J Biol Chem* **295**:7452–7469. doi:10.1074/jbc.RA119.012094

Mo A, Luo C, Davis FP, Mukamel EA, Henry GL, Nery JR, Urich MA, Picard S, Lister R, Eddy SR, Beer MA, Ecker JR, Nathans J. 2016. Epigenomic landscapes of retinal rods and cones. *Elife* **5**:e11613. doi:10.7554/eLife.11613

Mongin AA, Hyzinski-García MC, Vincent MY, Keller RW. 2011. A simple method for measuring intracellular activities of glutamine synthetase and glutaminase in glial cells. *Am J Physiol - Cell Physiol* **301**:814–822. doi:10.1152/ajpcell.00035.2011

Moore CL, Guberg ER. 1974. The distribution of succinic semialdehyde dehydrogenase in the brain and retina of the tiger salamander. *Brain Res* **67**:467–478. doi:10.1016/0006-8993(74)90495-8

Moy SS, Nadler JJ, Young NB, Perez A, Holloway LP, Barbaro RP, Barbaro JR, Wilson LM, Threadgill DW, Lauder JM, Magnuson TR, Crawley JN. 2007. Mouse behavioral tasks relevant to autism: Phenotypes of 10 inbred strains. *Behav Brain Res* **176**:4–20. doi:10.1016/j.bbr.2006.07.030

Mrosovsky N, Foster RG, Salmon PA. 1999. Thresholds for masking responses to light in three strains of retinally degenerate mice. *J Comp Physiol A* **184**:423–428. doi:10.1007/s003590050341

Mustari MJ. 2017. Nonhuman primate studies to advance vision science and prevent blindness. *ILAR J* **58**:216–225. doi:10.1093/ilar/ilx009

Nag TC, Bhattacharjee J. 1995. Retinal ellipsosomes: morphology, development, identification, and comparison with oil droplets. *Cell Tissue Res* **279**:633–637. doi:10.1007/BF00318176

Nag TC, Wadhwa S. 2016. Immunolocalisation pattern of complex I–V in ageing human retina: Correlation with mitochondrial ultrastructure. *Mitochondrion* **31**:20–32. doi:10.1016/j.mito.2016.08.016

Nath AK, Ryu JH, Jin YN, Roberts LD, Dejam A, Gerszten RE, Peterson RT. 2015. PTPMT1 Inhibition Lowers Glucose through Succinate Dehydrogenase Phosphorylation. *Cell Rep* **10**:694–701. doi:10.1016/j.celrep.2015.01.010

Neitz M, Neitz J. 2014. Curing color blindness—mice and nonhuman primates. *Cold Spring Harb Perspect Med* **4**:a017418. doi:10.1101/cshperspect.a017418

Nielsen J, Hedeholm RB, Heinemeier J, Bushnell PG, Christiansen JS, Olsen J, Ramsey CB, Brill RW, Simon M, Steffensen KF, Steffensen JF. 2016. Eye lens radiocarbon reveals centuries of longevity in the Greenland shark (Somniosus microcephalus). *Science (80-)* **353**:702–704. doi:10.1126/science.aaf1703

Nishikawa T, Bellancce N, Damm A, Bing H, Zhu Z, Handa K, Yovchev MI, Sehgal V, Moss TJ, Oertel M, Ram P, Pipinos II, Soto-Gutierrez A, Fox IJ, Nagrath D. 2014. A switch in the source of ATP production and a loss in capacity to perform glycolysis are hallmarks of hepatocyte failure in advance liver disease. *J Hepatol* **60**:1203–1211. doi:doi:10.1016/j.jhep.2014.02.014

Niven JE, Laughlin SB. 2008. Energy limitation as a selective pressure on the evolution of sensory systems. *J Exp Biol* **211**:1792–1804. doi:10.1242/jeb.017574

Nork TM, McCormick SA, Chao GM, Odom J V. 1990. Distribution of carbonic anhydrase among human photoreceptors. *Invest Ophthalmol Vis Sci* **31**:1451–1458.

Norkett R, Modi S, Birsa N, Atkin TA, Ivankovic D, Pathania M, Trossbach S V., Korth C, Hirst WD, Kittler JT. 2016. DISC1-dependent regulation of mitochondrial dynamics controls the morphogenesis of complex neuronal dendrites. *J Biol Chem* **291**:613–629. doi:10.1074/jbc.M115.699447

Ogawa F, Malavasi ELV, Crummie DK, Eykelenboom JE, Soares DC, Mackie S, Porteous DJ, Millar JK. 2014. DISC1 complexes with TRAK1 and Miro1 to modulate anterograde axonal mitochondrial trafficking. *Hum Mol Genet* **23**:906–919. doi:10.1093/hmg/ddt485

Ohlendieck K. 2011. Proteomic profiling of fast-to-slow muscle transitions during aging. *Front Physiol* **2**. doi:10.3389/fphys.2011.00105

Okawa H, Sampath AP, Laughlin SB, Fain GL. 2008. ATP Consumption by Mammalian Rod Photoreceptors in Darkness and in Light. *Curr Biol* **18**:1917–1921. doi:10.1016/j.cub.2008.10.029

Orlov N V., Coletta C, van Asten F, Qian Y, Ding J, AlGhatrif M, Lakatta E, Chew E, Wong W, Swaroop A, Fiorillo E, Delitala A, Marongiu M, Goldberg IG, Schlessinger

D. 2019. Age-related changes of the retinal microvasculature. *PLoS One* **14**:e0215916. doi:10.1371/journal.pone.0215916

Ortin-Martinez A, Tsai ELS, Nickerson PE, Bergeret M, Lu Y, Smiley S, Comanita L, Wallace VA. 2017. A Reinterpretation of Cell Transplantation: GFP Transfer From Donor to Host Photoreceptors. *Stem Cells* **35**:932–939. doi:10.1002/stem.2552

Owsley C. 2011. Aging and vision. *Vision Res* **51**:1610–1622. doi:10.1016/j.visres.2010.10.020

Pal S, Tyler JK. 2016. Epigenetics and aging. *Sci Adv* e1600584. doi:10.1126/sciadv.1600584

Park J, Chen Y, Tishkoff DX, Peng C, Tan M, Dai L, Xie Z, Zhang Y, Zwaans BMM, Skinner ME, Lombard DB, Zhao Y. 2013. SIRT5-mediated lysine desuccinylation impacts diverse metabolic pathways. *Mol Cell* **50**:919–930. doi:10.1016/j.molcel.2013.06.001

Park Y-U, Jeong J, Lee H, Mun JY, Kim J-H, Lee JS, Nguyen MD, Han SS, Suh P-G, Park SK. 2010. Disrupted-in-schizophrenia 1 (DISC1) plays essential roles in mitochondria in collaboration with Mitofilin. *Proc Natl Acad Sci U S A* **107**:17785–17790. doi:10.1073/pnas.1004361107

Pennington KL, DeAngelis MM. 2015. Epigenetic mechanisms of the aging human retina. *J Exp Neurosci* **9**:51–79. doi:10.4137/JEN.S25513

Perkins GA, Ellisman MH, Fox DA. 2003. Three-dimensional analysis of mouse rod and cone mitochondrial cristae architecture: Bioenergetic and functional implications. *Mol Vis* **9**:60–73.

Peterson WM, Miller SS. 1995. Identification and functional characterization of a dual GABA/taurine transporter in the bullfrog retinal pigment epithelium. *J Gen Physiol* **106**:1089–1122. doi:10.1085/jgp.106.6.1089

Piccolino M. 1988. Cajal and the retina: a 100-year retrospective. *Trends Neurosci* **11**:521–525. doi:10.1016/0166-2236(88)90175-0

Pino LK, Searle BC, Bollinger JG, Nunn B, MacLean B, MacCoss MJ. 2020. The Skyline ecosystem: Informatics for quantitative mass spectrometry proteomics. *Mass Spectrom Rev* **39**:229–244. doi:10.1002/mas.21540

Ploumi C, Daskalaki I, Tavernarakis N. 2017. Mitochondrial biogenesis and clearance: a

balancing act. *FEBS J* **284**:183–195. doi:10.1111/febs.13820

Poeschla M, Valenzano DR. 2020. The turquoise killifish: A genetically tractable model for the study of aging. *J Exp Biol* **223**:jeb209296. doi:10.1242/jeb.209296

Popov VN, Eprintsev AT, Fedorin DN, Igamberdiev AU. 2010. Succinate dehydrogenase in Arabidopsis thaliana is regulated by light via phytochrome A. *FEBS Lett* **584**:199–202. doi:https://doi.org/10.1016/j.febslet.2009.11.057

Potier S, Mitkus M, Kelber A. 2020. Visual adaptations of diurnal and nocturnal raptors. *Semin Cell Dev Biol* **106**:116–126. doi:10.1016/j.semcdb.2020.05.004

Potter VR, Dubois KP. 1943. STUDIES ON THE MECHANISM OF HYDROGEN TRANSPORT IN ANIMAL TISSUES : VI. INHIBITOR STUDIES WITH SUCCINIC DEHYDROGENASE. *J Gen Physiol* **26**:391–404. doi:10.1085/jgp.26.4.391

Prolla TA, Denu JM. 2014. NAD+ deficiency in age-related mitochondrial dysfunction. *Cell Metab* **19**:178–180. doi:10.1016/j.cmet.2014.01.005

Punzo C, Kornacker K, Cepko CL. 2009. Stimulation of the insulin/mTOR pathway delays cone death in a mouse model of retinitis pigmentosa. *Nat Neurosci* **12**:44–52. doi:10.1038/nn.2234

Punzo C, Xiong W, Cepko CL. 2012. Loss of daylight vision in retinal degeneration: Are oxidative stress and metabolic dysregulation to blame? *J Biol Chem* **287**:1642–1648. doi:10.1074/jbc.R111.304428

Rajala RVS, Rajala A, Kooker C, Wang Y, Anderson RE. 2016. The warburg effect mediator pyruvate kinase M2 expression and regulation in the retina. *Sci Rep* **6**:37727. doi:10.1038/srep37727

Raymond PA, Barthel LK, Curran GA. 1995. Developmental patterning of rod and cone photoreceptors in embryonic zebrafish. *J Comp Neurol* **359**:537–550. doi:https://doi.org/10.1002/cne.903590403

Raymond PA, Colvin SM, Jabeen Z, Nagashima M, Barthel LK, Hadidjojo J, Popova L, Pejaver VR, Lubensky DK. 2014. Patterning the cone mosaic array in zebrafish retina requires specification of ultraviolet-sensitive cones. *PLoS One* **9**:e85325. doi:10.1371/journal.pone.0085325

Rea R, Li J, Dharia A, Levitan ES, Sterling P, Kramer RH. 2004. Streamlined synaptic vesicle cycle in cone photoreceptor terminals. *Neuron* **41**:755–766.

doi:10.1016/s0896-6273(04)00088-1

Rebrin I, Kamzalov S, Sohal RS. 2003. Effects of age and caloric restriction on glutathione redox state in mice. *Free Radic Biol Med* **35**:626–635. doi:10.1016/S0891-5849(03)00388-5

Reddy AB, Karp NA, Maywood ES, Sage EA, Deery M, O'Neill JS, Wong GKY, Chesham J, Odell M, Lilley KS, Kyriacou CP, Hastings MH. 2006. Circadian orchestration of the hepatic proteome. *Curr Biol* **16**:1107–1115. doi:10.1016/j.cub.2006.04.026

Reidel B, Thompson JW, Farsiu S, Moseley MA, Skiba NP, Arshavsky VY. 2011. Proteomic profiling of a layered tissue reveals unique glycolytic specializations of photoreceptor cells. *Mol Cell Proteomics* **10**:M110.002469. doi:10.1074/mcp.M110.002469

Reyes-Reveles J, Dhingra A, Alexander D, Bragin A, Philp NJ, Boesze-Battaglia K. 2017. Phagocytosis-dependent ketogenesis in retinal pigment epithelium. *J Biol Chem* **292**:8038–8047. doi:10.1074/jbc.M116.770784

Richardson A, Fischer KE, Speakman JR, De Cabo R, Mitchell SJ, Peterson CA, Rabinovitch P, Chiao YA, Taffet G, Miller RA, Rentería RC, Bower J, Ingram DK, Ladiges WC, Ikeno Y, Sierra F, Austad SN. 2016. Measures of healthspan as indices of aging in Mice-A recommendation. *Journals Gerontol - Ser A Biol Sci Med Sci* **71**:427–430. doi:10.1093/gerona/glv080

Riepe RE, Norenburg MD. 1977. Müller cell localisation of glutamine synthetase in rat retina. *Nature* **268**:3–4.

Ritterhoff J, Tian R. 2017. Metabolismin cardiomyopathy: Every substrate matters. *Cardiovasc Res* **113**:411–421. doi:10.1093/cvr/cvx017

Rodríguez-Muela N, Hernández-Pinto AM, Serrano-Puebla A, García-Ledo L, Latorre SH, de la Rosa EJ, Boya P. 2015. Lysosomal membrane permeabilization and autophagy blockade contribute to photoreceptor cell death in a mouse model of retinitis pigmentosa. *Cell Death Differ* **22**:476–487. doi:10.1038/cdd.2014.203

Ronchi JA, Figueira TR, Ravagnani FG, Oliveira HCF, Vercesi AE, Castilho RF. 2013. A spontaneous mutation in the nicotinamide nucleotide transhydrogenase gene of C57BL/6J mice results in mitochondrial redox abnormalities. *Free Radic Biol Med*

63:446–456. doi:10.1016/j.freeradbiomed.2013.05.049

Roseboom PH, Namboodiri MAA, Zimonjic DB, Popescu NC, R. Rodriguez I, Gastel JA, Klein DC. 1998. Natural melatonin `knockdown' in C57BL/6J mice: rare mechanism truncates serotonin N-acetyltransferase. *Mol Brain Res* **63**:189–197. doi:https://doi.org/10.1016/S0169-328X(98)00273-3

Roser M, Ortiz-Ospina E, Ritchie H. n.d. Life Expectancy. *OurWorldInData.org*. https://ourworldindata.org/life-expectancy

Rozenblit F, Gollisch T. 2020. What the salamander eye has been telling the vision scientist's brain. *Semin Cell Dev Biol* **106**:61–71. doi:10.1016/j.semcdb.2020.04.010

Rueda EM, Johnson JE, Giddabasappa A, Swaroop A, Brooks MJ, Sigel I, Chaney SY, Fox DA. 2016. The cellular and compartmental profile of mouse retinal glycolysis, tricarboxylic acid cycle, oxidative phosphorylation, and ~p transferring kinases. *Mol Vis* **22**:847–885.

Rui L. 2014. Energy Metabolism in the Liver. *Compr Physiol* **4**:177–197.

Rydström J. 2006. Mitochondrial NADPH, transhydrogenase and disease. *Biochim Biophys Acta - Bioenerg* **1757**:721–726. doi:10.1016/j.bbabio.2006.03.010

Sabesan R, Hofer H, Roorda A. 2015. Characterizing the human cone photoreceptor mosaic via dynamic photopigment densitometry. *PLoS One* **10**:e0144891. doi:10.1371/journal.pone.0144891

Saftari LN, Kwon O-S. 2018. Ageing vision and falls: A review. *J Physiol Anthropol* **37**:11. doi:10.1186/s40101-018-0170-1

Sajdak BS, Salmon AE, Litts KM, Wells C, Allen KP, Dubra A, Merriman DK, Carroll J. 2019. Evaluating seasonal changes of cone photoreceptor structure in the 13-lined ground squirrel. *Vision Res* **158**:90–99. doi:10.1016/j.visres.2019.02.009

Salminen A, Kauppinen A, Hiltunen M, Kaarniranta K. 2014. Krebs cycle intermediates regulate DNA and histone methylation: Epigenetic impact on the aging process. *Ageing Res Rev* **16**:45–65. doi:10.1016/j.arr.2014.05.004

Samanta A, Aziz AA, Jhingan M, Singh SR, Khanani AM, Chhablani J. 2021. Emerging Therapies in Nonexudative Age-Related Macular Degeneration in 2020. *Asia-Pacific J Ophthalmol* **Publish Ah**:1–9. doi:10.1097/apo.0000000000000355

Samuel MA, Zhang Y, Meister M, Sanes JR. 2011. Age-related alterations in neurons of the mouse retina. *J Neurosci* **31**:16033–16044. doi:10.1523/JNEUROSCI.3580-11.2011

Santos LRB, Muller C, de Souza AH, Takahashi HK, Spégel P, Sweet IR, Chae H, Mulder H, Jonas JC. 2017. NNT reverse mode of operation mediates glucose control of mitochondrial NADPH and glutathione redox state in mouse pancreatic β-cells. *Mol Metab* **6**:535–547. doi:10.1016/j.molmet.2017.04.004

Sartori-Rupp A, Cordero Cervantes D, Pepe A, Gousset K, Delage E, Corroyer-Dulmont S, Schmitt C, Krijnse-Locker J, Zurzolo C. 2019. Correlative cryo-electron microscopy reveals the structure of TNTs in neuronal cells. *Nat Commun* **10**:342. doi:10.1038/s41467-018-08178-7

Saul AB, Cui X, Markand S, Smith SB. 2017. Detailed electroretinographic findings in rd8 mice. *Doc Ophthalmol* **134**:195–203. doi:10.1007/s10633-017-9585-y

Scarpulla RC, Vega RB, Kelly DP. 2007. Transcriptional integration of mitochondrial biogenesis. *Trends Endocirnol Metab* **23**:789–811. doi:10.1007/978-0-387-30411-3_29

Schiller PW, Nguyen TMD, Berezowska I, Dupuis S, Weltrowska G, Chung NN, Lemieux C. 2000. Synthesis and in vitro opioid activity profiles of DALDA analogues. *Eur J Med Chem* **35**:895–901. doi:10.1016/S0223-5234(00)01171-5

Schiller PW, Nguyen TMD, Chung NN, Lemieux C. 1989. Dermorphin Analogues Carrying an Increased Positive Net Charge in Their “Message” Domain Display Extremely High μ Opioid Receptor Selectivity. *J Med Chem* **32**:698–703. doi:10.1021/jm00123a035

Schousboe A, Waagepetersen HS, Sonnewald U. 2019. Astrocytic pyruvate carboxylation: Status after 35 years. *J Neurosci Res* **97**:890–896. doi:10.1002/jnr.24402

Schummer C, Delhomme O, Appenzeller BMR, Wennig R, Millet M. 2009. Comparison of MTBSTFA and BSTFA in derivatization reactions of polar compounds prior to GC/MS analysis. *Talanta* **77**:1473–1482. doi:10.1016/j.talanta.2008.09.043

Senanayake P deS., Calabro A, Hu JG, Bonilha VL, Darr A, Bok D, Hollyfield JG. 2006. Glucose utilization by the retinal pigment epithelium: Evidence for rapid uptake and

storage in glycogen, followed by glycogen utilization. *Exp Eye Res* **83**:235–246. doi:10.1016/j.exer.2005.10.034

Sengillo JD, Justus S, Cabral T, Tsang SH. 2017. Correction of monogenic and common retinal disorders with gene therapy. *Genes (Basel)* **8**:53. doi:10.3390/genes8020053

Shaqiri A, Roinishvili M, Grzeczkowski L, Chkonia E, Pilz K, Mohr C, Brand A, Kunchulia M, Herzog MH. 2018. Sex-related differences in vision are heterogeneous. *Sci Rep* **8**:7521. doi:10.1038/s41598-018-25298-8

Shin J, Chen J, Solnica-Krezel L. 2014. Efficient homologous recombination-mediated genome engineering in zebrafish using TALE nucleases. *Development* **141**:3807–3818. doi:10.1242/dev.108019

Shinnick FL, Harper AE. 1976. Branched-chain amino acid oxidation by isolated rat tissue preparations. *Biochim Biophys* **437**:477–486.

Siegel MP, Kruse SE, Percival JM, Goh J, White CC, Hopkins HC, Kavanagh TJ, Szeto HH, Rabinovitch PS, Marcinek DJ. 2013. Mitochondrial-targeted peptide rapidly improves mitochondrial energetics and skeletal muscle performance in aged mice. *Aging Cell* **12**:763–771. doi:10.1111/acel.12102

Simon MM, Greenaway S, White JK, Fuchs H, Gailus-Durner V, Wells S, Sorg T, Wong K, Bedu E, Cartwright EJ, Dacquin R, Djebali S, Estabel J, Graw J, Ingham NJ, Jackson IJ, Lengeling A, Mandillo S, Marve J, Meziane H, Preitner F, Puk O, Roux M, Adams DJ, Atkins S, Ayadi A, Becker L, Blake A, Brooker D, Cater H, Champy MF, Combe R, Danecek P, Di Fenza A, Gates H, Gerdin AK, Golini E, Hancock JM, Hans W, Hölter SM, Hough T, Jurdic P, Keane TM, Morgan H, Müller W, Neff F, Nicholson G, Pasche B, Roberson LA, Rozman J, Sanderson M, Santos L, Selloum M, Shannon C, Southwel A, Tocchini-Valentini GP, Vancollie VE, Westerberg H, Wurst W, Zi M, Yalcin B, Ramirez-Solis R, Steel KP, Mallon AM, De Angelis MH, Herault Y, Brown SDM. 2013. A comparative phenotypic and genomic analysis of C57BL/6J and C57BL/6N mouse strains. *Genome Biol* **14**:R82. doi:10.1186/gb-2013-14-7-r82

Simpson CF, Kling JM. 1968. The mechanism of mitochondrial extrusion from phenylhydrazine-induced reticulocytes in the circulating blood. *J Cell Biol* **36**:103–

109.

Simpson EM, Linder CC, Sargent EE, Davisson MT, Mobraaten LE, Sharp JJ. 1997. Genetic variation among 129 substrains and its importance for targeted mutagenesis in mice. *Nat Genet* **16**:19–27. doi:10.1038/ng0597-19

SLAUTTERBACK DB. 1965. MITOCHONDRIA IN CARDIAC MUSCLE CELLS OF THE CANARY AND SOME OTHER BIRDS. *J Cell Biol* **24**:1–21. doi:10.1083/jcb.24.1.1

Sloat S, Jankowski C, Hutto R, Giarmarco M, Cleghorn WM, Tran V, Shandar G, Brockerhoff SE, Hurley J. 2016. Quantification of Mitochondrial Structure in Photoreceptors. *Invest Ophthalmol Vis Sci* **57**:566.

Solovei I, Kreysing M, Lanctôt C, Kösem S, Peichl L, Cremer T, Guck J, Joffe B. 2009. Nuclear Architecture of Rod Photoreceptor Cells Adapts to Vision in Mammalian Evolution. *Cell* **137**:356–368. doi:10.1016/j.cell.2009.01.052

Someya E, Mori A, Asano D, Morita A, Sakamoto K, Nakahara T. 2018. Role of Glial Cells in μ-Opioid Receptor-Mediated Vasodilation in the Rat Retina. *Curr Eye Res* **43**:350–356. doi:10.1080/02713683.2017.1403631

Someya E, Mori A, Sakamoto K, Ishii K, Nakahara T. 2017. Stimulation of μ-opioid receptors dilates retinal arterioles by neuronal nitric oxide synthase-derived nitric oxide in rats. *Eur J Pharmacol* **803**:124–129. doi:10.1016/j.ejphar.2017.03.043

Son MJ, Kwon Y, Son T, Cho YS. 2016. Restoration of Mitochondrial NAD+ Levels Delays Stem Cell Senescence and Facilitates Reprogramming of Aged Somatic Cells. *Stem Cells* **34**:2840–2851. doi:10.1002/stem.2460

Song HK, Hwang DY. 2017. Use of C57BL/6N mice on the variety of immunological researches. *Lab Anim Res* **33**:119–123. doi:10.5625/lar.2017.33.2.119

Sonoda S, Spee C, Barron E, Ryan SJ, Kannan R, Hinton DR. 2009. A protocol for the culture and differentiation of highly polarized human retinal pigment epithelial cells. *Nat Protoc* **4**:662–673. doi:10.1038/nprot.2009.33

Soubannier V, McLelland G-L, Zunino R, Braschi E, Rippstein P, Fon EA, McBride HM. 2012. A vesicular transport pathway shuttles cargo from mitochondria to lysosomes. *Curr Biol* **22**:135–141. doi:10.1016/j.cub.2011.11.057

Soultoukis GA, Partridge L. 2016. Dietary Protein, Metabolism, and Aging. *Annu Rev Biochem* **85**:5–34. doi:10.1146/annurev-biochem-060815-014422

Stone J, van Driel D, Valter K, Rees S, Provis J. 2008. The locations of mitochondria in mammalian photoreceptors: Relation to retinal vasculature. *Brain Res* **1189**:58–69. doi:10.1016/j.brainres.2007.10.083

Strappazzon F, Nazio F, Corrado M, Cianfanelli V, Romagnoli A, Fimia GM, Campello S, Nardacci R, Piacentini M, Campanella M, Cecconi F. 2015. AMBRA1 is able to induce mitophagy via LC3 binding, regardless of PARKIN and p62/SQSTM1. *Cell Death Differ* **22**:419–432. doi:10.1038/cdd.2014.139

Strauss O. 2005. The retinal pigment epithelium in visual function. *Physiol Rev* **85**:845–881. doi:10.1152/physrev.00021.2004

Subramanian K, Weigert M, Borsch O, Petzold H, Garcia A, Myers E, Ader M, Solovei I, Kreysing M. 2019. Rod nuclear architecture determines contrast transmission of the retina and behavioral sensitivity in mice. *bioRxiv* **8**:e49542. doi:10.1101/752444

Sugiura A, Mattie S, Prudent J, McBride HM. 2017. Newly born peroxisomes are a hybrid of mitochondrial and ER-derived pre-peroxisomes. *Nature* **542**:251–254. doi:10.1038/nature21375

Sugiura A, McLelland G-L, Fon EA, McBride HM. 2014. A new pathway for mitochondrial quality control: mitochondrial-derived vesicles. *EMBO J* **33**:2142–2156. doi:10.15252/embj.201488104

Sun N, Youle RJ, Finkel T. 2016. The Mitochondrial Basis of Aging. *Mol Cell* **61**:654–666. doi:10.1016/j.molcel.2016.01.028

Swarup A, Samuels IS, Bell BA, Han JYS, Du J, Massenzio E, Abel ED, Boesze-Battaglia K, Peachey NS, Philp NJ. 2019. Modulating GLUT1 expression in the RPE decreases glucose levels in the retina: Impact on photoreceptors and Müller glial cells. *Am J Physiol Physiol* **316**:C121–C133.

Sweet IR, Cook DL, Wiseman RW, Greenbaum CJ, Lernmark Å, Matsumoto S, Teague JC, Krohn KA. 2002a. Dynamic perifusion to maintain and assess isolated pancreatic islets. *Diabetes Technol Ther* **4**:67–76. doi:10.1089/15209150252924111

Sweet IR, Khalil G, Wallen AR, Steedman M, Schenkman KA, Reems JA, Kahn SE, Callis JB. 2002b. Continuous Measurement of Oxygen Consumption by Pancreatic Islets. *Diabetes Technol Ther* **4**:661–672.

Sweetwyne MT, Pippin JW, Eng DG, Hudkins KL, Chiao YA, Campbell MD, Marcinek DJ, Alpers CE, Szeto HH, Rabinovitch PS, Shankland SJ. 2017. The mitochondrial-targeted peptide, SS-31, improves glomerular architecture in mice of advanced age. *Kidney Int* **91**:1126–1145. doi:10.1016/j.kint.2016.10.036

Szél Á, Röhlich P, Caffé AR, Juliussn B, Aguirre G, Van Veen T. 1992. Unique topographic separation of two spectral classes of cones in the mouse retina. *J Comp Neurol* **325**:327–342.

Szeto HH. 2006. Cell-permeable, mitochondrial-targeted, peptide antioxidants. *AAPS J* **8**:277–283. doi:10.1208/aapsj080232

Tait SWG, Green DR. 2012. Mitochondria and cell signalling. *J Cell Sci* **125**:807–815. doi:10.1242/jcs.099234

Takechi M, Kawamura S. 2005. Temporal and spatial changes in the expression pattern of multiple red and green subtype opsin genes during zebrafish development. *J Exp Biol* **208**:1337–1345. doi:10.1242/jeb.01532

Taormina G, Ferrante F, Vieni S, Grassi N, Russo A, Mirisola MG. 2019. Longevity: Lesson from model organisms. *Genes (Basel)* **10**:518. doi:10.3390/genes10070518

Tarantini S, Valcarcel-Ares NM, Yabluchanskiy A, Fulop GA, Hertelendy P, Gautam T, Farkas E, Perz A, Rabinovitch PS, Sonntag WE, Csiszar A, Ungvari Z. 2018. Treatment with the mitochondrial-targeted antioxidant peptide SS-31 rescues neurovascular coupling responses and cerebrovascular endothelial function and improves cognition in aged mice. *Aging Cell* **17**:1–12. doi:10.1111/acel.12731

Tarboush R, Novales Flamarique I, Chapman GB, Connaughton VP. 2014. Variability in mitochondria of zebrafish photoreceptor ellipsoids. *Vis Neurosci* **31**:11–23. doi:10.1017/S095252381300059X

Tarlow DM, Watkins PA, Reed RE, Miller RS, Zwergel EE, Lane MD. 1977. Lipogenesis and the synthesis and secretion of very low density lipoprotein by avian liver cells in nonproliferating monolayer culture. Hormonal effects. *J Cell Biol* **73**:332–353. doi:10.1083/jcb.73.2.332

Terluk MR, Kapphahn RJ, Soukup LM, Gong H, Gallardo C, Montezuma SR, Ferrington DA. 2015. Investigating mitochondria as a target for treating age-related macular degeneration. *J Neurosci* **35**:7304–7311. doi:10.1523/JNEUROSCI.0190-15.2015

TeSlaa T, Bartman CR, Jankowski CSR, Zhang Z, Xu X, Xing X, Wang L, Lu W, Hui S, Rabinowitz JD. 2021. The Source of Glycolytic Intermediates in Mammalian Tissues. *Cell Metab* **33**:367–378. doi:10.1016/j.cmet.2020.12.020

Thoen HH, How MJ, Chiou TH, Marshall J. 2014. A different form of color vision in mantis shrimp. *Science (80-)* **343**:411–413. doi:10.1126/science.1245824

Thomas JL, Ranski AH, Morgan GW, Thummel R. 2016. Reactive gliosis in the adult zebrafish retina. *Exp Eye Res* **143**:98–109. doi:10.1016/j.exer.2015.09.017

Thomson PA, Malavasi ELV, Grünewald E, Soares DC, Borkowska M, Millar JK. 2013. DISC1 genetics , biology and psychiatric illness, Frontiers in Biology (Beijing). doi:doi:10.1007/s11515-012-1254-7

Tomczyk S, Fischer K, Austad S, Galliot B. 2015. Hydra, a powerful model for aging studies. *Invertebr Reprod Dev* **59**:11–16. doi:10.1080/07924259.2014.927805

Toye AA, Lippiat JD, Proks P, Shimomura K, Bentley L, Hugill A, Mijat V, Goldsworthy M, Moir L, Haynes A, Quarterman J, Freeman HC, Ashcroft FM, Cox RD. 2005. A genetic and physiological study of impaired glucose homeostasis control in C57BL/6J mice. *Diabetologia* **48**:675–686. doi:10.1007/s00125-005-1680-z

Trefely S, Ashwell P, Snyder NW. 2016. FluxFix: Automatic isotopologue normalization for metabolic tracer analysis. *BMC Bioinformatics* **17**:485. doi:10.1186/s12859-016-1360-7

Truett GE, Heeger P, Mynatt RL, Truett AA, Walker JA, Warman ML. 2000. Preparation of PCR-quality mouse genomic dna with hot sodium hydroxide and tris (HotSHOT). *Biotechniques* **29**:52–54. doi:10.2144/00291bm09

Tsukamoto Y, Morigiwa K, Ueda M, Sterling P. 2001. Microcircuits for night vision in mouse retina. *J Neurosci* **21**:8616–8623. doi:10.1523/jneurosci.21-21-08616.2001

Tyrrell LP, Teixeira LBC, Dubielzig RR, Pita D, Baumhardt P, Moore BA, Fernández-Juricic E. 2019. A novel cellular structure in the retina of insectivorous birds. *Sci Rep* **9**:15230. doi:10.1038/s41598-019-51774-w

Uhlén M, Fagerberg L, Hallström BM, Lindskog C, Oksvold P, Mardinoglu A, Sivertsson Å, Kampf C, Sjöstedt E, Asplund A, Olsson I, Edlund K, Lundberg E, Navani S, Szigyarto CA-K, Odeberg J, Djureinovic D, Takanen JO, Hober S, Alm T, Edqvist P-H, Berling H, Tegel H, Mulder J, Rockberg J, Nilsson P, Schwenk JM, Hamsten

M, von Feilitzen K, Forsberg M, Persson L, Johansson F, Zwahlen M, von Heijne G, Nielsen J, Pontén F. 2015. Tissue-based map of the human proteome. *Science (80-)* **347**:1260419. doi:10.1126/science.1260419

Unuma K, Aki T, Funakoshi T, Hashimoto K, Uemura K. 2015. Extrusion of mitochondrial contents from lipopolysaccharide-stimulated cells: Involvement of autophagy. *Autophagy* **11**:1520–1536. doi:10.1080/15548627.2015.1063765

Urschel MR, O'Brien KM. 2008. High mitochondrial densities in the hearts of Antarctic icefishes are maintained by an increase in mitochondrial size rather than mitochondrial biogenesis. *J Exp Biol* **211**:2638–2646. doi:10.1242/jeb.018598

US Census Bureau. 2017. Projections of the Population by Sex and Age for the United States: 2017 to 2060. *United States Census Bur - 2017 Natl Popul Proj*. https://www.census.gov/data/tables/2014/demo/popproj/2014-summary-tables.html

Utsumi S, Sakamoto K, Yamashita T, Tomita H, Sugano E, Ishida K, Ishiyama E, Ozaki T. 2020. Presence of ES1 homolog in the mitochondrial intermembrane space of porcine retinal cells. *Biochem Biophys Res Commun* **524**:542–548. doi:10.1016/j.bbrc.2020.01.127

Valenzano DR, Benayoun BA, Singh PP, Zhang E, Etter PD, Hu CK, Clément-Ziza M, Willemsen D, Cui R, Harel I, MacHado BE, Yee MC, Sharp SC, Bustamante CD, Beyer A, Johnson EA, Brunet A. 2015. The African Turquoise Killifish Genome Provides Insights into Evolution and Genetic Architecture of Lifespan. *Cell* **163**:1539–1554. doi:10.1016/j.cell.2015.11.008

Van houcke J, Bollaerts I, Geeraerts E, Davis B, Beckers A, Van Hove I, Lemmens K, De Groef L, Moons L. 2017. Successful optic nerve regeneration in the senescent zebrafish despite age-related decline of cell intrinsic and extrinsic response processes. *Neurobiol Aging* **60**:1–10. doi:10.1016/j.neurobiolaging.2017.08.013

Van houcke J, De Groef L, Dekeyster E, Moons L. 2015. The zebrafish as a gerontology model in nervous system aging, disease, and repair. *Ageing Res Rev* **24**:358–368. doi:10.1016/j.arr.2015.10.004

Van Laar VS, Arnold B, Howlett EH, Calderon MJ, St. Croix CM, Greenamyre JT, Sanders LH, Berman SB. 2018. Evidence for compartmentalized axonal mitochondrial biogenesis: Mitochondrial DNA replication increases in distal axons

as an early response to Parkinson's disease-relevant stress. *J Neurosci* **38**:7505–7515. doi:10.1523/JNEUROSCI.0541-18.2018

Vatine G, Vallone D, Gothilf Y, Foulkes NS. 2011. It's time to swim! Zebrafish and the circadian clock. *FEBS Lett* **585**:1485–1494. doi:10.1016/j.febslet.2011.04.007

Vecino E, Rodriguez FD, Ruzafa N, Pereiro X, Sharma SC. 2016. Glia-neuron interactions in the mammalian retina. *Prog Retin Eye Res* **51**:1–40. doi:10.1016/j.preteyeres.2015.06.003

Venkatesh A, Ma S, Le YZ, Hall MN, Rüegg MA, Punzo C. 2015. Activated mTORC1 promotes long-term cone survival in retinitis pigmentosa mice. *J Clin Invest* **125**:1446–1458. doi:10.1172/JCI79766

Verdin E. 2015. NAD+ in aging, metabolism, and neurodegeneration. *Science (80-)* **350**:1208–1213. doi:10.1126/science.aac4854

Vihtelic TS, Doro CJ, Hyde DR. 1999. Cloning and characterization of six zebrafish photoreceptor opsin cDNAs and immunolocalization of their corresponding proteins. *Vis Neurosci* **16**:571–585. doi:DOI: 10.1017/S0952523899163168

Vincent AE, White K, Davey T, Philips J, Ogden RT, Lawess C, Warren C, Hall MG, Ng YS, Falkous G, Holden T, Deehan D, Taylor RW, Turnbull DM, Picard M. 2019. Quantitative 3D Mapping of the Human Skeletal Muscle Mitochondrial Network. *Cell Rep* **26**:996–1009. doi:10.1016/j.celrep.2019.01.010

Vitorica J, Satrustegui A, Machado A. 1981. Metabolic Implications of Ageing: Changes in Activities of Key Lipogenic and Gluconeogenic Enzymes in the Aged Rat Liver. *Enzyme* **26**:144–152.

Wacharasint P, Nakada T, Boyd JH, Russell JA, Walley KR. 2012. Normal-range blood lactate concentration in septic shock is prognostic and predictive. *Shock* **38**:4–10. doi:10.1097/SHK.0b013e318254d41a

Wang AL, Lukas TJ, Yuan M, Neufeld AH. 2010. Age-related increase in mitochondrial DNA damage and loss of DNA repair capacity in the neural retina. *Neurobiol Aging* **31**:2002–2010. doi:10.1016/j.neurobiolaging.2008.10.019

Wang L, Törnquist P, Bill A. 1997. Glucose metabolism in pig outer retina in light and darkness. *Acta Physiol Scand* **160**:71–74.

Wang M, Zhong Z, Zhong Y, Zhang W, Wang H. 2015. The zebrafish period2 protein

positively regulates the circadian clock through mediation of retinoic acid receptor (RAR)-related orphan receptor α (Rorα). *J Biol Chem* **290**:4367–4382. doi:10.1074/jbc.M114.605022

Wang W, Lee SJ, Scott PA, Lu X, Emery D, Liu Y, Ezashi T, Roberts MR, Ross JW, Kaplan HJ, Dean DC. 2016. Two-Step Reactivation of Dormant Cones in Retinitis Pigmentosa. *Cell Rep* **15**:372–385. doi:10.1016/j.celrep.2016.03.022

Wang X, Gerdes H-H. 2015. Transfer of mitochondria via tunneling nanotubes rescues apoptotic PC12 cells. *Cell Death Differ* **22**:1181–1191. doi:10.1038/cdd.2014.211

Wang Y, Grenell A, Zhong F, Yam M, Hauer A, Gregor E, Zhu S, Lohner D, Zhu J, Du J. 2018. Metabolic signature of the aging eye in mice. *Neurobiol Aging* **71**:223–233. doi:10.1016/j.neurobiolaging.2018.07.024

Warburg O. 1925. The metabolism of carcinoma cells. *J Cancer Res* **9**:148–163. doi:10.1158/jcr.1925.148

Wei H, Xun Z, Granado H, Wu A, Handa JT. 2016. An easy, rapid method to isolate RPE cell protein from the mouse eye. *Exp Eye Res* **145**:450–455. doi:10.1016/j.exer.2015.09.015

Wei Y, Jiang H, Shi Y, Qu D, Gregori G, Zheng F, Rundek T, Wang J. 2017. Age-related alterations in the retinal microvasculature, microcirculation, and microstructure. *Investig Ophthalmol Vis Sci* **58**:3804–3817. doi:10.1167/iovs.17-21460

Wen X, Saltzgaber GW, Thoreson WB. 2017. Kiss-and-Run Is a Significant Contributor to Synaptic Exocytosis and Endocytosis in Photoreceptors. *Front Cell Neurosci* **11**:286. doi:10.3389/fncel.2017.00286

Wenig P, Odermatt J. 2010. OpenChrom: a cross-platform open source software for the mass spectrometric analysis of chromatographic data. *BMC Bioinformatics* **11**:405. doi:10.1186/1471-2105-11-405

Weyand CM, Goronzy JJ. 2016. Aging of the immune system: Mechanisms and therapeutic targets. *Ann Am Thorac Soc* **13**:S422–S428. doi:10.1513/AnnalsATS.201602-095AW

Whitson JA, Bitto A, Zhang H, Sweetwyne MT, Coig R, Bhayana S, Shankland EG, Wang L, Bammler TK, Mills KF, Imai S-I, Conley KE, Marcinek DJ, Rabinovitch PS.

2020. SS-31 and NMN: Two paths to improve metabolism and function in aged hearts. *Aging Cell* **19**:e13213. doi:10.1111/acel.13213

Wiley CD, Velarde MC, Lecot P, Liu S, Sarnoski EA, Freund A, Shirakawa K, Lim HW, Davis SS, Ramanathan A, Gerencser AA, Verdin E, Campisi J. 2016. Mitochondrial dysfunction induces senescence with a distinct secretory phenotype. *Cell Metab* **23**:303–314. doi:10.1016/j.cmet.2015.11.011

Wilson MSC, Saiardi A. 2017. Importance of Radioactive Labelling to Elucidate Inositol Polyphosphate Signalling. *Top Curr Chem* **375**:14. doi:10.1007/s41061-016-0099-y

Winkler BS. 1981. Glycolytic and oxidative metabolism in relation to retinal function. *J Gen Physiol* **77**:667–692. doi:10.1085/jgp.77.6.667

Winkler BS, Starnes CA, Twardy BS, Brault D, Taylor RC. 2008. Nuclear magnetic resonance and biochemical measurements of glucose utilization in the cone-dominant ground squirrel retina. *Investig Ophthalmol Vis Sci* **49**:4613–4619. doi:10.1167/iovs.08-2004

Wohl SG, Reh TA. 2016. The microRNA expression profile of mouse Müller glia in vivo and in vitro. *Sci Rep* **6**:35423. doi:10.1038/srep35423

Wong YC, Peng W, Krainc D. 2019. Lysosomal Regulation of Inter-mitochondrial Contact Fate and Motility in Charcot-Marie-Tooth Type 2. *Dev Cell* **50**:339-354.e4. doi:10.1016/j.devcel.2019.05.033

Wu X, Pang Y, Zhang Z, Li X, Wang C, Lei Y, Li A, Yu L, Ye J. 2019. Mitochondria-targeted antioxidant peptide SS-31 mediates neuroprotection in a rat experimental glaucoma model. *Acta Biochim Biophys Sin (Shanghai)* **51**:411–421. doi:10.1093/abbs/gmz020

Xu H, Chen M, Manivannan A, Lois N, Forrester J V. 2008. Age-dependent accumulation of lipofuscin in perivascular and subretinal microglia in experimental mice. *Aging Cell* **7**:58–68. doi:10.1111/j.1474-9726.2007.00351.x

Yam M, Engel AL, Wang Y, Zhu S, Hauer A, Zhang R, Lohner D, Huang J, Dinterman M, Zhao C, Chao JR, Du J. 2019. Proline mediates metabolic communication between retinal pigment epithelial cells and the retina. *J Biol Chem* **294**:P10278-10289. doi:10.1074/jbc.RA119.007983

Yang N-C, Ho W, Chen Y-H, Hu M-L. 2002. A convenient one-step extraction of cellular

ATP using boiling water for the luciferin-luciferase assay of ATP. *Anal Biochem* **306**:323–327. doi:10.1006/abio.2002.5698

Yerges-Armstrong, Laura M. Ellero-Simatos S, Georgiades A, Zhu H, Lewis J, Horenstein RB, Beitelshees AL, Dane A, Reijmers T, Hankemeier T, Fiehn O, Shuldiner AR, Kaddurah-Daouk R, Network PR. 2013. Purine Pathway Implicated in Mechanism of Resistance to Aspirin Therapy: Pharmacometabolomics-Informed-Pharmacogenomics Laura. *Clin Pharmacol Ther* **94**:525–532. doi:10.1038/clpt.2013.119

Yoshioka K, Takahashi H, Homma T, Saito M, Oh KB, Nemoto Y, Matsuoka H. 1996. A novel fluorescent derivative of glucose applicable to the assessment of glucose uptake activity of Escherichia coli. *Biochim Biophys Acta* **1289**:5–9. doi:10.1016/0304-4165(95)00153-0

Youle RJ, Narendra DP. 2011. Mechanisms of mitophagy. *Nat Rev Mol Cell Biol* **12**:9–14. doi:10.1038/nrm3028

Yuan R, Peters LL, Paigen B. 2011. Mice as a mammalian model for research on the genetics of aging. *ILAR J* **52**:4–15. doi:10.1093/ilar.52.1.4

Yuan R, Tsaih S-W, Petkova SB, de Evsikova CM, Xing S, Marion MA, Bogue MA, Mills KD, Peters LL, Bult CJ, Rosen CJ, Sundberg JP, Harrison DE, Churchill GA, Paigen B. 2009. Aging in inbred strains of mice: Study design and interim report on median lifespans and circulating IGF1 levels. *Aging Cell* **8**:277–287. doi:10.1111/j.1474-9726.2009.00478.x

Žák J, Dyková I, Reichard M. 2020. Good performance of turquoise killifish (Nothobranchius furzeri) on pelleted diet as a step towards husbandry standardization. *Sci Rep* **10**:8986. doi:10.1038/s41598-020-65930-0

Zetterberg M. 2016. Age-related eye disease and gender. *Maturitas* **83**:19–26. doi:10.1016/j.maturitas.2015.10.005

Zhang H, Alder NN, Wang W, Szeto H, Marcinek DJ, Rabinovitch PS. 2020. Reduction of elevated proton leak rejuvenates mitochondria in the aged cardiomyocyte. *Elife* **9**:1–18. doi:10.7554/eLife.60827

Zhang L, Du J, Justus S, Hsu C-W, Bonet-Ponce L, Wu W-H, Tsai Y-T, Wu W-P, Jia Y, Duong JK, Mahajan VB, Lin C-S, Wang S, Hurley JB, Tsang SH. 2016.

Reprogramming metabolism by targeting sirtuin 6 attenuates retinal degeneration. *J Clin Invest* **126**:4659–4673. doi:10.1172/JCI86905

Zhang Q, Padayatti PS, Leung JH. 2017. Proton-translocating nicotinamide nucleotide transhydrogenase: A structural perspective. *Front Physiol* **8**:1–6. doi:10.3389/fphys.2017.01089

Zhao C, Yasumura D, Li X, Matthes M, Lloyd M, Nielsen G, Ahern K, Snyder M, Bok D, Dunaief JL, LaVail MM, Vollrath D. 2011. mTOR-mediated dedifferentiation of the retinal pigment epithelium initiates photoreceptor degeneration in mice. *J Clin Invest* **121**:369–383. doi:10.1172/JCI44303

Zhao GM, Qian X, Schiller PW, Szeto HH. 2003. Comparison of [Dmt1]DALDA and DAMGO in Binding and G Protein Activation at μ, δ, and κ Opioid Receptors. *J Pharmacol Exp Ther* **307**:947–954. doi:10.1124/jpet.103.054775

Zhao K, Luo G, Giannelli S, Szeto HH. 2005. Mitochondria-targeted peptide prevents mitochondrial depolarization and apoptosis induced by tert-butyl hydroperoxide in neuronal cell lines. *Biochem Pharmacol* **70**:1796–1806. doi:10.1016/j.bcp.2005.08.022

Zhao K, Zhao GM, Wu D, Soong Y, Birk A V., Schiller PW, Szeto HH. 2004. Cell-permeable peptide antioxidants targeted to inner mitochondrial membrane inhibit mitochondrial swelling, oxidative cell death, and reperfusion injury. *J Biol Chem* **279**:34682–34690. doi:10.1074/jbc.M402999200

Zhu S, Yam M, Wang Y, Linton JD, Grenell A, Hurley JB, Du J. 2018. Impact of euthanasia, dissection and postmortem delay on metabolic profile in mouse retina and RPE/choroid. *Exp Eye Res* **174**:113–120. doi:10.1016/j.exer.2018.05.032